Multifunctional Microbots for Therapeutics

A thesis submitted

in partial fulfillment of the requirements

for the degree of

Doctor of Philosophy

by

Tamanna Bhuyan

Centre for Nanotechnology

Indian Institute of Technology Guwahati

March 2020

C E R T I F I C A T E

It is certified that the works contained in this thesis entitled **"Multifunctional Microbots for Therapeutics"**, by Ms. Tamanna Bhuyan, have been carried out under our supervision and have not been submitted as a thesis elsewhere for a Ph.D degree.

Thesis supervisors

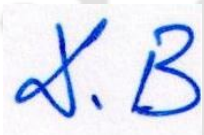

12-08-2020

12-08-2020

Prof. Dipankar Bandyopadhyay
Professor
Centre for Nanotechnology and
Department of Chemical Engineering
Indian Institute of Technology Guwahati
Assam, India

Prof. Siddhartha Sankar Ghosh
Professor
Department of Biosciences and Bioengineering
Indian Institute of Technology Guwahati,
Assam, India

March 2020

ACKNOWLEDGEMENT

The journey undertaken for the completion of this thesis has been one of the most amazing experiences of my life, which would have been impossible without these people.

First and foremost, I would like to thank my thesis supervisors **Prof. Dipankar Bandyopadhyay** and **Prof. Siddhartha Sankar Ghosh,** for giving me the opportunity to work in a fascinating area of research. I am very grateful to them for their continuous guidance, valuable advice, and stimulating discussions. Despite their busy schedule, they were always happy to dedicate their time to analyze the problems and give necessary suggestions for the betterment of my work. I am confident that the experience of working under their supervision will have far-reaching influences on my life. Their devotion towards their work, their untiring zeal to achieve perfection, and their patience in guiding novice researchers, will always inspire me. I consider it an honor to have been guided by them. I wish to thank my doctoral committee members, **Prof. B. Anand**, Department of Biosciences and Bioengineering, **Prof. Tapas K. Mandal**, and **Dr. Partho Sarathi Gooh Pattader**, Department of Chemical Engineering, for their valuable suggestions and efforts during my thesis work.

My sincere thanks to **Dr. Amit Kumar Singh, Dr. Mitradip Bhattacharjee, Dr. Nilanjan Mandal** and **Dr. Deepanjalee Dutta,** alumni from our research group, and **Dr. Nayanmani Das and Dr. Dhrubajyoti Roy,** Institute Post-Doctoral Fellows, for their unhesitating assistance and continuous encouragement throughout my PhD tenure. I wish to express my deepest gratitude to **Prof. Aynur Unal,** former Dean of Engineering and Technology at Ansal University and Founder of Digital Monozukuri for her insightful comments and suggestions. Also, I am particularly grateful to **Mr. Surjendu Maity and Mrs. Anitha T Simon** for their support in experiments.

I am also thankful to all the members of our research group, **Mr. Pritam Roy, Mr. Aniruddha Deb, Mr. Ankur Pandey, Mr. Debdatta Ghosh, Mr. Harsha Lankipalli, Mr. Joydip Chaudhuri, Dr. Abir Ghosh, Mr. Kaniska Murmu, Mr. Manash Pratim Borthakur, Ms. Mitali Basak, Mr. Nayanjyoti Kakati, Mr. Nirmal Roy, Mr. Prathu Raja Parmar, Ms. Prerona Gogoi, Mr. Sagnik Midda, Dr. Saptak Rarotra, Ms. Satarupa Dutta, Dr. Seim Timung, Mr. Shirsendu Mitra, Mr. Siddharth Thakur,**

Dr. Sunny Kumar, Mr. Sunil Kumar Singh, Mr. Subhradip Ghosh, Ms. Tanusree Ghoshal and last but not the least **Mr. Vinod Vanarse.** I cannot forget to thank my friends and colleagues **Dr. Shyam Trivedi, Dr. Shamim Rahman, Mr. Saptarshi Gupta, Mr. Siddhanta Roy, Mrs. Soumi Sarkar, Dr. Upashi Goswami, Ms. Debashree Debasmita, Ms. Kasturi Gogoi, Dr. Madhumita Das, Ms. Konika Choudhury, Ms. Srirupa Bhattacharyya, Mr. Yogendra Pratap Singh, Mr. Anil Parsram Bidkar, Mr. Sahil Jagnani, Mr. Rajib Shome, Dr. Sandipan Mukherjee, Mr. Somorjit Singh, Ms. Larionette Mawlong, Dr. Anamika Dey, Dr. Anamika Kalita, Dr. Ashish Singh, Dr. Dipjyoti Das, Ms. Nilanjana Nandi, Ms. Anwesha Chowdhury, Mrs. Niharika Haloi Kashyap, Mr. Ritesh Kant Gupta, Mr. Rahul Narasimhan, Mrs. Namami Goswami, Mrs. Anushikha Roy** and last but not the least **Ms. Shreya Mehrotra** for their role in making my stay at IIT Guwahati memorable. I want to thank all of my friends, whose name is not mentioned, for their help and support.

My special thanks to all the **faculties** and **staff members** of **Centre for Nanotechnology**, **Department of Chemical Engineering**, **Department of Chemistry**, and **Central Instruments Facility**, **IIT Guwahati**, for their supports and co-operations during all this time. I also acknowledge the support from the Analytical Laboratory in Chemical Engineering, Centre for Nanotechnology, Department of Chemistry and Central Instruments Facility, IIT Guwahati for characterization facilities.

Above all, I wish to thank my **parents, in-laws** and **family members** for their love and support throughout everything, as always. Most importantly, I would like to express gratitude to my brother, **Mr. Tridev Bhuyan** and my husband, **Mr. Ankur Bhuyan,** for their much-needed support.

Tamanna Bhuyan

TAMANNA BHUYAN

DEDICATION

To my family.

EPIGRAPH

So far as it goes, a small thing may give an analogy of great things, and show the tracks of knowledge."

- Lucretius

SYNOPSIS

Multifunctional Microbots for Therapeutics

1. Introduction

Micro-nano motors (MNMs) are intelligent machines with microscopic to nanoscopic dimensions that can transform varied energy sources into kinetic movements to accomplish sophisticated and cooperative tasks in a fluidic environment. The small size and autonomous motion of the miniaturized machines offer unique advantages for which tremendous efforts have been devoted toward the advancement of MNMs. These systems have shown promise in complicated tasks ranging from targeted drug/gene delivery, fuel cell technology, surface patterning, non-invasive nanosurgery, chemical and biological sensing, cell manipulation, cell isolation, bioimaging to environmental remediation. The advancement of such miniaturized synthetic motors has been evidenced in the form of the developed functionality and well-defined controllability. Traditionally, standard photolithography techniques, followed by e-beam deposition of metals and optional supercritical point drying, was used to prepare spherical, helical or tubular-shaped MNMs that involves more cost, time and limits biomedical applications. The possibility of using MNMs for practical biomedicine therapeutics, the biocompatibility of materials for i*n vivo* applications is still far from satisfactory.

The motion of MNMs mostly depends on the conversion of nearby fuel into thrust of gas microbubbles facilitating bubble propulsion or establishment of a concentration gradient for diffusiophoresis. However, fuel-based propulsion of micromotors hinders some *in vivo* biomedical applications, as most of the fuel used is incompatible with living systems. On the other hand, fuel-free propulsion of MNMs based on externally applied light, sound,

temperature gradient, external electric and magnetic fields provide possibilities for the application of micromotors in the domain of *in vivo* therapeutic. This enables the navigation of micro/nanomotors in various types of biological media obviating the need of chemical fuels. Notably, low-intensity magnetic and acoustic fields are considered harmless to biological systems as they have shown great promise for many biomedical applications.

Most importantly, the biosafety of MNMs primarily relies on the properties of materials for fabrication in concert with interactions between chosen materials and biological entities in the vicinity. While considerable efforts have been made towards fabrication of synthetic MNMs, further innovation is required in the– (i) use of plant-based materials in MNM design, (ii) simple and low-cost fabrication processes, (iii) fuel-free navigation of MNMs, (iv) multi-functionality of MNMs, particularly drug loading and on-demand release, before these artificial systems can be promoted for real-world applications.

In this context, the objectives of the present thesis are as follows:

- Development of micromotors using edible mushroom tissues (*Agaricus bisporus*) namely, iMushbots, for targeted anticancer therapeutics.
- Developing self-propelling motor, namely a 'Logibot', as a functional unit for the construction of a host of optimized binary logic gates based on pH taxis.
- Development of magnetotactic iButtonbots for targeting model *Escherichia coli* in contaminated drinking water.
- Development of bioactive nanomotors, namely Teabots, from *Camellia sinensis*, undergoing acoustic propulsion for targeted oxidative stress and amyloid therapeutics.
- Development of magnetically controlled bactericidal microbots using Tea buds, namely T-Budbots, for biofilm destruction and removal of biofilm debris from the substrate.

In particular, the thesis reports the fabrication of a host of micro and nanobots/motors (MNMs) derived from plants. The miniaturized motors could be efficiently guided to achieve a controlled motion under the influence of either *in situ* chemical fuel gradient or fuel-free acoustic or magnetic field. These fabricated micromotors were employed in pH sensing, drug loading, on-demand sustained drug release at a targeted site to perform vital therapeutic tasks. The details of the thesis objectives have been divided into five consecutive chapters preceded by an introductory chapter while at the end of the thesis, a chapter containing the summary and future scopes have been included. A brief detail of contributions from this thesis in terms of publications, patent and conferences has been provided at the end of this document as an APPENDIX.

2. Magnetic Field Guided Chemotaxis of iMushbots for Targeted Anticancer Therapeutics

In **Chapter 2,** controlled migration of an intelligent and biocompatible "iMushbot" composed of *Agaricus bisporus* microcapsules coated with magnetite nanoparticles has been studied (Figure 1). The otherwise randomly moving microbot could meticulously direct itself toward and away from the acid- and alkali-rich regions with the help of acid, acidic catalase, and alkali stimuli, emulating the chemotaxis of microorganisms. Although the catalytic decomposition of peroxide-fuel in alkali engendered the directed alkali taxis toward higher pH region, decomposition of peroxide fuel by the acidic catalase activity led to directed acid taxis toward the lower pH region. The presence of magnetite nanoparticles not only helped in improving the "activity" of the motor through the heterogeneous catalytic decomposition of the peroxide fuel but also provided a remote magnetic control on the chemotaxis.

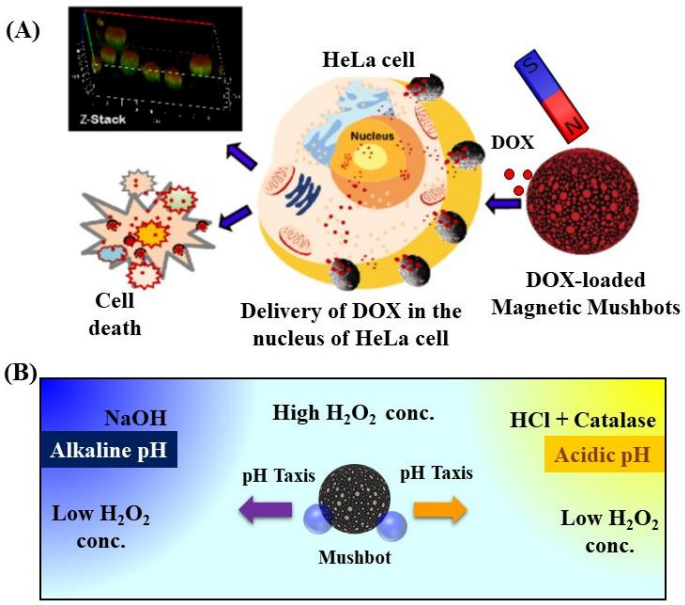

Figure 1. **(A)** Schematic diagram shows the *in vitro* delivery of the doxorubicin (DOX) by the iMushbots to the nucleus of the cancerous HeLa cells and thereby causing cell death. The inset shows the z-stacking from the confocal microscopy, which depicts the localization of the anticancer agent (depicted in red) inside the nucleus of the cancer cells. **(B)** Schematic diagram of the motor undergoing acid and alkali chemotaxis under the pH gradient. The decomposition of the H_2O_2 by the acidic catalase enzyme (sodium hydroxide) promote chemotaxis from basic (acidic) toward the acidic (basic) region.

The mesoporous iMushbots having negative ζ-potential could easily be loaded with the cationic anticancer drugs, which were magnetically guided toward the cancerous cells to cause apoptosis. The iMushbots exhibited a higher degree of drug retaining capacity inside alkaline pH and showed facile drug release preferentially in the lower pH environments. The experiments show the potential of the iMushbots in retaining and transporting drugs in an alkaline medium such as human blood and releasing them in an acidic medium such as the cancerous tissues for cell apoptosis.

3. Boolean-chemotaxis of Logibots Deciphering the Motions of Self-propelling Microorganisms.

In the **Chapter 3,** the feasibility of a self-propelling mushroom motor, namely a 'logibot' has been explored, as a functional unit for the construction of a host of optimized binary logic gates (Figure 2). Emulating the chemokinesis of unicellular prokaryotes or eukaryotes, the logibots made stimuli responsive conditional movements at varied speeds towards a pair of acid–alkali triggers. A series of integrative logic operations and cascaded logic circuits, namely, AND, NAND, NOT, OR, NOR, and NIMPLY, have been constructed employing the decisive chemotactic migrations of the logibot in the presence of the pH gradient established by the sole or coupled effects of acid (HCl-catalase) and alkali (NaOH) drips inside a peroxide bath.

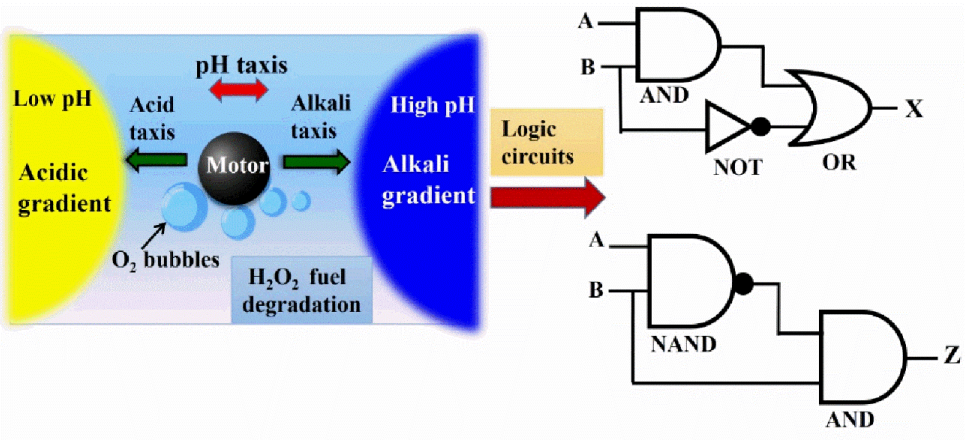

Figure 2. Schematic representing the motions of a microbot at different values of pH under the influence of acid and/or alkali stimuli. The arrows indicate the direction of migration in response to respective acid and/or alkali (colour coded) stimuli and the numbers represent the pH value of the chemical drip inside peroxide bath. Versatile operational logic gates and cascaded circuits were constructed based on pH sensing ability of tissue-based mushroom logibots.

The imposed acid and/or alkali triggers across the logibots were realized as inputs while the logic gates were functionally reconfigured to several operational modes by varying the pH of the acid–alkali inputs. The self-propelling logibot could rapidly sense the external stimuli,

decide, and act on the basis of intensities of the pH triggers. The impulsive responses of the logibots towards and away from the external acid–alkali stimuli were interpreted as the potential outputs of the logic gates. The external stimuli-responsive self-propulsion of the logibots following different logic gates and circuits can not only be an eco-friendly alternative to the silicon-based computing operations yet also be a promising strategy for the development of intelligent pH-responsive drug delivery devices.

4. Magnetotactic Curcumin iButtonbots as Efficient Bactericidal Agents

The microbial contamination of drinking water is one of the most major concerns of community health in the developing world. Numerous water-borne pathogens are rapidly evolving and becoming resistant to traditional antibiotics. In order to get an efficacious bactericidal response, an assembly of several antibiotics or increased dosage are being administered, which may produce adverse side effects after prolonged use.

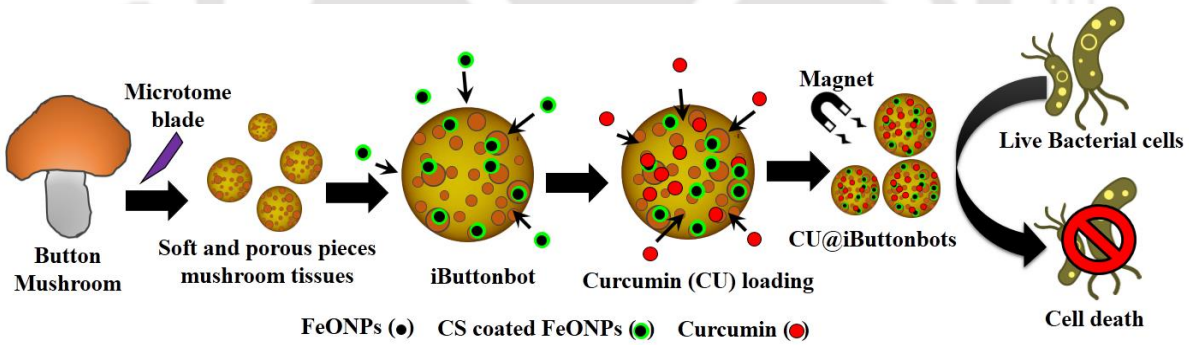

Figure 3. A brief illustration depicts the fabrication of micromotors and the destruction of *E. coli* cells using CU@iButtonbots. The edible mushrooms were cut into small fragments of the dimension 40-200 µm using fine microtome blade. The mushroom fragments were treated with a solution containing freshly prepared chitosan (CS) coated magnetic iron-oxide nanoparticles (FeONPs) to yield magnetic iButtobots. The as-obtained motors were further treated with the ethanolic solution of curcumin to yield curcumin (CU) laden iButtonbots, namely CU@iButtonbots, for antimicrobial studies.

The **Chapter 4** describes a proficient method for disinfecting water-borne coliform bacterial strains of *Escherichia coli DH5α* from contaminated water samples using magnetic microbots decorated with curcumin conjugates (Figure 3). These magnetic microbots, namely iButtonbots, were composed of soft *Agaricus bisporus* (button mushroom) microcapsules with inherent antimicrobial properties. The locomotives were coated with magnetite nanoparticles for their remote guidance towards cells and collection along with curcumin for more enhanced bactericidal response. Curcumin, a major active constituent of the Indian dietary spice turmeric, and edible button mushrooms are known to exhibit antimicrobial activity against a wide range of bacterial species. The synergic antibacterial effect of curcumin and mushroom constituents imparts a profound bactericidal property to these magnetic microbots. The microbots are capable of efficient destruction of the majority of bacterial cells in contaminated water samples. After the extermination of bacteria, magnetic properties of embedded magnetite nanoparticles in porous mushroom matrix allows collection of microbots from water samples. The presented biocompatible microbots offer an innovative method for rapid decontamination of bacteria-laden drinking water samples.

5. Acoustic Propulsion of Vitamin C Loaded Teabots for Targeted Oxidative Stress and Amyloid Therapeutics

In **Chapter 5,** the fabrication of ascorbic acid (AA) template nanomotors has been reported using buds of *Camelia sinensis*, undergoing fuel-free propulsion (Figure 4). The motors, namely, Teabots, display propulsion by converting the sound energy from the acoustic field into a mechanical one. The mesh-like structures of the anionic Teabots facilitate superior adsorption of ascorbic acid (AA-Teabots) undergoing a controlled release. The motors show antioxidant properties at the physiological pH range by scavenging

intracellular reactive oxygen species. Interestingly, the percentage release of ascorbic acid is significantly higher under the influence of ultrasound exposure, as compared to the normal pH-dependent release.

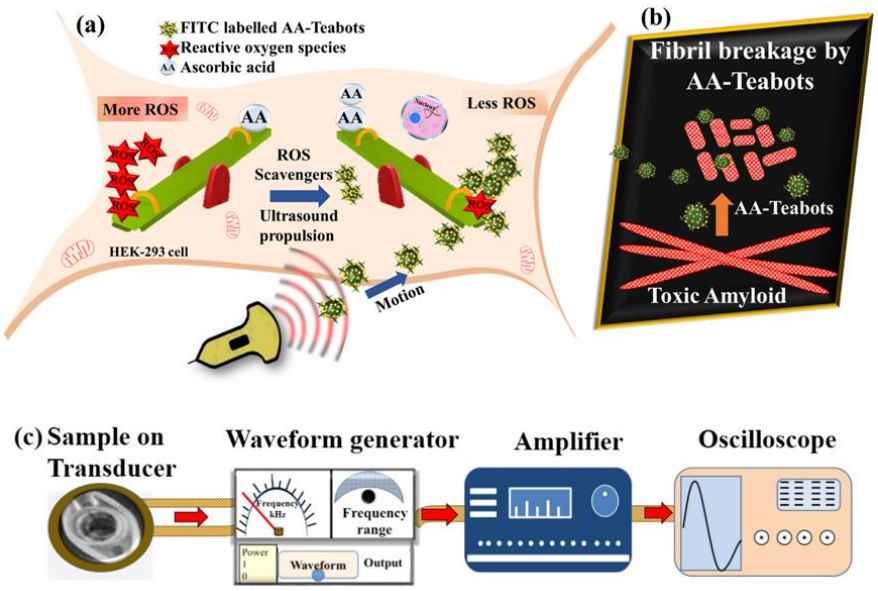

Figure 4. Schematically describes acoustic propulsion of ascorbic acid-functionalized Tea bots (AA-Teabots) **(a)** inhibiting intracellular oxidative stress by scavenging ROS and **(b)** exhibiting anti-amyloidogenic properties. **(c)** Schematic representing the experimental set up for ultrasound-powered propulsion of AA-Teabots where the sample holder was placed on a piezoelectric transducer (0.5 × 10 × 5 mm) connected to waveform generator, power amplifier and monitored using an oscilloscope.

The motors were also efficient in the degradation of artificially synthesized toxic amyloid fibrils. The acoustic delivery of AA-Teabots could protect HEK-293 cells from oxidative injuries alongside preventing protein-aggregation derived diseases. Soon, such acoustic powered biocompatible AA-Teabots are envisioned to provide an attractive approach in proficient delivery and controlled release of therapeutic payloads at targeted zones.

6. Magnetically Controlled Tea Microbots to Target Biofilms in a Kill-Clean Way

Treatment of persistent biofilm infection is formidable, even with broad-spectrum antibiotic therapies. Thus, low-cost and intelligent micromachines may serve as an active mechanical means to dislodge such deleterious bacterial communities.

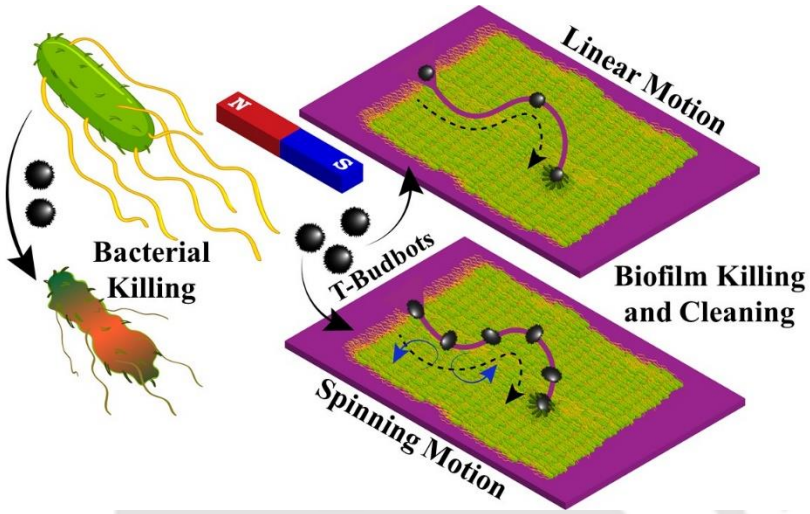

Figure 5. Schematic illustration of magnetically driven Tea-based microbots for bacterial killing and biofilm eradication in a "Kill-Clean" Way.

In **Chapter 6**, biocompatible micromotors were from Tea buds, namely, T-Budbots that can be magnetically driven on the biofilm matrix to kill and remove the fragmented biofilm segments with precision, a "Kill-Clean" strategy **(Figure 5)**. With these principles, bactericidal robotic platform was designed and decorated with magnetite nanoparticles aimed at clearing biofilm on the surfaces. The smart T-Budbots can integrate antibiotic Ciprofloxacin on their surface and increase their antibacterial efficacy against pathogenic bacterial communities of *Pseudomonas aeruginosa* and *Staphylococcus aureus*. It is noteworthy that the release of bound drug from the porous T-Budbots was triggered by the acidic environment of the biofilm. This work represents a first step in the involvement of a plant-based microbot exhibiting magneto-robotic therapeutic properties, providing a non-invasive and safe approach to dismantle harmful biofilm infections.

7. Conclusions and future scope of the study

The **Chapter 7** concludes with the thesis summary and a brief discussion on the future prospects of microbots discussed in this thesis work.

List of Figures

List of Tables

Contents

Topic **Page No.**

Nomenclature

Abbreviation	Definition	Abbreviation	Definition
ATP	Adenosine triphosphate	**CU**	Curcumin
MNMs	Micro and nanomotors	**CFU**	Colony-forming unit
FeONPs	Magnetite nanopartilces	**AA**	Ascorbic acid
DOX	Doxorubicin	**US**	Ultrasound
FETEM	Field emission transmission electron microscope	**DMEM**	Dulbecco's Modified Eagle Medium
XRD	X-ray powder diffraction	**ROS**	Reactive oxygen species
FESEM	Field emission scanning electron microscope	**HEK-293**	Human embryonic kidney 293
DLS	Dynamic light scattering	**ThT**	Thioflavin T
VSM	Vibrating-sample magnetometer	**DCFH-DA**	Dichloro-dihydro-fluorescein diacetate
CLSM	Confocal laser scanning microscope	**DPPH**	2,2-diphenyl-1-picrylhydrazyl
EDX	Energy-dispersive X-ray spectroscopy	**CIP-HCl**	Ciprofloxacin hydrochloride
HeLa	Henrietta Lacks	**LMB**	Leuco-methylene blue
NB	Nutrient broth	**ANOVA**	Analysis of variance

Abbreviation	Definition	Abbreviation	Definition
AO/EB	Acridine orange/Ethidium bromide	**TEM**	Transmission electron microscope
MIC	Minimum inhibitory concentration	**$MBIC_{50}$**	Minimum biofilm inhibitory concentration
MBC	Minimum bactericidal concentration	**AO/PI**	Acridine orange /propidium iodide
AB	Alamar Blue	**BHI**	Brain heat infusion
DPPH	2,2-diphenyl-1-picrylhydrazyl	**FT-IR**	Fourier-transform infrared spectroscopy
NBT	Nitroblue tetrazolium	**HEWL**	Hen egg-white lysozyme
MB	Methylene blue	**CV**	Crystal violet
MTT	3-(4,5-dimethylthiazol-2-yl)-2,5-diphenyl tetrazolium bromide	**LCMS**	Liquid chromatography–mass spectrometry
ζ- potential	Zeta Potential	**PBS**	Phosphate buffer saline

CHAPTER 1

Introduction

Contents

1.1. Overview

Life implies motion, expressly a movement from here to there in macroscopic and nanoscopic phases. To cite an instance, animals move away from danger, while cells use mobile molecular nanomotors for intracellular cargo transport. Further, nature has perfected a fantastic inventory of tiny protein machines that embraces control in living organisms by evolutionary modification.[1-4] These fascinating molecular machines are responsible for most forms of remarkable motion realized in the cellular world. They convert accessible chemical energy into mechanical movement in a simple and ingenious manner by involving energy-rich adenosine triphosphate (ATP) molecules.[3,5] Spontaneous reactions using ATP hydrolysis induces small conformational changes in the domain of biological motors that is amplified and translated into precise movements.[6,7] Three types of miniaturized cytoskeletal motors are well-known: myosins that propel themselves on actin filaments, and dyneins and kinesins, which uses microtubule as linear tracks for motion.[8-10] Other motor proteins include cytoplasmic ribosomes for protein synthesis and proton-gradient driven rotary ATP synthase to drive bacterial flagellar motion.[11,12]

The combination of proficiency, consistency, and ubiquity of such biological machines inspires the scientists to mimic the efficient biomotors for designing artificial small-scale machines.[13-15] Nevertheless, the inherent structural complexity of the molecular motors represents one of the significant challenges that limit the complete blending of their capabilities in the synthetic models. Also, the propulsion at macroscale may not be suitable for the thrust at nanoscale due to the domination of viscous forces.[16,17] Often, the synthetic micro/nanoscale machines successfully mimic the functionalities of biomotors, yet unable to self-reproduce and self-repair as efficiently as their biological counterparts.[16,18-20] As new

competencies are being developed considering the challenges, major efforts have been devoted by various groups to fabricate efficient high-speed synthetic micro/nanomotors (MNMs) offering great promise for realistic biomedical and environmental applications.[21-28] The sophistication of a variety of fuel-driven and fuel-free MNMs has been increasing rapidly over the past ten years, presenting unlimited opportunities. The design of self-propelled micro/nanorobots involves the integration of catalytic components with suitable materials that include polymers[29], biomolecules[30-33], biological cells[34-36], quantum dots[37,38], inorganic, and organic moieties[39-43] for autonomous movement. The specific orientation of the motors could be defined by optimizing their hydrophobic surface area to design innumerable shapes comprising helical structure[41,44,45], rod-shaped[23,24,46], tubular[47-49] and spherical geometry.[51-52] A variety of fabrication techniques[53] were employed for the synthesis of MNMs involving physical vapor deposition[54-57], template-based electrodeposition[58-60], colloidal synthesis[61-63], microfluidics[64-66] and rolled-up photolithography.[67-70]

Argued that in the year 2002, Whitesides and co-workers[21] have pioneered the self-propulsion of synthetic motors powered by asymmetric decomposition of peroxide fuel. The polymeric motor was a centimeter-sized boat with catalytic platinum strips on their stern at air-water interface. Drawing inspiration, Sen and Mallouk's[71] team at Penn State University (USA, 2004) and Ozin[23] group at the University of Toronto (Canada, 2005) developed self-electrophoretic non-Brownian motion of bimetallic Au – Pt and Au – Ni nanorods in peroxide fuel. Ever since, the growing innovations and development in the field of MNMs have led to a rapid increase in the number of research, ensuring large-scale therapeutic and environmental benefits.

1.1.1. Classification of synthetic MNMs

The efficiency of man-made motors can be increased by controlling the composition and concentration of fuel, designing robust fuel-driven motors, or exploring various fuel-free propulsion mechanisms.

1.1.2. Fuel-driven MNMs

Since the time first catalytic propulsion was demonstrated by Whitesides and co-workers[21], numerous synthetic motors were fabricated based on the use of catalytic materials that decomposes hydrogen peroxide (H_2O_2) solution into thrust of gaseous oxygen (O_2) bubbles and water. The autonomous propulsion of fuel-powered motors is due to the chemical reactions created between the catalytic motor surface and the nearby fuel, particularly peroxide[23,59,60,71,72], halogens[73], water[74-77], citric acid[78], formic acids[79], bases[80], borohydrides[81], hydrazine[82], alcohols[83], acetylene[84,] and urea[85]. Oddly enough, the molecular motors that do not depend on conformational changes also use chemical fuel for propulsion in a biological media. The propulsive thrust of fuel-driven micro/nanomotors were mostly generated by self-diffusiophoresis, self-electrophoresis, and bubble-recoil phenomenon:

- **Self-diffusiophoresis:** In this phenomenon, a non-uniform local concentration gradient of the reaction product gets established across the reactive surface of motor, as shown in **Figure 1.1 A**. [86,87] This is mostly due to the gradual and differential accumulation of end products of the decomposed fuel by the asymmetric catalytic motors, ideally on one side of the motor. As a result, the increase in local concentration allows the products to

diffuse away from motor surroundings, which initiates motor propulsion by generating adequate hydrodynamic stress.

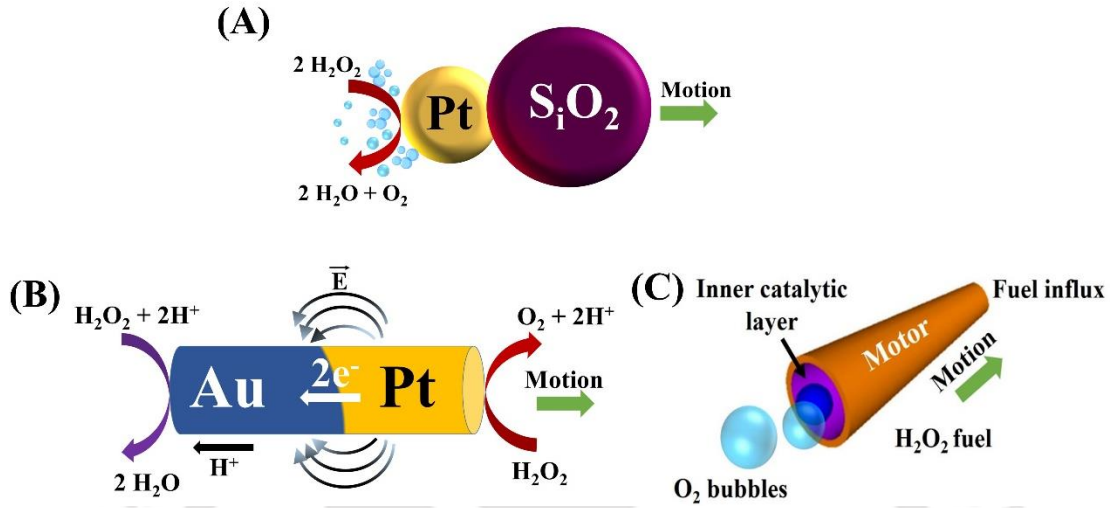

Figure 1.1. Schematic illustration of fuel-driven motions of micro/nanomotors (MNMs) undergoing **(A)** Self-diffusiophoresis **(B)** Self-electrophoresis and **(C)** Bubble propulsion. The figure has been conceptualized and drawn with reference to the reported articles.[23,59,71 60,69,86-88]

- **Self-electrophoresis:** In this phoretic mechanism, the movement of motors is due to self-generated local electric field gradient because of a non-uniform ionic distribution, as shown in **Figure 1.1 B**.[23,71] For example, an asymmetric and conductive bimetallic Au – Pt nanorods undergoes motion due to the generation of an electric gradient inside, hence acting as a small-scale electrochemical cell in peroxide fuel. The development of a proton gradient confirms the oxidation of fuel at anodic Pt end and reduction of fuel at cathodic Au end, thereby leading to a higher proton concentration at the anode. The proton deficient cathode end results in an asymmetric distribution-based establishment of local electric field gradient. Thus, the anionic Au – Pt nanorods propel towards the Pt end, thus moving in a direction opposite to the immediate proton concentration gradient.

- **Bubble-recoil mechanism:** The oxygen-bubble propulsion has been considered as the most widely explored mechanism that rapidly drives tubular and catalytic Janus particles in solutions of high ionic strength, including blood and serum. The mechanism of a bubble-propelled motor is based on spontaneous decomposition of a fuel (mostly hydrogen peroxide) by a reactive or catalytic surface of motor to generate a thrust of oxygen (O_2) or hydrogen (H_2) gas bubbles, as shown in **Figure 1.1 C**. The bubbles gradually nucleate and grows on the motor surface and eventually gets excluded from the surface. This, in turn, translates into a considerable bubble-recoil thrust for the propulsion of the motor in the opposite direction.[59, 60,69,70,88] The speed of the motor can be further improved by adding surfactants (such as sodium cholate or benzalkonium chloride) to enhance the formation and detachment rate of gaseous bubbles by reducing the surface tension. Equally significant is the reduction in the concentration of fuel required for propulsion along with the purity of fuel.

1.1.3. Fuel-free MNMs

The fuel-based propulsion systems can be applicable to remediation systems, still unsuitable for real-time biomedical therapeutics. For instance, the ultra-low concentrations of peroxide fuel are insufficient to drive the fuel-based motors, and high peroxide concentrations cause toxicity to nearby healthy cells. Thus, to enhance the biocompatibility desired for varied *in vivo* biomedical applications, several groups have investigated fuel-free propulsion of micro/nanomotors based on harnessing energy from different sources, particularly light energy[89-93], elevated thermal excitations[94-96], ultrasonic waves[97-99], electric[100,101] and magnetic fields[102-105] **(Figure 1.2)**.

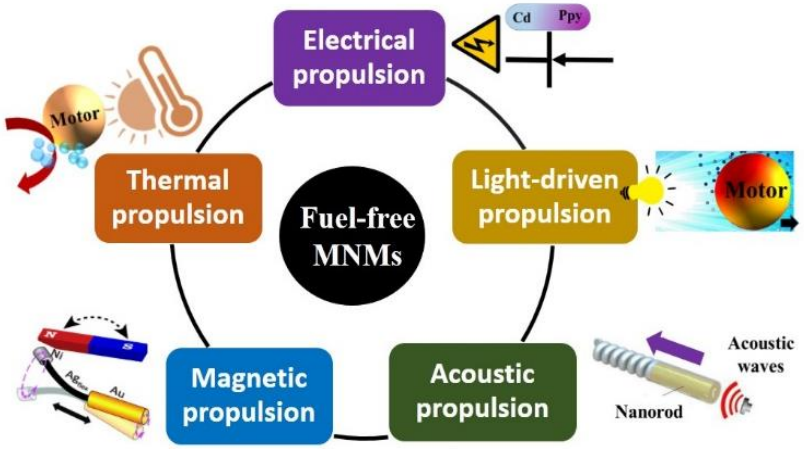

Figure 1.2. Different propulsion mechanisms of fuel-free micro/nanomotors (MNMs). The figure has been conceptualized and drawn with reference to the reported articles.[89,94,97,100-105]

Also, the external energy sources have been employed to achieve multimodal navigation on the fuel-driven propellers.

1.1.4. Plant-based biomotors

As discussed in the previous sections, tremendous advances have been made towards improving the velocity and power of synthetic MNM to facilitate more demanding tasks. Proper attention has been given to bubble-propelled synthetic micromotors relying on inner catalytic Pt layers owing to their efficient propulsion in biological media.[59,60,67,69,88] Unfortunately, the demanding *in vivo* therapeutic applications greatly precludes the development of fuel-based synthetic motors. Particular requirements would be biocompatible micro/nanorobots that can exhibit fuel-free motions coupled with optimal surface morphology and microporosity for therapeutic benefits. Intrinsic biocatalytic layers of catalase and peroxidases in plant tissues represent an attractive alternative to catalytic metals for chemically-powered propulsion of micromotors.[58,106]

The efficient plant materials could result in new ultrafast MNMs due to the intrinsic enzymatic properties required for modulation of self-propulsion. To date, few reports are available demonstrating the self-propulsion and fuel-free motion of small-scale plant tissues either by imparting the asymmetry necessary for the ejection of bubbles or an inert coating.[44,107,108] Such natural tissue MNMs eliminates immobilization of pure enzymes for propulsion, offers ultrafast motion, excellent operational stability, thermal stability at high temperatures and large-scale fabrication at remarkably low costs.[107-109] In this way, the MNMs endowed with smart biomaterials might take over the advanced life-saving drug carriers to accomplish therapeutic aids with negligible side effects. The new generation of plant-based motors needs further research to shed more light on various therapeutic and environmental applications.

1.2. Potential applications of MNMS

Self-propelling micro/nanomotors represents a novel approach for transportation of biomolecules[110-113], sensing[114,115], immunoassay[116-118], cancer therapy[119-122], drug delivery[123-125], non-invasive surgery[126,127] and gene editing[97,128]. The ability of synthetic MNMs to create local mixing and improved mass transfer have shown important prospects for environmental remediation, such as eradication and/or degradation of industrial dyes[78,129], water-borne microorganisms[75,130], oil spills[131,132], pharmaceutical pollutants[133], warfare agents[75,134,135,] and heavy metals[136]. Moreover, the MNMs has been employed for imaging[137], energy harvesting[81], nanolithography[138], designing logic gates[139,140], and repairing of electrical circuits.[141]

1.3. Brief layout of the Thesis

With this brief overview on the relevant features and applications of the MNMs, the objectives of the present thesis have been directed to implement - (i) simple, and low-cost fabrication processes (ii) the use of plant-based materials in MNM design, (iii) fuel-free navigation of MNMs, (iv) multi-functionality of MNMs, particularly drug loading and on-demand release, before these artificial systems can be promoted for real-world applications.

In this context, the objectives of the present thesis are as follows:

- Development of micromotors using edible mushroom tissues (*Agaricus bisporus*), namely, iMushbots, for targeted anticancer therapeutics.
- Developing a self-propelling motor, namely a 'Logibot', as a functional unit for the construction of a host of optimized binary logic gates based on pH taxis.
- Development of magnetotactic iButtonbots for targeting model *Escherichia coli* in contaminated drinking water.
- Development of bioactive nanomotors, namely Teabots, from *Camellia sinensis*, undergoing acoustic propulsion for targeted oxidative stress and amyloid therapeutics.
- Development of magnetically controlled bactericidal microbots using Tea buds, namely T-Budbots, for biofilm destruction and removal of biofilm debris from the surface.

In particular, the thesis reports the fabrication of a host of micro and nanorobots derived from plants. The miniaturized motors could be efficiently guided to achieve a controlled motion under the influence of either *in situ* chemical fuel gradient or fuel-free acoustic or magnetic field. These fabricated microbots were employed in pH sensing, drug loading, and on-demand sustained drug release at a targeted site to perform vital therapeutic tasks. The details of the thesis objectives have been divided into five consecutive chapters preceded by an introductory chapter, while at the end of the thesis, a chapter containing the summary and future scopes have been included.

References

(1) Chiu, W.; Baker, M. L.; Almo, S.c. Structural biology of cellular machines. *Trends. Cell. Biol*. **2006**, 16, 144-50.

(2) Kassem, S.; van Leeuwen, T.; Lubbe, A. S.; Wilson, M. R.; Feringa, B. L.; Leigh, D. A. Artificial molecular motors. *Chem. Soc. Rev*. **2017**, 46, 2592-2621

(3) Schliwa, M.; Woehlke, G. Molecular motors. *Nature* **2003**, 422, 759-65.

(4) Vale, R. D.; Milligan, R. A. The way things move: looking under the hood of molecular motor proteins. *Science* **2000**, 288, 88-95.

(5) Yewdall, N. A.; Mason, A. F.; van Hest, J. C. M. The hallmarks of living systems: towards creating artificial cells. *Interface Focus* **2018**, 8, 20180023-38.

(6) Wiegand, T.; Cadalbert, R.; Lacabanne, D.; Timmins, J.; Terradot, L.; Böckmann, A.; Meier, B. H. The conformational changes coupling ATP hydrolysis and translocation in a bacterial DnaB helicase. *Nat. Commun*. **2019**, 10, 31-42.

(7) Prieß, M.; Göddeke, H.; Groenhof, G.; Schäfer, L.V. Molecular Mechanism of ATP Hydrolysis in an ABC Transporter. *ACS Cent. Sci*. **2018**, 4, 1334−1343.

(8) Sweeney, H. L.; Houdusse, A. Structural and functional insights into the Myosin motor mechanism. *Annual Rev. Biophys*. **2010**, 39, 539-57.

(9) Carter, A. P. Crystal clear insights into how the dynein motor moves. *J. Cell Sci*. **2013**, 126, 705-13.

(10) Gennerich, A.; Vale, R. D. Walking the walk: how kinesin and dynein coordinate their steps. *Curr. Opin. Cell Biol*. **2009**, 21, 59-67.

(11) Ramakrishnan, V. Ribosome structure and the mechanism of translation. *Cell* **2002**, 108, 557-72.

(12) Oster, G.; Wang, H. ATP synthase: two motors, two fuels. *Structure* **1999**, 7, R67-R72.

(13) Erbas-Cakmak, S.; Leigh, D. A.; McTernan, C. T. Nussbaumer, A. L. Artificial Molecular Machines. *Chem. Rev*. **2015**, 115, 10081-206.

(14) Cheng, C.; Stoddart, J. F. Wholly Synthetic Molecular Machines. *ChemPhysChem*. **2016**, 17, 1780-93.

(15) Paxton, W. F.; Sundararajan, S.; Mallouk, T. E.; Sen, A. Chemical locomotion. *Angew. Chem. Int. Ed*. **2006**, 45, 5420-9.

(16) Wang, J. Can Man-Made Nanomachines Compete with Nature Biomotors? *ACS Nano* **2009**, 3, 4-9.

(17) Li, J.; Rozen, I.; Wang, J. Rocket Science at the Nanoscale. *ACS Nano* **2016**, 10, 5619−5634.

(18) Goel, A.; Vogel, V. Harnessing Biological Motors to Engineer Systems for Nanoscale Transport and Assembly. *Nat. Nanotechnol*. **2008**, 3, 465–475.

(19) Vogel, V. Reverse Engineering: Learning from Proteins how to enhance the Performance of Synthetic Nanosystems. *MRS Bull*. **2002**, 27, 972–978.

(20) Asturian, R. D. Making Molecules into Motors. *Sci. Am*. **2001**, 285, 56–64.

(21) Ismagilov, R. F.; Schwartz, A.; Bowden, N.; Whitesides, G. M. Autonomous Movement and Self-Assembly. *Angew. Chem. Int. Ed*. **2002**, 41, 652-654.

(22) Catchmark, J. M.; Subramanian, S.; Sen, A. Directed rotational motion of microscale objects using interfacial tension gradients continually generated via catalytic reactions. *Small* **2005**, 1, 202-206.

(23) Fournier-Bidoz, S.; Arsenault, A. C.; Manners, I.; Ozin, G. A.; Synthetic self-propelled nanorotors. *Chem. Commun*. **2005**, 441-443.

(24) Laocharoensuk, R.; Burdick, J.; Wang, J. Carbon-Nanotube-Induced Acceleration of Catalytic Nanomotors. *ACS Nano***, 2008**, 2, 1069-1075.

(25) Abdelmohsen, Loai K. E. A.; Peng, F.; Tu, Y.; Wilson, D. A. Micro- and nano-motors for biomedical applications. *J. Mater. Chem. B*. **2014**, 2, 2395–2408.

(26) Wang, S.; Liu, X.; Wang, Y.; Xu, D.; Liang, C.; Guo, J.; Ma, X. Biocompatibility of artificial micro/nanomotors for use in biomedicine. *Nanoscale* **2019**, 11, 14099–14112.

(27) Parmar, J.; Vilela, D.; Villa, K.; Wang, J.; Sanchez, S. Micro- and Nanomotors as Active Environmental Microcleaners and Sensors. *J. Am. Chem. Soc*. **2018**, 140, 9317−9331.

(28) Soler, L.; Sánchez, S. Catalytic nanomotors for environmental monitoring and water remediation. *Nanoscale* **2014**, 6, 7175-7182.

(29) Hermanová, S.; Pumera, M. Polymer platforms for micro- and nanomotors fabrication. *Nanoscale*, **2018**, 10, 7332-7342.

(30) Ma, X.; Hortelão, A.C.; Patiño, T.; Sánchez, S. Enzyme Catalysis to Power Micro/ Nanomachines. *ACS Nano* **2016**, 10, 9111-9122.

(31) Sengupta, S.; Dey, K. K.; Muddana, H. S.; Tabouillot, T.; Ibele, M. E.; Butler, P. J.; Sen, A. Enzyme Molecules as Nanomotors. *J. Am. Chem. Soc*. **2013**, 135, 1406-1414.

(32) Schattling, P. S.; Ramos-Docampo, M. A.; Salgueiriño, V.; Städler, B. Double-Fueled Janus Swimmers with Magnetotactic Behavior. *ACS Nano* **2017**, 11, 3973-3983.

(33) Van Nguyen. K.; Minteer, S. D. DNA-functionalized Pt nanoparticles as catalysts for chemically powered micromotors: toward signal-on motion-based DNA biosensor. *Chem. Commun*. **2015**, 51, 4782-4784.

(34) Wu, Z.; Li, T.; Li, J.; Gao, W.; Xu, T.; Christianson, C.; Gao, W.; Galarnyk, M.; He, Q.; Zhang, L.; Wang, J. Turning Erythrocytes into Functional Micromotors. *ACS Nano* **2014**, 8, 12041-12048.

(35) Wu, Z.; Esteban-Fernández de Ávila, B.; Martín, A.; Christianson, C.; Gao, W.; Thamphiwatana, S. K.; Escarpa, A.; He, Q.; Zhang, L.; Wang, J. RBC micromotors carrying multiple cargos towards potential theranostic applications. *Nanoscale* **2015**, 7, 13680-6.

(36) Magdanz, V.; Sanchez, S.; Schmidt, O. G. Development of a sperm-flagella driven micro-bio-robot. *Adv. Mater*. **2013**, 25, 6581-8.

(37) Jurado-Sánchez, B.; Escarpa, A.; Wang, J. Lighting up micromotors with quantum dots for smart chemical sensing. *Chem. Commun*. **2015**, 51, 14088-14091.

(38) Jurado-Sánchez, B.; Pacheco, M.; Rojo, J.; Escarpa, A. Magnetocatalytic Graphene Quantum Dots Janus Micromotors for Bacterial Endotoxin Detection. *Angew. Chem. Int. Ed*. **2017**, 56, 6957-6961.

(39) Soler, L.; Magdanz, V.; Fomin, V. M.; Sanchez, S.; Schmidt, O. G. Self-propelled micromotors for cleaning polluted water. *ACS Nano* **2013**, 7, 9611-20.

(40) Kuralay, F.; Sattayasamitsathit, S.; Gao, W.; Uygun, A.; Katzenberg, A.; Wang, J. Self-propelled carbohydrate-sensitive microtransporters with built-in boronic acid recognition for isolating sugars and cells. *J. Am. Chem. Soc*. **2012**, 134, 15217-20.

(41) Venugopalan, P. L.; Jain, S.; Shivashankar, S.; Ghosh, A. Single coating of zinc ferrite renders magnetic nanomotors therapeutic and stable against agglomeration. *Nanoscale* **2018**, 10, 2327-2332.

(42) Wang, W.; Duan, W.; Ahmed, S.; Mallouk, T. E.; Sen, A. Small power: Autonomous nano- and micromotors propelled by self-generated gradients. *Nano Today* **2013**, 8, 531-554.

(43) Chen, X. Z.; Hoop, M.; Mushtaq, F.; Siringil, E.; Hu, C.; Nelson, B. J.; Pané, S. Recent developments in magnetically driven micro- and nanorobots. *Appl. Mater. Today*. **2017**, 9, 37-48.

(44) Gao, W.; Feng, X.; Pei, A.; Kane, C. R.; Tam, R.; Hennessy, C.; Wang, J. Bioinspired Helical Microswimmers Based on Vascular Plants. J. *Nano Lett*. **2014**, 14, 305-310.

(45) Ghosh, A.; Dasgupta, D.; Pal, M.; Morozov, K. I.; Leshansky, A. M.; Ghosh, A. Helical Nanomachines as Mobile Viscometers. *Adv. Funct. Mater.* **2018**, 1705687, 1-6.

(46) Ying, Y.; Pourrahimi, A. M.; Sofer, Z.; Matejkova, S.; Pumera, M. Radioactive Uranium Preconcentration via Self-Propelled Autonomous Microrobots Based on Metal–Organic Frameworks. *ACS Nano* **2019**, 13, 11477-11487.

(47) Zha, F.; Wang, T.; Luo, M.; Guan, J. Tubular Micro/Nanomotors: Propulsion Mechanisms, Fabrication Techniques and Applications. Micromachines **2018**, 9, 78-104.

(48) Bing, X.; Zhang, X.; Li, J.; Ng Dickon, H. L.; Yang, W; Yang, J. 3D hierarchical tubular micromotors with highly selective recognition and capture for antibiotics. *J. Mater. Chem. A.* **2020**, 8, 2809–2819.

(49) Xu, B.; Zhang, B.; Wang, Lu.; Huang, G.; Mei, Y. Tubular Micro/Nanomachines: From the Basics to Recent Advances. *Adv. Funct. Mater*. **2018**, 28, 1705872-96.

(50) Gibbs, J. G.; Zhao, Y. P. Autonomously motile catalytic nanomotors by bubble propulsion. *Appl. Phys. Lett*. **2009**, 94, 1631041-3.

(51) Pourrahimi, A. M.; Pumera, M. Multifunctional and self-propelled spherical Janus nano/micromotors: recent advances. *Nanoscale* **2018**, 10, 16398–16415.

(52) Howse, J. R.; Jones, R. A. L.; Ryan, A. J.; Gough, T.; Vafabakhsh, R.; Golestanian, R. Self-Motile Colloidal Particles: From Directed Propulsion to Random Walk. *Phys. Rev. Lett*. **2007**, 99, 1-4.

(53) Wang, H.; Pumera, M. Fabrication of Micro/Nanoscale Motors. *Chem. Rev*. **2015**, 115, 8704-8735.

(54) Jurado-Sánchez, B.; Escarpa, A. Janus Micromotors for Electrochemical Sensing and Biosensing Applications: A Review. *Electroanalysis* **2017**, 29, 14-23.

(55) Choudhury, U.; Soler, L.; Gibbs, J. G.; Sanchez, S.; Fischer, P. Surface roughness-induced speed increase for active Janus micromotors. *Chem. Commun*. **2015**, 51, 8660-8663.

(56) Li, J.; Yang, S.; Jiang, J. Z.; Xiao, Q.; Yao, F. Z.; Sun, J. J. Fabrication and characterization of Au–Fe/Ni/(Mo/Co) alloy microsphere motors (AMSM) based on physical vapor deposition. *J. Electroanal. Chem*. **2016**, 781, 245-250.

(57) Zhang, Q.; Dong, R.; Chang, X.; Ren, B. Tong, Z. Spiropyran-Decorated SiO_2-Pt Janus Micromotor: Preparation and Light-Induced Dynamic Self-Assembly and Disassembly. *ACS Appl. Mater. Interfaces*. **2015**, 7, 24585-91.

(58) Gao, W.; Sattayasamitsathit, S.; Uygun, A.; Pei, A.; Ponedal, A.; Wang, J. Polymer-based tubular microbots: role of composition and preparation. *Nanoscale* **2012**, 4, 2447-53.

(59) Manesh, K. M; Cardona, M.; Yuan, R.; Clark, M.; Kagan, D.; Balasubramanian, S.; Wang, J. Template-assisted fabrication of salt-independent catalytic tubular microengines. *ACS Nano* **2010**, 4, 1799-804.

(60) Li, Y.; Wu, J.; Xie, Y.; Ju, H. An efficient polymeric micromotor doped with Pt nanoparticle@carbon nanotubes for complex bio-media. *Chem. Commun*. **2015**, 51, 6325-6328.

(61) Gao, W.; Liu, M.; Liu, L.; Zhang, H.; Dong, B.; Li, C. Y. One-step fabrication of multifunctional micromotors. *Nanoscale* **2015**, 7, 13918-13923.

(62) Del Mercato, L. L.; Carraro, M.; Zizzari, A.; Bianco, M.; Miglietta, R.; Arima, V.; Viola, I.; Nobile, C.; Sorarù, A.; Vilona, D.; Gigli, G.; Bonchio, M.; Rinaldi, R. Catalytic Self-Propulsion of Supramolecular Capsules Powered by Polyoxometalate Cargos. *Chem. A Eur. J*. **2014**, 20, 10910-10914.

(63) Peng, F.; Tu, Y.; Van Hest, J. C. M.; Wilson, D. A. Self-Guided Supramolecular Cargo-Loaded Nanomotors with Chemotactic Behavior towards Cells. *Angew. Chem. Int. Ed*. **2015**, 54, 11662-11665.

(64) Yu, Y.; Shang, L.; Gao, W.; Zhao, Z.; Wang, H.; Zhao, Y. Microfluidic Lithography of Bioinspired Helical Micromotors. *Angew. Chem. Int. Ed*. **2017**, 56, 12127-12131.

(65) Chen, A.; Ge, X.; Chen, J.; Zhang, L.; Xu, J. H. Multi-functional micromotor: microfluidic fabrication and water treatment application. *Lab Chip*. **2017**, 17, 4220-4224.

(66) Kherzi, B.; Pumera, M. Self-propelled autonomous nanomotors meet microfluidics. *Nanoscale* **2016**, 8, 17415–17421.

(67) Mei, Y.; Solovev, A. A.; Sanchez, S.; Schmidt, O. G. Rolled-up nanotech on polymers: from basic perception to self-propelled catalytic microengines. *Chem. Soc. Rev*. **2011**, 40, 2109-19.

(68) Solovev, A. A.; Mei, Y.; Ureña, E. B.; Huang, G.; Schmidt, O. G. Catalytic microtubular jet engines self-propelled by accumulated gas bubbles. *Small* **2009**, 5, 1688-92.

(69) Restrepo-Pérez, L.; Soler, L.; Martínez-Cisneros, C.; Sánchez, S.; and Schmidt, O. G. Biofunctionalized self-propelled micromotors as an alternative on-chip concentrating system. *Lab Chip*. **2014**, 14, 2914-2917.

(70) Mei, Y.; Huang, G.; Solovev, A. A.; Ureña, E. B.; Mönch, I.; Ding, F.; Reindl, T.; Fu, R. K. Y.; Chu, P. K.; Schmidt, O. G. Versatile Approach for Integrative and Functionalized Tubes by Strain Engineering of Nanomembranes on Polymers. *Adv. Mater*. **2008**, 20, 4085-4090.

(71) Paxton, W. F.; Kistler, K. C.; Olmeda, C. C.; Sen, A.; Angelo, S. K. S.; Cao, Y.; Mallouk, T. E.; Lammert, P. E.; Crespi, V. H. Catalytic nanomotors: autonomous movement of striped nanorods. *J. Am. Chem. Soc*. **2004**, 13424-13431.

(72) Ye, H.; Ma, G.; Kang, J.; Sun, H.; Wang, S. Pt - Free microengines at extremely low peroxide levels. *Chem. Commun*. **2018**, 54, 4653-4656.

(73) Liu, R.; Sen, A. Autonomous Nanomotor Based on Copper–Platinum Segmented Nanobattery. *J. Am. Chem. Soc*. **2011**, 133, 20064-20067.

(74) Gao, W.; Pei, A.; Wang, J. Water-Driven Micromotors. *ACS Nano* **2012**, 6, 8432-8438.

(75) Li, J.; Singh, V. V.; Sattayasamitsathit, S.; Orozco, J.; Kaufmann, K.; Dong, R.; Gao, W.; Jurado-Sanchez, B.; Fedorak, Y.; Wang, J. Water-driven micromotors for rapid photocatalytic degradation of biological and chemical warfare agents. *ACS Nano* **2014**, 8, 11118-25.

(76) Wang, R.; Guo, W.; Li, X.; Liu, Z.; Liu, H.; Ding, S. Highly efficient MOF-based self-propelled micromotors for water purification. *RSC Adv*. **2017**, 7, 42462-42467.

(77) Chen, C.; Karshalev, E.; Guan, J.; Wang, J. Magnesium-Based Micromotors: Water-Powered Propulsion, Multifunctionality, and Biomedical and Environmental Applications. *Small* **2018**, 14, 1704252.

(78) Teo, W. Z.; Zboril, R.; Medrik, I.; Pumera, M. Fe^0 Nanomotors in Ton Quantities (10^{20} Units) for Environmental Remediation. *Chem. Eur. J.* **2016**, 22, 4789-4793.

(79) Singh, A. K.; Rarotra, S.; Pasumarthi, V.; Mandal, T. K.; Bandyopadhyay, B. Formic acid powered reusable autonomous ferrobots for efficient hydrogen generation under ambient conditions. *J. Mater. Chem. A*, **2018**, 6, 9209–9219.

(80) Gao, W.; Agostino, M. D.; Garcia-Gradilla, V.; Orozco, J.; Wang. J. Multi-Fuel Driven Janus Micromotors. *Small*, **2013,** 9, 467-471

(81) Singh, V. V.; Soto, F.; Kaufmann, K.; Wang, J. Micromotor-based energy generation. *Angew. Chem. Int. Ed*. **2015**, 54, 6896-9.

(82) Dong, R.; Li, J.; Rozen, I.; Ezhilan, B.; Xu, T.; Christianson, C.; Gao, W.; Saintillan, D.; Ren, B.; Wang, J. Vapor-Driven Propulsion of Catalytic Micromotors. *Sci Rep*. **2015**, 5, 13226-34.

(83) Yamamoto, D.; Takada, T.; Tachibana, M.; Iijima, Y.; Shioi, A; Yoshikawa, K. Micromotors working in water through artificial aerobic metabolism. *Nanoscale* **2015**, 7, 13186-13190.

(84) Moo, J. G. S.; Wang, H.; Pumera, M. Acetylene bubble-powered autonomous capsules: towards in situ fuel. *Chem. Commun*. **2014**, 50, 15849-.15851.

(85) Ma, X.; Wang, X.; Hahn, K.; Sanchez, S. Motion Control of Urea-Powered Biocompatible Hollow Microcapsules. *ACS Nano*, **2016**, 10, 3597-3605.

(86) Yang, F.; Qian, S.; Zhao, Y.; Qiao, R. Self-Diffusiophoresis of Janus Catalytic Micromotors in Confined Geometries. *Langmuir* **2016**, 32, 5580-92.

(87) Velegol, D.; Garg, A.; Guha, R.; Kar, A.; Kumar, M. Origins of concentration gradients for Diffusiophoresis. *Soft Matter* **2016**, 12, 4686-4703.

(88) Gao, W.; Sattayasamitsathit, S.; Orozco, L.; Wang, J. Highly Efficient Catalytic Microengines: Template Electrosynthesis of Polyaniline/Platinum Microtubes. *J. Am. Chem. Soc*., **2011**, 133, 11862-11864.

(89) Enachi, M.; Guix, M.; Postolache, V.; Ciobanu, V.; Fomin, V. M.; Schmidt, O. G.; Tiginyanu, I. Light-Induced Motion of Microengines Based on Microarrays of TiO_2 Nanotubes. *Small* **2016**, 12, 5497-5505.

(90) Zhou, D.; Li, Y. C.; Xu, P.; McCool, N. S.; Li, L.; Wang, W.; Mallouk, T. E. Visible-light controlled catalytic Cu_2O–Au Micromotors. *Nanoscale* **2017**, 9, 75-78.

(91) Eskandarloo, H.; Kierulf, A.; Abbaspourrad, A. Light-harvesting synthetic nano- and micromotors:A review. *Nanoscale* **2017**, 9, 12218-12230.

(92) Safdar, M.; Simmchen, J.; Janis, J. Light-driven micro- and nanomotors for environmental remediation. *Environ. Sci. Nano*. **2017**, 4, 1602-1616.

(93) Villa, K.; Pumera, M. Fuel-free light-driven micro/nanomachines: artificial active matter mimicking nature. *Chem. Soc. Rev*. **2019**, 48, 4966-4978.

(94) Lin, X.; Si, T.; Wu, Z.; He, Q. Self-thermophoretic motion of controlled assembled micro-/nanomotors. *Phys. Chem. Chem. Phys*. **2017**, 19, 23606-23613.

(95) He, W.; Frueh, J.; Hu, N.; Liu, L.; Gai,M.; He, Q. Guidable Thermophoretic Janus Micromotors Containing Gold Nanocolorifiers for Infrared Laser Assisted Tissue Welding. *Adv. Sci*. **2016**, 3, 1600206-15.

(96) Baraban, L.; Streubel, R.; Makarov, D.; Han, L.; Karnaushenko, D.; Schmidt, O. G.;. Cuniberti, G. Fuel-free locomotion of Janus motors: magnetically induced thermophoresis. *ACS Nano* **2013**, 7, 1360-7.

(97) Hansen-Bruhn, M.; de Ávila, B. E. F.; Beltrán-Gastélum, M.; Zhao, J.; Ramírez Herrera, D. E.; Angsantikul, P.; Vesterager Gothelf, K.; Zhang, L.; Wang, Active Intracellular Delivery of a Cas9/sgRNA Complex Using Ultrasound-Propelled Nanomotors. *J. Angew. Chem. Int. Ed*. **2018**, 57, 2657-2661.

(98) Uygun, M.; Jurado-Sánchez, B.; Uygun, D. A.; Singh, V. V.; Zhang, L.; Wang, J. Ultrasound-propelled nanowire motors enhance asparaginase enzymatic activity against cancer cells. *Nanoscale* **2017**, 9, 18423-18429.

(99) Lu, X.; Shen, H.; Zhao, K.; Wang, Z.; Peng, H.; Liu, W. Micro-/Nanomachines Driven by Ultrasonic Power Sources. *Chem. Asian J.* **2019**, 14, 2406 – 2416.

(100) Calvo-Marzal, P.; Sattayasamitsathit, S.; Balasubramanian, S.; Windmiller, J. R.; Dao, C.; Wang, J. Propulsion of nanowire diodes. *Chem. Commun*. **2010**, 46, 1623-1624.

(101) Bouf, L.; Ravaine, V.; Sojic, N.; Kuhn, A. Electric fields for generating unconventional motion of small objects. *Curr. Opin. Colloid Interface Sci*. **2016**, 21, 57-64.

(102) Wang, J.; Manesh, K. M. Motion control at the nanoscale. *Small* **2010**, 6, 338-45.

(103) Chen, X. Z.; Hoop, M.; Mushtaq, F.; Siringil, E.; Hu, C.; Nelson, B. J.; Pané, S. Recent developments in magnetically driven micro- and nanorobots. *Appl. Mater. Today* **2017**, 9, 37-48.

(104) Chen, X. Z.; Liu, J. H.; Dong, M.; Muller, L.; Chatzipirpiridis, G.; Hu, C.; Terzopoulou, A.; Torlakcik, H.; Wang, X.; Mushtaq, F.; Puigmartı´-Luis, J.; Shen, Q. D.; Nelson, B. J.; Pane, S. Magnetically driven piezoelectric soft microswimmers for neuron-like cell delivery and neuronal differentiation. *Mater. Horiz.* **2019**, 6, 1512-1516.

(105) Liu, M.; Wang, Y.; Kuai, Y.; Cong, J.; Xu, Y.; Piao, H. G.; Pan, L.; Liu, Y. Magnetically Powered Shape-Transformable Liquid Metal Micromotors. *Small* **2019**, 15, 1905446-13.

(106) Sanchez, S.; Solovev, A. A.; Mei, Y.; Schmidt, O. G. Dynamics of biocatalytic microengines mediated by variable friction control. *J Am Chem Soc*. **2010**, 132, 13144-5.

(107) Gu, Y.; Sattayasamitsathit, S.; Kaufmann, K.; Vazquez-Duhalt, R.; Gao, W.; Wang, C.; Wang, J. Self-propelled chemically-powered plant-tissue biomotors. *Chem. Commun*. **2013**, 49, 7307-7309.

(108) Arque, X.; Romero-Rivera, A.; Feixas, F.; Patino, T.; Osuna, S.; Sanchez, S. Intrinsic enzymatic properties modulate the self-propulsion of micromotors. Nat. Commun. **2019**, 10, 2826-38.

(109) Wang, J.; Lin, M. S. Mixed plant tissue carbon paste bioelectrode. *Anal. Chem*. **1988**, 60, 1545-1548.

(110) Shao, J.; Xuan, M.; Zhang, H.; Lin, X.; Wu, Z.; He, Q. Chemotaxis-Guided Hybrid Neutrophil Micromotors for Targeted Drug Transport. *Angew. Chem. Int. Ed*. **2017**, 56, 12935-12939.

(111) Dogra, N.; Izadi, H.; Vanderlick, T. K. Micro-motors: A motile bacteria based system for liposome cargo transport. *Sci. Rep*. 2**016**, 6, 29369-78.

(112) Baraban, L.; Tasinkevych, M.; Popescu, M. N.; Sanchez, S.; Dietrich, S.; Schmidt, O. G. Transport of cargo by catalytic Janus micro-motors. *Soft Matter* **2012**, 8, 48-52.

(113) Baeza, A.; Regi, M. V. Nanomotors for Nucleic Acid, Proteins, Pollutants and Cells Detection. *Int J Mol Sci*. **2018**, 19, 1579-1592.

(114) Wang, J. Self-propelled affinity biosensors: Moving the receptor around the sample. *Biosens. Bioelectron*. **2016**, 76, 234-42.

(115) Zhang, Y.; Yuan, K.; Zhang, L. Micro/Nanomachines: from Functionalization to Sensing and Removal. *Adv. Mater. Technol*. **2019**, 4, 1800636-58.

(116) Maria-Hormigos, R.; Jurado-Sánchez, B.; Escarpa, A. Labs-on-a-chip meet self-propelled micromotors. *Lab Chip*. **2016**, 16, 2397-2407.

(117) de Ávila, B. E. F.; Zhao, M.; Campuzano, S.; Ricci, F.; Pingarrón, J. M.; Mascini, M.; Wang, J. Rapid micromotor-based naked-eye immunoassay.*Talanta* **2017**, 167, 651-657.

(118) García, M.; Orozco, J.; Guix, M.; Gao, W.; Sattayasamitsathit, S.; Escarpa, A.; Merkoçi. A.; Wang, J. Micromotor-based lab-on-chip immunoassays. *Nanoscale* **2013**, 5, 1325.

(119) Peng, F.; Tu, Y.; Wilson, D. A. Micro/nanomotors towards in vivo application: cell, tissue and biofluid. *Chem. Soc. Rev*. **2017**, 46, 5289-5310.

(120) Xu, H.; Medina-Sánchez, M.; Magdanz, V.; Schwarz, L.; Hebenstreit, F.; Schmidt, O. G. Sperm-Hybrid Micromotor for Targeted Drug Delivery. *ACS Nano* **2018**, 12, 327-337.

(121) Reinisova, L.; Hermanova, S.; Pumera, M. Micro/nanomachines: what is needed for them to become a real force in cancer therapy? *Nanoscale* **2019**, 11, 6519–6532.

(122) Wang, J.; Dong, R.; Wu, H.; Cai, Y.; Ren, B. A Review on Artifcial Micro/Nanomotors for Cancer-Targeted Delivery, Diagnosis, and Therapy. *Nano-Micro Lett*. **2020**, 12, 1-19.

(123) Chałupniak, A.; Morales-Narváez, E.; Merkoçi, A. Micro and nanomotors in diagnostics. *Adv. Drug Deliv. Rev*. **2015**, 95, 104-16.

(124) De Ávila, B. E. F.; Angsantikul, P.; Li, J.; Angel Lopez-Ramirez, M.; RamírezHerrera, D. E.; Thamphiwatana, S.; Chen, C.; Delezuk, J.; Samakapiruk, R.; Ramez, V.; Zhang, L.; Wang, J. Micromotor-enabled active drug delivery for in vivo treatment of stomach infection. *Nat. Commun*. **2017**, 8, 272-281.

(125) Erkoc, P.; Yasa, I. C.; Ceylan, H.; Yasa, O.; Alapan, Y.; Sitti, M. Mobile Microrobots for Active Therapeutic Delivery. *Adv. Therap*. **2019**, 2, 1800064-82.

(126) Xi, W.; Solovev, A. A.; Ananth, A. N.; Gracias, D. H.; Sanchez, S.; Schmidt, O. G. Rolled-up magnetic microdrillers: towards remotely controlled minimally invasive surgery. *Nanoscale* **2013**, 5, 1294-1297.

(127) Solovev, A. A.; Xi, W.; Gracias, D. H.; Harazim, S. M.; Deneke, C.; Sanchez, S.; Schmidt, O. G. Self-Propelled Nanotools. *ACS Nano*, **2012,** 6, 1751-1756.

(128) Xu, X.; Hou, S.; Wattanatorn, N.; Wang, F.; Yang, Q.; Zhao, C.; Yu, X.; Tseng, H. R.; Jonas, S. J.; Weiss, P. S. Precision-Guided Nanospears for Targeted and High-Throughput Intracellular Gene Delivery. *ACS Nano* **2018**, 12, 4503-4511.

(129) Srivastava, S. K.; Guix, M.; Schmidt, O. G. Wastewater Mediated Activation of Micromotors for Efficient Water Cleaning. *Nano Lett*. **2016**, 16, 817-821.

(130) Delezuk, J. A.M.; Ramírez-Herrera, D. E.; de Ávila, B. E.; Wang, J. Chitosan-based water-propelled micromotors with strong antibacterial activity. *Nanoscale* **2017**, 9, 2195-2200.

(131) Seah, T. H.; Zhao, G.; Pumera, M. Surfactant Capsules Propel Interfacial Oil Droplets: An Environmental Cleanup Strategy. *ChemPlusChem*. **2013**, 78, 384.

(132) Mou, F.; Pan, D.; Chen, C.; Gao, Y.; Xu, L.; Guan, J. Magnetically Modulated Pot-Like $MnFe_2O_4$ Micromotors: Nanoparticle Assembly Fabrication and their Capability for Direct Oil Removal *Adv. Funct. Mater*. **2015**, 25, 6173-6181.

(133) Parmar, J.; Villa, K.; Vilela, D.; Sánchez, S. Platinum-free cobalt ferrite based micromotors for antibiotic removal. *Appl. Mater. Today*. **2017**, 9, 605-611.

(134) Singh, V. V.; Kaufmann, K.; Orozco, J.; Li, J.; Galarnyk, M.; Arya, G.; Wang, J. Micromotor-based on–off fluorescence detection of sarin and soman simulants. *Chem. Commun*. **2015**, 51, 11190-11193.

(135) Singh, V. V.; Martin, A.; Kaufmann, K.; De Oliveira, S. D. S.; Wang, J. Zirconia/Graphene Oxide Hybrid Micromotors for Selective Capture of Nerve Agents. *Chem. Mater*. **2015**, 27, 8162-8169.

(136) Vilela, D.; Parmar, J.; Zeng, Y.; Zhao, Y.; Sánchez, S. Graphene-Based Microbots for Toxic Heavy Metal Removal and Recovery from Water. *Nano Lett*. **2016**, 16, 2860-2866.

(137) Li, J.; Liu, W.; Li, T.; Rozen, I.; Zhao, J.; Bahari, B.; Kante, B.; Wang, J. Swimming Microrobot Optical Nanoscopy. *Nano Lett*. **2016**, 16, 6604-6609.

(138) Manesh, K. M.; Balasubramanian, S.; Wang, J. Nanomotor-based 'writing' of surface microstructures. *Chem. Commun*. **2010**, 46, 5704-5706.

(139) Zhang, L.; Zhang, H.; Liu, M.; Dong, B. Reprogrammable Logic Gate and Logic Circuit Based on Multistimuli-Responsive Raspberry-like Micromotors. *ACS Appl. Mater. Interfaces*. **2016**, 8, 15654-15660.

(140) Dong, Y.; Liu, M.; Zhang, H.; Dong, B. Reconfigurable OR and XOR logic gates based on dual responsive on-off-on micromotors. *Nanoscale* **2016**, 8, 8378-83.

(141) Li, J.; Shklyaev, O. E.; Li, T.; Liu, W.; Shum, H.; Rozen, I.; Balazs, A. C.; Wang, J. Self-Propelled Nanomotors Autonomously Seek and Repair Cracks. *Nano Lett*. **2015**, 15, 7077-85.

CHAPTER 2

Magnetic Field Guided Chemotaxis of iMushbots for Targeted Anticancer Therapeutics

Contents

Abstract

The controlled migrations of an intelligent and biocompatible 'iMushbot' was studied, composed of *Agaricus bisporus* – mushroom microcapsules coated with magnetite nanoparticles. The otherwise randomly moving microbot could meticulously direct itself towards and away from the acid and alkali rich regions with the help of acid, acidic-catalase, and alkali stimuli, emulating the chemotaxis of microorganisms. While the catalytic decomposition of peroxide-fuel in alkali engendered the directed alkali taxis towards higher pH region, decomposition of peroxide-fuel by the acidic-catalase activity led to directed acid taxis towards the lower pH region. The presence of magnetite nanoparticles not only helped in improving the 'activity' of the motor through the heterogeneous catalytic decomposition of the peroxide-fuel but also provided a remote magnetic control on the chemotaxis. The mesoporous iMushbots having negative ζ-potential could easily be loaded with the cationic anti-cancer drugs, which were magnetically guided towards the cancerous cells to cause apoptosis. The iMushbots exhibited a higher degree of drug retaining capacity inside alkaline pH and showed facile drug release preferentially in the lower pH environments. The experiments show the potential of the iMushbots in retaining and transporting drugs in an alkaline medium such as human blood and releasing them in an acidic medium such as the cancerous tissues for cell apoptosis.

This chapter is published in *ACS Biomaterials Science and Engineering* **2017**, 3, 1627-1640. I gratefully acknowledge the assistance of Dr. A. K. Singh, Dr. D. Dutta, and Prof. A. Unal.

भारतीय प्रौद्योगिकी संस्थान गुवाहाटी
Indian Institute of Technology Guwahati

2.1. Introduction

Development of artificial self-propelling objects having faculties to deliver medicines in the targeted locations of the human body for the therapy of life-threatening diseases have attracted a lot of attention in the past few decades.[1-4] A number of seminal contributions led to the fabrication of diverse micro or nanoscale robots responsive towards various stimuli, which include chemical[5,6] or enzymatic[7,8] reactions, photonic[9] or acoustic [10,11] waves, thermal [12] or concentration gradients,[13-15] and electric[16,17] and/or magnetic fields,[18,19] among others. These locomotives have also been envisioned to serve diverse uses ranging from target isolation,[20,21] sensing,[22,23] therapeutics or diagnostics,[24-26] microsurgery,[27,28] transport of payloads,[29,30] and mitigation of pollutants through detoxification.[31] Presently, the biocompatible micro or nanosystems empowered with the specialties of the smart inorganic, organic, or biomaterials are poised to take over as the futuristic drug carriers to achieve therapeutic benefits with minimal side effects. The said mesoscale active systems are expected to show multi-functionalities such as the loading of the hydrophobic or hydrophilic drugs alongside the capacity to stimuli sensitive release of the same.[32] However, in the current scenario, one of the major challenges is to synthesize non-toxic, biocompatible micro/nanoscale motors capable of *in situ* transport and on-demand release of life-saving drugs in the targeted locations.

Thus far, a host of state-of-art fabrication methodologies, for example, angled electron beam evaporation,[10] sputter coating,[9,12] photolithography,[30] template-assisted deposition,[33] or 3-D printing[34] were employed to fabricate the multifunctional self-propelling objects. The specialties of micro or nanoscale particles,[9,12] rods,[1,10,11] tubes[20,21] of noble metals, carbonaceous materials,[16,31] and/or synthetic polymers [14,15] have been employed to impart

various functionalities to the locomotion. The issues related to the cost-effectiveness and biocompatibility have also been addressed by synthesizing biomotors form the plant tissues.[35-38] For example, millimeter-scale robots[36] synthesized from the enzyme-rich plant tissues were found to self-propel in the peroxide fuel while catalase differentially decomposed hydrogen peroxide around the motor to engender the chemically-powered locomotion. Microscale calcified biotubes[35] in the idioblast cells of the Dracaena sp. plant leaf coated with Fe–Ti layer were employed to perform drug release studies of anti-cancer agent Camptothecin under the remote magnetic control.

In the present study, biocompatible microbots have been developed composed of mesoporous mushroom (*Agaricus bisporus*) fragments coated with magnetite nanoparticles (FeONPs), namely iMushbots, could be employed for the transport and delivery of anti-cancer drugs. Unlike the previous reports, which demonstrated the migration of metal nanoparticle-coated polymeric microbots exclusively towards alkaline higher-pH regions,[14-16] the proposed iMushbots showed pH-induced chemotaxis towards and away from both acidic and alkaline pH regions, respectively.

While the homogeneous catalytic decomposition of peroxide fuel by alkali ensured that iMushbot moved towards the higher pH region, a mixture of the catalase bio-enzyme with acid enabled the migration of the iMushbot towards the lower pH region. The pH taxes demonstrated towards and away from an acid or alkali source also emulated the chemotaxis of various microorganisms. The innate catalase content of the mushroom tissues[39] and the FeONPs caused heterogeneous catalytic decomposition of the peroxide fuel on the surface of the iMushbots to engender random chaotic motion. In such a situation, the external acid-catalase or alkali drip helped in generating directed acid or alkali taxis, while the FeONPs on the motor surface provided a remote magnetic control on these motions.

Importantly, the proposed twin-trigger chemistry originating from the variation in the proportion of acid in catalase decided the chemotactic motion of the motor towards or away from an acid-rich target, which provided a clue to move objects inside human systems from higher pH blood serum to lower pH cancerous cells or vice versa, employing the enzyme responsive materials. The study also brings new insights into the interaction of asymmetrically distributed FeONPs on the surface of iMushbots with the peroxide fuel to improve the functionality of the microbots through continued propulsion. The incorporation of FeONPs also mediated the remotely guided motion of the microbots under the influence of an external magnetic field.

Interestingly, recent studies indicated that the mesoporous nature of drug delivery vehicles could improve the drug loading capacity as they possessed abundant cavities and electrostatic interactions for enhanced drug loading.[40,41] Herein, highly porous iMushbot has been synthesized with improved drug-loading capacity in conjunction with the capability of the controlled release of cancerous drugs under the influence of external pH stimulus to cause apoptosis of cancerous cells.

For this purpose, the omnipresent negative ζ-potential of a mushroom microparticle got electrostatically bound the cationic anti-cancer drug. The coating of the magnetite nanoparticles helped in magnifying the magnitude of the negative ζ-potential and subsequently strengthened the electrostatic bondage of the drug with the microbot. Mesoporous nature of the surface of the iMushbot alongside the presence of the negative ζ-potential facilitated efficient loading of the cationic anti-cancer drug doxorubicin into the self-propelling motor. The process for synthesis was optimized in such a manner that the drug-loaded motor could retain a significant part of its negative ζ-potential after binding with the cationic drug, which allowed the motor to transport inside an alkaline environment

without much loss of the drugs before a facile release in the acidic cell lines of cancerous cells. The experiments suggested that the proposed iMushbots could be employed for carrying drugs in marginally basic human blood before releasing the same to the marginally acidic cancerous tissues. Examples are shown where a drug-loaded iMushbot could be magnetically guided to attach with a cancerous HeLa cell before causing apoptosis through the delivery of doxorubicin into it. The binding and release efficiencies of the drugs with the iMushbots could be tuned to successfully induce cell death under the *in vitro* physiological conditions. The iMushbots reported in the present study have been expected to be employed for a host of controlled release studies for diverse therapeutics and diagnostic applications in the near future.

2.2. Experimental Section

2.2.1. Materials

Edible mushroom (*Agaricus bisporus*) was obtained from a local market (Guwahati, India). Ammonium hydroxide (NH_4OH), sodium hydroxide (NaOH), hydrogen peroxide (H_2O_2) (50%), hydrochloric acid (HCl), sodium hydroxide (NaOH) pellets, ethanol (C_2H_5OH), formaldehyde (HCHO) (37%), potassium permanganate ($KMnO_4$) and acetone (CH_3COCH_3) were purchased from Merck (India). Ferrous sulphate ($FeSO_4.7H_2O$) powder, bovine catalase, phosphate buffer saline (PBS), acetate buffer, acridine orange ($C_{17}H_{19}N_3$•HCl) (AO), DAPI ($C_{16}H_{15}N_5$•2HCl), ethidum bromide (EtBr), and thymol blue was procured from Sigma-Aldrich (India). Doxorubicin hydrochloride (DOX) and MTT ($C_{18}H_{16}BrN_5S$) were purchased from Parental Drugs Limited (India) and Himedia (India), respectively. All the chemicals were of analytical grade and used directly without further purification. Highly purified Milli-Q grade water was used in all of the experiments.

2.2.2. Methods

(a) Synthesis of DOX loaded magnetic iMushbots: The magnetite nanoparticles were synthesized using the reverse co-precipitation method.[42] Briefly, in a beaker containing 50 mL of deionized water, 50 mL of 25 % NH_4OH was added, and the pH of the solution was adjusted to ~13. A solution of 0.6 M $FeSO_4.7H_2O$ was prepared and added in the NH_4OH solution and mixed for 1 h. The addition of 0.6 M $FeSO_4.7H_2O$ solution into the base solution resulted in a black colored solution indicating the formation of magnetite nanoparticles (FeONPs). The nanoparticles were obtained with the help of a neodymium bar magnet, washed thrice with deionized water, and the obtained sample was dried overnight in a vacuum oven at 50ºC.

The commercially available mushrooms (*Agaricus bisporus*) were washed thoroughly and dried on filter paper. Initially, the Mushbots were prepared by cutting on the cross-section of mushrooms with a ~1 mm thickness, followed by vacuum drying at 30ºC for 3 h. Thereafter, ~ 3 g of the mushroom slices were crushed into the dimensions 50-160 µm using a mortar and pestle. The fragments were then treated with ethanol solution of freshly prepared FeONPs. The sample was dried overnight in a vacuum oven at 50ºC to remove ethanol by evaporation. After the heat treatment, a certain amount of FeONP-loaded motors (iMushbots) were obtained. The iMushbots were incubated in a 15 µL Doxorubicin (DOX) solution (166 µg mL^{-1}) in phosphate buffer (PBS) for 1 h at 37ºC. The DOX-loaded iMushbots (DOX@iMushbots) were magnetically separated from the solution and dried at 40ºC. Freshly prepared micromotors were used to carry out all the experiments.

(b) Measurement of speed: The autonomous propulsion of iMushbots was tested in various (v/v) H_2O_2 concentrations (0.5% - 8.0%). The motors (size ~ 150 µm) were suspended in a petridish (diameter 4 cm) filled with 6 mL of varying concentrations of aqueous peroxide

solution. The displacement of the motors was measured by placing the petridish on a paper-grid (dimension 1 mm × 1 mm).[15] The velocity of the motors was evaluated by measuring their displacement from initial point to the final position per unit of time. The experiments were performed thrice to obtain the mean value and error bars.

The iMushbots (size ~ 150 µm) were suspended in a petridish filled with 8 mL of water. The displacement of the micromotors was measured by placing the petridish on a paper-grid (dimension 1 mm × 1 mm).[15] An external magnetic field of strength varying from 10 to 30 mT was applied across the petridish with the use of an electromagnet. The velocity of the motors was measured after every ~1 mm displacement of the motor per unit time towards one of the magnetic poles. The experiments were performed thrice to obtain the mean value and error bars.

An iMushbot (size ~l50 µm) was immersed inside a petridish (3 cm dia.) containing 6 mL of 8.0% (v/v) H_2O_2 solution. The alkali gradient was established at the center of the petridish, using a cotton thread connected to a chemical reservoir. The displacement of the motor was calculated by placing the petridish on a paper with a scale bar of 2 mm.[16] The thymol blue indicator (0.2 g in 50 mL) was added to the H_2O_2 bath in order to track pH gradient. The speed of the micromotor was studied by varying the pH values of the chemical solution in the reservoir. The motor speed was calculated by measuring the displacement of the motor from an initial point to a position of ~ 6.5 mm away from the thread in order to nullify the thread effect on the displacement of the motor.[15] The experiments were carried out thrice for each pH value, and the average speed of the motor was reported. The velocity of the motor was studied at different pH values of the chemical drip.

For alkali pH taxis, the speed of the micromotor was measured by varying the pH of NaOH drip from 8 to 13. For repulsion motion (negative acid taxis) studies, the speed of the micromotor was measured by varying the pH of the HCl drip from 2.5 to 5.5. For positive acid taxis with varying pH values, the speed of the motor was measured by varying the pH of catalase-HCl drip from 2.5 to 5.5. The concentration of the catalase was maintained at 2 ppm in all the catalase-HCl drips. For positive acid taxis with varying catalase amounts, the speed of the motor was measured by varying the concentration of the enzyme in catalase-HCl drip from 2 mg mL^{-1} to 10 mg mL^{-1}. The concentration of the HCl and pH of drip was maintained at 0.005 M and ~ 4.5, respectively, for all the catalase-HCl drips.

(c) Measurement of catalase activity: The activity of catalase content of the Mushbot, iMushbot, and catalase-HCl drip solutions was evaluated by a standard method.[43] The catalase activity of the uncoated and coated motors was evaluated by suspending ~1 gm of homogenized tissue motors in a total volume of 20 mL phosphate buffer and diluted to 50X with water. After two cycles of centrifugation (4000 rpm, 4ºC for 10 min), the supernatants were collected and used for the enzyme assay. The intensity of UV absorption peak at 240 nm for catalase enzyme was recorded. Now for measuring the catalase activity in catalase-HCl drip solutions at different pH, the pH of solutions was adjusted from 2.5 to 5.5. The peroxide – phosphate buffer was prepared fresh by diluting 0.16 mL of H_2O_2 (8.0% v/v) to 100 mL with phosphate buffer. A 100 µL of H_2O_2 - phosphate buffer was added in the wells of a 96-well microtitre plate. After this, each solution of varying pH was mixed with 10 µg mL^{-1} of catalase in 1:1 ratio. All of the samples (100 µL) were rapidly added to the wells in a 96-well microtitre plate containing H_2O_2-phosphate buffer and mixed well. Phosphate buffer (0.067 M, pH 7.0) served as a control. The microtitre plate samples were subjected to UV absorbance measurement, and the intensity of catalase peak 240 nm (A_{240}) peak was

measured for quantification. Also, the activity of a solution containing only catalase (10 µg mL^{-1}) was measured. The time required for a decrease in intensity of A_{240} peak (ΔT) by 0.05 units was noted in seconds using a TECAN microplate reader. The assay was performed thrice for each of the samples. The activity of catalase was calculated as follows:

$$\text{Units in the assay mixture: } \frac{17}{\Delta T}. \quad (1)$$

(d) Drug loading and release efficiencies: An aqueous solution of DOX (15 µL of 166 µg mL^{-1}) was added to a varying concentration of iMushbots (0.5 mg - 3 mg) in 100 µL acetate solution (pH 7.4) and incubated for 1 h at 37ºC. The drug was absorbed on the surface of the motor due to electrostatic interactions. Following this, the drug-loaded iMushbots (DOX@iMushbots) were centrifuged at 4000 rpm for 10 min, in order to remove the unloaded DOX. After centrifugation, the retrieved pellets (DOX@iMushbots) was dispersed in distilled water. The supernatants containing the unloaded DOX were collected, and the intensity of 590 nm peak for DOX molecules were recorded at 480 nm excitation. Simultaneously, the emission intensity of total free DOX (15 µL of 166 µg mL^{-1}) was also recorded as initial DOX concentration. All the experiments were carried out thrice to ensure repeatability. After this, Binding Efficiency (B.E.) was calculated [44] using the following formula:

$$B.E.(\%) = \frac{(DOX)_i - (DOX)_s}{(DOX)_i} \times 100. \quad (2)$$

Here, $(DOX)_i$ denotes the initial concentration of DOX in the solution, and $(DOX)_s$ denotes the concentration of unloaded DOX present in the supernatant.

The DOX released from 3 mg of DOX@iMushbots were studied at different time intervals (0 min – 40 h). The pellets obtained after centrifugation of DOX-treated motors in acetate solution (pH 7.4) were washed carefully with water and then dispersed in 100 µL of acetate buffer of pH 4.5 and pH 7.4, respectively. The solution was incubated in acetate buffer at 37ºC for 1 h followed by centrifugation, and the supernatants were collected. Finally, the intensity of 590 nm peak at 480 nm excitation was recorded for the supernatants using a spectrofluorometer, taking water as the baseline reference.

(e) Cell culture: HeLa cells were purchased from National Centre for Cell Sciences (NCCS), Pune, India. The cells were cultured in Dulbecco's modified Eagle's medium, which contained streptomycin (50 mg mL^{-1}), L-glutamine (4 mM), penicillin (50 mg mL^{-1}, purchased from Sigma-Aldrich) and 10% (v/v) fetal bovine serum (procured from PAA Laboratories, Austria). The cultured cells were preserved at 37 ºC in 5% CO_2 humidified incubator.[44,45]

For analysis, ~10^5 HeLa cells were seeded in a glass slide and allowed to grow overnight. After this, cells were treated with 3 mg of DOX@iMushbots. The cells were incubated in a 5% CO_2 humidified incubator at 37ºC for 3 h. For understanding the co-localization of DOX in the nucleus, after 3 h treatment, DAPI stain was used to stain the nuclei of the treated cells. Following this, the cells were washed with PBS and fixed with 0.1% formaldehyde solution for 20 min in the dark at 37ºC and then dipped in 70% chilled ethanol. Finally, coverslips were mounted on a glass slide and sealed. Control HeLa cells (without treatment) were prepared in a similar manner. The samples were visualized under the confocal microscope (ZEISS LSM 880) at 340 nm – 490 nm excitation. For time-dependent uptake studies, samples were prepared in a similar manner with varying time points of treatment (0.5 h – 12 h), and the cells were fixed in a similar way described above.

For cell viability assay, a 96 well microplate was taken where ~10^4 HeLa cells per well were seeded and allowed to grow overnight. The cells were then treated with varying concentrations of magnetic iMushbots and DOX@iMushbots micromotors ranging from 0.30 mg mL^{-1} to 1.07mg mL^{-1}. An MTT based cell viability assay was carried out after incubating cancer cells with motors for 24 h. Following this, the MTT dye was added to determine the number of viable cells. The viable cells reduced MTT to colored formazon, and the formation of formazon was confirmed by recording the absorbance at 550 nm (A_{550}), using a TECAN microplate reader. The observed absorbance at 690 nm (A_{690}) was due to the presence of background interference. The assay was performed in triplicates for each of the samples. The % cell viability was calculated as follows: [45]

$$\%\,Viable\,cells = \frac{(A_{550} - A_{690})\,of\ the\,DOX@iMushbot\,treated\,cells}{(A_{550} - A_{690})\,of\ the\,untreated\,cells} \times 100. \qquad (3)$$

Additionally, MTT assay was performed for varying concentrations of FeONPs, free DOX, and uncoated Mushbots in a similar manner. About 10^5 HeLa cells per well were grown in a 96-well microtiter plate overnight in a 5% CO_2 humidified incubator at 37°C and treated with DOX free (0.027 mg mL^{-1}), and DOX loaded micromotors (1.07 mg mL^{-1}) for 24 h. Cells were stained by adding 5 µL of 1 mg mL^{-1} ethidium bromide and 2 µL of 1 mg mL^{-1} acridine orange followed by incubated for 10 min. The treated cells were washed with PBS for visualization under a fluorescence microscope (Nikon ECLIPSE, TS100, Tokyo) with an excitation filter of 480/30 nm.

(f) Equipment: Transmission electron microscope (TEM, JEOL JEM 2100, operated at 200 kV) was used to examine the particle morphologies. The samples were dispersed in ethanol before drop-casted onto a carbon-coated copper TEM grid and dried at room temperature. Field emission scanning electron microscopy (Zeiss Sigma FESEM, Germany) was used to

examine the surface of the motors and cancer cells. A 15 µL of the micromotor dispersion was deposited on a glass side wrapped with an aluminum foil left for drying before coating with a gold film (using SC7620 "Mini", Polaron Sputter Coater, Quorum Technologies, England). For the FESEM analysis of the untreated and treated HeLa cells, the cells were seeded in a cell culture plate and grown overnight. The samples were treated with DOX loaded micromotors with IC_{50} dosage. Following this, the cells were incubated for 24 h and washed twice with PBS before trypsinization. Following this, the cells were centrifuged for 6 min and fixed by re-dispersing the cells in 70% chilled ethanol at room temperature. Similarly, untreated HeLa cell suspension was prepared, and both treated and untreated cells were deposited glass slides covered with aluminum foil. The prepared samples were visualized under FESEM.

The elemental analysis of the sample was measured by energy-dispersive X-ray spectroscopy (EDX) in FESEM. The characterization of magnetite nanoparticles was done by X-ray diffraction (XRD, Bruker AXS Advance D8 diffractometer, Cu Kα source, X-ray wavelength 1.54 Å). The ζ-potential of the particles was measured using a DLS (Dynamic Light Scattering)-based particle size analyzer (Malvern Zetasizer Nano ZS). A flame atomic absorption spectrophotometer (AAS Model AA240) was used to assess the iron content of the samples. The magnetization curve was obtained by using a vibrating sample magnetometer (VSM, Lakeshore magnetic systems 7410 series). The electromagnet Model EMU-50V with constant current power supply unit (DPS – 50) and neodymium bar magnet, N52 grade of dimension 20 mm × 8 mm × 8 mm having magnetic field gradient of 1 mT mm^{-1} were used to apply the magnetic field in various experiments, and the applied magnetic field was measured by Digital Gaussmeter Model DGM-102 (purchased from SES instruments, India).

The treated HeLa cells were also assessed under the Epifluorescence microscope (Nikon ECLIPSE, TS100, Tokyo) by imaging under UV at an excitation of 480 nm. The samples were prepared by seeding HeLa cells (10^5) in a coverslip and incubated for 24 h. Thereafter, the cells were treated with DOX loaded motors for 3 h, followed by washing the cells with PBS buffer solution and visualized under a microscope. Confocal Laser Scanning Microscopy (CLSM) micrographs were recorded using a confocal microscope (ZEISS LSM 880). The fluorescence spectra were recorded using a Perkin-Elmer fluorescence spectrophotometer (Perkin-Elmer LS55). The pH was measured by pH meter (CyberScan pH 510, Eutech Instruments). The motion of the micromotors was captured with a digital camera (Cybershot DSC-HX, Sony Corp., Japan).

2.3. Results and Discussion

2.3.1. Synthesis of DOX@iMushbots

The plant-derived micromotors were fabricated using the edible mushrooms - *Agaricus bisporus*, owing to their nutritional and therapeutic values. The mushrooms, in comparison to other catalase-enriched food resources,[36] have higher protein and lower starch and lipid contents alongside being the source for many essential amino acids, minerals, and vitamins. Furthermore, particular attention could be drawn towards the biocompatibility of these Mushbots derived from an edible source, which are not considered to be foreign in the biological environments and fight destructive immune attacks.

Apart from their utility as dietary supplements, mushrooms are also considered among the nutraceuticals to prevent hypertension, hypercholesterolemia, and hyperglycemia.[46,47] A schematic description in **Figure 2.1A** shows an experimental setup employed to characterize the self-propelling motions of the motors. A micropipette tip was used as an alkali or acid reservoir while the peroxide fuel was placed on a petridish as shown in the figure.

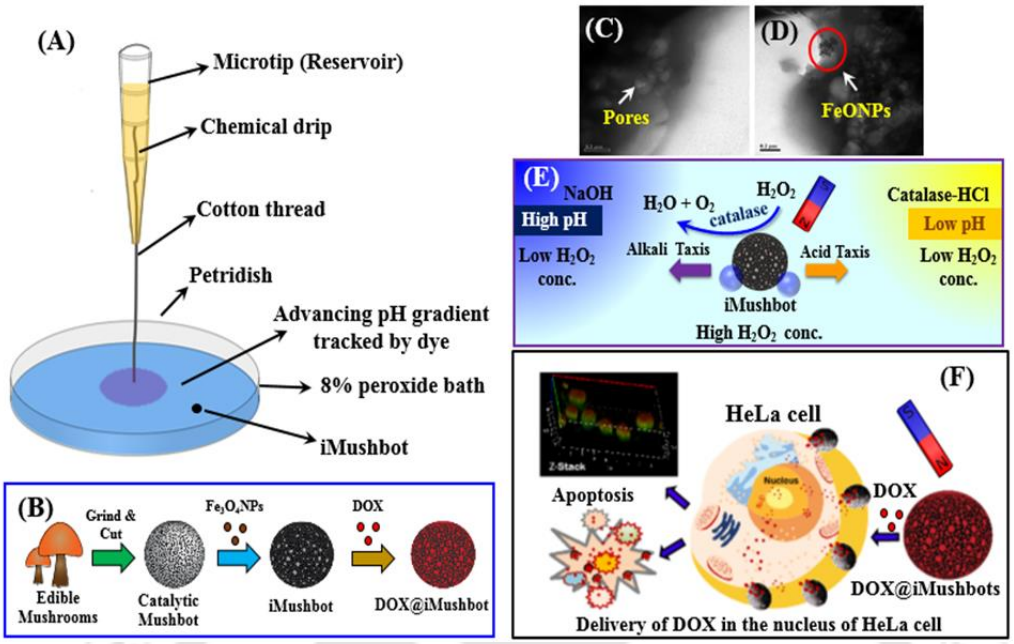

Figure 2.1. (A) Schematic diagram of the experimental set-up to study and characterize the motions of an iMushbot. **(B)** Schematically depict the steps to fabricate the magneto-catalytic (iMushbot) and drug-loaded motors (DOX@iMushbot). Transmission electron microscopy (TEM) image of **(C)** uncoated (Mushbot) and **(D)** FeONP coated motor (iMushbot). The scale bar is 0.2 µm. **(E)** Schematic diagram of the motor undergoing acid and alkali chemotaxis under the pH gradient. The decomposition of the H_2O_2 by the acidic catalase enzyme (sodium hydroxide) promotes chemotaxis from basic (acidic) towards the acidic (basic) region. The FeONP coating also facilitated magnetic remote control on the motions of the motor. **(F)** Schematic diagram shows the *in vitro* delivery of the Doxorubicin (DOX) by the iMushbots to the nucleus of the cancerous HeLa cells and thereby causing cell death. The inset shows the z-stacking from the confocal microscopy, which depicts the localization of the anti-cancer agent (depicted in red) inside the nucleus of the cancer cells.

The thymol blue indicator was dispensed on the peroxide bath to follow the pH gradient. The iMushbot was placed away from the thread to capture its motion towards or away from the alkali or acid trigger. **Figure 2.1B** shows the steps followed to synthesize the mushroom-based self-propelled micromotors. After purchasing from commercial resources, the mushrooms were sliced into pieces of ~ 1 mm thickness after washing and then vacuum dried at 30ºC for 3 h to remove excess water. Thereafter, 3 g of the dried mushroom slices were crushed using a mortar and pestle, and catalytic Mushbots of size nearly 50-160 µm

were obtained. The detailed steps of fabrication and characterization of the micromotors have been discussed in the experimental section.

2.3.2. Characterization of the materials

The Mushbots thus prepared were highly porous, as shown from the TEM micrographs in **Figure 2.1C**, and inherently possessed catalase enzyme. The micromotors of size ~ 150 µm were used for all the experiments reported in the manuscript unless stated otherwise. When the catalytic Mushbots were immersed in 8.0% (v/v) H_2O_2 solution, the spontaneous generation of O_2 bubbles was observed due to the catalase-induced decomposition of H_2O_2 into water and O_2.

In this situation, no net displacement of the motor was observed in a peroxide bath. In order to infuse a magnetic remote control on the motions, the Mushbots were coated with magnetite (Fe_3O_4) nanoparticles (FeONPs), which was termed as iMushbots. The random FeONPs deposition on the surface of the iMushbots also improved their catalytic activity through the heterogeneous catalytic decomposition of peroxide fuel. The surface morphology and porosity of the iMushbots were characterized using transmission electron microscopy (TEM) that were found to be deposited on the surface and inside the pores of the iMushbots, as shown in the **Figure 2.1D.** In contrast to the Mushbots, the immersion of the iMushbot in the peroxide bath led to an autonomous chaotic motion.

The heterogeneous catalytic decomposition of the peroxide on the iMushbots was clearly visible as the gas bubbles issued out from the surface of the motor. Control experiments suggested that same iMushbot remained stationary when immersed in deionized water (DI) water. Importantly, directionality could be infused to these randomly moving iMushbots, when a pH gradient was imposed on the experimental chamber. A few previous works showed that such directed motions were specific towards alkali rich regions.[14-16]

In the present study, motions towards the alkali rich (higher pH) and alkali lean (lower pH) zones with the help of a pair of chemical triggers could be achieved. **Figures 2.1E** shows that when 0.3 M sodium hydroxide (NaOH) solution was dripped from a micro-tip alkali reservoir into an 8.0% (v/v) peroxide bath at the center of a petridish using a thin cotton thread, a pH gradient could be established in the peroxide bath.[14-16] Schematic 1F shows the *in vitro* delivery of the Doxorubicin (DOX) by the iMushbots to the nucleus of the cancerous HeLa cells and thereby causing cell death.

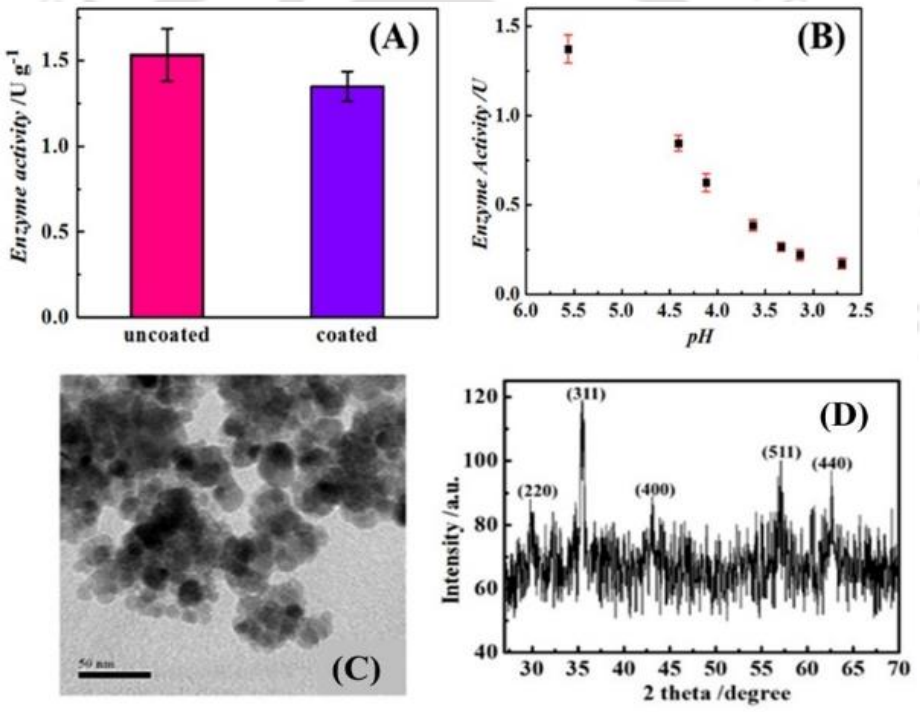

Figure 2.2 (**A)** Enzyme activity of the innate catalase in uncoated Mushbots and iMushbots samples for 8.0% (v/v) H_2O_2 decomposition **(B)** Variation in catalase enzyme activity with the change in pH values. **(C)** Transmission electron microscopy (TEM) image and **(D)** XRD pattern of freshly prepared magnetite nanoparticles. The scale bar at the bottom is 50 nm.

Figure 2.2A shows the specific activity[43] of the mushroom catalase content in uncoated motor for of H_2O_2 decomposition was around 1.5 U g^{-1} (1500 U mg^{-1}) whereas the same of the iMushbots were found to be 1.35 U g^{-1} (1350 U mg^{-1}). The decrease in the catalase activity in iMushbots accounts for the slight decrease in the rate of peroxide decomposition,

as shown later in **Figure 2.2B** that shows the decrease in catalase enzyme activity with the increase in acidic pH. **Figure 2.2C** shows the TEM image of freshly prepared magnetite nanoparticle (FeONPs). TEM images revealed that the FeONPs were ~ 35 nm or less in size. The XRD pattern **(Figure 2.2D)** showed characteristic diffraction peaks at $2\theta = 30.1^{\circ}$, 35.5°, 43.15°, 57.6°, 62.6° corresponding to the (220), (311), (400), (511), 440) crystallographic planes of FeONPs (JCPDS 19-0629).[48,49]

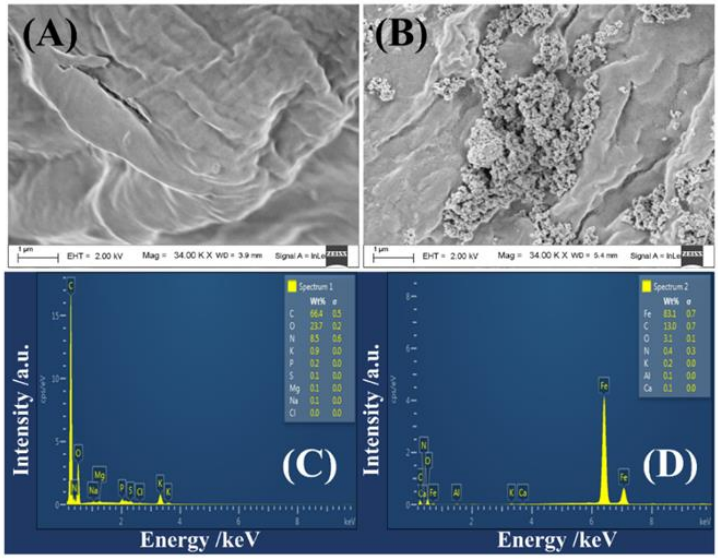

Figure 2.3. **(A)** Field emission scanning electron microscopy (FESEM) image of an uncoated Mushbot. The scale bar at the bottom is 1 µm. **(B)** FESEM image of iMushbot in which the FeONPs were observed over the mushroom surface. The scale bar at the bottom is of 1 µm. **(C)** Energy Dispersive X-ray (EDX) of the uncoated Mushbot. **(D)** EDX of an iMushbot surface shows the Fe peaks.

FESEM image **Figure 2.3A** shows the surface of Mushbot before the magnetite nanoparticle (FeONPs) coating. EDX of the uncoated Mushbot shows the presence of mineral content **(Figure 2.3C)**. **Figure 2.3B** shows the aggregates of FeONPs of average size ~ 30 - 40 nm. The figure confirmed the presence of a magnetic coating on the motor surface. The EDX of FeONPs-coated iMushbot shows the presence of elemental iron (Fe) peaks from FeONPs **(Figure 2.3D)**.

The rate of decomposition of H_2O_2 solution by a catalase-rich uncoated Mushbots and iMushbots were analyzed by volumetric titration with $KMnO_4$.[19] The strength of the $KMnO_4$ was standardized by 0.2 N oxalic acid. Firstly, for Mushbots, a 30 mL of 8.0% (v/v) H_2O_2 was taken in a beaker, and then 10 mg motors (~ 150 µm size) were suspended in the peroxide solution. After every 5 min time interval, a 300 µL aliquot was withdrawn from the beak and added to 10 mL of 0.2 N H_2SO_4 solution. Following this, the solution was titrated against standard 0.2 N $KMnO_4$ solutions.

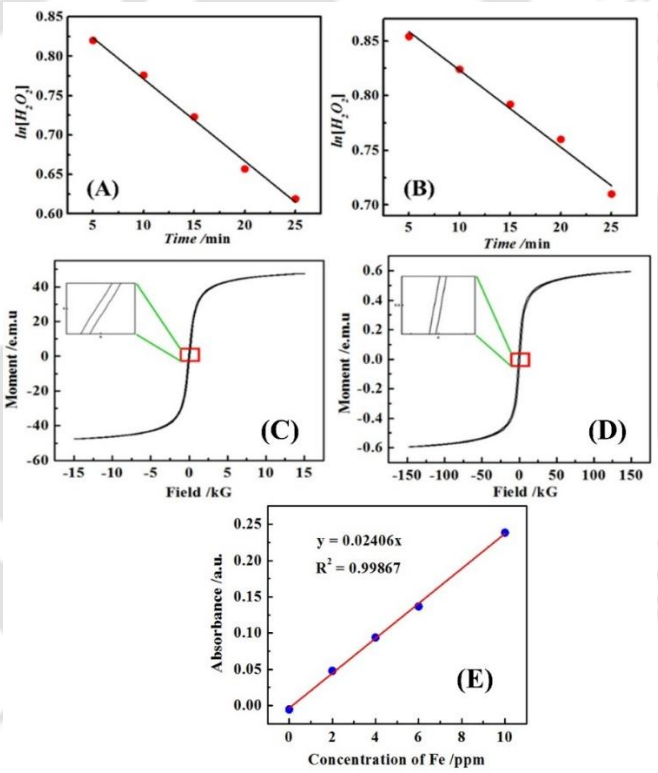

Figure 2.4. Rate constant (k) of 8.0% (v/v) H_2O_2 decomposition for **(A)** uncoated Mushbots and **(B)** iMushbots. Vibrating sample magnetometry (VSM) hysteresis loop of **(C)** freshly prepared FeONPs and **(D)** iMushbots. **(E)** Concentration of iron determined by using the standard curve obtained from atomic absorption spectroscopy.

The appearance of a permanent faint pink coloration confirmed the endpoint of the titration. The rate constant (*k*) for the H_2O_2 decomposition was estimated. The same procedure was repeated for iMushbots. In the presence of a Mushbots, the rate of decomposition of 8.0%

(v/v) peroxide followed first-order kinetics with the rate constant, k = 0.010 min^{-1} (**Figure 2.4A**) whereas for iMushbots the rate constant was measured to be k = 0.007 min^{-1} (**Figure 2.4B**). It is evident from the results that the Fe_3O_4NPs coating on the motor resulted in a slight decrement in the rate of peroxide decomposition.

The magnetization curve was obtained from the VSM at 25 $^{\circ}$C by varying the magnetic field from −15 to 15 kG. The magnetization curve for FeONPs (**Figure 2.4C**) suggested that the FeONPs were soft ferromagnetic in nature with a saturation magnetization (M_s) value of ~ 47.624 emu g^{-1}. **Figure 2.4D** shows the magnetization curve for iMushbots having M_s value of ~ 0.594 emu g^{-1}.The presence of non-magnetic mushroom tissue in the motor resulted in the decrement of M_s value in this case. The determination of the iron content in FeONPs and iMushbots was done by AAS by taking ferrous sulfate salt ($FeSO_4$) as standard (**Figure 2.4E**). From the plot, it was determined that for 20 ppm of FeONPs and iMushbots, the samples have 5. 29 ppm and 3.41 ppm of iron content, respectively.

2.3.3. Measurement of average speed of iMushbots

Figure 2.5A shows that when an iMushbot was immersed inside a bath of 8.0% (v/v), aqueous H_2O_2 solution and an alkali pH gradient was imposed, the motor migrated towards the thread. Figures 2.1A and 2.1E together show that when 0.3 M sodium hydroxide (NaOH) solution was dripped from a micro-tip alkali reservoir into an 8.0% (v/v) peroxide bath at the center of a petridish using a thin cotton thread, a pH gradient could be established in the peroxide bath.[14-16] The color gradient employing the thymol blue indicator in **Figure 2.5A** shows the regions of high (blue) to low (yellow) pH zones. In such a situation, when an iMushbot was placed in the peroxide bath, it migrated towards the thread – the alkali rich higher pH region.

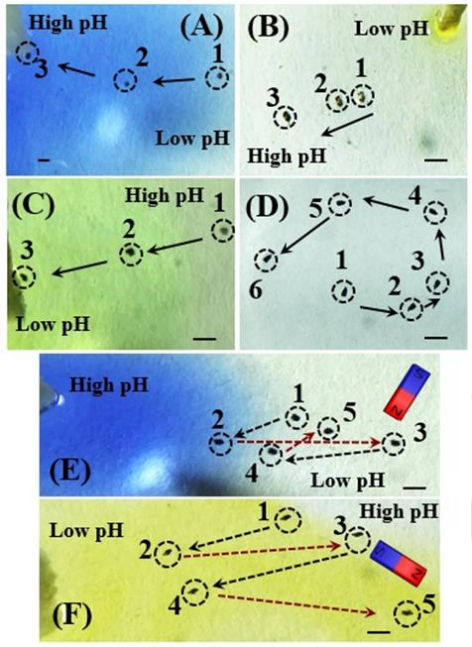

Figure 2.5. (A) shows the chemotactic motion of the motor (~ 150 µm) towards a thread under a continuous dripping of aqueous NaOH (0.3 M) to the H_2O_2 bath. The numbers 1 – 3 represent the position of the motor at *t* = 0 s, 18 s, and 21 s, respectively. **(B)** shows the repulsion of the motor (~ 150 µm) towards a thread under a continuous dripping of aqueous HCl (0.005 M) to the H_2O_2 bath. The numbers 1 – 3 represent the position of the motor at *t* = 0 s, 7 s, and 13 s, respectively. **(C)** shows the acid taxis motion of the motor (~ 150 µm) towards a thread under a continuous dripping of aqueous HCl (0.005 M) and catalase (2 ppm) to the H_2O_2 bath. The numbers 1 – 3 show the position of the motor at *t* = 0 s, 10 s, and 12 s, respectively. **(D)** Shows magnetically guided migration of motor in water with the aid of bar magnet. The numbers 1 – 6 represent the position of the motor at *t* = 0 s, 2 s, 4 s, 6 s, 12 s, and 27 s, respectively. **(E)** Shows reciprocating motion of a motor (~150 µm) under the coupled influence of the internal alkali pH gradient (NaOH drip) and the external magnetic field. The numbers 1 – 5 represent the position of the motor at *t* = 0 s, 8 s, 15 s, 27 s, and 29 s, respectively. The broken brown arrows depicted the magnetically controlled trajectory, and the broken black arrows show the trajectory under the influence of internal pH gradient. **(F)** Shows reciprocating motion of a motor (~150 µm) under the coupled influence of the internal acid pH gradient (catalase-HCl drip) and the external magnetic field. The numbers 1 – 5 show the position of the motor at *t* = 0 s, 14 s, 21 s, 39 s, and 44 s, respectively. The advancing alkali and acid front in all the experiments were observed using thymol blue indicator. In all the images, the instantaneous position of the motor is encircled in black color. The black arrows represent the trajectory of the migrating motor. The scale bar on all the images is 300 µm.

The migration of the motor could be attributed to the coupled effects of, (a) catalase-assisted decomposition of peroxide on the motor surface, (b) heterogeneous catalytic depletion of the peroxide fuel on the FeONPs on the motor surface,[50] and (c) homogeneous catalytic

decomposition of peroxide by the imposed pH gradient. The presence of catalase and FeONPs on the surface of the iMushbot ensured rapid decomposition of the peroxide fuel around the motor surface. It is well known that the peroxide fuel decomposes faster in the presence of the homogeneous catalyst NaOH.[51] Thus, the alkali drip ensured the presence of less amount of peroxide at the front side of the moving motor than at the rear side, which ensured larger decomposition of the peroxide fuel at the front side of the motor than on the rear side. This provided the required directional thrust for the motion towards the thread dripping alkali. The recoiling of O_2 bubbles from the motor surface also played an important role in this motion.[15] Concisely, **Figure 2.5A** showed alkali taxis of an iMushbot towards a higher pH region.

Interestingly, instead of alkali, when 0.005 M (pH ~ 4.5) hydrochloric acid (HCl) was dripped into the peroxide bath through the micro-tip drip, the motor moved away from the thread (**Figure 2.5B**). Since HCl acted as a negative catalyst against the peroxide decomposition,[52] in this situation, the HCl drip ensured more peroxide decomposition on the rear surface of the iMushbot than in the front, which caused the directed migration away from the thread. The differential catalytic decomposition of the H_2O_2 on the motor surface was clearly visible as the frequency of bubbles issued out from the motor surface facing towards the low pH region (acidic zone) was more as compared to the side facing towards high pH domain.

The motions shown in **Figure 2.5B** could be termed as "negative" acid taxis as the iMushbot again migrated from the lower pH region towards the higher pH region. Notably, when the reservoir dripped a solution of 2 ppm of catalase enzyme in 0.005 M HCl into the peroxide bath, the iMushbot migrated towards the lower pH region. Addition of catalase in the HCl drip fueled up the homogeneous catalytic decomposition of peroxide fuel by subduing the

negative catalysis due to HCl. In this situation, the catalase enzyme dripped from the reservoir succeeded in generating a differential solute concentration inside the peroxide bath, which ensured a stronger decomposition of the peroxide fuel on the rear side of the motor than in the front to provide the required thrust for the motion towards the lower pH region. The optimum pH window for the acid taxis was found to be between 2.7 to 5.5 in the micro-tip reservoir because catalase lost its enzymatic activity under extreme acidic or alkaline conditions. The highly acidic or basic pH disrupts the tertiary protein structure, leading to inactivation of the catalase enzyme.[53-56]

The experimental results shown here suggested that, while the alkali drip shown ensured that the motor migrated towards the alkali rich region (blue color for thymol blue in **Figure 2.5A**), the catalase-HCl drip ensured that the motor moved towards the acid-rich region (yellow color for thymol blue in **Figure 2.5C**). The motions shown in **Figure 2.5C** could be termed as "positive" acid taxis as the iMushbot migrated from the higher pH region towards the lower pH region. It is well known that the pH of the human blood is marginally alkaline in nature ranging ~7.35 to 7.45 [57] while the cancerous tissues are marginally acidic having the extracellular pH in the range of ~5.7 to 7.8 (average ~6.5).[58,59] In comparison, for the healthy human somatic tissues the extracellular pH varies from ~7.1 to 7.4.[60]

Furthermore, during the first stages of the *Trichophyton rubrum* skin infection, the human skin surface pH shifts from the acidic pH of 4.7 to alkaline pH values ranging from pH 8.3 to 8.9.[61,62] The experiments shown here confirmed that both acid and alkali taxis could be achieved under the *in vitro* conditions, which can be employed to migrate the iMushbots injected in blood into the cancerous cells as well as *Trichophyton rubrum*-infected cells with the help of the acid and alkali taxis, respectively. Briefly, the experiments suggested that the NaOH (pH 8.35 to 12.9) and catalase-HCl (pH 2.7 - 5.5) drips acted as chemical stimulants

to attract the iMushbots whereas the sole HCl drip (pH < 2.7) served as a repulsive trigger for the iMushbots.

The motions of the iMushbot were similar to the positive chemotaxis of bacterium, *Pseudomonas putida F1* towards its nutrient toluene[63] (chemo-attractant), and negative chemotaxis of *Escherichia coli* in gradients of noxious compounds (chemo-repellents).[64] The previously reported works highlighted the necessity to change either the fuel or fabrication protocol or material of the micromotor to achieve either acid or alkali taxis. For example - calcium carbonate-based Janus microparticles showed migration in the presence of ultra-low acidic conditions while the palladium nanoparticle (PdNPs)-coated polymeric beads exhibited alkali taxis at a higher pH in a peroxide bath.[14]

In comparison, the results reported here are exceptional owing to the fact that the motor could conditionally undergo acid or alkali taxis under the same *in vitro* condition. The proposed twin-trigger chemistry based on the homogeneous catalytic decomposition of peroxide fuel under the influence of alkali and catalase enzyme provides the scientific clue for such locomotion. Further, deposition of the FeONPs rendered magnetic remote control on the motions of the iMushbots motor, as shown in **Figure 2.5D-5F**. The magnetic control enabled quick change in the direction of the iMushbot while in motion moving under the chemical trigger.[15]

Figure 2.5D shows the veering motion of an iMushbot under the sole influence of an external magnetic field in an aqueous medium. The induced magnetization of the FeONPs allowed the iMushbot to be sensitive towards the magnetic field gradient. The microbot could be immediately steered in different directions by moving bar magnet to different positions. **Figure 2.5E (Figure 2.5F)** shows the magnetically guided chemotaxis of a motor under the coupled effect of NaOH (catalase-HCl) drip and external magnetic field.

The color gradient employing the thymol blue indicator in **Figure 2.5E** (**Figure 2.5F**) shows the regions of high (low) to low (high) pH zones. In such a situation, when an iMushbot was placed in the peroxide bath, the motor migrated towards the alkali (acid) rich higher (lower) pH region (thread) in the absence of a magnetic field. Before reaching the thread, the iMushbot was pulled away from the higher (lower) pH region, into the reverse direction of its alkali (acid) taxis using a neodymium bar magnet.

In this process, the directionality of micromotor under the influence of the alkali (acid) pH gradient was changed externally by the magnetic field. The motor was drawn out from the higher (lower) pH zone to the lower (higher) pH region of the alkali (acid) gradient, and then the external bar magnet was moved away from the motor. Under the sole influence of internal pH gradient and no external magnetic field, the iMushbot re-oriented itself spatially and resumed its directed migration towards the thread. The magnetic field was again re-introduced near the motor and the migrating motor was again veered away from the established pH gradient and the cycle was repeated twice leading to the reciprocating motion of the motor - towards and away from the thread.

Importantly, the iMushbot could recommence its migration towards the thread under the effect of the pH gradient once the magnetic stimulus was withdrawn. The remote magnetic guidance of iMushbots on a predefined route improved their applicability as drug delivery vehicles. In the near future, these proof-of-concept "on the fly" pH sensing iMushbots could be exploited for various theranostic applications such as (i) diagnostics - *in vivo* differentiation of diseased tissues from the healthy ones on the basis of extracellular pH[65,66] and/or (ii) therapeutics - *in vivo* delivery of drugs towards the diseased tissues from blood.

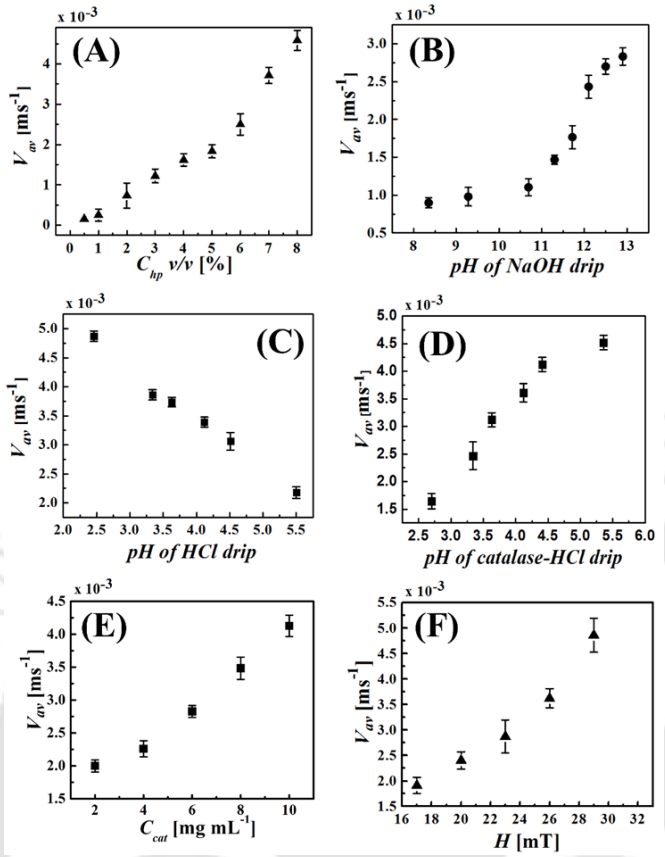

Figure 2.6. (A) Variation in the average speed (V_{av}) a ~150 µm iMushbot with increase in concentration of the hydrogen peroxide (C_{hp}) in the peroxide fuel. **(B)** Variation in the average speed (V_{av}) of the motor inside 8.0% (v/v) peroxide bath when the pH of NaOH drip was varied. **(C)** Variation in the average speed (V_{av}) of the motor undergoing repulsion inside 8.0% (v/v) peroxide bath when the pH of HCl drip was varied. **(D)** Variation in the average speed (V_{av}) of the motor inside 8.0% (v/v) peroxide bath when the pH of catalase-HCl drip was varied. **(E)** Variation in the average speed (V_{av}) of the motor inside 8.0% (v/v) peroxide bath when the concentration of catalase (C_{cat}) in catalase-HCl drip was varied. **(F)** Variation in the average speed (V_{av}) of the motor inside water bath with the increase in the strength of the external magnetic field (H).

In order to investigate the impact of various parameters on the motion of iMushbots, a series of experiments were performed. **Figure 2.6A** shows that the average speed (V_{av}) of the iMushbot increased with the increase in peroxide concentration (C_{hp}) inside the H_2O_2 fuel. When the motor was immersed in a bath of 0.5% (v/v) peroxide fuel, the motor attained the speed of ~ 0.15×10^{-3} ms^{-1} (~ 1 body lengths per second), and with gradual increment in peroxide concentration, the speed of the motor is enhanced to ~ 4.5×10^{-3} ms^{-1} (~ 30 body

lengths per second) in the 8.0% (v/v) peroxide fuel. The plot also shows that the low peroxide concentrations (0.5% - 2%) could be employed for the motions. For alkali taxis, the experiments were performed by immersing a ~150 µm motor inside 8.0% (v/v) peroxide bath while the pH of the alkali (NaOH) drip was varied from 8.35 to 12.9.

Figure 2.6B shows a monotonic increment in the average speed of the motor (V_{av}) with an increase in pH of the NaOH drip. At pH value of 8.35, the average speed of the motor was ~ 0.9×10^{-3} ms^{-1}. However, beyond pH 10.7 the speed increased rapidly, and at pH 12.9, the speed recorded was ~ 2.8×10^{-3} ms^{-1} (~ 19 body lengths per second). The repulsion of the motor in response to the acid drip in the absence of the extrinsic catalase was studied by varying the pH from 2.46 to 5.5 where the motor migrated away from the acid source. **Figure 2.6C** shows average repulsion speed (V_{av}) of the motor; the motor attained the maximum speed of as high as ~ 4.87×10^{-3} ms^{-1} (~ 32 body lengths per second) at pH 2.46. At this pH, the acid-rich zone at the rear part of the iMushbot ensured the presence of more peroxide fuel to be decomposed on the surface as compared to the front part of the motor which was away from the thread. With the reduction in the acidity, the repulsion weakened and the motor attained a speed of ~ 2.17×10^{-3} ms^{-1} at pH 5.5, which was equivalent to ~ 14 body lengths per second.

Figure 2.6D and **Figure 2.6E** correlate the speed of the motor undergoing acid taxis under the influence of the catalase-HCl drip with the variation in pH and the concentration of extrinsic catalase in acid-enzyme drip, respectively. **Figure 2.6D** shows the effect of the pH of catalase-HCl drip on average speed (V_{av}) of the motor towards the thread at different pH values ranging from 2.7 to 5.5 achieved by varying the HCl concentrations (0.1 M – 0.0028 M) with a constant concentration of extrinsic catalase at 2 ppm. The average speed attained by the motor was around 1.37×10^{-3} ms^{-1} (~ 9 body lengths per second) at pH 2.7. With the

increase in pH, the extrinsic catalase in the acid-enzyme drip shows an increment in its catalytic activity as the pH approaches to its optimal value. The enhancement in the catalytic activity of the extrinsic catalase in the acid-enzyme drip magnifies the homogeneous peroxide decomposition, and thus, the speed of the motor increased to ~ 4.52×10^{-3} ms^{-1} (~ 30 body lengths per second) at pH 5.5. Furthermore, the speed of the motor was measured by varying the concentration of catalase with a fixed concentration of HCl (0.005 M, pH 4.51).

It was found that the velocity of the micromotor increased significantly with an increase in the concentration of catalase, as shown in **Figure 2.6E**. It was observed that the velocity of the micromotor increased gradually from ~ 2×10^{-3} ms^{-1} (~ 13 body length per second) to ~ 4.13×10^{-3} ms^{-1} (~ 27 body length per second) when the concentration was increased from ~ 2 µg mL^{-1} to ~ 10 µg mL^{-1}. The effect of the magnetic field on average velocity (V_{av}) of the motor was also obtained by varying the magnetic field from 17 mT to 29 mT. **Figure 2.6F** shows that the velocity increased with the increase of the magnetic strength (H) exerted on the motor. The average speed attained by the motor was around 1.91×10^{-3} ms^{-1} (~ 13 body length per second) at ~ 17 mT. However, with the escalation in the magnetic field strength, the speed increased to 4.86×10^{-3} ms^{-1} (~ 32 body length per second) at ~29 mT. Concisely, **Figure 2.6** showed that the variations in the process parameters related to the acid, alkali, and magnetic field-driven motions of the iMushbots under various conditions.

2.3.4. iMushbots in intracellular drug delivery studies

In order to utilize the motors for drug delivery, the iMushbots were loaded with a fluorescent anticancer drug, doxorubicin (DOX), and were magnetically guided towards HeLa cells. A schematic illustration in Figure 2.1F demonstrated the usage of DOX-loaded iMushbots (DOX@iMushbot) as a drug carrier.

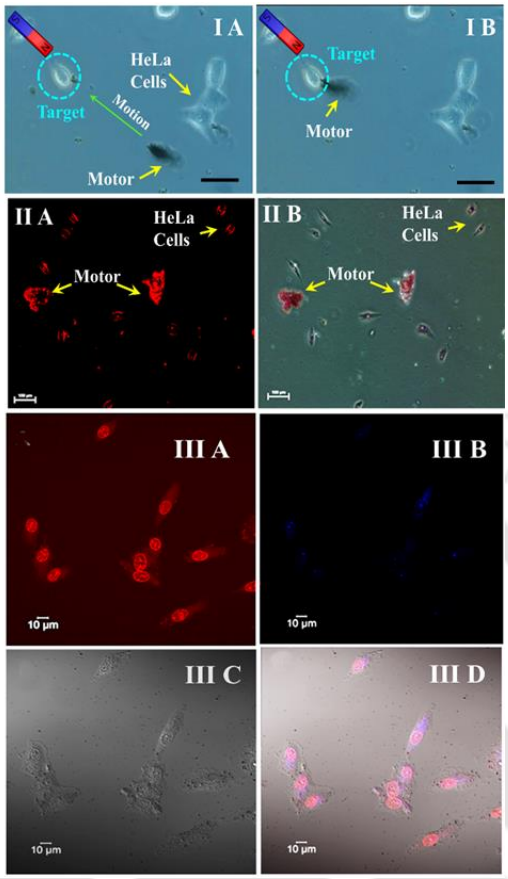

Figure 2.7. (IA-B) shows the magnetic guidance of a DOX@iMushbot (~ 100 µm) towards a target cell using a bar magnet. The scale bar is 100 µm. (**IIA-B**) shows epifluorescence microscopy images of HeLa cells after its treatment with DOX@iMushbots for 1 h. The scale bar is 100 µm. **(IIA)** shows HeLa cells and the motor showing the bright red fluorescence of the DOX uptake and drug loading, respectively. **(IIB)** shows the bright field image of DOX loaded motors (red). **(IIIA-B)** Fluorescence (**IIIC)** bright field and **(IIID)** merged images of HeLa cells after 3 h treatment with DOX@iMushbots and DAPI. The scale bar is 10 µm.

The DOX@iMushbots were immersed in the culture plate consisting of HeLa cells and phosphate buffer saline (PBS) solution devoid of peroxide and the motor was remotely guided towards the HeLa cells with the help of an external bar magnet having magnetic field gradient of 1 mT mm^{-1}, as shown in **Figure 2.7 (IA-B).** The HeLa cells were treated with DOX@iMushbots of ~ 100 µm size for 1 h and were imaged under the Nikon ECLIPSE TS100 epifluorescence microscope after thorough washing with PBS buffer. **Figure 2.7**

(IIA-B) shows the Epifluorescence microscopy images of HeLa cells after its treatment with DOX@iMushbots for 1 h, the corresponding bright-field image of the drug-laden motors, and the treated HeLa cells.

The images suggest successful loading of the drug in DOX@iMushbots along with the cellular uptake of the DOX by the HeLa cells. In these microscopy images, the DOX molecules could easily be identified on the surface of the HeLa cells by its characteristic red fluorescence emission under 480 nm excitation. Free DOX molecules successfully intercalated into the nuclear DNA of cell nuclei. The red fluorescence signal indicated the release of DOX from DOX@iMushbots and delivery into the cell nuclei and cytoplasm of the HeLa cells. The DOX@iMushbot treated HeLa cells were subjected to the nuclear stain using the DAPI (4', 6-diamidino-2-phenylindole) dye, and the cells were analyzed under ZEISS LSM 880 confocal laser scanning microscope (CLSM) at excitations of 488 nm and 405 nm.

Figure 2.7 IIIA represents the CLSM images of treated cells, which showed red auto-fluorescence due to the internalization of DOX molecules. **Figure 2.7 IIIB** shows the binding of DAPI dye to the AT regions of nuclear DNA resulted in blue auto-fluorescence near the nuclear region and thus helped to locate the DNA content inside the cells. The bright-field image of the sample was captured in **Figure 2.7 IIIC,** while **Figure 2.7 IIID** shows the superimposed images of DOX co-localization and DAPI stain. The CLSM images show that the distribution of released DOX was homogeneous inside the cells along with acute localization of DOX in the nuclear region, suggesting the successful uptake of DOX by the cells and nuclei. Additionally, a time-dependent controlled release study of the drug from the iMushbots was carried out by incubating the HeLa cells with the drug-loaded motors for a period of 0.5 h - 12 h and imaged under a confocal microscope.

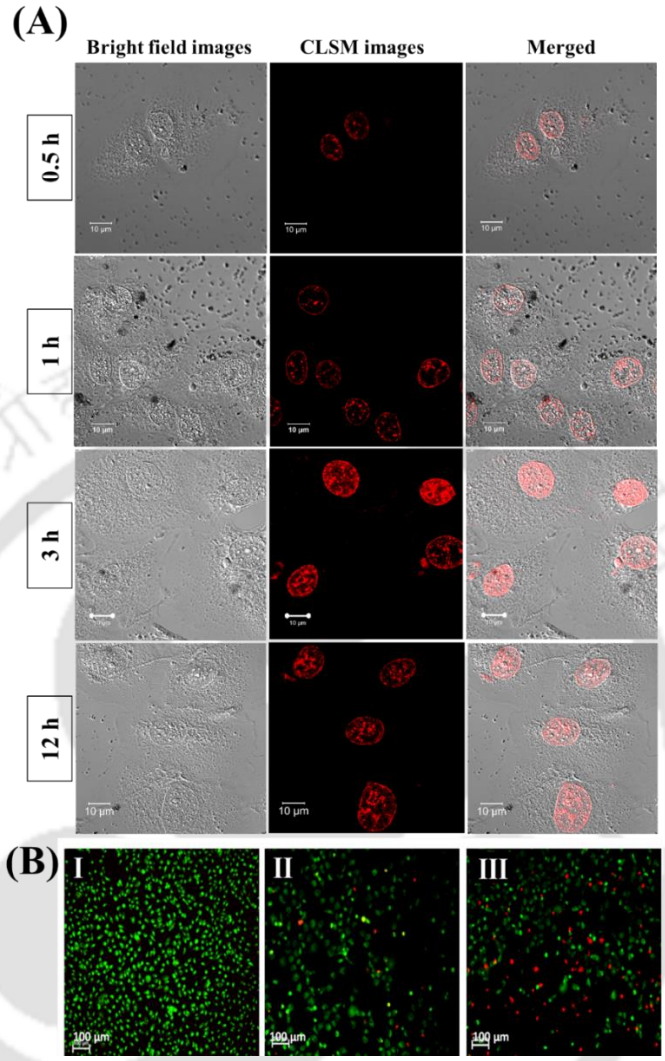

Figure 2.8. (A) shows the bright-field, fluorescence, and merged confocal images of HeLa cells after treatment with DOX@iMushbots for a period of 0.5 h - 12 h at 37°C. **(B)** Fluorescent images of (I) untreated (control) (II) free DOX and (III) DOX@iMushbot treated HeLa cells after ethidium bromide-acridine orange dual staining. Dead cells show red emission due to uptake of ethidium bromide and live cells green due to uptake of acridine orange dye.

Figure 2.8A shows the time-dependent bright-field and fluorescent images of the internalization of DOX into the nucleus of the HeLa cells. The figure confirmed the intrinsic release of drug DOX from the motor to the cancer cells. With increasing culture time, the red region inside the cell gradually increased due to the release of DOX into the cytoplasm. The DOX released from the motors passed through the nuclear membrane into the nucleus

and accumulated in the nuclei. The nuclei of the cancer cells enriched by DOX molecules appeared red in color under the CLSM. In order to quantify the apoptotic effects of the drugs after 24 h of treatment with free DOX (0.027 mg mL^{-1}) and DOX@iMushbots (1.07 mg mL^{-1}) on HeLa cells, dual acridine orange/ethidium bromide (AO/EB) fluorescent staining technique was employed.[67] The AO dye penetrated the live cells or early apoptotic cells with membranes intact and attached with the nuclear DNA resulting in green fluorescence. In contrast, the EB dye only entered into the dead cells with dented membranes, thereby emitting orange-red fluorescence after binding with DNA fragments or apoptotic bodies. **Figure 2.8B** shows the fluorescent micrographs of cells after AO/EB double staining assay. No reduction in cell viability was observed in case untreated cells (control) after 24 h, as indicated by AO dye-mediated green fluorescence (**Figure 2.8B I**).

Figure 2.8B II shows the treatment of cells with free DOX after 24 h time point. A minimal number of dead cells (red) were visible in this case, thereby suggesting that the existing cell population consists of mainly live and/or early apoptotic cells. In **Figure 2.8B III**, it was noted that the drug intake by DOX@iMushbots-treated cells resulted in more reduction in cell viability as compared to free DOX treatment. The number of dead cells (in red) was more as compared to viable cells (green), which signified the high efficacy of DOX@iMushbots in causing the cellular apoptosis.

No red fluorescence was observed in the CLSM image in **Figure 2.9A and 2.9B**. The Bright field and the CLSM images of the untreated HeLa cells do not show the characteristic red auto-fluorescence of DOX molecules due to the absence of DOX in the cellular compartment. From the binding efficiency calculations, it was determined that the 1.07 mg mL^{-1} equivalent of DOX@iMushbots contained 0.024 mg mL^{-1} of DOX, shown in **Figure 2.9C**.

The plot was constructed using the binding efficiency protocol, as stated in the experimental section of the manuscript, and shows the concentration of DOX loading in a definite amount of DOX@iMushbots. From the plot, it was determined that the 1.07 mg mL^{-1} equivalent of DOX@iMushbots contained 0.024 mg mL^{-1} of DOX.

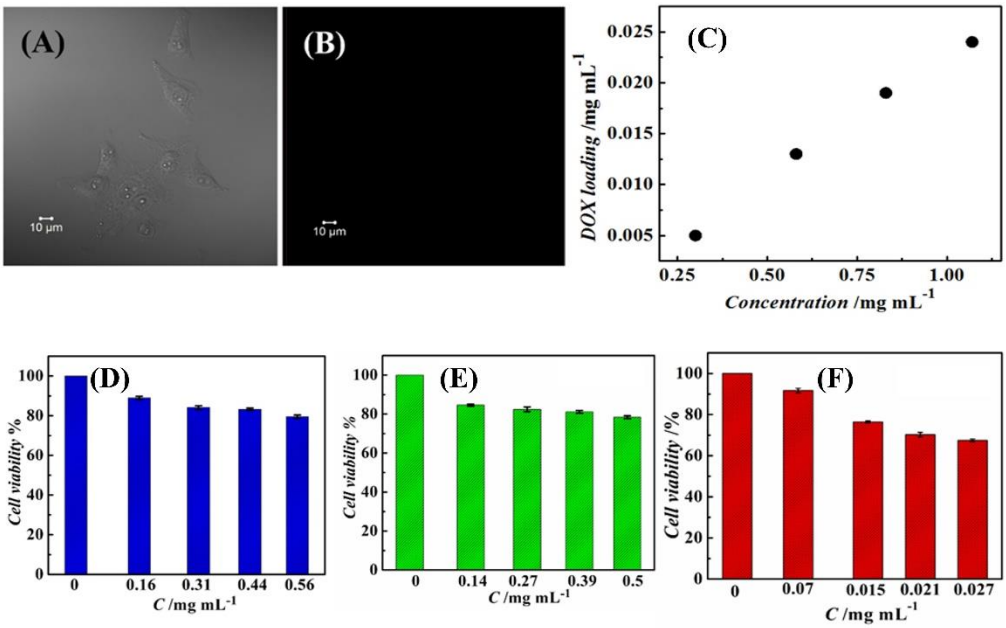

Figure 2.9 (A) Bright field and **(B)** CLSM image of the untreated HeLa cells. **(C)** Variation in concentration of loaded drug DOX with an increase in the amount of iMushbots. The concentration of DOX in the motors was determined by observing the intensity of the characteristic 590 nm fluorescence peak for DOX molecules. MTT assay of HeLa cells treated with **(D)** FeONPs, **(E)** uncoated Mushbots, and **(F)** free DOX for 24 h. The values are represented as mean ± SD of results from three individual experiments.

The **Figure 2.9D** and **2.9E** revealed marginal anti-cancer activity of uncoated Mushbots (*Agaricus bisporus*) and free FeONPs respectively, which showed slight toxicity to HeLa cells at concentrations (*C*) of 0.5 mg mL^{-1} of uncoated mushbot and FeONPs, as ~ 78-80% of HeLa cells were found to be viable in a culture medium. For free DOX **(Figure 2.9F)**, more than ~ 60% of HeLa cells were found to be viable at 0.027 mg mL^{-1} dosage whereas only ~ 48% of viable cells were observed at 0.024 mg mL^{-1} of DOX dosage, which clearly indicated that HeLa cells were more sensitive to DOX@iMushbots compared to free DOX

treatment. Thus, the measured IC_{50} value for DOX@iMushbots was equivalent to 0.024 mg mL^{-1} of DOX. It was observed that the percentage of cell viability was high for DOX-free iMushbots compared to DOX@iMushbots and free DOX, thereby indicating their minimal contribution in cell death. Further analysis revealed an additional anti-cancer activity of uncoated Mushbots (*Agaricus bisporus*) and free FeONPs, which showed marginal toxicity to HeLa cells at concentrations of 0.5 mg mL^{-1} as ~ 78-80% of HeLa cells were found to be viable.

The observations reported here resemble a recent work where a dose-dependent effect of DOX-loaded titania nanosystems has been performed to uncover the cytotoxicity assays and proliferation of BT-20 breast cancer cells.[41] Although all the components in DOX@iMushbots are capable of anti-cancer activity, the majority of cell death recorded in the case of DOX@iMushbot-treatment was primarily due to the release of DOX from the drug-laden motors in the acidic microenvironment.

The DOX@iMushbots were synthesized by incubating definite numbers of motors in 15 µL of DOX (166 µg mL^{-1}) aqueous solution for 1 h at 37°C (refer to experimental section for details). **Figure 2.10A** shows the ζ-potential of the uncoated motor (Mushbot), FeONPs, iMushbot, free DOX, and DOX@iMushbots. The ζ-potential of free DOX was measured to be 5.27 ± 0.5 mV, and the same of iMushbots was found to be – 22.2 ± 0.5 mV. The coating of negatively charged FeONPs (ζ-potential – 27.4 ± 1.0 mV) enhanced the net negative surface charge on the motor from – 15.6 ± 2.0 mV to – 22.2 ± 0.5 mV. The electrostatic interactions between the cationic DOX and negatively-charged mushroom surface led to the absorption of DOX molecules on the cavities inside the mushroom.[40]

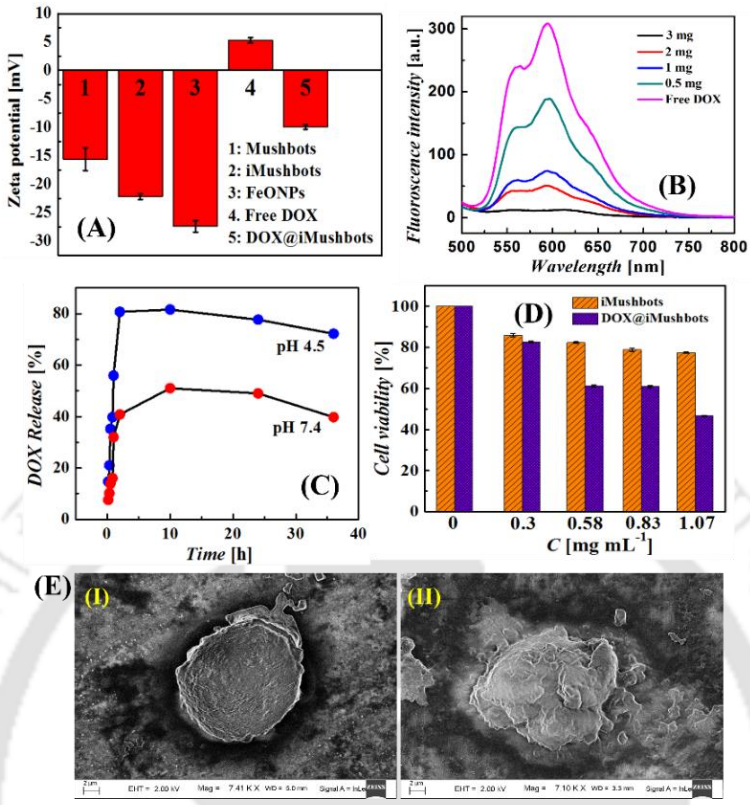

Figure 2.10. (A) The ζ-potential measurements for various samples. **(B)** shows the fluorescence spectra of the supernatant obtained after treatment of DOX solution with motors of varying amount for 1 h at 37°C in PBS buffer. **(C)** Release profile of DOX from micromotors at time intervals in acetate buffer at pH 4.5 and 7.4. **(D)** MTT based cell viability assay of HeLa cells after 24 h treatment with DOX@iMushbots and DOX-free iMushbots with varying concentrations (*C*). The values are represented in MTT assay are mean ± SD of results from three individual experiments. **(E)** FESEM images of **(I)** untreated and **(II)** treated HeLa cell.

In the process, the cationic DOX was electrostatically immobilized on the iMushbots. After binding with DOX, the ζ-potential of the DOX@iMushbots was found to be – 9.94 ± 0.2 mV. The overall negative charge on the DOX@iMushbots might reduce the chances of engulfment of motors by macrophages during *in vivo* drug delivery.[44] The drug loading and binding efficiency are one of the significant parameters used to assess the usability of drug delivery vectors. The mesoporous mushroom surface provided minimal exposure of loaded DOX to the external environment, which shielded the DOX from rapid degradation while the pharmacokinetics and bio-distribution of the loaded drug could be altered by the

variation in the pH microenvironment.[32] **Figure 2.10B** shows the amount of drug-loaded on various amounts of DOX@iMushbots, ranging from 0.5 mg to 3 mg. It was observed that with an increase in the amount of the micromotors (0.5 mg to 3 mg), the binding efficiency of DOX increased. A gradual decrease in fluorescence intensity of unbound DOX in supernatant confirmed the increase in binding of DOX with the motor. The binding capacity of DOX saturated to ~88.09% when the concentration of the micromotor exceeded beyond 3 mg. Thus, 3 mg of DOX@iMushbots were used for controlled release studies and drug delivery experiments unless stated otherwise.

It may be noted here that the release profile study of the drug from the DOX@iMushbots was carried out by incubating the motors (3 mg) at 37°C in acetate buffer (pH 4.5 and 7.4) for 1 h followed by centrifugation (4000 rpm for 10 min), as described in the experimental section. The supernatant was collected after definite time intervals (0 min – 36 h), and fluorescence intensity of DOX at 590 nm was observed for each time interval using a spectrofluorometer.

Figure 2.10C shows the release profile of drug DOX and the plot clearly suggests that at pH 4.5, ~ 81% of the DOX released from the motor within 10 h. It was observed that the motors released DOX at a rapid rate in the beginning, and the amount of released DOX reached ~50% in 1 h. The rate of DOX released at pH 7.4 was considerably slower as compared to pH 4.5 as only ~ 51% of DOX released at pH 7.4 within the first 10 h. In both the conditions, the rate of drug release from motor became slow after 10 h, and no further improvement in drug release was observed. Thus, the release of the hydrophobic DOX molecules enhanced in acidic pH due to the increase in solubility of DOX molecules at slightly acidic pH conditions.[68] The DOX from the motors was mostly retained on the motors at pH 7.4, which signified that the drug rarely released in normal tissues at this pH.

The DOX release profile at pH 4.5 suggested that the DOX@iMushbots might sustainably release the drug after encountering the acidic environment of cancerous cells. The slow release of DOX from motors at normal blood pH could help in retaining the DOX while transported through the blood vessels in the body and allow controlled release of the same near the cancerous cells enabling targeted therapeutics.

The observations reported resembled a recent work, which reported the synthesis of organo-inorganic nanoparticles for faster release of drugs at lower pH.[32] In order to analyze the cytotoxicity of the iMushbots and DOX@iMushbots, MTT based *in vitro* cell viability assays were performed on HeLa cells. For the MTT assay, the HeLa cells were treated for 24 h with different concentrations (*C*) of iMushbot and DOX@iMushbot within a range of 0.3 to 1.07 mg mL^{-1}. It was observed that the number of viable HeLa cells decreased with an increment in the concentration of micromotors. As shown in **Figure 2.10D**, when the HeLa cells were subjected to 1.07 mg mL^{-1} of the DOX@iMushbots, the ~50% cancer cells were killed efficiently, keeping viable only ~ 48% of cells.

Figure 2.10E I & II shows the field emission scanning electron microscopy (FESEM) micrographs of untreated HeLa cells (control) and the cells treated with DOX loaded micromotors, respectively. The FESEM micrographs in **Figure 2.10 E II** revealed the occurrence of characteristic membrane blebbing and disoriented cell morphology, suggesting the DOX@iMushbot treated HeLa cells underwent apoptosis. The released DOX components from the motors interacted with DNA strands and inhibited the DNA replication, which caused cell death.

2.4. Conclusions

The simple and economic micromotors were synthesized from the mesoporous edible button mushrooms and coated with sparsely populated magnetite nanoparticles to infuse the magnetic remote control. Emulating the movements of the microorganisms, the micromotors showed a chemotactic response to external alkali and acid stimuli by migrating directionally toward or away from the chemical trigger. While the magnetite nanoparticles and the catalase enzyme present on the motor surface 'activated' the motor through heterogeneous catalytic decomposition of peroxide fuel in the surroundings, the asymmetric homogeneous catalytic decomposition of the peroxide fuel across the motor surface due to the imposed acid or acid-enzyme or alkali stimulus on the peroxide bath engendered the necessary thrust for the motion.

The motor migrated towards the alkali stimulus with speed as high as ~19 body lengths per second, whereas the acid-enzyme induced attractive direction motion was as high as ~30 body lengths per second. The influence of the simple acid stimulus repelled the motor away with speed as high as ~32 body lengths per second. The speed and directionality of these micromotors depended on the concentration and nature of the chemical trigger and could be tuned by changing the chemical potential across the motor. The chemotaxis of the micromotors could be controlled in different directions with the help of external magnetic guidance.

Furthermore, the micromotors with negative ζ-potential could easily be loaded with cationic anti-cancer drug doxorubicin, which was transported to the vicinity of HeLa cells and perform a controlled release of drugs under *in vitro* conditions. The micromotors could retain and transport the drugs when the pH of the outside fluidic environment was similar to the human blood – marginally alkaline, and perform a controlled release of the drugs

when the fluidic environment had pH similar to the cancerous tissues – marginally acidic. Examples are shown for targeted release and delivery of the drugs inducing the death of cancerous cells with the help of the micromotors. The efficiency of the micromotors was found to be much higher than the same as the simple drug in performing cell apoptosis.

The reported self-propelling micromotor holds significant promise in the development of mushrooms as an effective and biocompatible drug delivery vector in the pH-responsive systems, apart from being a rich dietary food source. The mushrooms can be thought of smart alternatives against the synthetic materials for controlled drug delivery applications with minimal side effects, which opens new avenues for mushroom-based futuristic biomaterials for theranostic applications.

References

(1) Kline, T. R.; Paxton, W. F.; Mallouk, T. E.; Sen, A. Catalytic Nanomotors: Remote-Controlled Autonomous Movement of Striped Metallic Nanorods. *Angew. Chem.* **2005**, 117, 754–756.

(2) Paxton, W. F.; Sundararajan, S.; Mallouk, T. E.; Sen, A. Chemical Locomotion. *Angew. Chem. Int. Ed.* **2006,** 45, 5420–5429.

(3) Guix, M.; Mayorga-Martinez, C.C.; Merkoci, A. Nano/Micromotors in (Bio) Chemical Science Applications. *Chem. Rev.* **2014**, 114, 6285−6322.

(4) Maria-Hormigos, R.; Jurado-Sanchez, B.; Escarpa, A. Labs-on-a-Chip Meet Self-Propelled Micromotors. *Lab Chip* **2016**, 16, 2397–2407.

(5) Sanchez, S.; Soler, L.; Katuri, J. Chemically Powered Micro- and Nanomotors. *Angew. Chem. Int. Ed.* **2015**, 54, 1414–1444.

(6) Paxton, W. F.; Sen, A.; Mallouk, T. E. Motility of Catalytic Nanoparticles through Self-Generated Forces. *Chem. Eur. J.* **2005**, 11, 6462–6470.

(7) Ma, X.; Hortelao, A. C.; Patino, T.; Sanchez, S. Enzyme Catalysis to Power Micro/ Nanomachines. *ACS Nano* **2016**, 10, 9111–9122.

(8) Dey, K. K.; Zhao, X.; Tansi, B. M.; Mendez-Ortiz, W. J.; Cordova-Figueroa, U. M.; Golestanian, R.; Sen, A. Micromotors Powered by Enzyme Catalysis. *Nano Lett.* **2015**, 15, 8311–8315.

(9) Dong, R.; Zhang, Q.; Gao, W.; Pei, A.; Ren, B. Highly Efficient Light-Driven TiO_2-Au Janus Micromotors. *ACS Nano* **2016**, 10, 839–844.

(10) Wang, W.; Castro, L. A.; Hoyos, M.; Mallouk, T. E. Autonomous Motion of Metallic Microrods Propelled by Ultrasound. *ACS Nano* **2012**, 6, 6122–6132.

(11) Ahmed, D.; Baasch, T.; Jang, B.; Pane, S.; Dual, J.; Nelson, B. J. Artificial Swimmers Propelled by Acoustically Activated Flagella. *Nano Lett.* **2016**, 16, 4968–4974.

(12) Baraban, L.; Streubel, R.; Makarov, D.; Han, L.; Karnaushenko, D.; Schmidt, O. G.; Cuniberti, G. Fuel-Free Locomotion of Janus Motors: Magnetically Induced Thermophoresis. *ACS Nano* **2013**, 7, 1360–1367.

(13) Velegol, D.; Garg, A.; Guha, R.; Kar, A.; Kumar, M. Origins of Concentration Gradients for Diffusiophoresis. *Soft Matter* **2016**, 12, 4686–4703.

(14) Dey, K. K.; Bhandari, S.; Bandyopadhyay, D.; Basu, S.; Chattopadhyay, A. The pH Taxis of an Intelligent Catalytic Microbot. *Small* **2013**, *9*, 1916–1920.

(15) Singh, A. K.; Dey, K. K.; Chattopadhyay, A.; Mandal, T. K.; Bandyopadhyay, D. Multimodal Chemo–magnetic Control of Self-Propelling Microbots. *Nanoscale* **2014**, 6, 1398–1405.

(16) Kumar, S.; Singh, A. K.; Dasmahapatra, A. K.; Mandal, T. K.; Bandyopadhyay, D. Graphene Based Multifunctional Superbots. *Carbon* **2015**, 89, 31–40.

(17) Bouffier, L.; Ravaine, V.; Sojic, N.; Kuhn, A. Electric Fields for Generating Unconventional Motion of Small Objects. *Curr. Opin. Colloid Interface Sci.* **2016**, 21, 57–64.

(18) Peyer, K. E.; Zhang, L.; Nelson, B. J. Bio-Inspired Magnetic Swimming Microrobots for Biomedical Applications. *Nanoscale* **2013**, 5, 1259–1272.

(19) Singh, A. K.; Mandal, T. K.; Bandyopadhyay, D. Magnetically Guided Chemical Locomotion of Self-Propelling Paperbots. *RSC Adv.* **2015**, 5, 64444–64449.

(20) Campuzano, S.; Orozco, J.; Kagan, D.; Guix, M.; Gao, W.; Sattayasamitsathit, S.; Claussen, J. C.; Merkoçi, A.; Wang, J. Bacterial Isolation by Lectin-Modified Microengines. *Nano Lett.* **2012**, 12, 396–401.

(21) Balasubramanian, S.; Kagan, D.; Jack Hu, C. M.; Campuzano, S.; Lobo-Castanon, M. J.; Lim, N.; Kang, D. Y.; Zimmerman, M.; Zhang, L.; Wang, J. Micromachine-Enabled Capture and Isolation of Cancer Cells in Complex Media. *Angew. Chem. Int. Ed.* **2011**, 50, 4161–4164.

(22) Wang, J. Self-Propelled Affinity Biosensors: Moving the Receptor around the Sample. *Biosens. Bioelectron.* **2016**, 76, 234–242.

(23) Campuzano, S.; Kagan, D.; Orozco, J.; Wang, J. Motion-Driven Sensing and Biosensing Using Electrochemically Propelled Nanomotors. *Analyst* **2011**, 136, 4621–4630.

(24) Abdelmohsen, L. K. E. A.; Peng, F.; Tu, Y.; Wilson, D. A. Micro-and Nano-Motors for Biomedical Applications. **2014**, 2, 2395–2408.

(25) Gao, W.; Wang, J. Synthetic Micro/nanomotors in Drug Delivery. *Nanoscale* **2014**, 6, 10486–10494.

(26) Patino, T.; Mestre, R.; Sanchez, S. Miniaturized Soft Bio-Hybrid Robotics: A Step Forward into Healthcare Applications. *Lab Chip* **2016**, 16, 3626–3630.

(27) Nelson, B. J.; Kaliakatsos, I. K.; Abbott, J. J. Microrobots for Minimally Invasive Medicine. *Annu. Rev. Biomed. Eng.* **2010**, 12, 55–85.

(28) Xi, W.; Solovev, A. A.; Ananth, A. N.; Gracias, D. H.; Sanchez, S.; Schmidt, O. G. Rolled-up Magnetic Microdrillers: Towards Remotely Controlled Minimally Invasive Surgery. *Nanoscale* **2013**, 5, 1294–1297.

(29) Medina-Sanchez, M.; Schwarz, L.; Meyer, A. K.; Hebenstreit, F.; Schmidt, O. G. Cellular Cargo Delivery: Toward Assisted Fertilization by Sperm-Carrying Micromotors. *Nano Lett.* **2016**, 16, 555–561.

(30) Tottori, S.; Zhang, L.; Qiu, F.; Krawczyk, K. K.; Franco-Obregon, A.; Nelson, B. J. Magnetic Helical Micromachines: Fabrication, Controlled Swimming, and Cargo Transport. *Adv. Mater.* **2012**, 24, 811–816.

(31) Orozco, J.; Mercante, L. A.; Pol, R.; Merkoci, A. Graphene-Based Janus Micromotors for the Dynamic Removal of Pollutants. *J. Mater. Chem. A* **2016**, 4, 3371–3378.

(32) Bastakoti, B. P.; Hsu, Y. C.; Liao, S. H.; Wu, K. C. W.; Inoue, M.; Yusa, S. I.; Nakashima, K.; Yamauchi, Y. Inorganic–Organic Hybrid Nanoparticles with Biocompatible Calcium Phosphate Thin Shells for Fluorescence Enhancement. *Chem. Asian J.* **2013**, 8, 1301 – 1305.

(33) Safdar, M.; Wani, O. M.; Janis, J. Manganese Oxide-Based Chemically Powered Micromotors. *ACS Appl. Mater. Interfaces* **2015**, 7, 25580–25585.

(34) Stanton, M. M.; Trichet-Paredes, C.; Sanchez, S. Applications of Three-Dimensional (3D) Printing for Microswimmers and Bio-Hybrid Robotics. *Lab Chip* **2015**, 15, 1634–1637.

(35) Srivastava, S. K.; Medina-Sanchez, M.; Koch, B.; Schmidt, O. G. Medibots: Dual-Action Biogenic Microdaggers for Single-Cell Surgery and Drug Release. *Adv. Mater.* **2016**, 28, 832–837.

(36) Gu, Y.; Sattayasamitsathit, S.; Kaufmann, K.; Vazquez-Duhalt, R.; Gao, W.; Wang, C.; Wang, J. Self-Propelled Chemically-Powered Plant-Tissue Biomotors. *Chem. Commun.* **2013**, 49, 7307–7309.

(37) Gao, W.; Feng, X.; Pei, A.; Kane, C. R.; Tam, R.; Hennessy, C.; Wang, J. Bioinspired Helical Microswimmers Based on Vascular Plants. *Nano Lett.* **2014**, 14, 305–310.

(38) Wang, H.; Moo, J. G. S.; Pumera, M. Tissue cell assisted fabrication of tubular catalytic platinum microengines. *Nanoscale* **2014**, 6, 11359–11363.

(39) Savoie, J.; Minvielle, N.; Largeteau, M. L. Radical-scavenging properties of extracts from the white button mushroom, *Agaricus bisporus*. *J. Sci. Food Agric.* **2008**, 88, 970–975.

(40) Li, Y.; Bastakoti, B.P.; Imura, M.; Tang, J.; Aldalbahi, A.; Torad, N. L.; Yamauchi, Y. Dual Soft-Template System Based on Colloidal Chemistry for the Synthesis of Hollow Mesoporous Silica Nanoparticles *Chem. Eur. J*. **2015**, 21, 6375 – 6380.

(41) Wu, K. C. W.; Yamauchi, Y.; Hong, C. Y.; Yang, Y. H.; Liang, Y. H.; Funatsu, T.; Tsunoda, M. Biocompatible, surface functionalized mesoporous titania nanoparticles for intracellular imaging and anticancer drug delivery. *Chem. Commun*. **2011**, 47, 5232–5234.

(42) Mahmed, N.; Heczko, O.; Soderberg, O.; Hannula, S. P. Room Temperature Synthesis of Magnetite ($Fe_{3-\delta}O_4$) Nanoparticles by a Simple Reverse Co-Precipitation Method. *IOP Conf. Ser. Mater. Sci. Eng.* **2011**, 18, 032020.

(43) Katoch, R. *Analytical Techniques in Biochemistry and Molecular Biology*, 1st ed; Springer-Verlag New York: USA, **2011.**

(44) Khandelia, R.; Bhandari, S.; Pan, U. N.; Ghosh, S. S.; Chattopadhyay, A. Gold Nanocluster Embedded Albumin Nanoparticles for Two-Photon Imaging of Cancer Cells Accompanying Drug Delivery. *Small* **2015**, 11, 4075–4081.

(45) Sahoo, A. K.; Goswami, U.; Dutta, D.; Banerjee, S.; Chattopadhyay, A.; Ghosh, S. S. Silver Nanocluster Embedded Composite Nanoparticles for Targeted Prodrug Delivery in Cancer Theranostics. *ACS Biomater. Sci. Eng.* **2016**, 2, 1395–1402.

(46) Prasad, S.; Rathore, H.; Sharma, S.; Yadav, A. S. Medicinal Mushrooms as a Source of Novel Functional Food. *Int. J. Food Sci. Nutr. Diet.* **2015**, 4, 221–225.

(47) Jaworska, G.; Pogon, K.; Bernas, E.; Duda-Chodak, A. Nutraceuticals and antioxidant activity of prepared for consumption commercial mushrooms *Agaricus bisporus* and *Pleurotus ostreatus. J. Food Qual.* **2015**, 38, 111–122.

(48) Mahadevan, S.; Behera, S. P.; Gnanaprakash, G.; Jayakumar, T.; Philip, J.; Rao, B. P. C. Size distribution of magnetic iron oxide nanoparticles using Warren–Averbach XRD analysis. *J. Phys. Chem. Solids* **2012**, 73, 867–872.

(49) Gautam, R. K; Gautam, P.K.; Banerjee, S.; Soni, S.; Singh, S. K.; Chandra, M. Removal of Ni(II) by magnetic nanoparticles . *J. Mol. Liq.* **2015**, 204, 60–69.

(50) Andrade, A. L.; Souza, D. M.; Pereira, M. C.; Fabris, J. D.; Domingues, R. Z. Catalytic Effect of Magnetic Nanoparticles Over the H_2O_2 Decomposition Reaction. *J. Nanosci. Nanotechnol.* **2009**, 9, 3695–3699.

(51) Guo, T. X.; Zhao, Y.; Ma, S. C.; Liu, S. T. Decomposition Characteristics of Hydrogen Peroxide in Sodium Hydroxide Solution. *Adv. Mater. Res.* **2012**, 610, 359–362.

(52) Dalton, A. I.; Bauer, J. V. (Air Products and Chemicals, Inc.), US4320102 A, **1982**.

(53) Chance, B. Effect of pH upon the reaction kinetics of the enzyme-substrate compounds of catalase. *J. Biol. Chem.* **1952**, 194, 471–481.

(54) Morgulis, S.; Beber, M.; Rabkin, I. Studies on the effect of the catalase reaction ion concentrations. iii. Temperature on the catalase. iv. A theory effect at different hydrogen reaction. *J. Biol. Chem*. **1926**, 68, 547–563.

(55) Ogura, Y. Catalase Activity at High Concentration of Hydrogen Peroxide. *Arch. Biochem. Biophys*. **1955**, 57, 288–300.

(56) Susmitha, S.; Ranganayaki, P.; Vidyamol, K. K.; Vijayaraghavan, R. Purification and characterization of Catalase enzyme from *Agaricus bisporus*. *Int. J. Curr. Microbiol. Appl. Sci.* **2013**, 2, 255–263.

(57) VanPutte, C.; Regan, J.; Russo, A. *Fundamentals of Human Anatomy & Physiology* (Special Indian Ed.), 7th ed; Tata MacGraw-Hill: New York, **2010**.

(58) Guix, M.; Meyer, A. K.; Koch, B.; Schmidt, O. G. Carbonate-based Janus micromotors moving in ultra-light acidic environment generated by HeLa cells in situ. *Sci. Rep.* **2016**, 6, 1–7.

(59) Lee, E. S.; Gao, Z.; Bae, Y. H. Recent progress in tumor pH targeting Nanotechnology. *J. Control. Release* **2008**, 132, 164–170.

(60) Gerweck, L. E; Seetharaman, K. Cellular pH Gradient in Tumor versus Normal Tissue: Potential Exploitation for the Treatment of Cancer1. *Cancer Res.* **1996**, 56, 1194–1198.

(61) Martinez-Rossi, N. M.; Persinoti, G. F.; Peres, N. T. A.; Rossi, A. Role of pH in the pathogenesis of dermatophytoses. *Mycoses* **2011**, 55, 381–387.

(62) Ferreira-Nozawa, M. S.; Nozawa, S. R.; Martinez-Rossi, N. M.; Rossi, A. The Dermatophyte Trichophyton Rubrum Secretes an Edta-Sensitive Alkaline Phosphatase On High-Phosphate Medium. *Brazilian J. Microbiol.* **2003**, 34, 161–164.

(63) Parales, R. E.; Ditty, J. L.; Harwood, C. S.; Harwood, C. S. Toluene-Degrading Bacteria Are Chemotactic towards the Environmental Pollutants Benzene, Toluene, and Trichloroethylene. *Appl. Environ. Microbiol.* **2000**, 66, 4098–4104.

(64) Benov, L.; Fridovich, I. Escherichia coli exhibits negative chemotaxis in gradients of hydrogen peroxide, hypochlorite, and N-chlorotaurine: Products of the respiratory burst of phagocytic cells. *Proc. Natl. Acad. Sci.* U. S. A. **1996**, 93, 4999–5002.

(65) Damaghi, M.; Wojtkowiak, J. W.; Gillies, R. J. pH sensing and regulation in cancer. *Front. Physiol*. **2013**, 4, 1–10.

(66) Kato, Y.; Ozawa, S.; Miyamoto, C.; Maehata, Y.; Suzuki, A.; Maeda, T.; Baba, Y. Acidic extracellular microenvironment and cancer. *Cancer Cell Int*. **2013**, 13, 89–97.

(67) Ribble, D.; Goldstein, N. B.; Norris, D. A.; Shellman, Y. G. A simple technique for quantifying apoptosis in 96-well plates. *BMC Biotechnol*. **2005**, 5, 12–19.

(68) Kamba, S. A.; Ismail, M.; Hussein-Al-Ali, S. H.; Ibrahim, T. A. T.; Zakaria, Z. A. B. In Vitro Delivery and Controlled Release of Doxorubicin for Targeting Osteosarcoma Bone Cancer. *Molecules* **2013**, 18, 10580–10598.

CHAPTER 3

Boolean-Chemotaxis of Logibots Deciphering the Motions of Self-Propelling Microorganisms

Contents

Abstract

The feasibility of a self-propelling mushroom motor, namely a 'logibot' has been investigated as a functional unit for the construction of a host of optimized binary logic gates. Emulating the chemokinesis of unicellular prokaryotes or eukaryotes, the logibots made stimuli-responsive conditional movements at varied speeds towards a pair of acid–alkali triggers. A series of integrative logic operations and cascaded logic circuits, namely, AND, NAND, NOT, OR, NOR, and NIMPLY, have been constructed employing the decisive chemotactic migrations of the logibot in the presence of the pH gradient established by the sole or coupled effects of acid (HCl-catalase) and alkali (NaOH) drips inside a peroxide bath. The imposed acid and/or alkali triggers across the logibots were realized as inputs, while the logic gates were functionally reconfigured to several operational modes by varying the pH of the acid–alkali inputs. The self-propelling logibot could rapidly sense the external stimuli, decide, and act on the basis of intensities of the pH triggers. The impulsive responses of the logibots towards and away from the external acid-alkali stimuli were interpreted as the potential outputs of the logic gates. The external stimuli-responsive self-propulsion of the logibots following different logic gates and circuits can not only be an eco-friendly alternative to the silicon-based computing operations but also be a promising strategy for the development of intelligent pH-responsive drug delivery devices.

This chapter is published in *Soft Matter* **2018**, 14, 3182-3191. I gratefully acknowledge the assistance of Dr. M. Bhattacharjee and Dr. A. K. Singh.

3.1. Introduction

Chemotaxis of microorganisms often follows a series of complex logical motions while executing different tasks.[1–3] Of late, the bio-mimetics of these natural processes have ushered the development of next-generation artificial micro or nanoscale machines for drug transport, targeted release, and other biomedical applications.[4,5] In the recent era of automation, the programmable logic gates have also made frequent appearances in bio-photonics,[6,7]synthetic circuits,[8] smart-sensing,[9] diagnostics, and therapeutics,[10] bio-computation[11,] and energy harvesting.[12] A number of previous studies have shown logic gate based sensing,[13] information processing,[14] drug-release,[15] detections,[16] preparation of circuits[17] and chemical synthesis.[18] Further, the colorimetric,[19] chemiluminescent,[20] fluorescent[21] or electrochemical[22] signals emulating a Boolean response have also been found to be suitable for a host of cutting-edge applications.

In this regard, one of the long-standing challenges has been the decoding of logical operations, which are, in general, manifested as chemotactic migrations of microorganisms.[1,2,23] It is now well known that a series of complex and systematic, logical operations have been executed for (a) bacteria moving towards a food source, namely, 'positive' chemotaxis, and away from the poison, namely, 'negative' chemotaxis;[1,2,24] (b)movement of sperms toward the egg during fertilization;[25] (c) locomotion of neutrophils against microorganisms as a defense mechanism;[26] and (d) neuronal imaging or other motility behaviors of multicellular frameworks.[27,28]

Emulating these natural processes, of late, NAND, XOR, AND, OR, NOR, and NOT logic circuits have been developed employing the living cells.[29,30] Further, various biomaterials are employed to create artificial logic gates targeting essential applications. For example, (i)

DNA-gates have been employed to identify the behaviors of base pairs;[31] (ii) RNA-bio-circuits are used for the advancement of electronic biosensors;[32] (iii) microbial logic systems have been developed for environmental remediation;[33] and (iv) reversible gates, such as CNOT, FREDKIN, or TOFFOLI, are constructed based on the motility of Physarumsp.[34] Interestingly, the logic gates with more than one input have been reported to be essential for cells to identify a combination of multiple signals, which is found to significantly increase the sensing specificity and accuracy of control. For instance, *Pseudomonas aeruginosa* responsive sensors could sense and nullify the toxic environmental conditions by wiring to a multiple-input AND gate.[35] Inspired by all these seminal contributions, herein, the development of an artificial micromachine, namely a 'logibot' could show a host of pH-responsive chemotactic migrations, which are implemented to design logical operations.

It is important to note here that over the past few decades expansive efforts have been devoted to fabricate artificial micro or nanobots.[36–38] In particular, emulating the various microorganisms, these prototypes have been designed with autonomous decision-making abilities for the execution of various tasks. The chemotactic migrations such as diffusiophoresis,[39] self-electrophoresis,[40] and enzymatic[41] or inorganic catalyst mediated bubble-propulsion[42–44] have been employed for targeted drug delivery,[45–48] environmental remediation,[49,50] microsurgery,[51] surveillance,[52] sensing,[53–55] and microfluidic applications.[56] Interestingly, the motions of these objects can be remotely controlled with the help of diverse external stimuli such as chemical triggers,[46] light,[57,58] ultrasound,[59] and electric and magnetic fields.[55,60] The stimuli-responsive behavior of these motors also makes them suitable candidates for the execution of various logical operations. For example, the silver-salt motors could execute a NOR gate under a coupled photonic and chemical trigger[61] while another non-spherical motor could show reconfigurable OR and XOR logic

gates under the same stimuli.[57] Further, a raspberry biomotor could explain AND, NOT, OR and INHIBIT logical migrations under the collective stimuli of hydrogen peroxide (H_2O_2), near-infrared (NIR) light, and NH3.[58]

In the context, the development of an artificial self-propelling microswimmer, namely a 'logibot' could display a host of interesting chemotactic migrations emulating the AND, NAND, NOT, OR, NOR, and NIMPLY logic gates. The logibots were synthesized from the naturally abundant button mushrooms coated with magnetite nanoparticles (FeONPs) on the surface. Mimicking the microbial chemokinesis,[1–3] the proposed microbots self-propelled randomly in peroxide fuel. This motion was stimulated by the propulsive thrust originating from the catalytic decomposition of the peroxide fuel under the influence of catalase enzyme, inherently present in mushroom tissue. The presence of FeONPs on the surface of microbots could enhance the propulsive thrust due to the additional heterogeneous catalytic decomposition of the peroxide field on the FeONPs.

The random nature of the migrations of these microbots was made directional with the use of acid and/or alkali triggers around them. It is well known that the decomposition of the peroxide fuel is negatively (positively) catalyzed in the presence of acid – HCl (alkali – NaOH). Thus, establishing a pH gradient around the microbot helped in maintaining a difference in the amount of the peroxide fuel across the logibot. The directed propulsion was achieved owing to the differential depletion of peroxide fuel around the logibot. The reported chemotaxis of the microbots following various logical motions can be employed as a model mesoscale prototype to decipher the scientific understanding of the diverse chemotactic migrations of biological entities. Further, they can also be employed for bio-computation and targeted drug delivery applications.

3.2. Experimental Section

3.2.1. Materials

Button mushroom (Agaricus *bisporus*) was purchased from a regional market (Guwahati, India). Hydrogen peroxide (H_2O_2) (50%), sodium hydroxide (NaOH), hydrochloric acid (HCl) and ethanol (C_2H_5OH) were procured from Merck (India). Magnetite nanoparticles, bovine catalase, and thymol blue were obtained from Sigma-Aldrich (India). All the chemicals were of analytical reagent grade and used directly as procured. Milli-Q grade water was used for cleaning and preparation of the solutions in all the experiments.

3.2.2. Methods

(a) Equipment. The surface morphologies of logibots were examined using a field emission scanning electron microscope (Zeiss Sigma FESEM, Germany) and a Transmission Electron Microscope (TEM, JEOL JEM 2100, operated at 200 kV). The optical micrographs were captured under a Leica DM 2500 upright microscope. The magnetization of the samples was analyzed using a Vibrating Sample Magnetometer (VSM, Lakeshore magnetic systems 7410 series). The characterization of magnetite nanoparticles deposited on the surface of the logibot was done by X-ray diffraction (XRD, Bruker AXS Advance D8 diffractometer, Cu Kasource, X-ray wavelength 1.54 Å). A pH meter (CyberScan pH 510, Eutech Instruments) was used to measure the pH of the solutions. The motions of the logibots were recorded using a Sony Cybershot DSC-HX digital Camera (Sony Corp., Japan).

(b) Fabrication of microbots: The synthesis of microbots was carried out by a similar method as described in the earlier reports.[1] In brief, button mushrooms (*Agaricus bisporus*) were cleaned in running water, cut into cross-sections of ~1mm thickness and dried at 30ºC

for 3 h to facilitate size reduction through grinding using a mortar and pestle. The crushed fragments of mushrooms (size 50–160 mm) were exposed to ethanol–FeONPs solution procured commercially and left for overnight drying at 50ºC to obtain logibots. In order to characterize the surface morphology, the logibots were dispersed in ethanol and then drop-cast on the carbon-coated copper TEM grid. The samples were dried at room temperature before analyzing under the TEM.

(c) Chemotaxis experiments: The logibot (~140mm) was introduced in a petridish (dia. 3 cm) containing 6 mL of 7.0% (v/v) aqueous H_2O_2 fuel. The dual chemical gradients were introduced onto the petridish using two cotton threads connected to respective chemical reservoirs (containing acid and alkali solutions) that provided multiple stimuli across the logibot. In order to nullify the thread effect, the motor speed was calculated by measuring the displacement of the motor from an initial point to a position of ~6.5 mm away from the threads. The experiments were carried out thrice for each pH value, and the velocity of the motor was studied at different pH values of the chemical drip.

3.3. Results and Discussion

3.3.1. The phenomenon

The tissue-based plant biomotors[62–66] has attracted considerable attention in recent years due to their biocompatibility and the possession of inherent enzymatic activity. The fabrication of logibots using mushroom tissue (*Agaricus bisporus*) has been carried out because inherent catalase activity[67]of the same enabled the logibot to behave like an active material inside an aqueous peroxide fuel. The catalase enzyme acted as a homogeneous catalyst to decompose H_2O_2 fuel into water (H_2O) and oxygen (O_2) gas bubbles.[63,64] The FeONPs coat

on the surface of the logibots magnified the activity of them through the heterogeneous catalytic decomposition of the H_2O_2 fuel on the FeONPs.[46,63–65] The random motions of the logibots were made directional when a pH gradient was imposed using either a single or a pair of thin cotton threads connected to acid and/or alkali reservoir(s). The presence of the thymol blue indicator (0.2g in 50mL) in the bath helped in differentiating the regions of high (blue) to low (yellow) pH zones, as shown in **Figure 3.1A**.

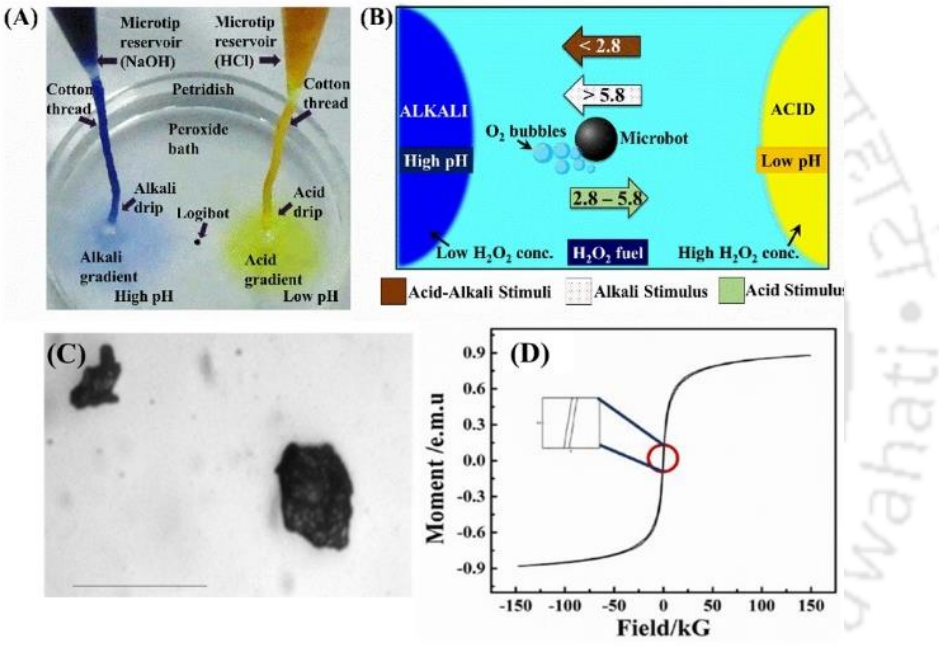

Figure 3.1. (A) Schematically shows the experimental setup to develop multiple stimuli across the microbot to engender the logical locomotion. **(B)** Schematic representing the motions of a microbot at different values of pH under the influence of acid and/or alkali stimuli. The arrows indicate the direction of migration in response to respective acid and/or alkali (color-coded) stimuli and the numbers represent the pH value of the chemical drip inside peroxide bath. Image **(C)** shows the optical micrographs of logibots observed under the Leica DM 2500 upright microscope, where the scale bar is 200 µm. Image **(D)** shows the vibrating sample magnetometry (VSM) of the logibots.

Dual micropipette tips were used as chemical reservoirs containing alkali and acid inputs in a petridish (3 cm diameter) containing 6 mL of 7.0% (v/v) H_2O_2 fuel. The acid (HCl) gradient was introduced ~ 3 mm away from the center of the petridish with the help of a

cotton thread connected to a chamber containing a uniform solution of 0.005 M HCl and 2 ppm of catalase. The alkali (0.3 M NaOH) gradient was established at ~11 mm away from the acid gradient by using a cotton thread connected to a reservoir. The thymol blue indicator (0.2 g in 50 mL) was dispensed on the peroxide bath to point out the pH gradient. The logibots (dia. ~ l40 µm) was introduced nearly at the midpoint of the two threads. In order to nullify the thread effect, the motor speed was calculated by measuring the displacement of the motor from an initial point to a position of ~ 6.5 mm away from the thread. The experiments were carried out thrice for each pH value, and the velocity of the motor was studied at different pH values of the chemical drip.

Interestingly, when the logibots were immersed in a petridish containing 7.0% (v/v) peroxide fuel, the spontaneous ejection of O_2 bubbles imparted the required thrust for motor propulsion, as schematically shown in **Figure 3.1B**. The figure also suggests that when an acid/alkali solution of known pH was dripped from the chemical reservoir with the help of the threads, a pH gradient could be established across the peroxide bath. It is well known that the decomposition of the peroxide fuel is negatively (positively) catalyzed in the presence of acid – HCl (alkali – NaOH). Thus, the drip with alkali (acid) ensured the presence of a peroxide lean (rich) zone in the bath. A host of interesting behaviors was observed after performing a series of experiments, as schematically illustrated in Figure 3.1B. For example, in the presence of alkali stimuli (NaOH drip), the logibot migrated towards the alkali source when pH >5.8 to show an alkali-taxis, as shown by the white arrow. However, in the presence of acid stimuli (HCl-catalase drip), the logibot migrated towards the acid source to show an acid-taxis when 2.8 < pH < 5.8, as shown by the green arrow. On the contrary, the logibot was repelled away from the acid showing a negative acid-taxis when the pH was < 2.8, as shown by the brown arrow.

3.3.2. Characterization of logibots

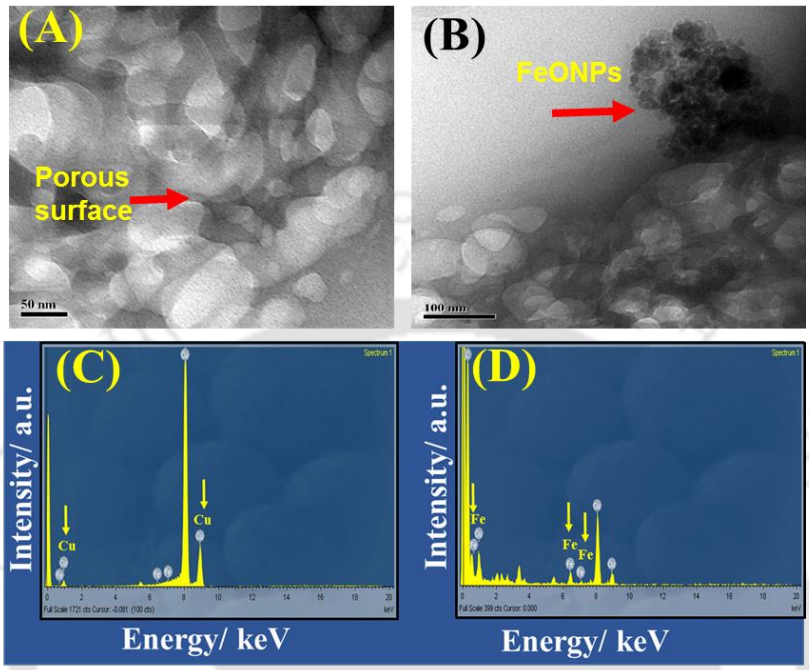

Figure 3.2. Transmission electron microscopy (TEM) image **(A)** shows a logibot displaying porous morphology. The scale bar is 50 nm. Image **(B)** shows a logibot having the magnetite nanoparticles (FeONPs) deposited on the surface where the scale bar is 100 nm. Energy Dispersive X-ray (EDX) spectra in the image **(C)** corresponds to the uncoated logibots. The EDX plot in the image **(D)** shows the presence of the FeONPs on the logibot, indicated by the downward yellow arrows.

The optical micrograph of the logibots is shown in **Figure 3.1C,** with size ranging from 50 – 150 µm. The magnetization saturation of the logibots was measured by the VSM analysis at 25°C when the magnetic field strength was varied from −15 to 15 kG. The magnetization curve of the logibots shown in **Figure 3.1D** has the M_s value of ~ 0.594 emu g^{-1}. The curve confirms the deposition of FeONPs aggregates on the surface of logibots.

The surface porosity of the logibot is displayed in TEM micrograph, **Figure 3.2A**. The deposition of aggregates of magnetite nanoparticles (FeONPs) on the motor surface was observed in the TEM micrograph **Figure 3.2B**. The surface of uncoated micromotor

displayed the presence of Cu from the TEM grid and small amount of inherent iron (Fe) in the uncoated logibot, as shown in EDX plot in **Figure 3.2C**. The EDX of FeONPs-coated logibot in **Figure 3.2D** shows the presence of elemental Fe (0.72%), indicated by the downward yellow arrows. The above figures confirmed the coating of FeONPs aggregates on the porous surface of logibots. The TEM micrographs of FeONPs in **Figure 3.3A** revealed that they exhibited a spherical shape with a narrow size distribution of ~ 7 – 5 nm.

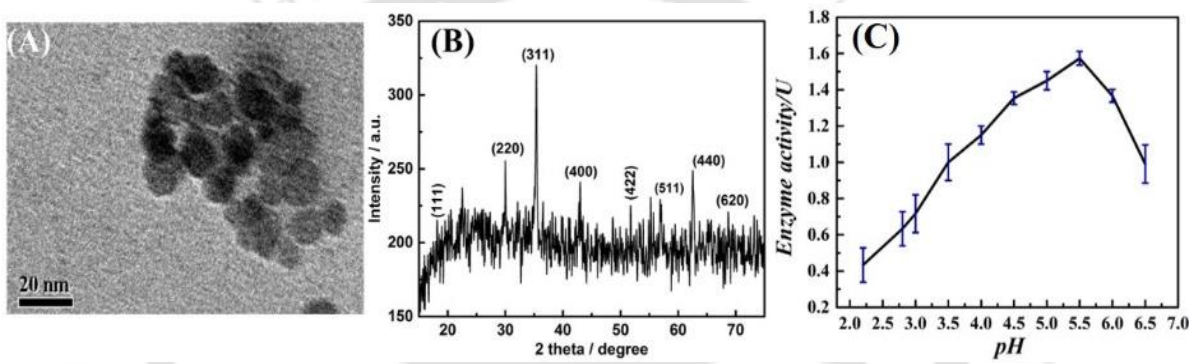

Figure 3.3. (A) TEM image of magnetite nanoparticles (FeONPs). **(B)** XRD analysis of FeONPs.The scale bar at the bottom is 20 nm. Image **(C)** shows catalase activity of logibots under a varying pH range.

The XRD pattern in **Figure 3.3B** showed consistent and broad diffraction peaks at 2θ = 18.55°, 30.1°, 35.5°, 43.15°, 53.45 °, 57.6°, 62.6°, and 68.88° corresponding to the (111), (220), (311), (400), (422), (511), (440), and (620) crystallographic planes of FeONPs with the standard pattern of JCPDS CARD No.19-0629.[46, 68-71] The activity of inherent catalase enzyme in the micromotors and catalase-HCl drip solutions were estimated by using a method reported previously.[46] The samples were prepared using the reported method and evaluated in triplicates for each sample by measuring the absorbance of catalase (A_{240}) using a TECAN microplate reader. The catalase activity of the logibots was evaluated considering a varying pH window of 2.5 to 6.0, as shown in **Figure 3.3C**. The optimum pH range for maximal activity of catalase was found to be between 2.8 to 5.5, beyond which the activity

was diminished. A gradual decrease in enzyme activity could be observed with pH < 2.8 and pH > 5.5, i.e., ~ 0.4 U and which and ~ 1.7 U, respectively.

3.3.3. Measurement of average velocity of logibots

The reasons behind these migrations were studied systematically, as discussed with the experimental results reported in Figure 3.4. **Figure 3.4A** shows the directed motion of logibots towards the alkali stimuli of high pH (pH 45.8) by introducing a 0.3 M NaOH solution drip in a petridish of 7% (v/v) peroxide fuel. In such a scenario, a logibot was always expected to have more (less) peroxide fuel towards the rear (front) side owing to its larger (smaller) distance from the alkali drip. Subsequently, larger catalytic decomposition of the peroxide fuel at the rear part (acid-rich yellow zone) of the logibot than on the front side (alkali rich blue zone) helped it in migrating towards the alkali drip. The migration of the motor could be attributed to the coupled effects of (a) catalase-assisted peroxide decomposition and heterogeneous catalytic depletion of the peroxide fuel on the FeONPs on the motor surface and (b) homogeneous rapid peroxide decomposition by the imposed pH gradient.[72] The pH gradient helped in maintaining an imbalance of solute concentration across the motor, which provided the directional osmotic thrust required for the motion towards the high pH region of the thread and engender the alkali-taxis.

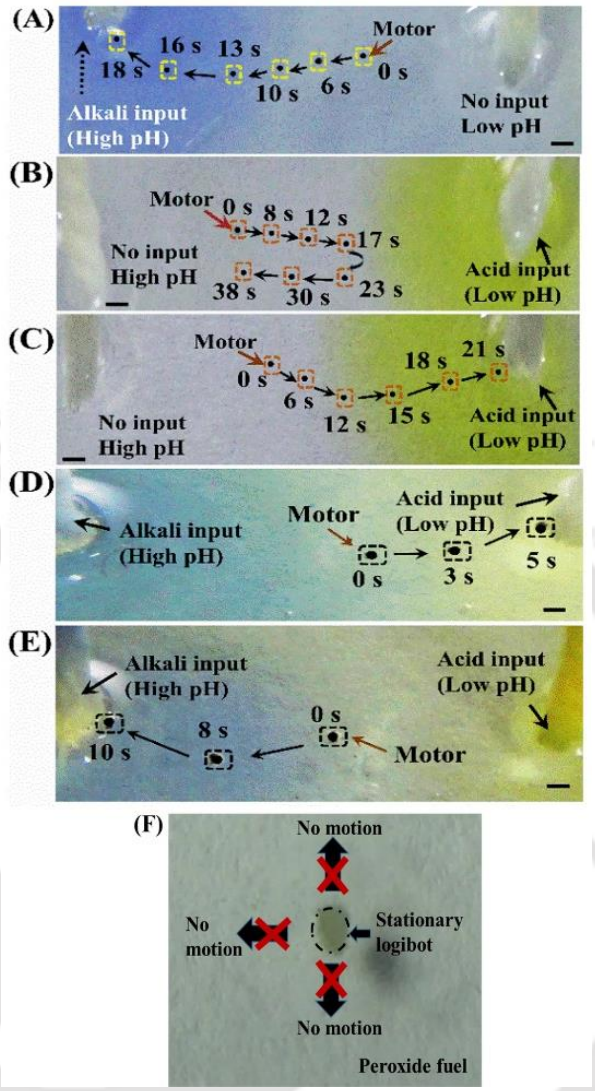

Figure 3.4. Image **(A)** depicts the chemotactic migration of a logibot towards the thread under the continuous dripping of alkali (0.3 M NaOH). Image **(B)** shows the repulsion of a logibot away from the thread under the continuous dripping of acid (0.005 M HCl). Image **(C)** shows chemotactic motion of a logibot under the influence of continuous aqueous acid (0.005 M HCl) and catalase (1 ppm) drip. Image **(D)** shows the motion of a logibot towards the HCl-catalase drip (pH 4.51) in the dual acid-alkali gradient system. Image **(E)** shows the motion of logibot away the HCl-catalase drip (pH 2.46) towards the NaOH drip in dual acid-alkali gradient system. The logibots (size ~ l40 µm) were immersed inside a petridish containing 7.0% (v/v) aqueous H_2O_2 solution for all the experiments, and thymol blue indicator was used to track the pH gradients. The scale bar on all the images is 300 µm, and the numbers denote the time in second. Image **(F)** shows the stationary state of motor in peroxide fuel with no net displacement.

Interestingly, a repulsive migration of the logibot was observed away from the acid-rich zone (yellow) upon the introduction of the HCl (0.005 M, pHo2.8) drip in the peroxide bath, as shown in **Figure 3.4B**. In this case, when the logibot was placed near an acid drip, more (less) peroxide fuel towards the rear (front) side of it, owing to the smaller (larger) distance from the acid drip, helped the microbot in migrating away from the acid drip. Larger catalytic decomposition of the peroxide fuel took place at the rear part (acid-rich darker yellow zone) of the microbot than on the front side (acid lean, pale yellow zone). As a consequence, the motor migrated away from the thread dripping acid when pH < 2.8 showing a negative acid-taxis.

The same logibot could be migrated towards the thread when the drip was a mixture of catalase (3 mg mL^{-1}) and HCl (0.005 M, 2.8 < pH < 5.8), as shown in **Figure 3.4C**. In this situation, the logibot showed directed acid taxis towards the lower pH region. The infusion of catalase in the acid-drip enhanced the rate of peroxide decomposition and disturbed the stabilization of peroxide due to the acid-drip. The catalase drip ensured the presence of more (less) peroxide fuel towards the rear (front) side of the microbot owing to its larger (smaller) distance from the acid-catalase drip. Consequently, the concentration gradient across the logibot induced the directed migration towards the low pH region, as indicated by yellow coloration. The acid-taxis was attuned to the optimal activity of the catalase enzyme, which in general falls in the pH range of 2.8 and 5.8.[73–75] The enzyme activity is usually affected by pH changes beyond its favorable range. Since pH is one of the factors responsible in protein denaturation, the exposure to enzyme catalase in highly acidic and basic pH solutions could destroy the secondary and tertiary structure of enzyme leading to a gross

reduction in the enzymatic activity.[74,75] Importantly, the observed acid and alkali taxis of the logibot were found to be very similar to the chemotactic migrations of microorganisms.[76] **Figure 3.4D** shows a case in which the logibot was immersed inside the bath in which, on one side there was an alkali drip (pH 7.5) while on the other side, there was an acid-catalase drip (pH 4.51), as schematically shown in Figure 3.1A.

The experimental setup ensured that the motor had nearly equal opportunity to move towards either the acid-catalase or the alkali drip. However, under the dual gradients, the logibot showed an acid-taxis owing to the larger osmotic thrust experienced towards the catalase-acid drip (yellow region). The intense catalase activity in the range of pH 2.8–5.8 played a crucial role in this acid taxis. In comparison, when the pH of the acid-catalase drip was lowered to ~2.46, and the pH of the alkali drip was kept at ~8.2, an alkali-taxis was witnessed, as shown in **Figure 3.4E**. The loss of catalase activity coupled with a larger osmotic thrust near the alkali-drip helped the logibot to migrate towards the alkali drip (blue region). **Figure 3.4F** shows the stationary state of the motor with no net displacement due to uniform ejection of oxygen bubbles from the surface of the motor in almost all the directions. This reflects a very high rate of peroxide fuel decomposition in the bath by the inbuilt catalase activity present in logibots. Concisely, Figures 3.1 and 3.4 together show the glimpses of the conditional chemotaxis, which was deciphered as the different logic gates and circuits later.

The impact of various parameters on the motions of logibots was studied by performing the series of experiments in triplicates. In the case of alkali taxis, the experiments were carried out by placing a logibot (size ~140 μm) inside the bath with 7.0% (v/v) peroxide fuel and varying the pH of the alkali (NaOH) drip from 8.3 to 12.9.

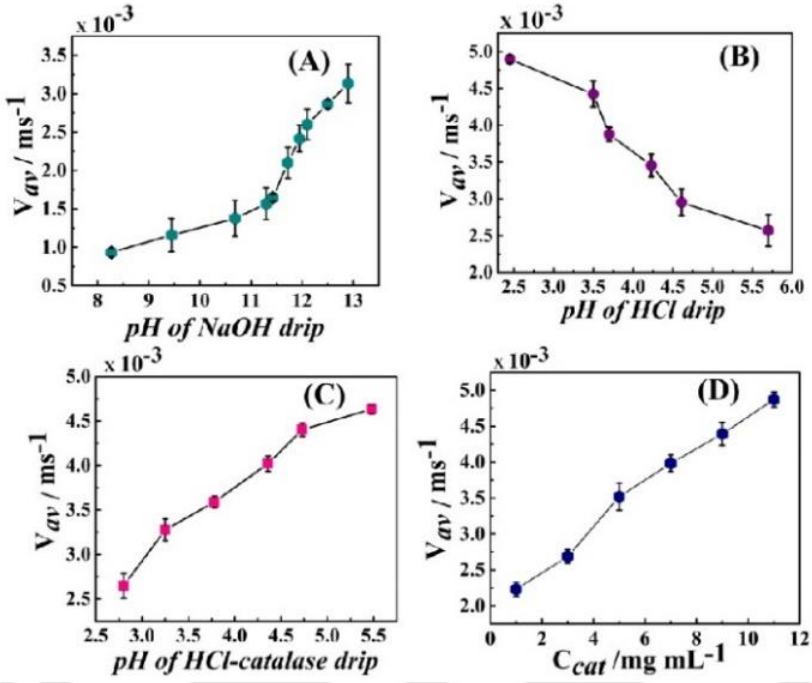

Figure 3.5. Image **(A)** depicts the variation in the average velocity (V_{av}) of logibot suspended in 7% (v/v) peroxide fuel under a continuous NaOH drip of different pH. Image **(B)** depicts the variation in the V_{av} of logibot suspended in 7% (v/v) peroxide under a continuous HCl drip with different pH. Image **(C)** depicts the variation in the V_{av} of logibot suspended in 7% (v/v) peroxide under a continuous HCl-catalase drip of different pH. Image **(D)** depicts the variation in the V_{av} of a logibot suspended in 7% (v/v) peroxide under the varying concentration of catalase (C_{cat}) in a continuous HCl-catalase drip. All the data reported in this figure is the outcome of the experiments performed in triplicates.

Figure 3.5A shows that the average speed of the logibot (V_{av}) increased progressively with the pH of the alkali reservoir. The average speed of the micromotor was found to be ~ 0.93 × 10^{-3} ms^{-1} at a pH of 8.3, which increase to ~ 3.15 × 10^{-3} ms^{-1} (~21 body lengths per second) at pH 12.9. Additionally, the repulsive motion of the logibot away from the thread was recorded under the influence of acid drip by varying the pH of HCl dripping from the reservoir between pH values 2.6 to 5.8. The V_{av} of the logibot away from the acid source is depicted in **Figure 3.5B**, where a maximum speed of ~ 4.95 × 10^{-3} ms^{-1} (~ 32.5 body lengths per second) was attained at pH 2.8 as the repulsion weakens, the average speed that was

around ~ 2.57 × 10^{-3} ms^{-1} at pH 5.8 (~ 16 body lengths per second). The variation in the V_{av} with the pH of HCl and catalase drip ranging from 2.8 to 5.8 was also studied. The HCl concentration was varied from 0.1M – 0.005M, while the concentration of catalase was kept constant (3 mg mL^{-1}). **Figure 3.5C** shows that at pH value of 2.8, the average speed of the motor was found to be 2.6 × 10^{-3} ms^{-1} (~17 body lengths per second). As the pH reaches an optimum value, an increase in the catalytic activity of the extrinsic catalase present in acid-enzyme drip was noted, which further enhanced the homogenous decomposition of peroxide fuel in the bath. This, in turn, increased the motor speed to ~4.5 × 10^{-3} ms^{-1} (~ 31 body lengths per second) at pH value of 5.8.

Further, the average speed of the micromotor was studied by changing the catalase concentration keeping the concentration of HCl constant (0.005 M, pH 4.51). **Figure 3.5D** shows the increase in the speed of the micromotor with an increase in catalase concentration (C_{cat}) from ~1 µg mL^{-1} to ~11 µg mL^{-1}. The speed of the micromotor was found to be ~2.5 × 10^{-3} ms^{-1} (~ 16 body length per second) at an initial concentration of ~1 µg mL^{-1}, which increased to ~4.9 × 10^{-3} ms^{-1} (~32 body length per second) when the catalase loading in the drip was ~11 µg mL^{-1}.

3.3.4. Mechanism of chemotactic motion

Intelligent MNMs with various propulsion mechanisms can be fabricated when surrounding fuel controlling the motor−fuel reactions exist as concentration gradients. Such chemical gradients are ubiquitous in biological environments, which attract or repel chemotactic micro/nanobots. Due to the presence of a signal source, a vector field is introduced in the system where the tactic micro/nanomotors move. Upon interaction with the local vector field, the motor propels toward or away from the signal source, which is similar to the

sensing of the signal source by the swimmers. A tactic MNM in the vector field retains an effective potential energy (U_{taxis}) that is determined by the vector field property.[77,78] The propulsion of the motor toward or away from the source lowers the total potential energy.

$$U_{\text{taxis}} = s_m \times \mu(x) \qquad (1)$$

where, $\mu(x)$ is the potential of the vector field, x is the position relative to the signal and, s_m is a parameter signifying the response of micro/nanobots upon interacting with the vector field.[77-79]

Establishment of directional propulsion forces are required to achieve effective movement towards or away from signal source along the vector field line. However, the miniaturized motors generally rotate randomly owing to their rotational Brownian diffusion, thus misaligning the symmetry axis of motors with the local vector field. When asymmetric motors interact with local vector fields (chemical gradient, flow, magnetic field), they experience an aligning torque **(M)** for temporary or continuous orientation.[80] Thus, the micro/nanomotors gain the required propulsion thrust to seek or move away from the source.

Whereas, the direction of propulsion forces for isotropic motors solely depends on local vector fields, irrespective of Brownian rotations. Force symmetry restricts the motion of isotropic micro/nanomachines in a uniform environment. But in a vector field, the motors produce asymmetrical distribution of field-induced chemical energy or products along the vector field line. Their isotropic structure restricts the change in the distribution of chemical products with Brownian rotations.[81] Hence, such chemotactic microbots demonstrate directional driving force along a vector field, where distribution of products is defined only by the vector field. In this regard, when an asymmetric motor exhibiting chemotaxis is

misaligned with the direction of concentration gradient, there will be an asymmetric distribution of the chemical product on the two sides of the symmetry axis of the motors. As a result, the propulsion thrust gets deviated from its symmetry axis and geometric center, thus producing an indirect torque **(M_P)** to rotate the micromotor for aligning its symmetry axis along with the direction of chemical gradient. The indirect torque arises from the geometric center of the particle and motor propulsion deviates in response to the gradient.

When the micromotors were exposed to a magnetic field, they were subjected to a force **F** arising directly from the local vector field. At this moment, any misalignment between the local vector field and micromotor symmetry axis could generate an aligning torque **(M_F)** for self-reorientation of motors along the vector field.[77-81] Broadly, the chemotactic motions of asymmetric micro/nanobots encompasses an amalgamation of directional propulsion along the vector field and random Brownian rotations. Strong M_P and M_F will suppress the Brownian diffusion, thus preventing the motors to wander towards or away from the signal source and allowing them to move linearly.

3.3.5. Logibots motion: gates and circuits

The response of the logibots under the dual stimuli shown the potential of these self-propelling objects as promising reconfigurable logic gates because they could be actuated in presence of both acid and alkali inputs to perform logical migrations. In a way, the logibot could sense the variation in the pH of the surrounding medium to regulate its migration. Some specific and rigorous logics of the migrations of the logibot was shown towards acid or alkali sources, which were previously reported in Figure 3.4.

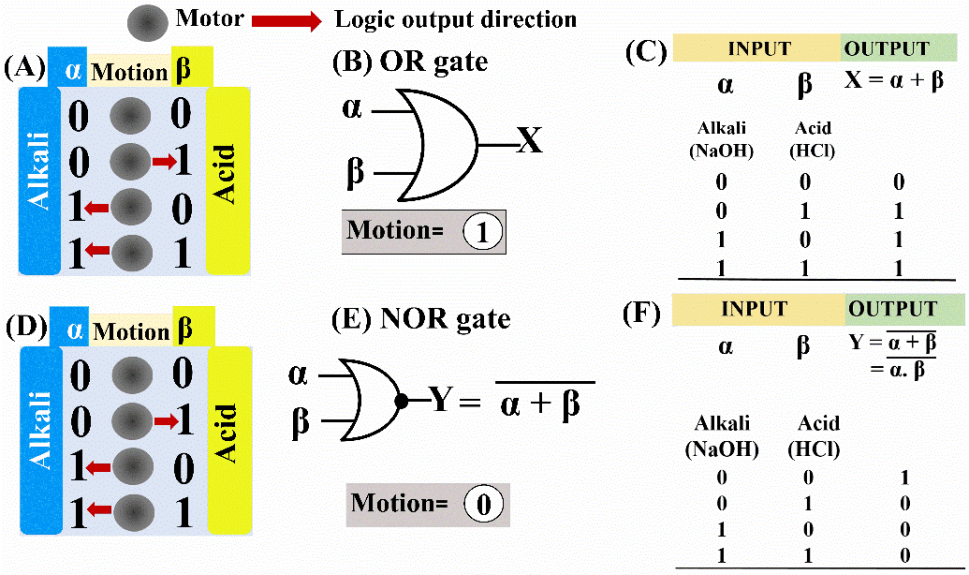

Figure 3.6. Image **(A)** shows the schemes for position and migration of the logibot towards alkali and acid inputs, respectively. Image **(B)** shows OR-gate considering the logibot motion as output "1". The corresponding truth table of OR-gate has been shown in the image **(C).** Images **(D-E)** show the schematics for position and migration of the logibot towards alkali and acid inputs and NOR-gate, respectively, considering the motion as output "0". The corresponding truth table of NOR logic gate has been shown in the image **(F).**

Figure 3.6 shows simple examples of the chemotactic migrations of a logibot under the dual acid-alkali stimuli, which could be interpreted as the OR- and NOR-gates. Initially, considered the motions of the logibot was considered as the indicators for the logical operations. For example, when the logibot moved towards a stimulus or away from the same, the motion was considered as the logic "1". In contrast, the logic for a stationary logibot was considered to be "0". **Figure 3.6A** shows the schemes for the motion of the logibot under the dual external stimuli acid (α) and alkali (β) as the inputs. The figures suggest that if the logibot moved under the acid (HCl) or alkali (NaOH) inputs the logic output was assumed to be "1" whereas the lack of motion was assumed to be the logic output

"0". It was assumed that the movement under any of the inputs α or β was sufficient to fulfill the criteria for the logic "1".

Under this framework, the chemotaxis of the logibot followed an OR-gate, as shown by the logic circuit in **Figure 3.6B** and the corresponding truth table in **Figure 3.6C**. **Figure 3.6D** shows the schemes for the motion of the logibot under the dual external stimuli acid (α) and alkali (β) as the inputs considering the motion as output "0". Interestingly, when the motion of the motor was considered as logic "0" and the lack of the motion as the logic "1", NOR-gate chemotaxis could be implemented with the similar dual stimuli acid (α) and alkali (β) inputs. The NOR-gate circuit and the corresponding truth table are shown in the **Figures 3.6E** and **3.6F**, where the presence of both the inputs (acid and alkali) triggered the motion to provide a logic output of "0". The logibot could also migrate in the presence of either of the inputs (acid or alkali), as represented by the logic output of "0". In contrast, the absence of the inputs was represented by the logic output of "1".

In **Figure 3.7**, some more rigorous logic gates have been developed analyzing the motions of the logibot between the ranges, (i) pH < 2.8 and pH > 5.8 – towards alkali source and (ii) 2.8 < pH < 5.8 – towards the acid source under dual stimuli whereas towards the alkali source under the sole alkali stimulus. For example, a chemotactic migration following OR-gate was observed in the situations where pH < 2.8 and pH > 5.8 when acid was considered as input α and, alkali as input β. The motion of logibot towards alkali source was considered as output "1", and everything else such as the lack of motion or motion towards the acid source as output "0", as shown by the schematic in the **Figures 3.7A** and **3.7B**. The absence of both the inputs α and β suppresses the motion leading to a digital output of "0" whereas the presence of either of the inputs or both the inputs resulted in movement of the logibot

towards the alkali input β defined by the digital output "1", as shown in the truth table **Figure 3.7C**.

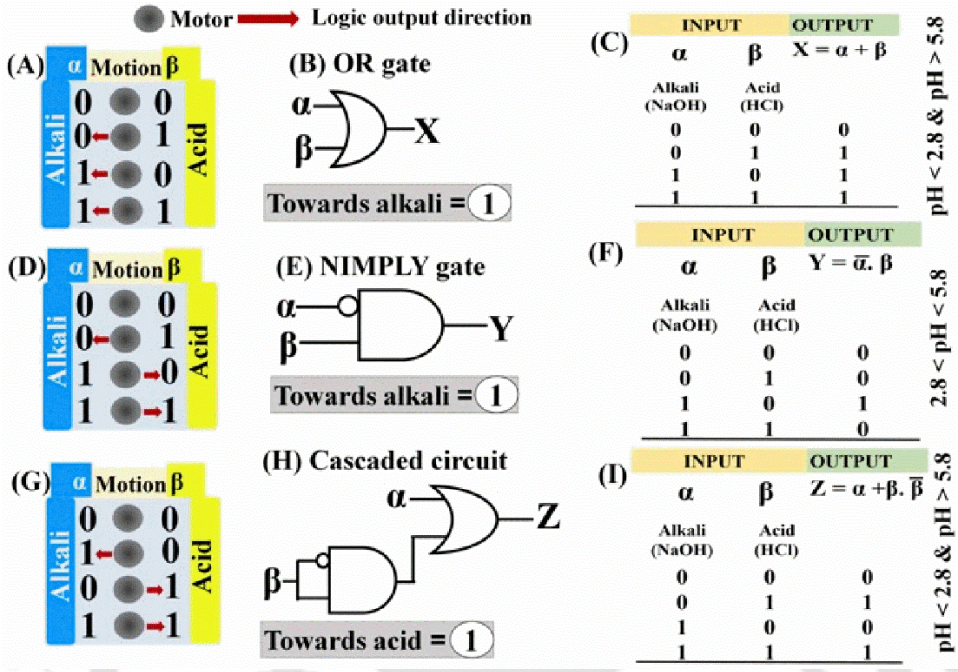

Figure 3.7. Images **(A, D, and G)** show the motion of the logibot towards alkali and acid inputs schematically. Image **(A)** shows the motion of the logibot, and **(B)** shows OR-gate considering the motion towards alkali as output "1". Two digital outputs "1" and "0" represent two different logic configurations in this case. The corresponding truth table of OR-gate has been shown in the image **(C)** for pH < 2.8 and pH > 5.8. Image **(D)** shows the position of the micromotor. Image **(E)** shows NIMPLY-gate considering the motion towards alkali as output "0" when 2.8 < pH < 5.8. The truth table of NIMPLY-gate has been shown in the image **(F)**. Image **(G)** shows the motion and image **(H)** shows the cascade-logic-circuit consisting of OR- and NAND-gates considering motion of the logibot towards acid as output "1" when pH < 2.8 and pH > 5.8. The corresponding truth table has been shown in the image **(I).**

Therefore, a successful OR gate could be achieved, considering the pH of the inputs between pH < 2.8 and pH > 5.8. **Figures 3.7D** and **3.7E** show the chemotaxis following the NIMPLY-gate when the pH of the acid and alkali inputs were between the range of 2.8 < pH <5.8. This system could also be defined as NOT-IMPLICATION-gate. In this situation, the logic was reconfigured as the motion of

the logibot towards alkali to be digital output "1" and anything else to be digital output "0". The logic circuit in the **Figure 3.7E** and the truth table in the **Figure 3.7F** together show that the presence and absence of both the inputs α and β within this pH range inhibits the motion of the logibot towards alkali, as defined by the output "0". Further, the sole presence acid input obstructs the migration of the logibot towards the alkali defined by output "0" whereas the sole alkali input exhibits the migration of the logibot towards the alkali indicated by digital output "1".

A chemotaxis following a cascade of logic circuits consisting of OR- and NAND-gates could also be achieved using both the inputs α and β when the pH was within the range of pH < 2.8 and pH >5.8, as schematically shown in the **Figure 3.7G** and the corresponding logic circuit and truth table in the **Figures 3.7H** and **3.7I**. In this case, the motion of the logibot towards alkali was considered as the logic output "1" and anything else was considered as the logic "0".

It may be noted here that in the presence of both the inputs α and β within the range of pH < 2.8 and pH >5.8, the logibot moved towards the alkali source represented by digital output "1". However, the absence of both the inputs (acid and alkali) inhibits the logibot motion represented by output "0". The presence of sole alkali input (β) facilitated the movement of logibot towards alkali implied as output "1". Conversely, the presence of acid input actuated the logibot motion towards alkali defined as digital output "1".

The speed of the logibot towards the acid or alkali stimuli could also be interpreted in terms of different logic gates, as shown in **Figure 3.8**. The digital outputs "1" and "0" were considered with respect to V_{av} of the logibot, which at different input pH values is shown in **Figure 3.8(i)**.

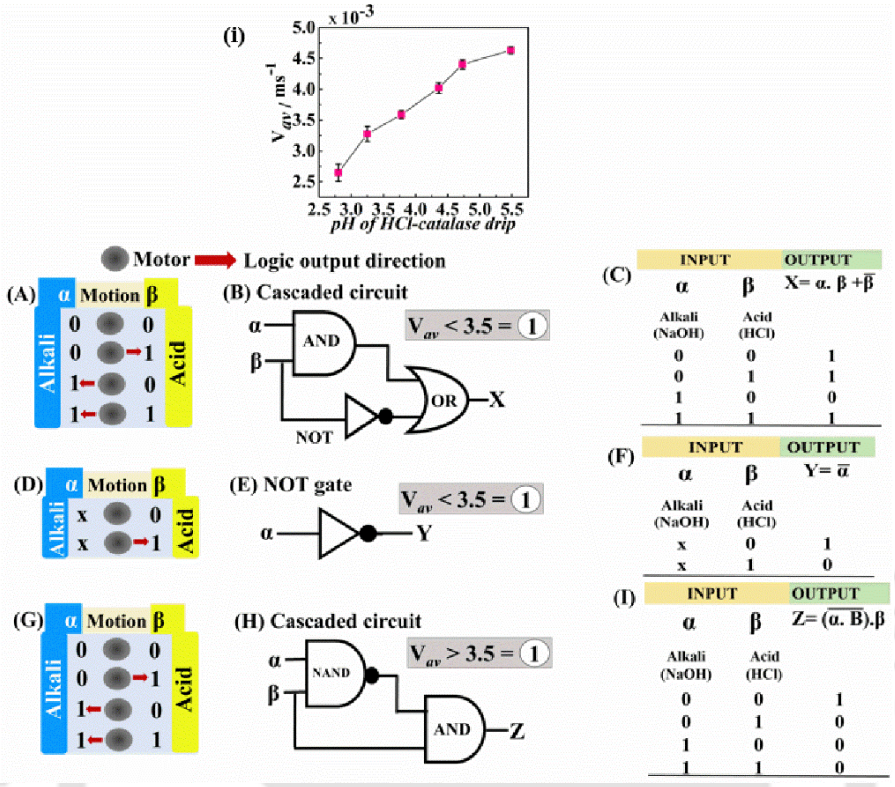

Figure 3.8. Image **(i)** shows the graph representing the variation in V_{av} of a motor with respect to pH changes of input (HCl-catalase drip). Image **(A)** shows the motion of the logibot either towards acid or alkali schematically. Image **(B)** shows the cascaded logic circuit consisting of AND, NOT, and OR logic gates considering the motion of the motor with $V_{av} < 3.5 \times 10\text{-}3ms^{-1}$ as digital output "1". The corresponding truth table of a cascaded logic circuit has been represented in image **(C).** Image **(D)** shows the micromotor motion only in the presence of acid (pH = 5) schematically. Image **(E)** shows a NOT gate designed using single input A of pH value 5 considering the motion of micromotor as digital output "1" when $V_{av} < 3.5 \times 10^{-3}ms^{-1}$. The truth table for corresponding NOT gate has been depicted in the image **(F)**. Image **(G)** shows the micromotor motion either towards acid or alkali schematically. Image **(H)** shows a cascaded logic circuit consisting of NAND and AND logic gates considering the motion of the motor with $V_{av} > 3.5\times 10^{-3}ms^{-1}$ as digital output "1". The corresponding truth table of the cascaded logic circuit has been represented in the image **(I)**.

For example, when the digital output "1" has been defined for $V_{av} < 3.5 \times 10^{-3}\ ms^{-1}$, a drip of pH 2 as input α and a drip of pH 5 as input β resulted in a solution of pH~2.3 for which the $V_{av} < 3.5\times 10^{-3}\ ms^{-1}$. In such a situation, the motion of the logibots in the presence/absence of inputs **(Figure 3.8A)** could be interpreted as logic circuit in

Figure 3.8B and the truth table in **Figure 3.8C**, showing the logic output of "1". The same output was observed during the absence of both the inputs α and β and the sole presence of input α when pH was 2. However, when input β was introduced, V_{av} > 3.5 × 10^{-3} ms-1, which was represented by digital output "0".

Figures 3.8B and 3.8C show that the motion of the logibots could be interpreted as a cascaded logic circuit consisting of the AND-, NOT-, and OR-gates. The stationary state of the motor in the absence of inputs and migration in the presence of multiple inputs for different outputs have been schematically represented in the **Figures 3.8D and 3.8G**. The conditional speed of the logibot could also be interpreted as a NOT-gate, as shown by the logic circuit and truth table in the Figures **3.8E and 3.8F**. This was achieved by considering a single input α of pH 5 while the output was represented as digital "1"" when V_{av} < 3.5 × 10-3 ms^{-1}. The figures suggest that the absence of input α (pH 5) resulted in V_{av} < 3.5 × 10^{-3} ms^{-1}, leading to the digital output "1". However, when input α was introduced, V_{av} > 3.5 × 10-3 ms^{-1}, leading to the digital output "0".

Additionally, the logic was reconfigured by defining V_{av} > 3.5× 10^{-3} ms^{-1} as the digital output "1", which is shown by the truth table in **Figure 3.8I**. The presence of both the inputs α and β resulted in V_{av} < 3.5× 10^{-3} ms^{-1}, which was indicated as digital "0". The logic output was digital "0" in the presence of either of the input α and β, which implied V_{av} < 3.5× 10^{-3} ms^{-1}. However, the absence of both the inputs α and β, the output state was "1", because of V_{av} > 3.5× 10^{-3} ms^{-1}. The logic followed by the logibot in varying pH of dual inputs was a cascaded logic circuit composed of NAND- and AND-gates, as displayed in **Figure 3.8H**.

The logic gates and cascaded circuits associated with the motions of the logibot with respect to varied pH values have been analyzed statistically and represented in **Figure 3.9A and 3.9B**. The bar graphs **(Figure 3.9A)** represent the average velocities of logibots under the influence of acid and alkali stimuli at the different ranges of pH, representing the designed Boolean gates.

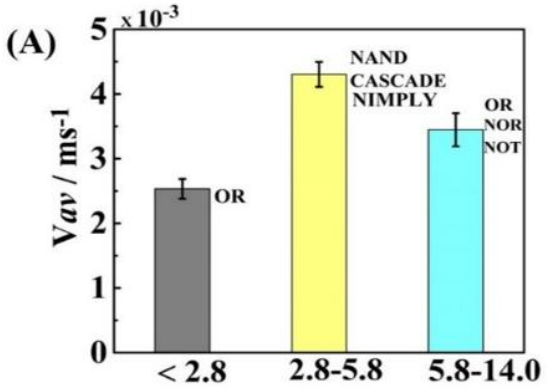

(B)

pH	LOGIC GATES	AVERAGE VELOCITIES (V_{av}) / ms^{-1}	% TOLERANCE
< 2.8	OR	2.45	6.02
2.8 - 5.8	NAND NIMPLY CASCADE	4.58	8.17
5.8 - 14	OR NOR NOT	3.56	6.49

Figure 3.9. **(A)** Statistical analysis of the performance of various Boolean gates. Here the logics are based on the variation in the average velocities of motion at different ranges of pH stimuli. **Table 3.1 (B)** displays the percentage of tolerance with respect to variations in the operating parameters, such as the pH of the input and average velocity of logibots.

The NAND, NIMPLY, and cascaded logic circuits could be designed upon the introduction of logibots in the presence of inputs of pH value between 2.8 to 5.8, achieving the highest V_{av} of ~ 4.43×10^{-3} ms^{-1}. Furthermore, on increasing the pH window beyond 5.8, the average velocity of logibots was found to be ~ 3.39×10^{-3} ms^{-1} resulting in the construction of OR, NOR, and NOT gates as depicted in the figure.

Table 3.1(B) shows the percentage of tolerance with respect to variations in the operating parameters, such as the pH of the input and average velocity of a logibot. The experiments were repeated several times to obtain the statistical percentage of

accuracy. The OR gate designed at pH <2.8 exhibited a percentage tolerance of ±6.02. Additionally, when pH was varied from 2.8 to 5.8, the NAND/NIMPLY gates and CASCADE circuit showed a percentage tolerance of ±8.17. The logic gates OR/NOR/NOT showed a percentage tolerance of ±6.49 on further increasing the pH from 5.8 to 14. The plot suggests the reliability and percentage accuracy of the chemotactic responses of the logibots towards a broad spectrum of pH, which could be utilized in the design and development of various logic circuits.

The proposed logibots were compared and contrasted with the previously reported ones.[15] It may be noted here that one of the major challenges with the construction of a taxis based Boolean gate is the consistency of the digital '0s' and '1s'.[9,82] In this study, logical operations were designed based on a uniform digital representation of '0s' and '1s' having percentage tolerance of less than 10. The variations in the average speed of logibots under the acid-alkali inputs were established after verifying a large amount of data. The motions of the motors were read as outputs and applied to logic gates and circuit-level analysis with the consideration of these statistical variations. The results reported also highlight the following salient attributes of the proposed logibots: (i) a number of different logic gates could be constructed from a single embodiment; (ii) the variations in the environmental parameters were key to the various logical migration; (iii) high output signal was obtained with a pair of inputs emulating the chemotaxis of microorganisms, and (iv) could also be employed to develop cascaded logic gates useful for molecular computing with complex data processing.

However, the following limitations were found to be associated with the proposed system: (i) the execution of these logical operations needs to be made more robust

for their independent *in vivo* functioning; (ii) the logibot operations did not allow reversibility, which restricted the recovery of the input information from the output; [82,83] and (iii) a combination of more than three or four logic gates into the cascaded system may lead to noise amplification. Thus, in the future, extensive research work may be necessary to improve upon these aspects. In particular, attention should be given to improve the sensitivity of the system to ultralow strength inputs and reusability of the logic circuits

3.4. Conclusions

In this work, versatile operational logic gates and cascaded circuits were constructed based on the pH sensing ability of tissue-based mushroom logibots. The logibots exhibited chemotactic motion towards or away from the extrinsic controlling elements – alkali and acid – inside a bath containing peroxide fuel, emulating the chemokinesis of unicellular prokaryotes or eukaryotes. Remarkably, the logibot could rapidly sense, decide, and respond on the basis of the logic input – the intensity of the pH stimuli in the surroundings – and logic output – the direction and speed of the logibot motion. The velocity and directionality of the logibots could be tuned by varying the pH of the alkali and/or acid inputs, which were utilized in achieving multiple reconfigurable AND, NAND, NOT, OR, NOR, and NIMPLY logic gates and cascaded logic circuits. In the present scenario, the use of intelligent biological systems for logic gate implementations has been considered as an eco-friendly alternative to silicon-based computing operations. Although the provided logical operations have exhilarating prospects, investigations for overcoming the challenges are still in the experimental stage. It is expected that this study may provide an important starting point for the forthcoming design of tissue-based logic gates, which

may also be of significance in various next-generation biomedical, mechanical, pharmaceutical and electronic applications at the micro or nanoscale.

References

(1) Adler, J.; Hazelbauer, G. L.; Dahl, M.M. Chemotaxis Toward Sugars in *Escherichia coli* *J. Bacteriol*. **1973**, 115, 824–847.

(2) Deshpande, A; Samanta, S.; Das, H.; Layek, R. K. A Boolean approach to bacterial chemotaxis. *Proc. Annu. Int. Conf. IEEE Eng. Med. Biol. Soc*. (EMBS), Orlando, FL, Oct. **2016**, 6125–6129.

(3) Pham, H. T.; Parkinson, J.S. Phenol Sensing by *Escherichia coli* Chemoreceptors: a Nonclassical Mechanism. *J. Bacteriol*. **2011**,193, 6597–6604.

(4) Wu, Z.; Li, T.; Li, J.; Gao, W.; Xu, T.; Christianson, X.; Gao, W.; Galarnyk, M.; He,Q.; Zhang, L.; Wang, J. Turning Erythrocytes into Functional Micromotors. *ACS Nano* **2014**, 8, 12041–12048.

(5) Guix, M.; Carmen, C.; Martinez, M.; Merkoci, A. Nano/Micromotors in (Bio) chemical Science Applications. *Chem. Rev*. **2014**, 114, 6285–6322.

(6) Claussen, J. C.; Algar, W. R.; Hildebrandt, N.; Susumu, K.; Ancona, M. G.; Medintz, I. L. Biophotonic logic devices based on quantum dots and temporally-staggered Förster energy transfer relays. *Nanoscale* **2013**, 5, 12156–12170.

(7) Claussen, J. C.; Hildebrandt, N.; Susumu, K.; Ancona, M. G.; Medintz, I. L. Complex Logic Functions Implemented with Quantum Dot Bionanophotonic Circuits. *ACS Appl. Mater*. **2014**, 6, 3771–3778.

(8) Wieland, M.; Fussenegger, M. Engineering molecular circuits using synthetic biology in mammalian cells. *Annu. Rev. Chem. Biomol. Eng*. **2012**, 3, 209–234.

(9) Lai, Y.-H.; Sun, S.-C.; Chuang, M. C. Biosensors with Built-In Biomolecular Logic Gates for Practical Applications. *Biosensors* **2014**, 4, 273-300.

(10) Zhang, P.; He, Z.; Wang, C.; Chen, J.; Zhao, J.; Zhu, X.; Li, C.-Z.; Min, Q.; Zhu, J.J. In Situ Amplification of Intracellular MicroRNA with MNAzyme Nanodevices for Multiplexed Imaging, Logic Operation, and Controlled Drug Release. *ACS Nano* **2015**, 9, 789–798.

(11) Nikitin, M.P.; Shipunova, V. O.; Deyev, S. M.; Nikitin, P. I. Biocomputing based on particle disassembly. *Nat. Nanotechnol*. **2014**, 9, 716–722.

(12) Ji, W.; Shi, H.; Zhang, H.; Sun, R.; Xi, J.; Wen, D.; Feng, J.; Chen, Y.; Qin, X.; Ma, Y.; Luo, W.; Deng, L.; Lin, H.; Yu, R.; Ouyang, Q. A formalized design process for bacterial consortia that perform logic computing. *PLoS One* **2013**, 8, e57482.

(13) Li, Z.; Rosenbaum, M. A.; Venkataraman, A.; Tam, T. K.; Katz, E.; Angenent, L. T. Bacteria-based AND logic gate: a decision-making and self-powered biosensor. *Chem. Commun*. **2011**, 47, 3060–3062.

(14) Katz, E.; Privman. Enzyme-based logic systems for information processing. *Chem. Soc. Rev*. **2010**, 39, 1835–1857.

(15) Komatsu, H.; Matsumoto, S.; Tamaru, S.-I.; Kaneko, K.; Ikeda, M.; Hamachi, I. Supramolecular Hydrogel Exhibiting Four Basic Logic Gate Functions To Fine-Tune Substance Release. *J. Am. Chem. Soc*. **2009**, 131, 5580–5585.

(16) Maurya, N.; Singh, A.K. Effective ensemble system for the identification of CN^- based on a cobalt(ii) complex: a logic gate mimic. *New J. Chem*. **2017**, 41, 4814–4819.

(17) Gentili, D.; Sonar, P.; Liscio, F.; Cramer, T.; Ferlauto, L.; Leonardi, F.; Milita, S.; Dodabalapur, A.; Cavallini, M. Logic-Gate Devices Based on Printed Polymer Semiconducting Nanostripes. *Nano Lett*. **2013**, 13, 3643–3647.

(18) Ma, D.-L.; He, H.-Z.; Chan, D. S.-H.; Leung, C.-H. Simple DNA-based logic gates responding to biomolecules and metal ions. *Chem. Sci.* **2013**, 4, 3366–3380.

(19) Dr Bi, S.;Yan, Y.; Hao, S.; Zhang, S. Colorimetric Logic Gates Based on Supramolecular DNAzyme Structures. *Angew. Chem. Int. Ed*. **2010**, 49, 4438–4442.

(20) He, Y.; Cui, H. Chemiluminescent Logic Gates Based on Functionalized Gold Nanoparticles/Graphene Oxide Nanocomposites. *Chem. -Eur. J*. **2013**, 19, 13584–13589.

(21) Yin, C.; Huo, F.; Cooley, N. P.; Spencer, D.; Bartholomew, K.; Barnes, C. L. Glass, T. E. A Two-Input Fluorescent Logic Gate for Glutamate and Zinc. *ACS Chem. Neurosci*. **2017**, 8, 1159–1162.

(22) Loget, G.; Fabre, B. Light-Driven Bipolar Electrochemical Logic Gates with Electrical or Optical Outputs. *Chem. Electro. Chem.* **2016**, 3, 366–371.

(23) Macia, J.; Manzoni, R.; Conde, N.; Urrios, A.; de Nadal, E.; Sole, R.; Posas, F. Implementation of Complex Biological Logic Circuits Using Spatially Distributed Multicellular Consortia. *PLoS Comput. Biol*. **2016**, 12, 1–24.

(24) Macnab, R. M.; Koshland, D. E. The Gradient-Sensing Mechanism in Bacterial Chemotaxis. *Proc. Natl. Acad. Sci. U. S. A.* **1972**, 69, 2509–2512.

(25) Morisawa, M.; Yoshida, M. Activation of motility and chemotaxis in the spermatozoa: From invertebrates to humans. *Reprod. Med. Biol.* **2005**, 4, 101–114.

(26) Kahle, N. A.;Brenner-Weiss, G.; Overhage, J.; Obst, U.; Ha¨nsch, G. M.; Bacterial quorum sensing molecule induces chemotaxis of human neutrophils via induction of p38 and leukocyte specific protein 1 (LSP1). *Immunobiology* **2013**, 218, 145–151.

(27) Hettie, K. S.; Klockow. J. L.; Glass, T. E. Three-Input Logic Gates with Potential Applications for Neuronal Imaging. *J. Am. Chem. Soc*. **2014**,136, 4877–4880.

(28) Guiziou, S.; Mayonove, P.; Ulliana, F.; Moreau, V.; Leclere, M.; Bonnet, J. Scalable composition frameworks for multicellular logic. **2017**, *bioRxiv:10.1101*/150987.

(29) Singh, V. Recent advances and opportunities in synthetic logic gates engineering in living cells. *Synthetic. Syst. Biol*. **2014**, 8, 271–282.

(30) Wang, B.; Kitney, R.; Joly, N.; Buck, M. Engineering modular and orthogonal genetic logic gates for robust digital-like synthetic biology. *Nat. Commun*. **2011**, 2, 508.

(31) Okamoto, A.; Tanaka, K.; Saito, I. DNA Logic Gates. *J. Am. Chem. Soc*. **2004**, 126, 9458–9463.

(32) Green, A.A.; Kim, J.; Ma, D.; Silver, P. A.; Collins, J.J.; Yin, P. Complex cellular logic computation using ribocomputing devices. *Nature* **2017**, 548, 117–121.

(33) Adamatzky, A.; Schubert, T. Slime mold microfluidic logical gates. *Mater. Today*. **2014**, 17, 86–91.

(34) Schumann, A. Conventional and unconventional reversible logic gates on *Physarum polycephalum*. *Int. J. Parallel, Emergent Distrib. Syst*. **2017**, 32, 218–231.

(35) Li, Z.; Rosenbaum, M. A.; Venkataraman, A.; Tam, T. K.; Katzb, E.; Angenent, L. T. Bacteria-based AND logic gate: a decision-making and self-powered biosensor. *Chem. Commun*. **2011**, 47, 3060–3062.

(36) Paxton, W. F.; Kistler, K. C.; Olmeda, C.C.; Sen, A.; Angelo, S. K. S.; Cao, Y.; Mallouk, T. E .; Lammert, P. E.; Crespi, V. H. Catalytic nanomotors: autonomous movement of striped nanorods. *J. Am. Chem. Soc*. **2004**, 126, 13424–13431.

(37) Katuri, J.; Ma, X.; Stanton, M.M.; Sanchez, S. Designing Micro- and Nanoswimmers for Specific Applications. *Acc. Chem. Res*. **2017**, 50, 2–11.

(38) Guix, M.; Weiz, S. M.; Schmidt, O.G.; Sa´nchez, M. M. Self –Propelled Micro/Nanoparticle Motors. *Part. Part. Syst. Charact*. **2018**, 1700382, 1–31.

(39) Velegol, D.; Garg, A.; Guha, R.; Kar, A.; Kumar, M. Origins of concentration gradients for diffusiophoresis. *Soft Matter* **2016**, 12, 4686–4703.

(40) Wu, Y.; Dong, R.; Zhang, Q.; Ren, B. Dye-Enhanced Self-Electrophoretic Propulsion of Light-Driven TiO2–Au Janus Micromotors. *Nano-Micro Lett*. **2017**, 9, 30.

(41) Sanchez, S.; Solovev, A. A.; Mei, Y.; Schmidt, O. G. Dynamics of Biocatalytic Microengines Mediated by Variable Friction Control. *J. Am. Chem. Soc.* **2010**, 132, 13144–13145.

(42) Baraban, L.; Harazim, S. M.; Sanchez, S.; Schmidt, O. G. Chemotactic behavior of catalytic motors in microfluidic channels. *Angew. Chem. Int. Ed.* **2013**, 52, 5552–5556.

(43) Mei, Y.; Huang, G.; Solovev, A. A.; Urena, E. B.; Monch, I.; Ding, F.; Reindl, T.; Fu, R. K. Y.; Schmidt, O. G. Versatile Approach for Integrative and Functionalized Tubes by Strain Engineering of Nanomembranes on Polymers. *Adv. Mater*. **2008**, 20, 4085–4090.

(44) Solovev, A. A.; Mei, Y.; Urea, E. B.; Huang, G.; Schmidt, O. G. Catalytic microtubular jet engines self-propelled by accumulated gas bubbles. *Small*, **2009**, 5, 1688–1692.

(45) Martel, S. Swimming microorganisms acting as nanorobots versus artificial nanorobotic agents: A perspective view from an historical retrospective on the future of medical nanorobotics in the largest known three-dimensional biomicrofluidic networks. *AIP Biomicrofluidics* **2016**, 10, 021301.

(46) Bhuyan, T.; Singh, A. K.; Dutta, D.; Unal, A.; Ghosh, S. S.; Bandyopadhyay, D. Magnetic Field Guided Chemotaxis of iMushbots for Targeted Anticancer Therapeutics. *ACS Biomater. Sci. Eng*. **2017**, 3, 1627–1640.

(47) de A´vila, B. E. F.; Angsantikul, P.; Li, J.; Lopez-Ramirez, M. A.; Ramı´rez-Herrera, D. E.; Thamphiwatana, S.; Chen, C.; Delezuk, J.; Samakapiruk, R.; Ramez, V.; Obonyo, M.; Zhang, L.; Wang, J. Micromotor-enabled active drug delivery for in vivo treatment of stomach infection. *Nat. Commun*. **2017**, 8, 1299.

(48) Xu, H.; Sa´nchez, M. M.; Magdanz, V.; Schwarz, L.; Hebenstreit, F.; Schmidt, O. G. Sperm-Hybrid Micromotor for Targeted Drug Delivery. *ACS Nano*, **2018**, 12, 327–337.

(49) Soler, L.; Sanchez, S. Catalytic nanomotors for environmental monitoring and water remediation. *Nanoscale*, **2014**, 6, 7175-7182.

(50) Gao, W.; Feng, X.; Pei, A.; Gu, Y.; Li, J.; Wang, J. Seawater-driven magnesium based Janus micromotors for environmental remediation. *Nanoscale* **2013**, 5, 4696–4700.

(51) Solovev, A. A.; Xi, W.; Gracias, D. H.; Harazim, S. M.; Deneke, C.; Sanchez, S.; Schmidt, O. G. Self-Propelled Nanotools. *ACS Nano* **2012**, 6, 1751–1756.

(52) Singh, V. V.; Wang, J. Nano/micromotors for security/defense applications. A review. *Nanoscale* **2015**, 7, 19377–19389.

(53) Campuzano, S.; Kagan, D.; Orozco, J.; Wang, Motion-driven sensing and biosensing using electrochemically propelled nanomotors. J. *Analyst*. **2011**,136, 4621–4630.

(54) Singh, A.K.; Dey, K. K.; Chattopadhyay, A.; Mandal, T.K.; Bandyopadhyay, D. Multimodal chemo–magnetic control of self-propelling microbots. *Nanoscale* **2014**, 6, 1398–1405.

(55) Kumar, S.; Singh, A. K.; Dasmahapatra, A. K.; Mandal, T. K.; Bandyopadhyay, D. Graphene based multifunctional superbots. *Carbon* **2015**, 89, 31–40.

(56) Kherzi, B.; Pumera, M. Self-propelled autonomous nanomotors meet microfluidics. *Nanoscale* **2016**, 8, 17415–17421.

(57) Dong, Y.; Liu, M.; Zhang, H.; Dong, B. Reconfigurable OR and XOR logic gates based on dual responsive on–off–on micromotors. *Nanoscale* **2016**, 8, 8378–8383.

(58) Zhang, L.; Zhang, H.; Liu, M.; Dong, B. Reprogrammable Logic Gate and Logic Circuit Based on Multistimuli-Responsive Raspberry-like Micromotors. *ACS Appl. Mater. Interfaces*. **2016**, 8, 15654–15660.

(59) Rao, K. J.; Li, F.; Meng, L.; Zheng, H.; Cai, F.; Wang, W. A Force to Be Reckoned With: A Review of Synthetic Microswimmers Powered by Ultrasound. *Small* **2015**, 11, 2836–2846.

(60) Solovev, A. A.; Sanchez, S.; Pumera, M.; Mei Y. F.; Schmidt, O. G. Magnetic Control of Tubular Catalytic Microbots for the Transport, Assembly, and Delivery of Micro-objects. *Adv. Funct. Mater*. **2010**, 20, 2430–2435.

(61) Duan, W.; Liu, R.; Sen, A. Transition between Collective Behaviors of Micromotors in Response to Different Stimuli. *J. Am. Chem. Soc*. **2013**, 135, 1280–1283.

(62) Srivastava, S. K.; Sa´nchez, M. M.; Koch, B.; Schmidt, O. G. Medibots: Dual-Action Biogenic Microdaggers for Single-Cell Surgery and Drug Release. *Adv. Mater*. **2016**, 28, 832–837.

(63) Gu, Y.; Sattayasamitsathit, S.; Kaufmann, K.; Vazquez-Duhalt, R.; Gao, W.; Wang, C.; Wang, J. Self-propelled chemically-powered plant-tissue biomotors. *Chem. Commun*. **2013**, 49, 7307–7309.

(64) Sattayasamitsathit, S.; Kaufmann, K.; Galarnyk, M.; Vazquez-Duhalt, R.; Wang, J. Dual-enzyme natural motors incorporating decontamination and propulsion capabilities. *RSC Adv*. **2014**, 4, 27565–27570.

(65) Gao, W.; Feng, X.; Pei, A.; Kane, C. R.; Tam, R.; Hennessy, C.; Wang, J. *Nano Lett*. **2014**, 14, 305–310.

(66) Wang, H.; Moo, J. G. S.; Pumera, M. Tissue cell assisted fabrication of tubular catalytic platinum microengines. *Nanoscale*, **2014**, 6, 11359–11363.

(67) Savoie, J. M.; Minvielle, N.; Largeteau, M. L. Radical-scavenging properties of extracts from the white button mushroom, *Agaricus bisporus*. *J. Sci. Food Agric*. **2008**, 88, 970–975.

(68) Aliramaji, S.; Zamanian, A.; Sohrabijam, Z. Characterization and Synthesis of Magnetite Nanoparticles by Innovative Sonochemical Method. *Procedia Mater. Sci*. **2015**, 11, 265-269.

(69) Bastami, T. R.; Entezari, M. H. High stable suspension of magnetite nanoparticles in ethanol by using sono-synthesized nanomagnetite in polyol medium. *Mater. Res. Bull*. **2013**, 48, 3149-3156.

(70) Mahadevan, S.; Behera, S. P.; Gnanaprakash, G.; Jayakumar, T.; Philip, J.; Rao, B. P. C. *J. Phys. Chem. Solids*. **2012**, 73, 867-872.

(71) Wang, Y.; Li, B.; Zhou, Y.; Jia, D. In Situ Mineralization of Magnetite Nanoparticles in Chitosan Hydrogel. *Nanoscale Res. Lett*. **2009**, 4, 1041-1046.

(72) Dey, K. K.; Bhandari, S.; Bandyopadhyay, D.; Basu, S.; Chattopadhyay, A. The pH taxis of an intelligent catalytic microbot. *Small* **2013**, 9, 1916–1920.

(73) Chance, B. Effect of pH upon the reaction kinetics of the enzyme-substrate compounds of catalase. *J. Biol. Chem*. **1952**, 194, 471–481.

(74) Susmitha, S.; Ranganayaki, P.; Vidyamol, K. K.; Vijayaraghavan, R. Phytochemical extraction and antimicrobial properties of *Azadirachta indica* (Neem). *Int. J. Curr. Microbiol. Appl. Sci.* **2013**, 2, 255–263.

(75) Morgulis, S.; Beber, M.; Rabkin, I. Studies on the effect of temperature on the catalase reaction: iii. Temperature effect at different hydrogen ion concentrations. iv. A theory of the catalase reaction. *J. Biol. Chem*. **1926**, 68, 547–563.

(76) Wadhams, G. H.; Armitage, J. P. Making sense of it all: bacterial chemotaxis. *Nat. Rev. Mol. Cell Biol.* **2004**, 5, 1024–1037.

(77) Bauer, A. L.; Jackson, T. L.; Jiang, Y. A Cell-Based Model Exhibiting Branching and Anastomosis during Tumor-Induced Angiogenesis. *Biophys. J*. **2007**, 92, 3105−3121.

(78) Jiang, Y.; Levine, H.; Glazier, J. Possible Cooperation of Differential Adhesion and Chemotaxis in Mound Formation of Dictyostelium. *Biophys. J*. **1998**, 75, 2615−2625.

(79) Montiel, O.; Sepú lveda, R.; Orozco-Rosas, U. Optimal Path Planning Generation for Mobile Robots Using Parallel Evolutionary Artificial Potential Field. *J. Intell. Rob. Syst.* **2015**, 79, 237−257.

(80) Dhont, J. K. G. *An Introduction to Dynamics of Colloids;* Elsevier: Amsterdam, **1996**; pp 183−186.

(81) You, M.; Chen, C.; Xu, L.; Mou, F.; Guan, J. Intelligent Micro/nanomotors with Taxis. *Acc. Chem. Res*. **2018**, 51, 3006-3014.

(82) Katz, E.; Fratto, B. E. Advances in Unconventional Computing. *Springer; 1st ed*. **2017**, 2, 1-812.

(83) Boruah, K.; Dutta, J. C. DNA Computing Models for Boolean Circuits and Logic Gates. *Proc. IEEE Int. Conf. Comput. Intell. Commun. Technol.* **2015**, 529–533.

CHAPTER 4

Magnetotactic Curcumin iButtonbots as Efficient Bactericidal Agents

Contents

Abstract

The microbial contamination of drinking water is one of the most major concerns of community health in the developing world. Numerous water-borne pathogens are rapidly evolving and becoming resistant to traditional antibiotics. In order to get an efficacious bactericidal response, an assembly of several antibiotics or increased dosage is being administered, which may produce adverse side effects after prolonged use. Here, a proficient method for disinfecting water-borne coliform bacterial strains of *Escherichia coli* DH5α has been reported from contaminated water samples using magnetic microbots decorated with curcumin conjugates. These magnetic microbots, namely iButtonbots, were composed of soft *Agaricus bisporus* (button mushroom) microcapsules with inherent antimicrobial properties. The locomotives were coated with magnetite nanoparticles for their remote guidance towards cells and collection along with curcumin for a more enhanced bactericidal response. The synergic antibacterial effect of curcumin and mushroom constituents imparts a profound bactericidal property to these magnetic microbots. The microbots have been capable of efficiently killing the majority of bacterial cells in contaminated water samples. After the extermination of bacteria, magnetic properties of embedded magnetite nanoparticles in the porous mushroom matrix allows the collection of microbots from water samples. The presented biocompatible microbots offer an innovative method for the rapid decontamination of bacteria-laden drinking water samples.

This chapter is published in *Bulletin of Material Sciences 2019 (under Galley Proof).* I gratefully acknowledge the assistance of Dr. A. K. Singh.

4.1. Introduction

Globally, in the water bodies, the proliferation of bacteria due to their cohesion is found to be responsible for spreading of severe infectious diseases.[1-3] This poses a global health risk as the antibiotic therapies are no longer practical to treat these infections because of multidrug-resistant genetic makeup in bacteria.[4-6] Therefore, new strategies of antibacterial research have now become urgent to combat multidrug-resistant microbial infections in water by non-toxic and inexpensive means.[7,8] Presently, there has been an accelerated interest towards the use of various inorganic antimicrobial materials[9], hydroxyl radicals[10], oxidants[11], photocatalytic degradation of bacteria[12,] and non- thermal plasma methods[13] for reducing serious microbial infections to an extent. Nonetheless, preventing massive - scale bacterial infections using such techniques still has significant drawbacks due to toxicity, active immune responses, inflammation, high renal clearance and potential risks.[14-16]

To overcome such challenges, the design of a biocompatible micromotor have been reported in a simple and cost-effective manner, with excellent antibacterial activity alongside having fuel-free propulsion towards a targeted destination. In particular, the natural edible button mushroom (*Agaricus bisporus*) could be one of the most promising mesoporous materials for designing of the micromotor. Recently, major efforts have been devoted to the development of fuel-free plant-tissue based microswimmers, in contrast to the toxicity and complexity of synthetic fabrication techniques. Being a button mushroom tissue-based motor, it showed excellent antibacterial activity against Gram-negative *Escherichia coli*, which is mostly present in contaminated water. The presence of several bioactive components, especially, phenolic contents influences the antibacterial activity of edible mushrooms.[17-19] Additionally, the inherent porosity of mushroom microtissue enabled

efficient loading of curcumin (CU), which in turn enhanced the antibacterial efficacy of the microbots due to the synergic effect.

It is well known that CU is a polyphenolic plant-derived product, which could be potentially transformed into an antibiotic in the future due to its effectiveness against a broad spectrum of bacteria. However, high dose cytotoxicity, poor water solubility, and low-bioavailability are some of the major issues that affect its pharmacological perspective.[20-22] Thus, the present work introduces the novel concept of delivering CU by loading it on the mesoporous surface of a biodegradable micromotor before using the same for the killing of bacteria. Furthermore, the button mushroom-based micromotors were coated with magnetite nanoparticles (FeONPs), namely iButtonbots, which allows magnetic propulsion of motors with precise directional control towards bacterial cells.

So far, powering of nano/micro scale motors have been explored by using fuel-free external fields or fuel-based catalytic decomposition for a variety of biomedical tasks.[23-28] Among these, magnetically actuated swimmers offer stability, safety, and compatibility with biological systems.[29-30] They can perform challenging tasks, remote operations, and advanced cargo transport in a fuel-free surrounding[31-33]. The antibacterial activity of a variety of methanolic mushrooms extracts have been shown previously[17-19]; however, arguably for the first time, the present study shows the bacterial destruction using magnetic curcumin (CU)-loaded mushroom micromotor, namely, CU@iButtonbots. Here, the envisioned antibacterial properties of iButtonbots in contaminated water has been studied, and hence strictly focussed on fuel-free magnetic actuation of iButtonbots towards bacterial colonies. The motion of such micromotors could be manipulated using a magnetic field due to the encapsulation of FeONPs on their surface[34].

The method of using mushroom tissue as the major component of micromotors greatly simplifies the fabrication method exhibiting ultra-high CU loading efficiency for bacterial destruction along with the magnetically guided motion. Very soon, such proof-of-concept "controlling on-demand" motion of microbots could be essential in achieving various therapeutic applications such as drug delivery, environmental remediation, cargo transport, sensing, and micro/nano surgeries. In this regard, these active iButtonbots offer efficient antibacterial performance and holds considerable promise for safe water treatment.

4.2. Experimental Section

4.2.1. Materials

Edible mushroom (*Agaricus bisporus*) was obtained from a commercial marketplace (Guwahati, India). Ammonium hydroxide (NH_4OH), ethanol (C_2H_5OH), and methanol (CH_3OH) were purchased from Merck (India). Ferrous sulphate ($FeSO_4.7H_2O$) powder, chitosan (CS), phosphate buffer saline (PBS), acetate buffer, and curcumin (CU) was procured from Sigma-Aldrich (India). Bacteriological grade agar powder, Nutrient broth (NB), and Luria-Bertani (LB) broth was procured form Hi-media. All the chemicals were of analytical grade. Highly purified Milli-Q grade water was used in all the experiments.

4.2.2. Methods

(a) Synthesis of CU@iButtonbots. The synthesis of magnetite nanoparticles was carried out using the reverse co-precipitation method with minor modifications.[35] In brief, 100 mL of 50 % NH_4OH was added in a 200 mL beaker, and the pH of the solution was adjusted to ~13. A solution of 1.2 M $FeSO_4.7H_2O$ was added to the NH_4OH solution and mixed well for 2 h. This resulted in the formation of a black colored solution that indicated the formation of magnetite nanoparticles (FeONPs). The FeONPs were washed properly and

was vacuum dried at 50ºC overnight. Following this, 0.5 g of anionic FeONPs were then dispersed in 200 mL of cationic chitosan (CS) solution (0.04 g in 200 mL, 2% acetic acid solution), and the mixture was stirred continuously for 2 h at room temperature. The CS coated FeONPs was washed thoroughly with ethanol and Milli Q water. Finally, the modified FeONPs were magnetically separated and dried overnight at 50ºC. The purpose of obtaining CS modified FeONPs was to alter the negative ζ-potential of FeONPs into positive ζ-potential.[34]

The edible mushrooms were cut into pieces of ~1 mm thickness and allowed to dry on the vacuum at 50ºC for 4 h. The mushrooms (~5 g) were sectioned using a microtome into the varying dimensions ranging from 40 µm to 200 µm, followed by treating them with a solution of freshly prepared CS coated FeONPs. The solution evaporated by drying it overnight in a vacuum oven at 50ºC. The heat treatment resulted in the fabrication of FeONP-loaded micromotors (iButtonbots). The iButtonbots were incubated in 20 µL of anionic CU (200 µg mL^{-1}) in an ethanol solution for 1 h at 37ºC with continuous stirring at pH 7.5. The CU-loaded iButtonbots (CU@iButtonbots) were separated from the solution by centrifugation at 5000 rpm for 10 min and washed with methanol to eliminate any free CU till the supernatant become colorless. The micromotors were then allowed to dry at 37ºC for 5 h. All the experiments were carried out using freshly prepared micromotors.

(b) Measurement of velocity: The iButtonbots (size ~ 150-170 µm) were introduced in a petriplate containing 8 mL of water. A paper grid (dimension 1 mm × 1 mm) was placed below the petriplate to measure the displacement of the micromotors. An external magnetic field of strength varying from 10 to 30 mT was applied using an electromagnet. Every ~1 mm displacement of iButtonbots per unit time towards one magnetic pole was considered

for the measurement of velocity. The experiments were carried out thrice for calculating mean value and standard deviation.

(c) Binding and Release Efficiency of CU: A solution of CU (200 µL of 20 mg mL^{-1}) was added to a varying concentration of iButtonbots (1 mg - 6 mg) in 100 µL PBS (pH 7.4) and incubated for 1 h at 37ºC. Anionic CU was absorbed on the surface of micromotor due to electrostatic interactions with positively charged CS coated FeONPs. Subsequently, the CU loaded iButtonbots (CU@iButtonbots) were centrifuged at 5000 rpm for 10 min, to remove the unloaded CU. The retrieved pellets obtained after centrifugation (CU@iButtonbots) was dispersed in distilled water. The supernatants containing the unloaded CU were collected and the fluorescence intensity of 560 nm peak was recorded at an excitation wavelength of 420 nm. Simultaneously, the emission intensity of free CU (200 µL of 20 mg mL^{-1}) was measured as initial CU concentration. All the experiments were carried out thrice to confirm reproducibility.

The Binding Efficiency (B. E.) of CU was calculated using the following equation:

$$B.E.(\%) = 1 - \frac{(CU)_s}{(CU)_i} \times 100. \quad (1)$$

Here, $(CU)_i$ represents the initial concentration of CU in the solution, and $(CU)_s$ represents the concentration of unloaded CU present in the supernatant.

The CU released from 5 mg of CU@iButtonbots were studied at different time intervals (0 min – 24 h). The pellets obtained after centrifugation of CU-treated motors were washed thoroughly with distilled water and then dispersed in 200 µL of acetate buffer of pH 4.5 and PBS buffer of pH 7.4. The solutions were incubated at 37ºC for 1 h followed by

centrifugation. Finally, supernatants were collected, and the fluorescence intensity of CU was recorded at 420 nm excitation using a spectrofluorometer. Water was considered as the baseline reference.

The confocal imaging of the CU@iButtonbots was done after loading of CU on the surface of iButtonbots for 1 h at 37ºC. Subsequently, the CU loaded iButtonbots (CU@iButtonbots) were centrifuged at 5000 rpm for 10 min, to remove the unloaded CU. The samples were mounted on a glass slide, covered with a sealed coverslip, and viewed under a Zeiss LSM 880 using a 405 nm excitation wavelength and a green fluorescence with emission ranging from 450 to 600 nm.

(d) Antibacterial Studies: For the antibacterial studies, Gram-negative bacteria *Escherichia coli* DH5α was grown in LB broth at 37ºC for 12 h under shaking conditions at 180 rpm. The bacterial culture was then treated with different concentrations of free CU, iButtonbots and CU@iButtonbots (20 to 100 µg mL^{-1}). The size of the micromotors was in the range of (~150-170 µm) that was treated with bacterial colony count of 8.6×10^{-7} CFU mL^{-1}. The bacterial growth was measured in triplicates by recording the optical density (OD) using a UV-visible spectrophotometer (Jasco V-630) at 595 nm. Additionally, the bacterial cultures were plated on nutrient agar media to determine the minimum inhibitory concentration (MIC) and minimum bactericidal concentration (MBC). In this method, 100 µL of bacterial culture treated with optimized MIC and MBC of free CU, iButtonbots, and CU@iButtonbots was spread-plated on the media plate using an L-rod and incubated at 37ºC for 12 h.

(e) Growth Curve Analysis: The growth kinetics study for *Escherichia coli* was carried out after treating the bacteria with MIC and MBC of free CU, iButtonbots and

CU@iButtonbots, followed by monitoring the bacterial growth for 12 h in an incubator at 37ºC under shaking conditions at 180 rpm. The growth curve was plotted and analyzed with respect to the time interval.

The bacterial cells treated with free CU, iButtonbots, and CU@iButtonbots were fixed in a suspension of 3% glutaraldehyde in 0.1 M PBS at pH 7.2 and incubated for 1 h at 37ºC. The cells were then washed carefully in buffer, followed by post fixing them using 1% osmium tetroxide for another 1 h. Subsequently, the cells were dehydrated in 30%, 50%, 75%, 90% and 100% ethanol, 5 min each. The fixed cells were then filtered using a 0.2-micron filter and mounted on FESEM stub for sputter coating. The treated cells were viewed and analyzed. Similarly, the morphology of untreated bacterial cells was also examined.

4.3. Results and Discussion

4.3.1. Characterization of the microbots

The present study focusses on the fabrication of magnetic microbots using button mushrooms (*Agaricus bisporus*) for evaluating their antibacterial efficacy due to their biocompatibility, therapeutic benefits, enriched nutritional value, and inherent antimicrobial components. The presence of bioactive like polysaccharides and triterpenes are mainly responsible for their antibacterial activity[17-19, 36]. Also, such biodegradable microbot could fight defensive immune attacks facing fewer rejections as foreign antigens in the biological systems. The fabrication of iButtonbots and the steps followed for the loading of curcumin (CU) on their surface (CU@iButtonbots) describing the destruction of *Escherichia coli* cells has been schematically illustrated in **Figure 4.1.**

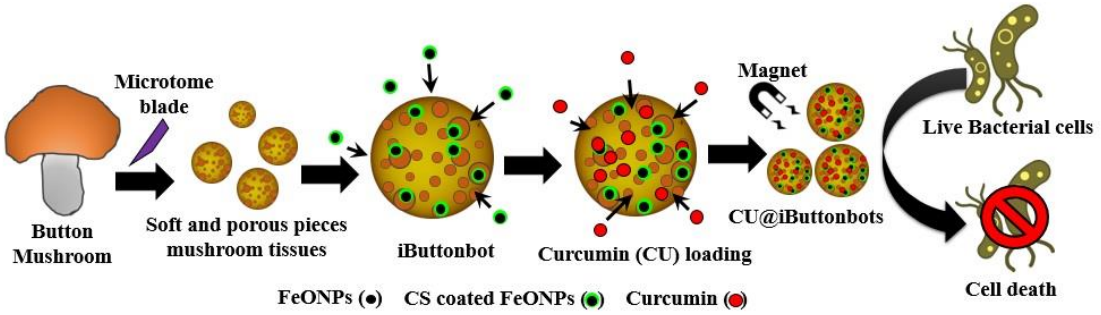

Figure 4.1. A brief illustration depicts the fabrication of micromotors and the destruction of *Escherichia coli* cells using CU@iButtonbots. The edible mushrooms were cut into small fragments of the dimension 40-200 µm using a fine microtome blade. The mushroom fragments were treated with a solution containing freshly prepared chitosan (CS) coated magnetic iron-oxide nanoparticles (FeONPs) to yield magnetic iButtonbots. The as-obtained motors were further treated with the ethanolic solution of curcumin to produce curcumin (CU) laden iButtonbots, namely CU@iButtonbots, for antimicrobial studies.

Briefly, the edible mushrooms were cut into pieces of ~1 mm thickness and allowed to dry on the vacuum at 50 ºC for 4 h. The mushrooms (~5 g) were sectioned using a microtome into the dimensions 40-200 µm, followed by treating them with a solution of freshly prepared CS coated FeONPs, to form iButtonbots. The antibacterial activity of iButtonbots was further enhanced by the efficient loading of CU on their surface, owing to its tremendous bacterial destruction potential. CU loaded microbots (CU@iButtonbots) were prepared by incubating iButtonbots in 20 µL of anionic CU solution (200 µg mL^{-1}) at 37ºC for 1 h. The detailed steps of fabrication have been discussed in the experimental section.

The mushroom microtissues were of size ~40-200 µm and possessed high porosity on their surface, as confirmed from the FESEM analysis, in **Figure 4.2(a).** With a view to present magnetically guided motion, the microtissues were coated with FeONPs, named as iButtonbots. The FeONPs were randomly deposited on their surface that enabled the magnetophoretic movement of iButtonbots under the influence of an applied magnetic field.

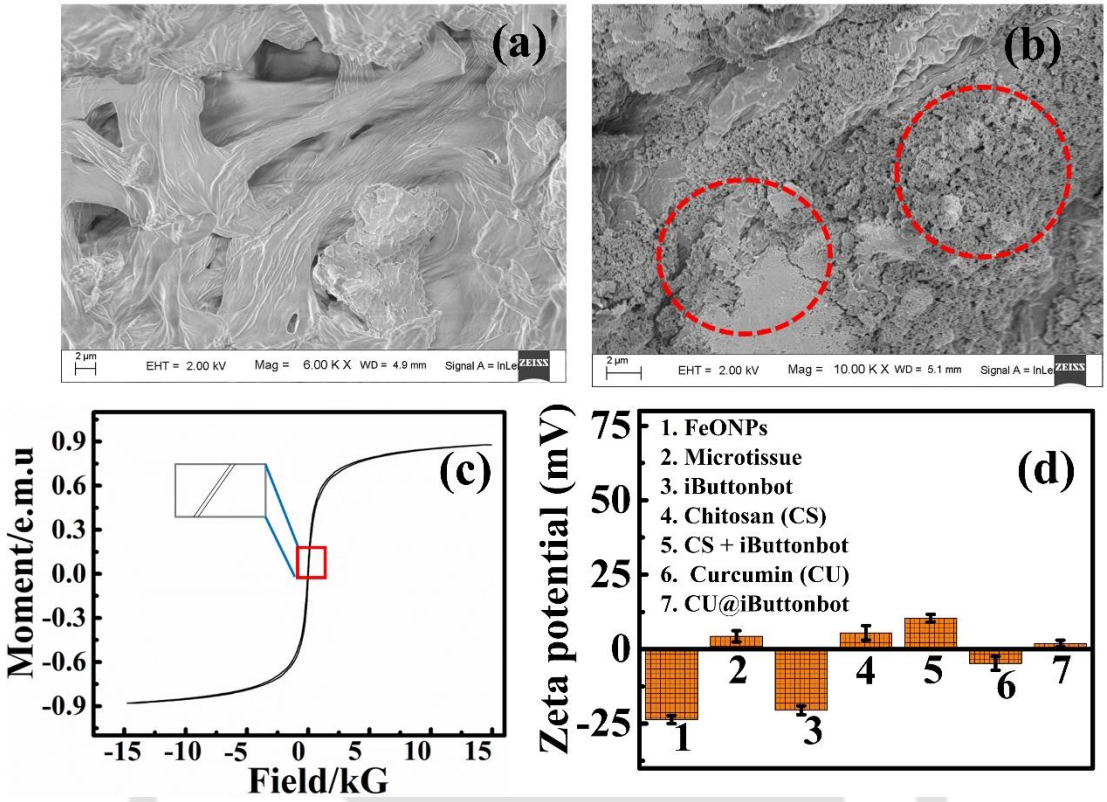

Figure 4.2. FESEM micrographs of **(a)** uncoated microtissue with mesoporous structures on their surface. **(b)** coated FeONPs on the surface encircled in red. The scale bar on all the images is 2 µm. **(c)** Vibrating sample magnetometer (VSM) analysis of iButtonbots with Magnetization saturation of 0.87 emu g^{-1}. **(d)** ζ potential values of the samples.

The surface morphology of iButtonbots was characterized FESEM, as shown in **Figure 4.2(b)**, which revealed the presence of coated FeONPs on the surface, encircled in red. The FeONPs were spherically shaped, exhibiting a size range of ~ 20 - 60 nm. The magnetization saturation of the iButtonbot was found to be 0.87 emu g^{-1} by vibrating sample magnetometer (VSM) analysis, as shown in **Figure 4.2(c)**. **Figure 4.2(d)** showed the ζ-potential of uncoated microtissue, FeONPs, iButtonbots, chitosan (CS), CS coated iButtonbots, free CU, and CU@iButtonbots. The ζ-potential of FeONPs and microtissues was found to be – 23.6 ± 1.0 mV and 4.32 ± 2.0 mV, respectively, which led to electrostatic binding of FeONPs on

the mushroom surface, besides their porous nature facilitating absorption. The ζ-potential of FeONPs coated iButtonbots was measured to be – 20.5 ± 2.0 mV. The coating of CS (5.42 ± 3.0 mV) enhanced the net positive charges of iButtonbots leading to a ζ-potential of 10.39 ± 0.5 mV. Finally, the electrostatic interactions between negatively charged CU (– 4.81 ± 2.0 mV) and positively charged CS coated iButtonbots (10.39 ± 0.5 mV) led to the binding of CU molecules on the mesoporous surface of micromotors. Accordingly, CU@iButtonbots exhibited a ζ-potential of 1.89 ± 1.5 mV.

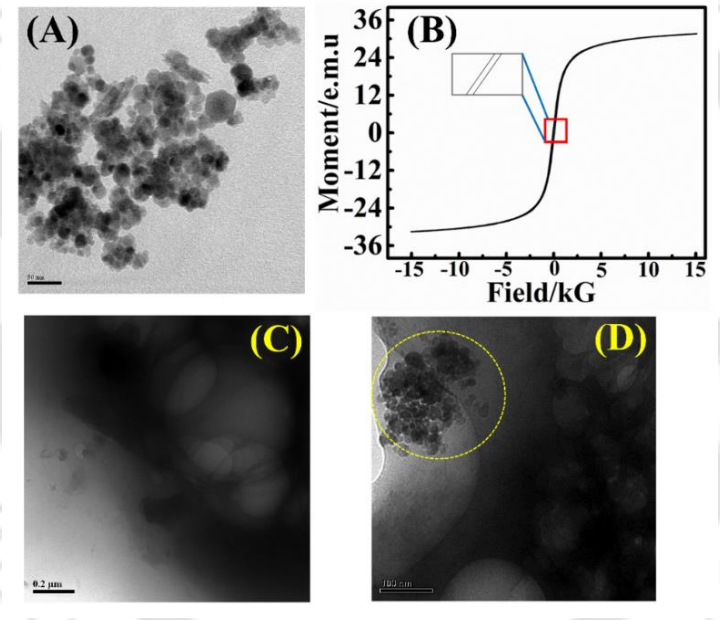

Figure 4.3. (A) TEM analysis of FeONPs. **(B)** Vibrating Sample Magnetometer (VSM) analysis of synthesized FeONPs. FETEM micrographs of **(C)** uncoated microtissue and **(D)** FeONPs coated micromotor, i.e., iButtonbots. The loaded FeONPs have been encircled in yellow.

Hence, immobilization of free CU could be achieved on the porous surface of iButtonbots, which prevents the interaction of bound CU with external surroundings and shields CU from instability and degradation. Thus, CU@iButtonbots could be considered as potential drug delivery vehicles, which could release a drug in a pH-dependent microenvironment by

altering their pharmacokinetic properties. The TEM analysis synthesized FeONPs has been shown in **Figure 4.3A,** indicating the size to be in the range of ~20 to 80 nm. The magnetization saturation of FeONPs was found to be 31.55 emu g^{-1} from VSM graph **Figure 4.3B**. Further, FETEM micrographs of uncoated microtissue and FeONPs coated iButtonbots have been shown in **Figure 4.3C & Figure 4.3D,** respectively, which confirmed FeONPs coating on the surface of iButtonbots.

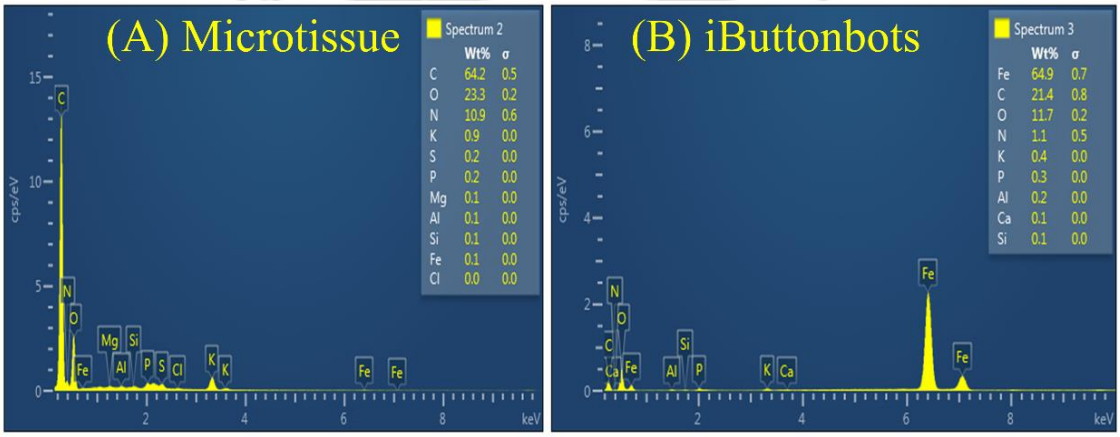

Figure 4.4. FESEM-EDX spectra of **(A)** uncoated microtissue and **(B)** FeONPs coated micromotor.

Additionally, FESEM-EDX analysis of uncoated microtissue **(Figure 4.4A)** and iButtonbots confirmed the loading of FeONPs on the surface of motors as shown in **Figure 4.4B.** Besides many elements, the presence of 64.9% of elemental Fe in iButtonbots confirmed the coating of magnetite nanoparticles. FESEM-EDX analysis of microtissue and iButtonbots confirmed the loading of FeONPs on the surface of motors.

4.3.2. Drug binding studies and motion-based studies

Magnetically guided propulsion of iButtonbots was studied after the FeONPs coating on the surface of micromotor by aid of a magnet. A control experiment was performed to show the

stationary state of iButtonbot in the absence of any magnetic field. Importantly, upon the introduction of an external magnetic field, the iButtonbots rendered guided motion in an aqueous medium due to induced magnetization of FeONPs, as shown in **Figure 4.5(a)**. The motion of the iButtonbots could be remotely controlled in many directions by stirring the magnet on a pre-defined route, thus improving their functionality as drug-delivering microbots. The iButtonbots could be navigated towards different positions at the desired time interval by regulating the strength of the magnetic field.

Figure 4.5(b) represented the magnetically guided motion of CU@iButtonbots towards the bacterial cell that got attached to the cell surface after targeted motion. The arrow indicated the path followed by the micromotor (yellow circled) towards the cells (red circled). **Figure 4.5(c)** shows that the average velocity (V_{av}) of iButtonbots increased with the increase of the magnetic strength (H). The average velocity attained was around 1.45×10^{-3} ms^{-1} at ~ 10 mT. However, with acceleration in the magnetic field strength, the velocity of iButtonbot increased to 6.51×10^{-3} ms^{-1} at ~30 mT. The non-invasive nature, strong remote controllability and high penetration capability of homogenous magnetic fields have been realized for navigating the motion. Such proof-of-concept "regulating on-demand" magnetic motion of microbots hold significant promise for controlling the directionality of micromotors.[29-33]

The iButtonbots were loaded with fluorescent CU in order to study the drug-delivering potential of the microbot for improved antibacterial efficiency. The electrostatic interactions between negatively charged CU (– 4.81 ± 2.0 mV) and positively charged CS coated iButtonbots (10.39 ± 0.5 mV) led to the binding of CU molecules on the mesoporous surface, with an absolute ζ-potential of 1.89 ± 1.5 mV (CU@iButtonbots).

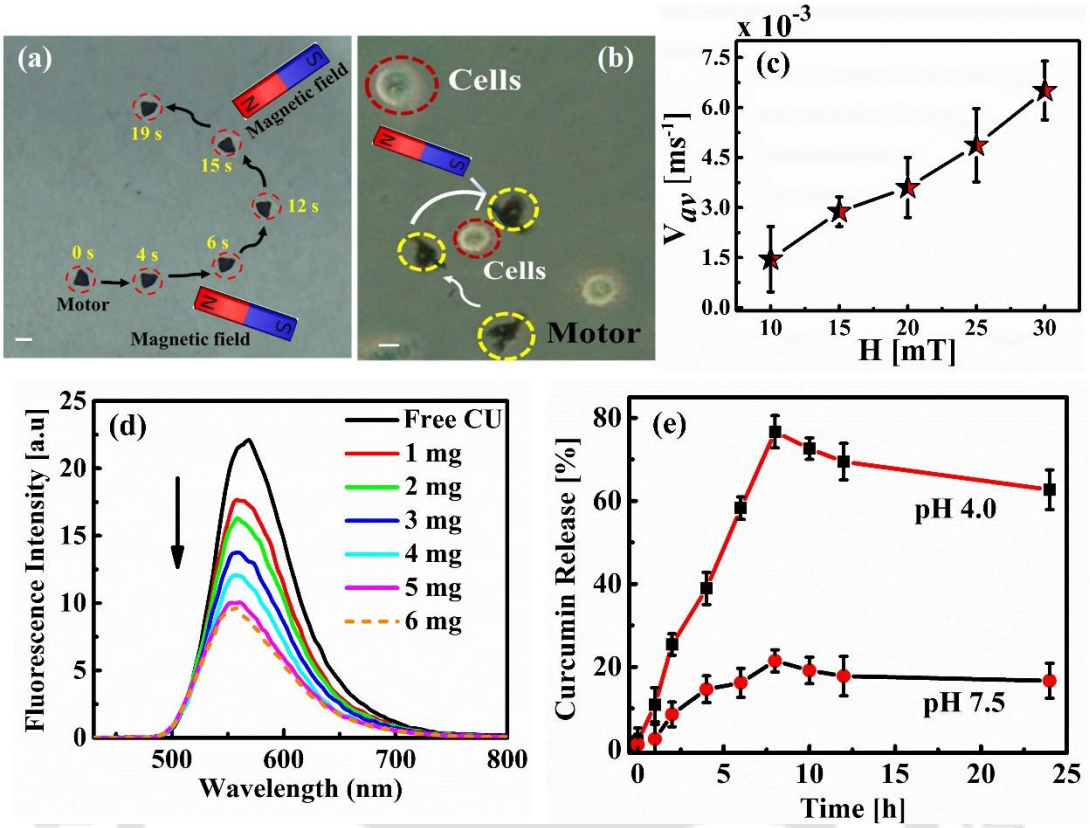

Figure 4.5. (a) Shows magnetically guided migration of iButtonbot in water using bar magnet. The respective positions of the micromotor (encircled in red) have been shown at t = 0 s, 2 s, 4 s, 6 s, 12 s, and 27 s. **(b)** Magnetically guided motion of CU@iButtonbots towards the bacterial microcolonies. The scale bar on all the images is of 200 µm. **(c)** Variation in the average velocity (V_{av}) of iButtonbots with an increase in the strength of the applied magnetic field (H). **(d)** Fluorescence spectra of the supernatant obtained after treatment of curcumin (CU) solution with iButtonbots of varying concentrations at 37°C in PBS buffer at pH 7.4. **(e)** The release profile of CU from iButtonbots with time at pH 4 and 7.5.

The amount of CU loaded on the various concentrations of iButtonbots, ranging from 1 mg to 6 mg, has been represented in **Figure 4.5(d)**. It was found that with a gradual increase in the concentration of iButtonbots, the binding efficiency of CU increased. The binding was confirmed by a steady decrease in fluorescence spectra of unbound CU in the supernatant. The binding efficiency of CU saturated to ~79.51% beyond a concentration of 5 mg, and the concentration of bound CU was found to be ~ 13.48 mg mL^{-1}. Thus, 5 mg of

CU@iButtonbots were used for pH-dependent release studies and antibacterial experiments. The time-dependent release study was carried out to quantify the *in vitro* release of bound CU from CU@iButtonbots. **Figure 4.5(e)** shows the time-dependent release profile that suggested the maximum release of CU (~76.4%) in pH 4.0 at 8th h. This further decreased to 68% and 37.2% at the end of 12 h and 24 h, respectively. At pH 7.5, a maximum release of 20% could be observed at 8th h that reduced thereafter, to 15% at 24 h.

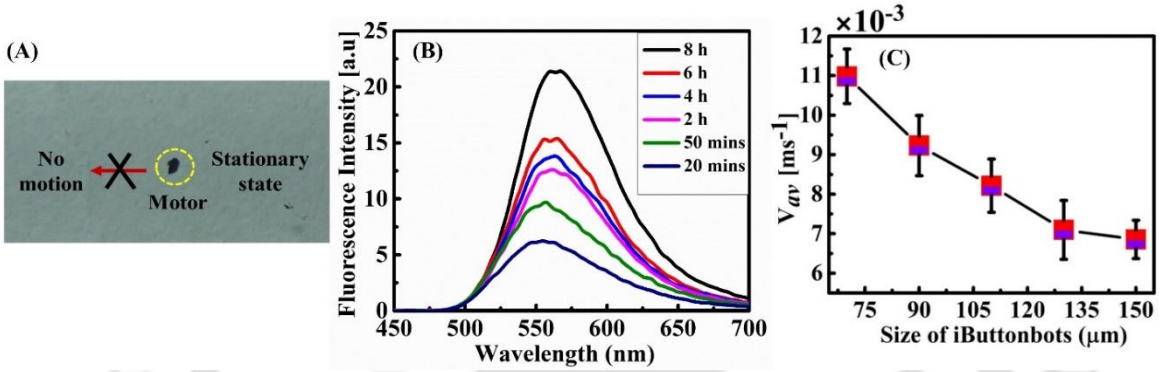

Figure 4.6. (A) Stationary state of iButtonbot in water without magnetic field. **(B)** Release fluorescence spectra of CU@iButtonbots with respect to varied time intervals at 420 nm excitation using spectrofluorometer. **(C)** Average velocity of iButtonbots of the varying size range (~70 µm -150 µm) using a constant magnetic field strength of 30 mT.

A control experiment was performed to show the stationary state of iButtonbot in the absence of any magnetic field by placing iButtonbot in a petridish filled with 8 mL of water, as shown in **Figure 4.6A**. The release spectra of 5g of CU@iButtonbots with respect to various time intervals (20 mins to 8 h) has been shown in **Figure 4.6B**. The intensity of fluorescence spectra progressively increased with time, confirming the maximum release at 8th h. The average velocity of iButtonbots with size ranging from 70 µm to 150 µm was increased to ~11×10^{-3} ms^{-1}, which gradually got reduced with bigger size of the iButtonbots.

Also, the average velocity of iButtonbots by narrowing down the size range (~70 µm -150 µm) using a constant magnetic field strength of 30 mT was investigated. An optimum size of iButtonbot (~150-170 µm) has been considered to study their average speed because the small-sized iButtonbot (~ 70-150 µm) exhibited rapid motion that was inconvenient to analyze and control their motility towards bacterial colonies. The pace of the iButtonbots with size ~150-170 µm displayed an average speed of (~ 6.5 $\times 10^{-3}$ ms^{-1}), which was optimum for antibacterial investigations, as shown in **Figure 4.6C.**

Thus, a biphasic release pattern of loaded CU could be observed form CU@iButtonbots with an early burst of release at pH 4 followed by a sustained release. The significant release of CU at pH 4 is well-off for its activity against pathogenic bacteria in acidic environments.[37] Notably, such early burst release is essential to prevent bacterial growth in infectious sites. In addition, the sustained release would prevent bacterial infections with lessened toxicity exhibiting an effective therapeutic ratio, which is favorable over long-term antibiotic doses.[5]

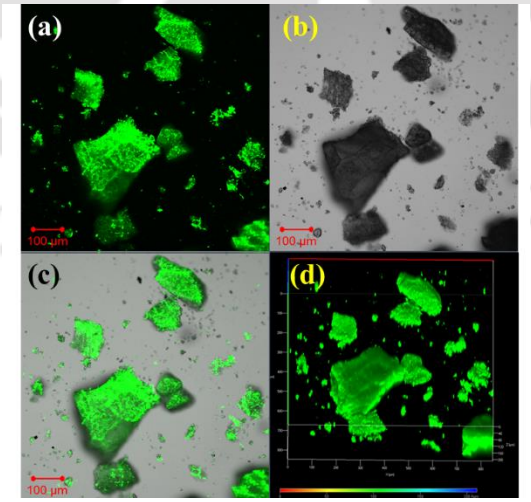

Figure 4.7. (a) Fluorescence **(b)** Bright field and **(c)** merged confocal images of curcumin loaded iButtonbots (CU@iButtonbots). **(d)** 3-D model of z stacks that depicted the internalization of CU molecules on iButtonbots. The scale bar on all the images is 100 µm.

The confocal micrographs (under ZEISS LSM 880) of CU@iButtonbots has been shown in **Figure 4.7**, where the image suggested successful loading of CU on the surface of iButtonbots. The fluorescence, bright field, and merged image has been shown in **Figures 4.7(a), (b),** and **(c)**, respectively. The CU molecules could be easily identified on the surface of iButtonbots by its characteristic green fluorescence emission under 405 nm excitation. The gallery images were reconstructed to get the 3-D model of z-stacks that depicted the internalization of CU molecules on mesoporous microbots, ensuring efficient loading, shown in **Figure 4.7(d)**.

4.3.3. Antibacterial studies

After the efficacious loading of CU, the antibacterial activity was further investigated on Gram-negative – bacteria, *Escherichia coli* DH5α. The size of the uncoated microtissues and micromotors was in the range of ~150-170 µm for antimicrobial studies. The standard bacterial plate count was found to be 8.6×10^7 CFU mL^{-1}, which was calculated using the standard bacterial plate count method. For the antibacterial studies, Gram-negative bacteria *Escherichia coli* DH5α was grown in LB broth at 37ºC for 12 h under shaking conditions at 180 rpm. The bacterial cultures were plated on nutrient agar media to determine the minimum inhibitory concentration (MIC) and minimum bactericidal concentration (MBC). In this method, 0.1 mL of 10^{-5} dilution of bacterial culture treated with optimized MIC and MBC of free CU, iButtonbots, and CU@iButtonbots was spread-plated on the media plate. All the samples were plated in triplicate plates using an L-rod and incubated at 37ºC for 12 h with approximate counts of 89, 93, and 77 colonies. The standard bacterial plate count was found to be 8.6×10^7 CFU mL^{-1}, which was calculated using the standard bacterial plate count method:

$$\text{CFU mL}^{-1} = \frac{\text{Average count}}{(\text{Dilution plated})(\text{mL plated})}. \quad (2)$$

where CFU mL^{-1} stands for colony-forming unit per mL.

The % bactericidal efficiency of iButtonbots was calculated with varying sizes of the microbot (~ 50 to 160 µm) by treating the bacterial colonies of 8.6×10^7 CFU mL^{-1} for 12 h. The inhibition efficiencies to *Escherichia coli* was calculated as

$$\%\, Bactericidal\ efficiency = \frac{[Abs]_t - [Abs]_t}{[Abs]_i}. \quad (3)$$

where $[Abs]_i$ is the absorbance of control bacterial culture and $[Abs]_t$ is the absorbance of treated bacterial colonies after a time interval of 12 h. The bacterial growth was measured by recording the optical density (OD) using a UV-visible spectrophotometer at 595 nm.

(µg mL^{-1})	Free CU	iButtonbots	CU@iButtonbots
MIC	69	50	33
MBC	87	61	51

Table 4.1: Data representing the minimum inhibition concentration (MIC) of and minimum bactericidal (MBC) values of free CU, iButtonbots, and CU@iButtonbots for *Escherichia coli.*

Vital factors monitoring the antibacterial activity have been revealed towards optimizing the bacterial killing operation of the functionalized micromotors. The MIC and MBC values of free CU, iButtonbots, and CU@iButtonbots has been displayed in **Table 4.1**. Comparatively, the MIC obtained for CU@iButtonbots was found to be least, i.e., 33 µg mL^{-1} that inhibited bacterial growth. Thus, among the different concentrations tested, the minimum concentration of CU@iButtonbots (33 µg mL^{-1}) that evidently inhibited the

growth of *Escherichia coli* was considered as MIC. Similarly, the MIC for free CU and iButtonbots was found to be 69 µg mL^{-1} and 47 µg $mL^{-1,}$ respectively that measurably inhibited bacterial growth. Interestingly, MIC for iButtonbots was lower as compared to free CU indicating the high antibacterial activity of mushroom-based micromotors as compared to native CU. Similarly, the MIC for free CU and iButtonbots was found to be 69 µg mL^{-1} and 50 µg mL^{-1}, respectively, which measurably inhibited bacterial growth. Interestingly, MIC for iButtonbots was lower as compared to free CU indicating the high antibacterial activity of mushroom-based micromotors as compared to native CU.

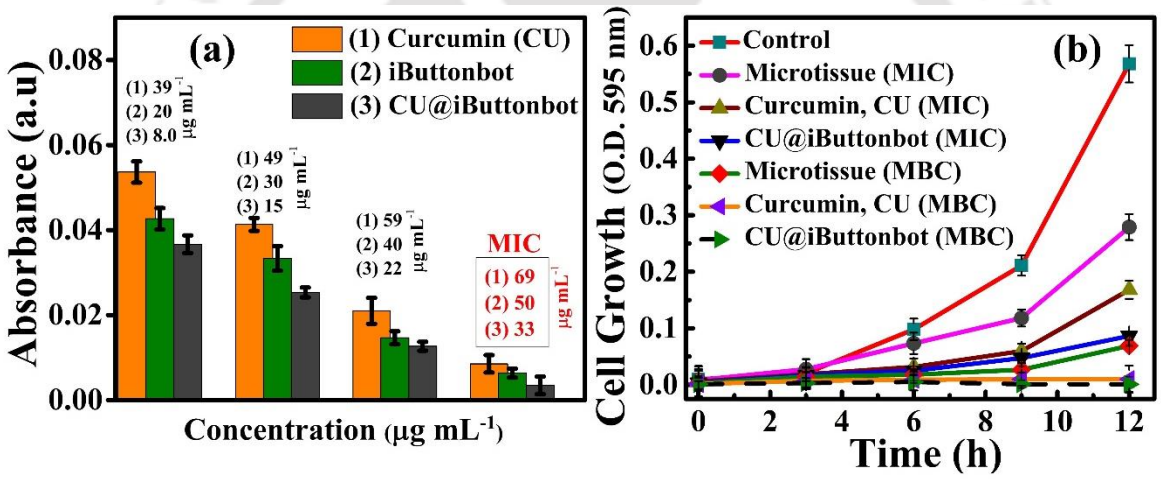

Figure 4.8. (a) Minimum Inhibitory Concentration (MIC) values of samples for *Escherichia coli*. **(b)** Growth curve of *Escherichia coli* in the presence of samples with respect to the varied time interval.

The maximum inhibition of bacterial growth could be observed for MIC of CU@iButtonbots, i.e., 33 µg $mL^{-1,}$ as shown in **Figure 4.8(a)**. This was probably due to the sustained release of CU from the surface of CU@iButtonbots that hindered bacterial proliferation.[5,38] Further, the culture was re-inoculated to a fresh medium, and the MBC for the samples was determined, as witnessed from the absence of turbidity in the medium.

Additionally**,** Table 4.1 shows the MBC concentrations of free CU, iButtonbots, and CU@iButtonbots that resulted in bacterial killing. The free CU exhibited a MIC and MBC value of 69 µg mL^{-1} and 87 µg mL^{-1}, respectively. In contrast, the MIC and MBC values for iButtonbots were less as compared to free CU, i.e., 50 µg mL^{-1} and 61 µg mL^{-1}. The growth curve studies on *Escherichia coli* revealed that at MIC (33 µg mL^{-1}) of CU@iButtonbots, bacterial growth inhibition was observed, and at its MBC (51µg mL^{-1}), the growth was completely stopped, as shown in **Figure 4.8(b)**. A dramatic increase in the antibacterial efficiency could be observed from the lowest obtained MIC and MBC of CU@iButtonbots at the end of 12 h, as compared to control bacterial culture with no added samples. This could be interpreted from the lowest optical density (OD) of the growth curve that can be directly correlated to minimum bacterial growth.

To confirm the MIC/ MBC values of free CU, iButtonbots and, CU@iButtonbots, the bacteria were plated on nutrient agar media. **Figure 4.9(a)** indicated the control of bacterial colonies with complete bacterial growth. Few bacterial colonies were observed in the case of CU@iButtonbots at their MIC (33 µg mL^{-1}), and no bacterial colony was seen at their MBC (51µg mL^{-1}), as shown in respective **Figures 4.9(b)** and **(c)**. The antibacterial compounds bound to such micromotors have numerous advantages over their free form in terms of their stability and decreased side-effects.[4] Thus, iButtonbots could protect the bound CU from initial degradation upon motioning with different molecules in the external environment.

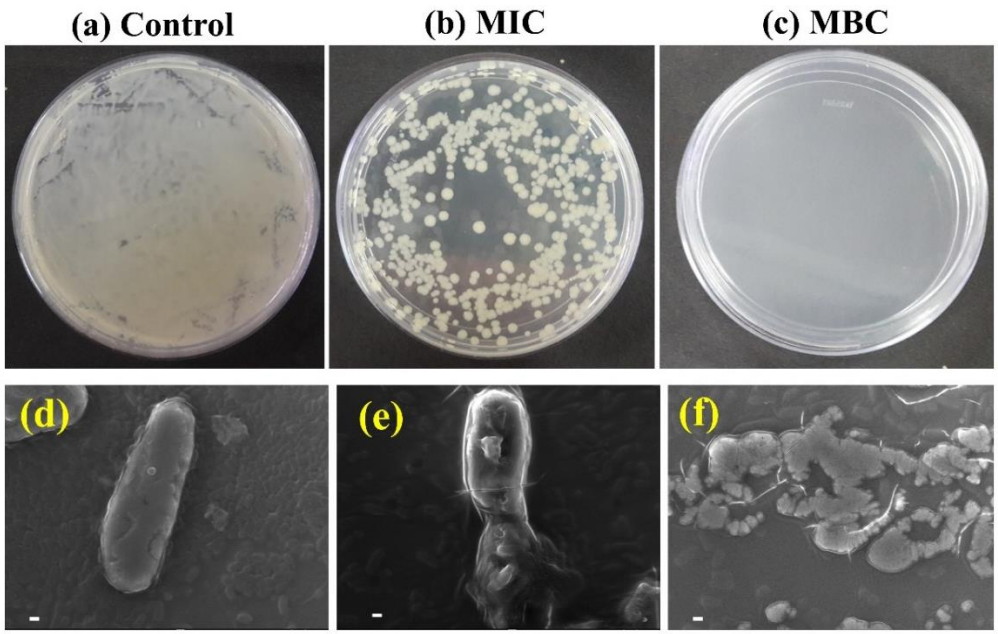

Figure 4.9. *Escherichia coli* bacterial colonies **(a)** with complete bacterial growth (control). **(b)** MIC for CU@iButtonbots at 33 µg mL^{-1} **(c)** MBC for CU@iButtonbots at 51 µg mL^{-1}, showing no growth using spread plate method on nutrient agar media. FESEM micrographs of bacterial cells **(d)** control **(e)** treated with uncoated microtissue and **(f)** treated with CU@iButtonbots. The scale bar on all the images is 1 µm.

Further, the interaction of CU@iButtonbots and iButtonbots with *Escherichia coli* was studied using FESEM analysis. The control bacterial cells exhibited a smooth cell surface with whole-cell morphology, as shown in **Figure 4.9(d)**. However, the bacterial cells treated with iButtonbots displayed disrupted cell wall morphology that strongly suggested the potent antibacterial activity of mushrooms, shown in **Figure 4.9(e)**. The mushroom tissues in iButtonbots could probably use their natural phenolic compounds for hydrolysis of glycosidic linkages in cells, exhibiting a synergistic effect with FeONPs resulting in cell damage.[39] Remarkably, a more profound loss of cellular integrity could be observed in bacterial cells treated with CU@iButtonbots due to the effective release of CU from the

motor and intrinsic antibacterial effect of mushroom[40], that led to complete bacterial cell lysis, as displayed in **Figure 4.9(f)**.

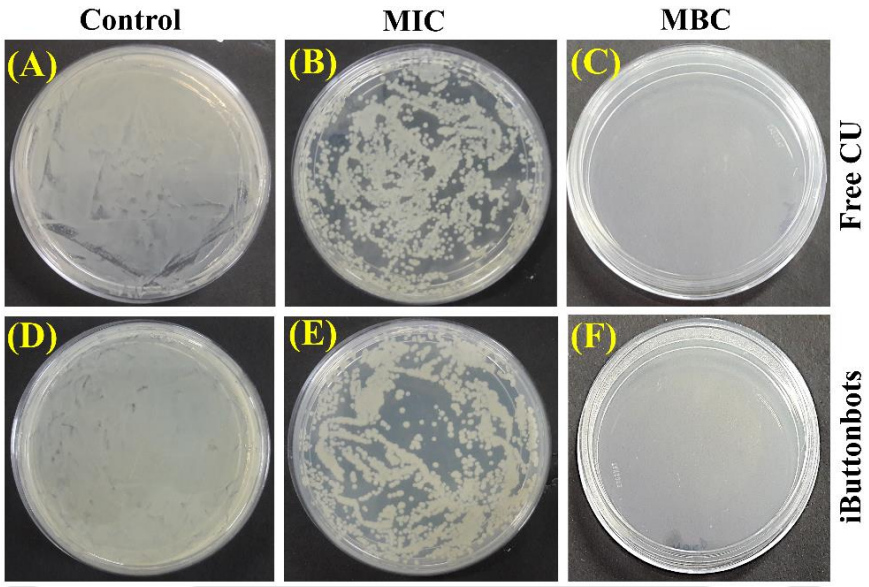

Figure 4.10. *Escherichia coli* grown on nutrient agar **(A)** control bacteria treated with free curcumin (CU) at their **(B)** minimum inhibitory concentration **(**MIC, 69 µg mL^{-1}), **(C)** minimum bactericidal concentration (MBC, 87 µg mL^{-1}. *Escherichia coli* grown on nutrient agar **(D)** control bacteria treated with iButtonbots at their **(E)** minimum inhibitory concentration **(**MIC, 50 µg mL^{-1}) and **(F)** minimum bactericidal concentration (MBC, 61 µg mL^{-1}).

The antibacterial compounds bound to such micromotors have numerous advantages over their free form in terms of their stability and decreased side-effects.[4] Thus, iButtonbots could protect the bound CU from initial degradation upon motioning with different molecules in the external environment. Similar results for free CU and iButtonbots were obtained at their respective MIC and MBC (**Figure 4.10 A-F**). Few bacterial colonies were observed in the case of iButtonbots at their MIC (50 µg mL^{-1}), and no bacterial colony was seen at their MBC (61µg mL^{-1}). However, for free drug CU, few bacterial colonies were observed at their MIC (69 µg mL^{-1}), and no bacterial colony was seen at their MBC (87 µg mL^{-1}). The

results further confirmed the heightened antibacterial efficacy of iButtonbots as compared to free drug.

The gallery images of the total 70 optical sections of CU@iButtonbots captured from their top to bottom surface using confocal microscopy at 405 nm excitation has been shown in **Figure 4.11A**. The% bactericidal efficiency of iButtonbots was calculated with varying sizes of the microbot (~ 50 to 160 µm) by treating the bacterial colonies of 8.6×10^7 CFU mL^{-1} for 12 h (**Figure 4.11B**). The bactericidal efficiency was less than 80% for a size range of ~ 50 to 80 µm.

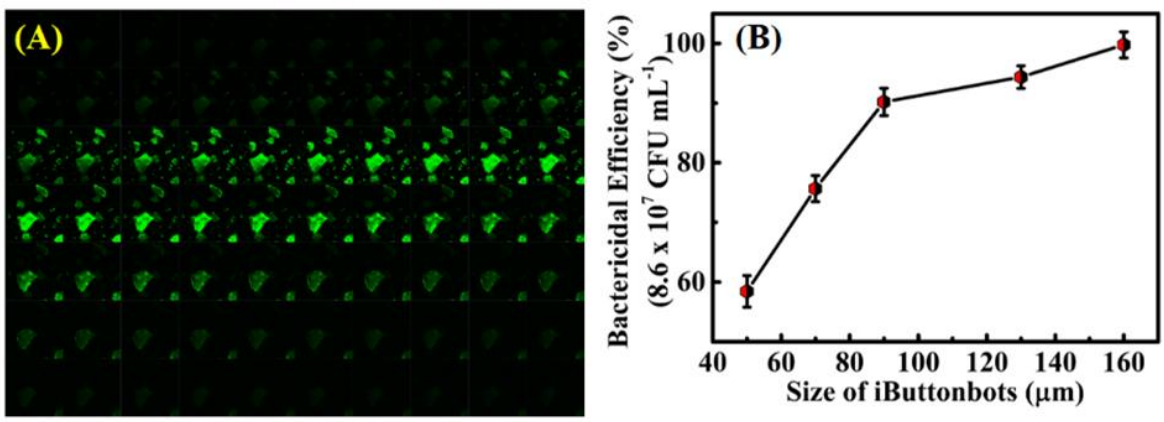

Figure 4.11. (a) Confocal images of the entire 70 optical sections of CU@iButtonbots at 405 nm excitation. **(b)** % Bactericidal efficiency of iButtonbots with varying sizes.

However, with a gradual increase in the size of iButtonbots, the efficacy was drastically elevated, reaching maxima of ~99.8% killing using microbots of size range ~150-160 µm. This could be attributed due to the higher amount of CU loaded on the surface of large-sized microbots, thus exhibiting a synergistic bactericidal effect. The enhanced antibacterial activity of CU@iButtonbots reflected the leakage of cytoplasmic contents outside the bacterial cell for effective bacterial killing. Therefore, the results signified that iButtonbots could significantly kill Gram-negative bacteria in a hasty and environment-friendly

approach. The magnetically driven CU@iButtonbots could be extremely operative for antibacterial water treatment as Gram-Negative infections are ever more challenging to treat due to their cell wall structures.

4.4. Conclusions

In brief, the motivation of our work was to demonstrate a highly effective bacterial killing approach based on the coupling of the antibacterial activity of biocompatible curcumin loaded micromotor (CU@iButtonbots) with their magnetically guided motion. The mesoporous iButtonbots of size ~40-200 µm were fabricated in a cost-effective manner from edible button mushroom and loaded with FeONPs for magnetic steering. The magnetic iButtonbots could be efficiently driven in *Escherichia coli* contaminated water samples that could enhance the mixing of bacteria in contaminated fluids.

The iButtonbots were immobilized with anionic curcumin by electrostatic interactions, and superior bacterial killing was thus obtained using CU@iButtonbots, compared to free curcumin. Even further improvements can be achieved by doping with other antimicrobial drugs and introducing a swarm of such magnetically handled iButtonbots for accelerated bacterial killing in highly contaminated areas. The present study encourages the fuel-free motion of biodegradable micromachines that could significantly improve water treatment strategies and environmental remediation. The biocompatibility of such bacterial micro fighters makes them promising candidates not only to *in vitro* applications but also for diverse *in vivo* therapeutics.

References

(1) Diez-Pascual, A. M. Antibacterial Activity of Nanomaterials. *J. Nanomater*. **2018**, 8, 359-365.

(2) Bhuyan T.; Khanuja M.; Sharma R.; Patel S.; Reddy M. R.; Anand S.; Varma A. A comparative study of pure and copper (Cu)-doped ZnO nanorods for antibacterial and photocatalytic applications with their mechanism of action. *J. Nanopart. Res.* **2015,** 17, 288-299.

(3) Delezuk, J. A. M.; Ramírez-Herrera, D. E.; Fernández de Ávila, B. E.; Wang, J. Chitosan-based water-propelled micromotors with strong antibacterial activity. *Nanoscale* **2017**, 9, 2195-2200.

(4) Kiristi, M.; Singh, V. V.; Fernández de Ávila, B. E.; Uygun, M.; Soto, F.; Uygun, D. A.; Wang, J. Lysozyme-Based Antibacterial Nanomotors. *ACS Nano* **2015**, 9, 9252-9259.

(5) Simon, A. T.; Dutta, D.; Chattopadhyay, A.; Ghosh, S. S. Copper Nanocluster-Doped Luminescent Hydroxyapatite Nanoparticles for Antibacterial and Antibiofilm Applications. *ACS Omega* **2019**, 4, 4697-4706.

(6) Bugli, F.; Cacaci, M.; Palmieri, V.; Di Santo, R.; Torelli, R.; Ciasca, G.; Di Vito, M.; Vitali, A.; Conti, C.; Sanguinetti, M.; De Spirito, M.; Papi, M. Curcumin-loaded graphene oxide flakes as an effective antibacterial system against methicillin-resistant *Staphylococcus aureus*. *Interface Focus* **2018**, 8, 201820170059-8.

(7) Bhuyan, T.; Mishra, K.; Khanuja, M.; Prasad, R.; Varma, A. Biosynthesis of zinc oxide nanoparticles from *Azadirachta indica* for antibacterial and photocatalytic applications. *Mater. Sci. Semicond. Process*. **2015**, 32 55-61.

(8) Karmakar, P.; Gaitonde, V. Promising Recent Strategies with Potential Clinical Translational Value to Combat Antibacterial Resistant Surge. *Medicines* **2019**, 6, 21-41.

(9) Li, M.; Liu, X.; Xu, Z.; Yeung, K. W. K.; Wu, S. Dopamine Modified Organic–Inorganic Hybrid Coating for Antimicrobial and Osteogenesis. *ACS Appl. Mater. Interfaces*. **2016**, 8, 49, 33972-33981.

(10) Liu I-F.; Annamalai, T.; Sutherland, J. H.; Tse-Dinh, Y. C. Hydroxyl Radicals Are Involved in Cell Killing by the Bacterial Topoisomerase I Cleavage Complex. *J. Bacteriol.* **2009**,191, 5315-5319.

(11) Harrison, R. E.; Touret, N.; Grinstein, S. Microbial Killing: Oxidants, Proteases, and Ions. *Curr. Biol*. **2002**, 12, 357-359.

(12) Hu, C.; Guo, J.; Qu, J.; Hu, X. Photocatalytic Degradation of Pathogenic Bacteria with AgI/TiO_2 under Visible Light Irradiation. *Langmuir* **2007**, 23, 4982-4987.

(13) Kratochvíl, J.; Kuzminova, A.; Kylián, O. State-of-the-Art, and Perspectives of, Silver/Plasma Polymer Antibacterial Nanocomposites. *Antibiotics* **2018**, 7, 78-95.

(14) Wei, T.; Tang, Z.; Yu, Q.; Cheng, H. Smart Antibacterial Surfaces with Switchable Bacteria-Killing and Bacteria-Releasing Capabilities. *ACS Appl. Mater. Interfaces*. **2017**, 9, 37511-37523.

(15) Seil, J. T.; Webster, T. J. Antimicrobial applications of nanotechnology: methods and literature *Int. J. Nanomed.* **2012**, 7, 2767-2781.

(16) Li, X.; Wu, B.; Chen, H.; Nan, K.; Jin, Y.; Sun, L.; Wang, B. Recent developments in smart antibacterial surfaces to inhibit biofilm formation and bacterial infections. *J. Mater. Chem. B*. **2018**, 6, 4274-4292.

(17) Priya, J. L.; Srinivasan, B. Studies on the antibacterial activities of mushroom. *Int. J. Microbiol. App. Sci*. **2013**, 2 184-189.

(18) Akyuz, M.; Onganer, A. N.; Erecevit, P.; Kirbag, S. Antimicrobial Activity of some Edible Mushrooms in the Eastern and Southeast Anatolia Region of Turkey. *Gu. J. Sci.* **2010**, 23, 125-130.

(19) Sharma, M. V.; Sagar, A.; Joshi, M. Study on Antibacterial Activity of *Agaricus bisporus* (Lang.) Imbach. *Int. J. Microbiol. App.* **2015**, 4, 553-558.

(20) Siviero, A.; Gallo, E.; Maggini, V.; Gori, L.; Mugelli, A.; Firenzuoli, F.; Vannacci, A. Curcumin, a golden spice with a low bioavailability. *J. Herb. Med.* **2015**, 5 57-70.

(21) Yoon, H. J.; Zhang, X.; Kang, M. G.; Kim, G. J.; Shin, S. Y.; Baek, S. H.; Lee, B. N.; Hong, S. J.; Kim, J. T.; Hong, K.; Bae, H. Cytotoxicity Evaluation of Turmeric Extract Incorporated Oil-in-Water Nanoemulsion. *Int. J. Mol. Sci*. **2018**, 19, 280-292.

(22) Dey, S.; Sreenivasan, K. Conjugating curcumin to water soluble polymer stabilized gold nanoparticles via pH responsive succinate linker *J. Mater. Chem. B.* **2013**, 3 824-833.

(23) Garcia-Gradilla, V.; Orozco, J.; Sattayasamitsathit, S.; Soto, F.; Kuralay, F.; Pourazary, A.; Katzenberg, A.; Gao, W.; Shen, Y.; Wang, J. *ACS Nano*. **2013**, 7, 9232-9240.

(24) Chi Q, Wang Z, Tian F, You J and Xu S. A Review of Fast Bubble-Driven Micromotors Powered by Biocompatible Fuel: Low-Concentration Fuel, Bioactive Fluid and Enzyme. *Micromachines* **2018**, 9, 537-552.

(25) Jurado-Sánchez, B. Nanoscale Biosensors Based on Self-Propelled Objects. *Biosensors* **2018**, 8, 59-74.

(26) Xu, L.; Mou, F.; Gong, H.; Luo, M.; Guan. Light-driven micro/nanomotors: from fundamentals to applications *J. Chem. Soc. Rev.* **2017**, 46, 6905-6926.

(27) Ahmed, D.; Baasch, T.; Jang, B.; Pané, S.; Dual, J.; Nelson, B. Artificial Swimmers Propelled by Acoustically Activated Flagella. *Nano Lett*. **2016**, 16, 4968-4976.

(28) Calvo, P.; Manian, M.; Kagan, D.; Balasubramanian, S.; Cardona, M.; Flechsig, G. U.; Posne, J.; Wang, J. *Chem. Commun*. **2009**, 45, 4509-4511.

(29) Singh, A.; Mandal, T.; Bandyopadhyay, D. Magnetically Guided Chemical Locomotion of Self-Propelling Paperbots. *RSC Adv*. **2015**, 5, 64444-64451.

(30) Gong, D.; Cai, J.; Celi, N.; Feng, L.; Jiang, Y.; Zhang, D. Bio-inspired magnetic helical microswimmers made of nickel-plated *Spirulina* with enhanced propulsion velocity. *J. Magn. Magn. Mater*. **2018**, 468, 148-154.

(31) Tu, Y.; Peng, T. F.; Wilson, D. A.; Motion Manipulation of Micro- and Nanomotors. *Adv. Mater*. **2017**, 29, 1701970-1701990.

(32) Gao, W.; Feng, X.; Pei, A.; Kane, C. R.; Tam, R.; Hennessy, C.; Wang, J. Bioinspired Helical Microswimmers Based on Vascular Plants. *Nano Lett*. **2014**, 14, 305-310.

(33) Li, J.; Li, T.; Kiristi, M.; Liu, W.; Wu, Z.; Wang, J. Magneto-Acoustic Hybrid Nanomotor. *Nano Lett*. **2015**, 15, 4814-4821.

(34) Bhuyan, T.; Singh, A. K.; Dutta, D.; Unal, A.; Ghosh, S. S.; Bandyopadhyay, D. Magnetic Field Guided Chemotaxis of iMushbots for Targeted Anticancer Therapeutics. ACS *Biomater. Sci. Eng*. **2017**, 3, 1627-1640.

(35) Mahmed, M.; Heczko, O.; Söderberg, O.; Hannula. S. P. Room Temperature Synthesis of Magnetite (Fe_3-δO_4) Nanoparticles by a Simple Reverse Co-Precipitation Method. *IOP Conf. Ser. Mater. Sci. Eng*. **2011**, 18, 032020-24.

(36) Cör, D.; Knez, Z.; Hrnčič, M. K. Antitumour, Antimicrobial, Antioxidant and Antiacetylcholinesterase Effect of *Ganoderma Lucidum* Terpenoids and Polysaccharides: A Review Molecules **2018**, 23, 649-670.

(37) El-Nashar, D. E.; Rozik, N. N.; Soliman, A. M.; Helaly, F. Study the release kinetics of curcumin released from PVA/curcumin composites and its evaluation towards hepatocarcinoma. *J. Appl. Pharma. Sci.* **2016**, 6, 067-072.

(38) Jourghanian, P.; Ghaffari, S.; Ardjmand, M.; Haghighat, S.; Mohammadnejad, M. Sustained Release Curcumin Loaded Solid Lipid Nanoparticles. *Adv. Pharm. Bull*. **2016**, 6, 17-21.

(39) Saavedra, M. J.; Borges, A.; Dias, C.; Aires, A.; Bennett, R. N.; Rosa, E. S.; Simões, M. Antimicrobial Activity of Phenolics and Glucosinolate Hydrolysis Products and their Synergy with Streptomycin against Pathogenic Bacteria. *Med. Chem*. **2010**, 6 174-183.

(40) Alves, M. J.; Ferreira, I. C. F. R.; Martins, A.; Pintado, M. Antimicrobial activity of wild mushroom extracts against clinical isolates resistant to different antibiotics. *J. Appl. Microbiol.* **2012**, 113, 466-475.

CHAPTER 5

Acoustic Propulsion of Vitamin C loaded Teabots for Targeted Oxidative Stress and Amyloid Therapeutics

Contents

Abstract

In this study, the fabrication of ascorbic acid (AA) template nanomotors was achieved using buds of *Camelia sinensis*, undergoing fuel-free propulsion. The motors, namely, Teabots, display propulsion by converting the sound energy from the acoustic field into a mechanical one. The mesh-like structures of the anionic Teabots facilitate superior adsorption of ascorbic acid (AA-Teabots) undergoing a controlled release. The motors show antioxidant properties at physiological pH range by scavenging intracellular reactive oxygen species. Interestingly, the percentage release of ascorbic acid is significantly higher under the influence of ultrasound exposure, as compared to the standard pH-dependent release. The motors were also efficient in the degradation of artificially synthesized toxic amyloid fibrils. The acoustic delivery of AA-Teabots could protect HEK-293 cells from oxidative injuries alongside preventing protein-aggregation derived diseases. Soon, such acoustic powered biocompatible AA-Teabots have been envisioned to provide an attractive approach in proficient delivery and controlled release of therapeutic payloads at targeted zones.

This chapter is published in *ACS Applied Bio Materials* **2019**, 2, 4571-4582. I gratefully acknowledge the assistance of Dr. D. Dutta, Dr. M. Bhattacharjee, and Dr. A. K. Singh.

5.1. Introduction

Artificial self-propellers for the guided transport of therapeutic agents in the diseased body-parts have been considered to be one of the most emerging areas of nanoscale research.[1,2] In this regard, while considerable attention has been given to the catalytic motors, various *in vivo* biomedical applications is expected to obviate the fuel-driven motions due to difficulties in modulating the motions.[3-7] In order to address these issues, efforts have been made to propel the motors under the remote excitations involving photons[8], magnetic field[9-11], acoustic waves[12] and/or electric field[13,14]. In particular, recent studies have shown that the propulsion of nanomotors using safe MHz ultrasound frequencies (3-10 MHz) can enhance the prospects of the self-propelling objects in diverse biomedical applications causing insignificant harm to biological samples and human body.[15] In a way, the rather innocuous acoustic waves enable a facile and fuel-free remote control on the motions of the self-propellers inside the biological systems alongside facilitating a controlled mechanical release.[16–20]

Apart from the driving force for the motion, another important factor in the design and development of micro or nanoscale motors has been the materials of construction. While the majority of the first-generation self-propellers were rather synthetic devices[21-26] of late, the usage of biomaterials has become nearly mandatory at least for the motors used in the biological realm due to low cost of fabrication and biocompatibility.[27-30] In this regard, the idea of acoustically driven plant-based motors could emerge as a novel candidate for intracellular drug delivery of unharmed biological samples.[31-35] Further, under confinement and inside the viscous biological mediums, the practice of ultrasound exposure is expected to facilitate the remotely guided propulsions of such devices.[15,36] Given these backgrounds,

herein, nanomotors have been fabricated from *C. sinensis* , which is capable of binding Ascorbic acid (AA) on their surface and exhibits sustained release when driven acoustically towards oxidatively stressed cells. In particular, the proposed ultrasound (US) propelled, L-Ascorbic acid (AA) functionalized Teabots aimed to act as an (a) unique reactive oxygen species (ROS) scavengers in the human embryonic kidney (HEK-293) cell model and (b) efficient amyloid inhibitors.

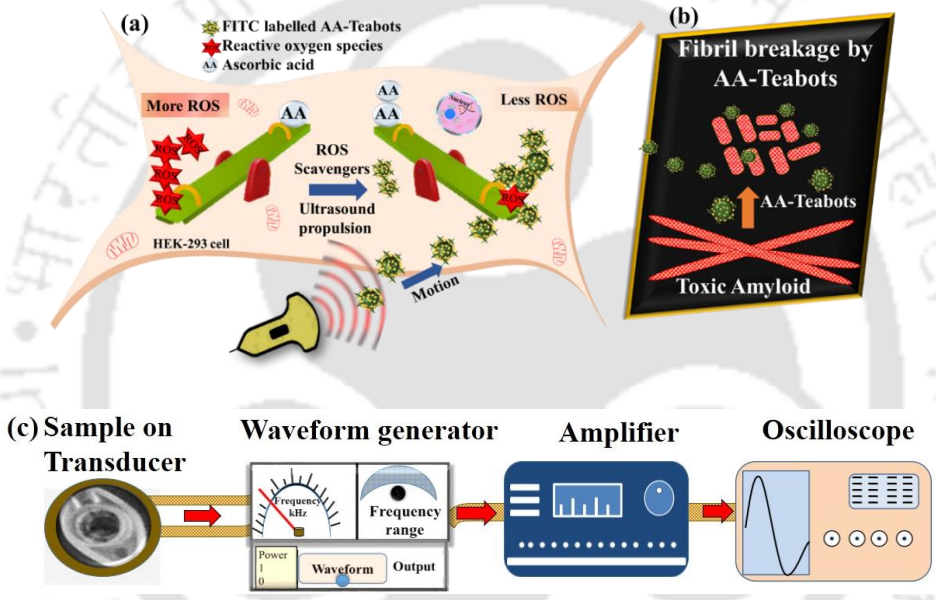

Figure 5.1. Schematically describes acoustic propulsion of ascorbic acid-functionalized Teabots (AA-Teabots) **(a)** inhibiting intracellular oxidative stress by scavenging ROS and **(b)** exhibiting anti-amyloidogenic properties. **(c)** Schematic representing the experimental set up for ultrasound-powered propulsion of AA-Teabots where the sample holder was placed on a piezoelectric transducer (0.5 × 10 × 5 mm) connected to waveform generator, power amplifier and monitored using an oscilloscope.

The Teabots were synthesized from unfermented white tea buds of *Camellia sinensis* comprising of polyphenols from catechin family exhibiting anti-tumor and immune-stimulatory activities, lowering blood pressure, HIV treatment, and restoration of the oxidative damages.[37-39]

In view of this background, Teabots were employed for the reduction of intracellular ROS on hydrogen peroxide (H_2O_2) induced HEK-293 cells, represented in **Figure 5.1a**. The metabolic state of these cells is found to be comparable to normal human cells, displaying rational levels of oxidative stress. Intracellular ROS mainly comprises of the non-radical peroxide, superoxide or hydroxyl radical, which causes signal transduction resulting in cell autophagy, necrosis, and physiological apoptotic damages.[40,41] The presence of H_2O_2 in cells enhances oxidative damage by generating more ROS, creating an imbalance between oxidation and anti-oxidation defense systems.[42,43]

In particular, the cytoprotective effects of Teabots have been monitored by their ROS scavenging capability in H_2O_2-induced oxidative stressed cells. It is also well known that ascorbic acid (AA) is one of the essential antioxidants in the human tissues, which is unstable, have low skin permeability and cannot be synthesized in a human body.[44–46] In order to overcome some of these challenges, AA was encapsulated on the Teabots that could perform US induced sustained release for ROS scavenging in the cells.[47–49]

Interestingly, several studies have associated neurological disorders such as Alzheimer's, Parkinson's, and Huntington's with the combined effects of the elevation of intracellular ROS and accumulation of β-amyloid fibrillar aggregates.[50,51] Although many reports demonstrated the dose-dependent inhibition of fibrillation process by chemical/biological mechanisms, very few reports revealed the complete dissolution of fibrils under *in vitro* conditions.[52–56] To achieve specific degradation of toxic amyloid fibrils, our research is directed towards the need for biocompatible acoustic delivery of AA-Teabots with anti-amyloidogenic properties, schematically described in **Figure 5.1b**. In a way, fuel-free US propulsion of AA functionalized Teabots achieved unprecedented inhibition of intracellular oxidative stress and amyloidogenic degradation through a sustained release of AA. The

experimental set up for ultrasound-powered propulsion of AA-Teabots has been shown in **Figure 5.1c.** The acoustic responses of the plant-based AA-Teabots passage the gap between artificial motors and biological systems, making a biocompatible design for *in vivo* biomedical applications.

5.2. Experimental Section

5.2.1. Materials

White tea (*Camellia sinensis*) was collected from IIT Guwahati. Hydrogen peroxide (50%) and sodium chloride were procured from Merck (India). L- Ascorbic Acid, DPPH (2, 2-diphenyl-1-picryl-hydrazyl-hydrate) and Thioflavin T were purchased from Sisco Research Laboratories Pvt. Ltd (SRL) while Alamar Blue (Resazurin Sodium salt) and 2,6-dichlorophenolindophenol(DCPIP) were procured from Himedia (India). Methylene Blue, 2′, 7′-Dichlorodihydrofluorescein diacetate (DCHFDA), nitro blue tetra-zolium (NBT), NADH (nicotinamide adenine dinucleotide), phenazinemethosulfate (PMS), sodium dodecyl sulphate (SDS), Fluorescein-5-isothiocyanate (FITC), Hen Egg White Lysozyme (HEWL), phosphate buffer saline (PBS), Sodium Chloride(NaCl) and Potassium chloride (KCl) were procured from Sigma-Aldrich (India). All the chemicals were of analytical grade and used as received without any purification. Piezoceramic Rings were purchased from PI Ceramic GmbH (Germany). Milli-Q grade water was used for all the experiments.

5.2.2. Methods

(a) Fabrication of AA-Teabots: The infusions of white tea were prepared by steeping 25 g of ground tea buds (*Camellia sinensis*) in 100 mL of boiling sterile water for 5 min. The infusion was then added with 0.5% of the chitosan solution and homogenized using vortex for 20 min. The resulting solution possessed suspended tea particles that were separated via

differential centrifugation at 4000 rpm, 14000 rpm, and 24000 rpm for 30 min, 1 h, and 2 h, respectively. The underlying idea behind this was to separate the tea particles concerning their sizes at macro, micro, and nanoscale levels, respectively. The supernatant obtained after centrifugation at 4000 rpm (4 K-S) was collected and re-centrifuged at 14000 rpm for 1 h. Similarly, the supernatant from 14000 rpm (14 K-S) centrifugation was again centrifuged at 24000 rpm for 2 h followed by removal of the supernatant (24 K-S). The retrieved pellet-particles obtained from centrifuged 4 K-S, 14 K-S, and 24 K-S was dispersed in sterile water after vacuum drying. The size of the tea particles was analyzed, and the nano-sized ones obtained from 24 K-S were considered for further experiments. The particles (0.5 to 12.5 mg) were incubated in a 0.1 M ascorbic acid (20 µg mL^{-1}) in phosphate buffer (PBS) for 4 h and at 37°C. Freshly prepared ascorbic acid loaded particles (AA-Teabots) were centrifuged for 5 min at 5000 rpm, vacuum dried at 26°C and used for further experiments.

(b) Ultrasound setup: The ultrasound-powered propulsion of AA-Teabots was performed using a previously reported acoustic cell method, shown in Figure 5.1c.[36] The Teabots were suspended on a hollow lid (diameter 2 cm) filled with 1 mL of PBS. Briefly, the ultrasonic field was generated by placing the lid at the center of a piezoceramic transducer, **(i)** with thickness 0.5 mm and an outer/inner diameter of 10 mm and 5 mm, respectively. The transducer was fixed to the bottom center of a glass slide and connected through a 15 MHz waveform generator **(ii)** coupled to a power amplifier **(iii)** for regulating the intensity of acoustic waves. The monitoring of the electric signal was carried out by using a 20 MHz storage oscilloscope **(iv)**. A continuous sine, pulse, and triangular waveform with varying frequencies (1 – 20 MHz) were applied to the piezoceramic transducer under the influence of a fixed voltage (20.0 V).

(c) Amyloid Fibrillation and Disintegration: The formation of amyloid fibrils was studied using a previous protocol with minor modifications.[56] The HEWL solution (2 mg ml^{-1}, 140 µM) was prepared in an aqueous solution of 137 mM and 2.7 mM of NaCl and KCl, respectively. The pH of the protein mixture was adjusted to 5.0, and magnetically stirred at 70°C for 48 h. The fibrillation of the amyloid samples was studied by mixing 20 µL of protein sample in 10µM ThT- PBS solution at different time intervals. Following this, the fluorescence intensity of ThT in the protein solution was measured at an excitation wavelength of 440 nm.

The matured fibrils were fabricated from HEWL protein by incubating standard solutions[56,] and the long fibrils were isolated by centrifugation at 5000 rpm for 15 min. The retrieved pellets were dispersed in PBS buffer of pH 7.4 followed by incubating 900 µL of dispersed fibrils with different concentration Teabots and AA-Teabots (3 – 20 µg mL^{-1}) at 60°C for a fixed time (72 h). Moreover, the effect of a fixed concentration of the samples (20 µg mL^{-1}) on fibrillar disintegration was checked at different time intervals (0 to 72 h). The degradation of fibrils was monitored by subjecting them to ThT fluorescence assay, FE-TEM analysis, and CD spectroscopy. The treated amyloid samples (20 µL) were mixed with 10µM ThT in 1 mL PBS buffer at pH 7.4 and incubated for 15 min before spectrofluorometric analysis. The excitation wavelength was set at 440 nm, and emission was recorded between 460 nm to 600 nm. The ThT emission peak was measured at 488 nm and the fibril growth curve was plotted concerning time. Field emission transmission electron microscope (FE-TEM) was used to monitor the effect of free AA (17.6 µg mL^{-1}), Teabots and AA-Teabots (20 µg mL^{-1}) on amyloid growth. For analysis of amyloid assembly, the treated protein samples were deposited on a copper TEM grid and dried in a vacuum oven overnight. The CD spectra analysis of the treated HEWL samples was carried

out in the range of 200-260 nm after proper baseline correction. The mean residual ellipticity (MRE) graph was plotted, and the percentage of α and β-sheets for the control and treated amyloid samples was obtained.[57,58]

(d) Effect of Nanomotors on Oxidative Stressed Cells: The HEK-293 cell lines for the cellular study were obtained from National Centre for Cell Sciences (NCCS), Pune, India. The HEK-293 cells were grown in Dulbecco's modified Eagle's medium (DMEM) with the supplementation of 10% (v/v) fetal bovine serum (PAA Laboratories, Austria), L-glutamine (4mM), penicillin (50 units/mL), streptomycin (50 mg/mL, Sigma-Aldrich) and maintained in a humidified incubator with 5% CO2 atmosphere at 37 °C.

HEK-293 cells were seeded in a 96-well microtiter plate at a density of 1×10^4 cells/well and cultured in 5% CO_2 incubator at 37°C for 24 h. To induce oxidative stress in cells, different concentrations of H_2O_2 solutions (0- 1000 µM) were added to the cells and incubated for 5 h at 37°C in the incubator. Alamar blue cell viability assay was performed, as described below, to evaluate the cytotoxicity and optimum H_2O_2 concentration for further studies.

A density of 1×10^4 cells/well were seeded and incubated in 5% CO_2 incubator at 37°C for 24 h. Then, different concentrations of free AA (17.6 µg mL^{-1}), Teabots and AA-Teabots with a final concentration of 4.5 to 12.5 µg mL^{-1} in PBS, pH 7.4 was added to the wells and incubated for another 24 h. Following this, the cells were exposed to optimum H_2O_2 concentration (400 µM) and incubated for an additional 5 h. The cells in the wells only with media were kept as control, and the cells treated with only 400 µM H_2O_2 in the media were also included. The cell viability was determined using the AB assay, as described earlier.

(e) Measurement of Intracellular ROS: The generation of ROS in HEK-293 cells was measured using fluorescent 2, 7-dichlorofluorescein – diacetate (DCFH-DA). The cells

were seeded in a 96-well plate at a density of 1×10^4 cells/well and incubated for 24 h in a humidified CO_2 incubator at 37 °C. Then, concentrations of free AA (17.6 µg mL^{-1}), Teabots and AA-Teabots with final concentrations of 4.5 to 12.5 µg mL^{-1} in PBS, pH 7.4 was added to the wells and incubated for another 24 h. Likewise, the cells were treated with 400 µM H_2O_2 and incubated for 5 h. The cells without any sample addition were kept as control. After treatment, the cells were added with 1mM DCFH-DA (5µL/well) and incubated for 10 min. The old media was discarded, and the cells were washed and dispersed in 100 µL of PBS. The non-fluorescent DCFH-DA dye freely penetrates the cell membrane and undergoes hydrolysis by esterase to form DCFH. In the presence of intracellular ROS, the hence formed DCFH gets oxidized to a highly green-fluorescent 2, 7-dichlorofluorescein (DCF) where the intensity is parallel to the amount of generated ROS inside the cells. The fluorescence intensity of DCF in all the samples was recorded using a Perkin Elmer fluorescence spectrophotometer at an excitation and emission wavelength of 488 nm and 530 nm, respectively, and represented graphically. Following this, the cells were imaged under an Epifluorescence microscope under green excitation of 340 – 380 nm.[43,59]

(f) Determination of ascorbic acid (AA) binding and release efficiency: A solution of ascorbic acid (AA) in water (20 µg mL^{-1}) was added to a varying concentration Teabots (0.5 mg – 12.5 mg) and incubated for 4 h under vigorous stirring conditions (1000 rpm) at 37°C. Nitrogen gas was flown through the reaction mixture continuously for 15 min, and the pH of the solution was adjusted to 7.4 by adding 0.1 M NaOH solution. The anionic ascorbic acid was bound on the surface of Teabots due to its porous structure. Following this, the solution was then centrifuged for 20 min at 5000 rpm; 4°C to remove the unbound AA and the retrieved pellets (AA-Teabots) was dispersed in sterile water. A calibration curve was constructed based on the known concentration of the free ascorbic acid solution.

Applying Beer's law, the supernatants containing the unbound AA were collected and quantified by UV – visible Spectrophotometer (Perkin Elmer) at 264 nm. The initial amount of AA concentration was obtained from the intensity of total free AA (20 µg mL^{-1}) in the solution. The experiments were performed thrice to ensure reproducibility. The binding efficiency (B.E.) was calculated using the following formula [10]:

$$B.E.(\%) = \frac{(AA)_i - (AA)_s}{(AA)_i} \times 100. \quad (1)$$

Here, $(AA)_i$ represents an initial concentration of ascorbic acid in the solution, and $(AA)s$ represents the concentration of unbound ascorbic in the supernatant.

The release of AA from AA-Teabots (8 mg) was studied at different time intervals (0 -12 h). The retrieved pellets collected after centrifugation of AA treated Teabots were appropriately washed and then dispersed in 100 µL of chloride buffer of pH 1.2 and PBS buffer of pH 7.4. The resulting solution was incubated for 3 h at 37°C followed by centrifugation. The supernatants were obtained, and the release study of bound AA was analyzed by a UV-visible spectrophotometer at 264 nm[60].

Additionally, the release of AA was also studied under the influence of a sine ultrasonic waveform of 8 MHz for a fixed time interval. The retrieved pellets were dispersed in PBS and exposed to ultrasound waves for 10 min. The solution was centrifuged, and the supernatant was analyzed spectrophotometrically for a comparative release study of bound AA.

(g) Stability of bound ascorbic acid (AA): The stability of bound AA on AA-Teabots and free AA in solution was carried out using a previously reported method.[61] The loaded AA on the surface of Teabots was extracted using 1.0 g of sample in 20 mL of extraction solution (5% NaCl and 1% SDS). The ascorbic acid level was measured by titration using a mixture

of 1% oxalic acid solution (w/w) and 0.025% DCPIP (w/v). The stability analysis was carried out for 0 to 20 days after the loading of ascorbic acid on the surface of Teabots. The samples were protected from sunlight at 37 ± 2°C. The experiments were performed in triplicates to ensure reproducibility.

The antioxidant activity of AA encapsulated on Teabots was analyzed by using methylene blue (MB) as an oxidizing agent. The reduction of MB dye to its leuco form by bound AA confirmed the antioxidant activity of AA after binding on the surface of Teabots. AA-Teabots (~ 3g) were mixed with 1mM MB solution and stirred vigorously until the blue MB dye turns colorless. The conversion of MB to the leuco form was confirmed by using UV-Vis spectroscopy at 264 nm.[60] Both the experiments were performed in triplicates to verify whether the AA bound on the surface of Teabots is as effective as free AA in solution.

(h) Measurement of Speed under Ultrasonic waves: The ultrasonic propulsion of AA-Teabots (size ~ 150 -300 nm) was evaluated by placing the nanomotors in a transparent hollow lid (~ 2 cm) filled with 1 mL of PBS. The displacement of the nanomotors from initial to the final point was calculated per unit time by placing the lid on a paper-grid with dimensions 1 mm × 1 mm.[10] The velocity of the nanomotors was measured under the influence of acoustic waves with varying frequencies (0 – 20 MHz) and voltage (10 – 20 V). The experiments were carried out in triplicates to attain the average value and error bars.

(i) Alamar Blue (AB) Cell Viability Assay: For the cell viability assay, HEK-293 cells/well were seeded in a 96-well microtiter plate at a density of 1×10^4 cells/well and cultured in 5% CO_2 incubator at 37°C for 24 h. The cells were then treated with AA (17.6 µg mL^{-1}), Teabots and AA-Teabots with a final concentration of 4.5 to 12.5 µg mL^{-1} and incubated for another 24 h followed by cell viability studies using Alamar blue (AB) assay. Briefly, an AB solution (10% v/v of AB dye) was prepared in sterile water, and 10 µM

solution was added to each well following 3 h incubation. The oxidized form of AB (Resazurin) gets reduced to resorufin by metabolically active cells. Thus, the cellular toxicity was measured spectrophotometrically by measuring the absorbance at wavelengths of 570 nm and 600 nm using a microplate reader.[62,63] The results obtained after independent experiments were averaged over 3 replicates per well. Also, negative controls with only AB solution in media (without cells) were included, and the background absorbance measured in those was subtracted. The percentage reduction of AB that is directly proportionate to the percentage of cell viability was calculated by using the following formula:

$$\%\ \textit{Cell Viability} = \frac{(O_2 \times A_1) - (O_1 \times A_2)}{(R_1 \times N_2) - (R_2 \times N_1)} \times 100. \qquad (2)$$

where O_1 is molar extinction coefficient (E) of oxidized AB at 570 nm, O_2 is E of oxidized AB at 600 nm, R_1 and R_2 are the E of reduced AB, A_1 and A_2 are the absorbance of test wells and N_1 and N_2 are the absorbance of negative control wells at 570 nm and 600 nm, respectively.

(j) Field Emission Scanning Electron Microscopy (FESEM) of Treated Cells: The morphological changes in the cells after their treatment with only H_2O_2 (400 µM) and H_2O_2+ AA-Teabots (400 µM + 12.5 µg mL^{-1}) was compared with the untreated cells using FESEM analysis. The cells were incubated overnight (37 °C) at a density of 1×10^5 cells in a 35 mm culture dish for 24 h inside a humidified CO_2 incubator. The grown cells were treated AA-Teabots (12.5 µg mL^{-1}) and incubated overnight at 37 °C. Following this, the cells were added with H_2O_2 (400 µM) in respective culture dishes and incubated for an additional 5 h. For sample preparation, the cells were washed with PBS and subsequently harvested by trypsinization. Next, the fixation was done by adding 70% chilled ethanol, and the cells

were finally drop-casted on a piece of glass slide covered with aluminum foil. The sample was allowed to vacuum dry in a desiccator and analyzed under FESEM.

(k) FITC on AA-Teabots for intracellular tracking: An aqueous solution of FITC in DMSO (5 mg mL^{-1}) was added to AA-Teabots (12.5 µg mL^{-1}) magnetically stirred for 3 h at 37 °C in the dark. FITC was absorbed on the surface of AA-Teabots due to electrostatic interactions forming fAA-Teabots. Following this, the formed fAA-Teabots were centrifuged at 5000 rpm for 15 min, to remove the unloaded dye. The retrieved pellets were then collected and dispersed in distilled water, and the intensity of the peak was measured at an excitation wavelength of 488 nm.[64] The CLSM analysis was carried out by seeding 1 × 10^5 HEK-293 cells on a coverslip placed in a 35 mm culture dish and incubating in a CO_2 incubator at 37 °C for 24 h. Thereafter, the cells were treated with FITC loaded AA-Teabots (fAA-Teabots) and incubated for 6 h followed by washing the cells with PBS. The fixing of cells was done by adding 0.1% formaldehyde and 70% chilled ethanol. The coverslips containing the control without Teabots and the treated cells were carefully mounted onto the glass slides with their sides sealed. The samples were then visualized under Zeiss CLSM microscopy at an excitation wavelength of 488 nm to ensure intracellular uptake of AA-Teabots.[64]

(l) 2, 2-diphenyl-1-picryl-hydrazyl-hydrate (DPPH) assay: The DPPH assay was carried out to assess the radical scavenging activity of AA, Teabots and AA-Teabots using a reported method,[65] which is based on reduction process of DPPH by accepting an electron or hydrogen. Here, 0.1 mM of DPPH was mixed with different concentrations of AA (17.6 µg mL^{-1}), Teabots and AA-Teabots (4.5 to 16.5 µg mL^{-1}) and incubated at room temperature in the dark for 20 min. The absorption spectra of the samples were recorded using a UV-

visible spectrophotometer at 517 nm. In this test, methanol was used as blank, and DPPH + methanol was considered as control. The bluish methanolic solution of DPPH turned to yellow with the addition of samples. The free radical scavenging activity of the samples was parallel to decreasing absorbance value that is represented by percentage inhibition as[65]:

$$\%\ Inhibition = \frac{Absorbance_{control} - Absorbance_{test}}{Absorbance_{control}} \times 100. \quad (3)$$

(m) Superoxide Scavenging Assay using Nitro Blue Tetra-Zolium (NBT): The quenching of superoxide radicals by AA (17.6 µg mL^{-1}), Teabots and AA-Teabots were evaluated by studying inhibition of NBT reduction. The oxidation of NADH generates superoxide radicals in the mixture assayed by NBT reduction. In this method, different concentration of the nanomotors (4.5 to 16.5 µg mL^{-1}) was mixed with 3 mL of reaction solution containing 100 mM PBS, 468 µM NADH (nicotinamide adenine dinucleotide), 156 µM NBT (nitro blue tetra-zolium) and 60 µM PMS (phenazinemethosulfate). The mixture was incubated at 25°C for 5 min, and a purple-colored product (diformazan) was formed upon reduction of NBT by superoxide. The detection of peroxide was carried out spectrophotometrically by measuring the diformazan at 560 nm against blank samples. The reaction mixture without the samples was used as a control. The decrease in absorbance of the solution corresponds to the increase of superoxide anion scavenging activity of the samples. The percentage of inhibition of superoxide radical was calculated using the same formula as described in DPPH assay.[65,66]

5.3. Results and Discussion

5.3.1. Fabrication and Characterization

The presence of phytochemicals is a significant motivation here for the fabrication of robust Teabots for targeted delivery of drugs in oxidative stressed cells, executing ultrasonic propulsion. Apart from the antioxidant properties of Teabots, the increase of intracellular ROS concentration levels in neurodegenerative disorders necessitates the functionalization of Teabots with antioxidant compounds such as AA, offering efficient ultrasound-mediated controlled cellular delivery. Therefore, this approach has been exploited for targeted delivery for the AA-Teabots where the chemical stability of AA was preserved. The study highlights the potential of their role in protecting stressed cells from oxidative challenge. Hence, this method satisfied all the principles for green chemistry without the intervention of any toxic chemicals, ensuing towards the development of biological friendly nanomachines that are not considered as foreign invaders by the immune system in the body. The detailed experimental procedure for fabrication of Teabots has been discussed previously in the Experimental Section 5.2.2. and represented schematically in **Figure 5.2a**. The schematic showing the encapsulation of Teabots using AA followed by and linear and circular US propulsion of AA-Teabots has been described in Experimental Section 5.5.2. and presented in **Figure 5.2b**.

A stable nano-suspension of Teabots was obtained from the supernatant after centrifugation at 24000 rpm (24 K-S), which was considered to be suitable for further experiments. To date, the mechanism behind nanoparticle formation from tea extract and their role in the developmental process is not well understood. However, the presence of various tentative microscale components in black and green tea have been reported that are highly bioactive.[67]

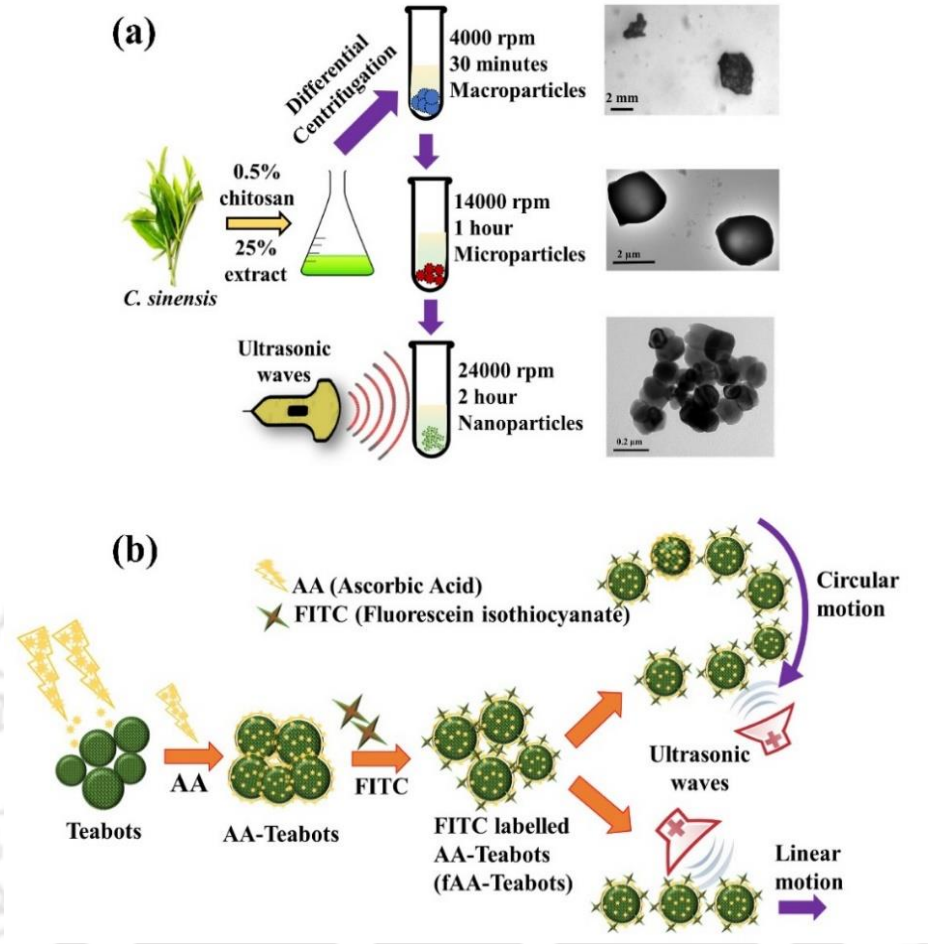

Figure 5.2. (a) Schematic depiction of the steps to fabricate Teabots from white tea buds (*C. sinensis*) by differential centrifugation. **(b)** A schematic diagram describing the fabrication of AA-Teabots by encapsulating ascorbic acid (AA, 30 µg mL^{-1}) on the surface of Teabots exhibiting linear and circular motion. The AA-Teabots were labeled with FITC (fAA-Teabots) for the *in vitro* intracellular tracking in cell studies.

In this direction, a few components of novel Teabots from unfermented white tea with their excellent biocompatibility was dissected. The TEM micrographs of nano Teabots of size range have been shown in **Figure 5.3a** reveals spherical shaped particles with size ranging from 200 – 500 nm. The retrieved pellet-particles obtained from centrifuged 14 K-S is represented in **Figure 5.3b**.

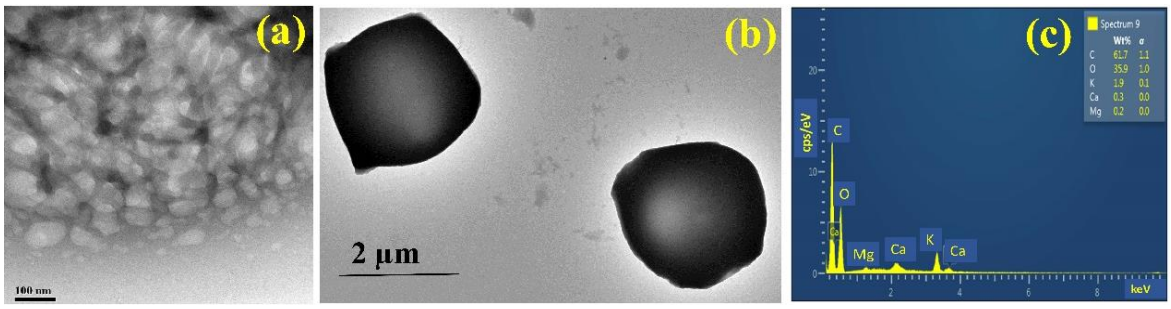

Figure 5.3. (a) TEM micrograph of nano AA-Teabots. **(b)** FETEM micrograph of microparticles of size ~1-2 µm synthesized from white tea bud (*C. sinensis*) after differential centrifugation at 14000 rpm. **(c)** EDX spectra of nanosized Teabots showing the presence of elements like carbon, oxygen, potassium, calcium, and magnesium.

The EDX spectra of the nanomotors obtained after 24 –S has been displayed in **Figure 5.3c,** ensuring the presence of elements like carbon, oxygen, potassium, calcium, and magnesium. The surface morphology of as-synthesized Teabots has been represented by the FETEM micrographs in **Figure 5.4a**, which revealed porous mesh-like structures on the surface. The mass spectra obtained from LCMS analysis has been shown in **Figure 5.4b,** which revealed the presence of phenolic acid derivatives and theaflavins.[68-70] The loading of AA into the Teabots could be due to electrostatic interaction, encapsulation or adsorption.[46] The mesh-like structures present on the surface of Teabots, along with their negative charges facilitated greater adsorption of positively charged AA through electrostatic interactions. The ζ-potential of free AA was found to be -4.27 ± 0.3 mV, and the same of Teabots was found to be 3.9 ± 0.5 mV. The coating of negatively charged AA reduced the net positive charge on Teabots with ζ-potential of ~1.92 ± 0.8 mV, as shown in **Figure 5.4c**. The localization of AA-Teabots inside the HEK-293 cells was tracked by using a negatively charged FITC tracker dye. The positive ζ-potential of AA-Teabots could load the negatively charged FITC (- 5.2 ± 3 mV) on their surface, forming fAA-Teabots exhibiting a ζ-potential of around 0.23 ± 0.3 mV.

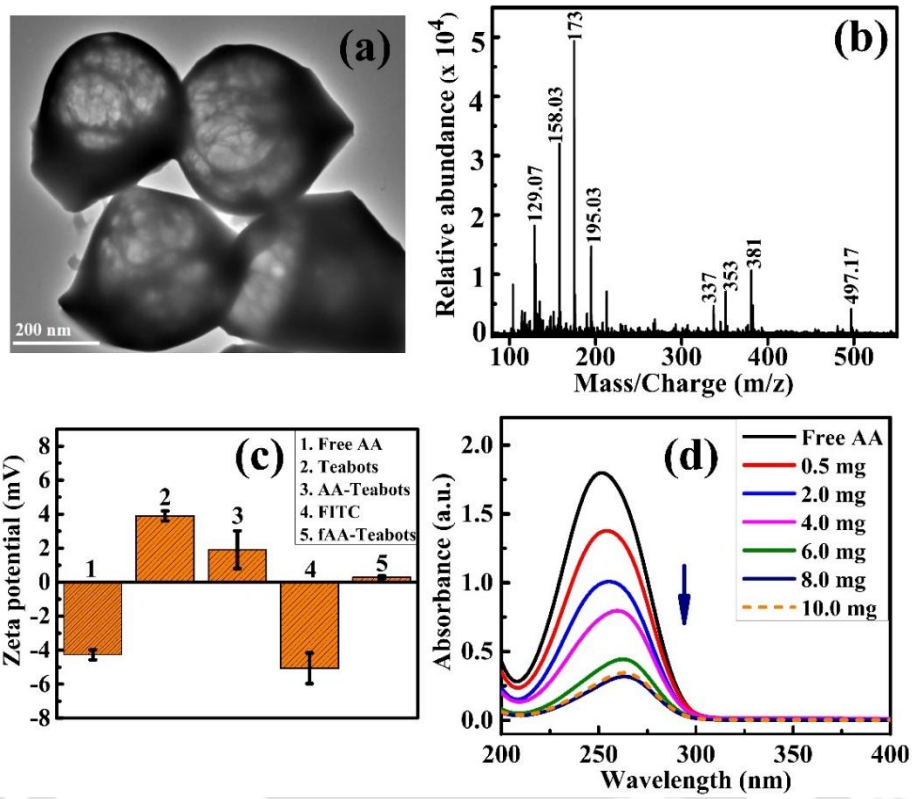

Figure 5.4. (a) Field Emission Transmission Electron Microscope (FETEM) micrographs and **(b)** Liquid Chromatography (LCMS) indicating the presence of phenolic acid derivatives and theaflavins w.r.t. m/z ratio. **(c)** ζ-potential measurement of samples. **(d)** UV-visible absorption spectra of the supernatant obtained after treatment of ascorbic acid (AA) solution (30 µg mL^{-1}) with various concentrations of Teabots for 4 h.

Peak no.	$[M + H]^+$ / $[M-H]^-$ (m/z)	Tentative Identification
1	129.07, 158.03	Theanine
2	381	1-O-caffeoyl-3-O-sinapoylquinic acid
3	173	Theanine
4	195.03	Caffeine
5	337	5-p-Coumaroylquinic acid
6	353	3-Caffeoylquinic acid
7	497.17	Dicaffeoylshikinic acid

Table 5.1. Presence of phenolic acid derivatives and theaflavins w.r.t. m/z ratio using LC.

The identification of building blocks of the Teabots was further validated by performing LCMS for protonated/deprotonated molecules ($[M + H]^+$/ $[M-H]^-$) at respective m/z ratios, as represented in **Table 5.1.**

Figure 5.4d represented the amount of AA loaded on various concentrations of AA-Teabots, ranging from 0.5 mg to 10 mg. It was observed that with a gradual increase in the concentration of nanomotors (0.5 mg to 10 mg), the binding efficiency of AA increased. This was confirmed by the gradual decrease in absorbance intensity of unbound AA in the supernatant. The binding capacity of AA saturated to ~89.41% at a concentration of 8 mg, corresponding to ~17.6 µg mL-1 of AA. Thus, 8 mg of AA-Teabots were used for release studies of AA and other experiments unless mentioned otherwise.

5.3.2. Encapsulation and Release of Ascorbic Acid

The binding efficiencies of AA were studied by loading and incubating AA on 8 mg of Teabots at different time intervals.

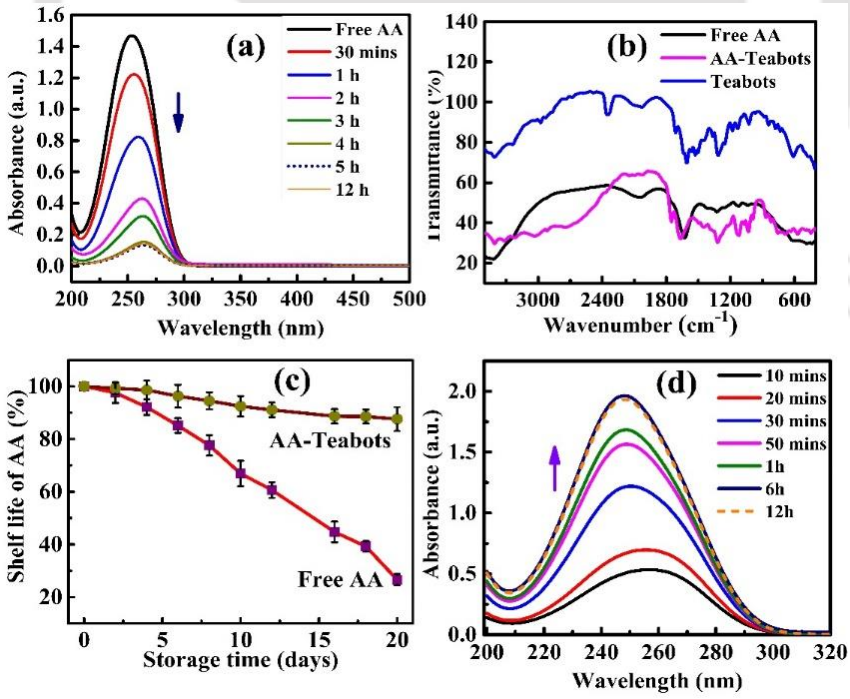

Figure 5.5. (a) UV-visible absorption spectra of the supernatant obtained after treatment of 8 mg ascorbic acid (AA) at different time intervals. **(b)** FTIR spectra of free AA, Teabots and AA-Teabots. **(c)** Stability analysis of free AA and encapsulated AA w.r.t time (10 min – 12 h). **(d)** UV-visible absorption spectra of AA released in the supernatant from AA-Teabots at different time intervals (10 min – 12 h).

A gradual decrease in absorbance of unbound AA in the supernatant could be observed, which confirmed the increased binding of AA w.r.t. varied time intervals (30 min to 12 h), as shown in **Figure 5.5a**. A gradual decrease in the absorption spectra of unbound AA in the supernatant could be observed with an increase in time. The binding efficiency got achieved saturation state to ~89.41% when the time exceeded beyond 5 h. The porous mesh-like structures on Teabots shielded the bound AA from rapid degradation providing minimal exposure towards external surroundings, thus enhancing the shelf life of loaded AA. The binding of AA on Teabots was also supported by FTIR spectra of free AA, Teabots, and AA-Teabots with direct evidence for the binding of AA on the surface of Teabots (**Figure 5.5b**). FTIR spectra of AA in the range 3,215–3,520 cm^{-1} corresponds to the different hydroxyl groups.[71] The characteristic peak of AA at 1,750 cm^{-1} due to stretching vibrations of the C=O of the five-membered lactone ring disappears after binding onto the surface of Teabots. A slight shift of the C=C stretching band from 1,665 to 1,635 cm^{-1} could be seen after AA loading.

Significant changes in the positions of different bands of AA-Teabots and free AA revealed a piece of direct evidence for the binding of AA on the surface of Teabots.[72] The stability of bound AA was carried performed for 0 - 20 days after loading of ascorbic acid on the surface of Teabots and compared with free AA.[61] As evident from **Figure 5.5c,** the shelf life of AA bound into the surface of Teabots was higher as compared to free AA during the 20-day storage period. In a way, the Teabots shield the bound AA entirely from the interactions with the external environment. **Figure 5.5d** shows the release behavior of AA from AA-Teabots, which achieved the highest release after 5 h, at pH 7.4, and could be interrelated

with the highest absorbance intensity. However, the amount of AA released from AA-Teabots attained saturation beyond 6 h.

Methylene blue (MB) assay was performed to determine the antioxidant activity of ascorbic acid (AA) encapsulated Teabots. The schematic for this magic blue bottle redox reaction depicting the reduction behavior of AA is represented in **Figure 5.6a,** where the reducing property of AA was retained even after encapsulation. The conversion of the colored oxidized form of MB (MB^+) to its reduced colorless leuco MB (LMB) by AA-Teabots confirmed the effectiveness of bound AA on the surface. The UV-visible spectra for free AA, uncoated Teabots and MB (before and after treatment) considered as control has been shown in from **Figure 5.6b**.

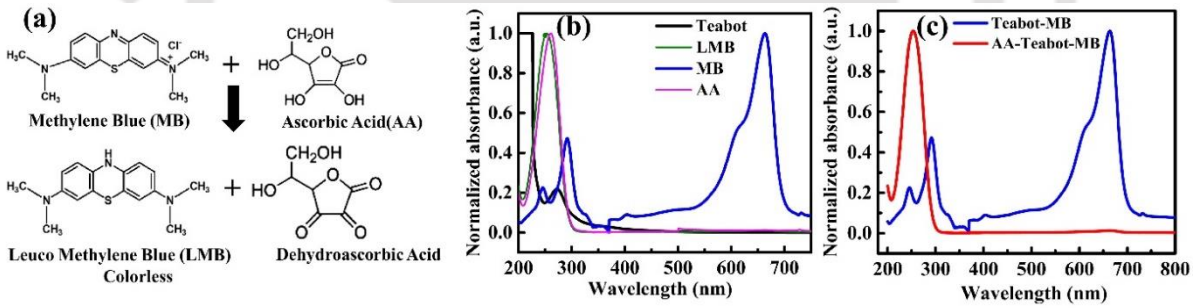

Figure 5.6. (a) Reaction showing reduction of methylene blue (MB) to Leuco-methylene blue (LMB) by encapsulated AA in AA-Teabots. **(b)** UV-visible spectra of Teabots (black line), bleached methylene blue (green line, LMB), methylene blue (blue line, MB) and AA (pink line). **(c)** UV-visible spectra of Teabots (blue line) and AA-Teabots in MB solution (red line).

A strong absorption peak at 237 nm and two sharp peaks (294 nm, 656 nm) indicated the presence of AA and MB, respectively. The MB solution treated with free AA formed LMB that is represented by a peak at 250 nm. The unbound Teabots displayed a peak of lower wavelength at around 270 nm. The UV-visible spectra of AA coated Teabots along with MB (before and after treatment) have been represented in **Figures 5.6c.**

The Teabots treated with MB exhibited two similar peaks as control MB (in Figure b), ensuring that MB is not converted to its reduced form LMB. However, the AA-Teabots treated with MB solution showed only one peak at 294nm, with the disappearance of peak at 656 nm corresponding to MB solution. This indicated that AA molecules bound on the surface of AA-Teabots retained their anti-oxidant property and chemical stability, which efficiently converts MB to LMB. This further proved that the bound AA molecules are not leached away from the Teabots when dispersed in aqueous solutions.

Traditionally, the controlled cellular delivery of AA at higher concentration has been very challenging due to their poor stability on the carriers.[45,46] In the present study, it was found that AA was quite stable on the Teabots. Therefore, the ultrasonic delivery of AA using Teabots could enhance the delivery performance of AA as compared to the conventional molecular form. Thus, the AA-Teabots exhibited less sensitivity towards light, temperature, oxygen, and heat permitting to propose them as potential candidates as stable antioxidants for intracellular delivery.

5.3.3. Motion-based release studies

The release profile of drug AA, which indicates that at pH 7.4, ~89.2% of the AA was released gradually from the Teabots until 300 min before saturating has been shown in **Figure 5.7a**. In contrast, there was a dramatic increase in the percentage of AA released (~64%) at pH 1.2 (chloride buffer) in the first 30 min interval. Thus, a sustained release of AA was observed from AA-Teabots at pH 7.4, with a gradual increase of release percentage at prolonged time intervals.

As stated earlier, the anionic AA got encapsulated onto the positively charged Teabots by electrostatic interactions; the higher percentage of release in neutral pH may be probably

due to an optimum pH condition that resulted in effective diffusion of the drug.[71,73] On the contrary, the abrupt increase in the release of AA from Teabots at a lower pH of 1.2 may occur probably due to a highly acidic condition in the surrounding medium. As expected, the sustained release of unstable antioxidants, such as AA, could be achieved by encapsulating them with Teabots offering slow and continuous delivery of AA under physiological conditions.

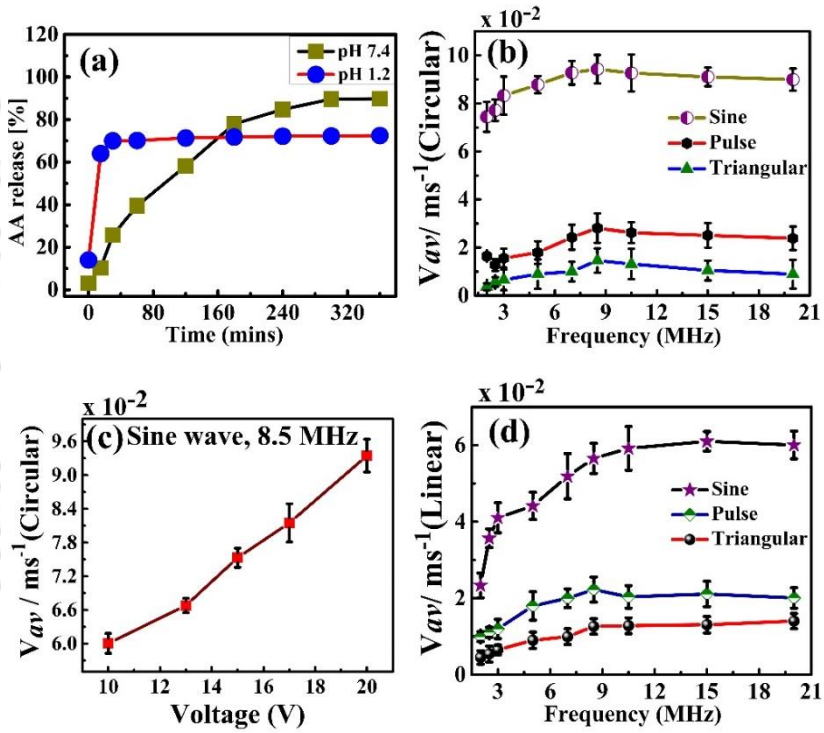

Figure 5.7. (a) Release profile of AA from AA-Teabots at intervals of time in PBS buffer of pH 7.4 and chloride buffer of pH 1.2. **(b)** Variation in average velocity (V_{av}) of AA-Teabots in PBS of pH 7.4 exhibiting circular motion under the influence of a varied ultrasound frequency range of sine, pulse and triangular waveforms at 20V. **(c)** Variation in average velocity (V_{av}) of AA-Teabots exhibiting circular motion in presence of fixed sine wave frequency (8.5 MHz) and different range of voltage (10 – 20 V). **(d)** Variation in average velocity (V_{av}) of AA-Teabots in PBS of pH 7.4 under the influence of a varied ultrasound frequency range of sine, pulse and triangular waveform at 20 V, linear motion.

The influence of fluid, pressure gradient, and acoustic forces have been previously explained, demonstrating the locomotion of nanoscale biological materials to identical levitation plane node and streaming.[36] The direction of acoustic waves falling on the surface of Teabots could be altered to achieve circular and linear motion. The placement of the sample holder directly at the center of the transducer allowed uniform scattering of waves on the Teabots from all directions, leading to circular motion.

Conversely, when the sample holder was placed sideways on the transducer, the motion was assumed to be axisymmetric with the standing acoustic wave generated by the transducer.[15-17] This resulted in a unidirectional distribution of waveforms on the surface of nanomotors, resulting in linear motion. Hence, AA-Teabots could convert the applied acoustic energy into mechanical energy achieving spontaneous directional motion.

In the present experimental setup, the Teabots were exposed to three different waveforms of ultrasound: sine, pulse and triangular of varying frequencies (1 - 20 kHz) and at a fixed voltage of 20 V. To investigate the impact of varying frequencies and waveforms on the motion of AA-Teabots, a series of experiments was carried out. **Figure 5.7b** shows the average velocities of AA-Teabots (V_{av}) exhibiting circular motion under the influence of three different ultrasonic waveforms at varying frequencies.

When the AA-Teabots were immersed in a bath of PBS buffer of pH 7.4 and introduced with varying frequencies of three different ultrasonic waves, the motors attained a maximum speed at 8.5 MHz followed by a gradual decrease in their speed with the further increase of frequencies. At 8.5 MHz, the AA-Teabots exhibited a maximum average velocity (V_{av}) of ~ 9.5×10^{-2} m s^{-1}, 2.7×10^{-2} m $s^{-1,}$ and 1.51×10^{-2} m s^{-1} for sine, pulse and triangular wave, respectively. Thus, the optimum frequency of ultrasonic waves was considered to be 8.5 MHz, beyond which the velocity decreases in the presence of a sine wave.

However, the V_{av} of AA-Teabots in the presence of a pulse and triangular waves was found to be reduced as compared to a sine wave. The motion of AA-Teabots was monitored under the influence of a constant sine wave frequency of 8.5 MHz with varying voltage range between 10 - 20 V. **Figure 5.7c** revealed the average velocities of the circular motion of AA-Teabots that was found to be maximum ~ 9.4×10^{-2} m s^{-1}, at 20 V, beyond which the nanomotors exhibited nearly constant V_{av}. **Figure 5.7d** displayed the average velocities (V_{av}) of AA-Teabots showing linear motion under the influence of sine, pulse, and triangle waveform at a frequency range of 0 – 20 MHz and a fixed voltage (20 V).

The V_{av} was found to be maximum in the presence of sine wave (5.9×10^{-2} m s^{-1}) and lowest in the triangular wave (1.29×10^{-2} m s^{-1}), which matched with the observed V_{av} of AA-Teabots following a circular path. Comparatively, there was a significant reduction in the maximum V_{av} of linearly moving AA-Teabots when compared with their circular locomotion. The reason for the reduced average velocity of linear motion might be attributed to the position of the transducer and sample holder, which could be improved with further investigation.

The random motion of AA-Teabots without PBS buffer was considered as control. The circular motions of AA-Teabots in PBS buffer of pH 7.4 was studied under the influence of sine, pulse, and triangular waves at ~8.5 MHz. The ultrasonic motion of nanomotors is driven primarily due to their rigid nature, which could propel without any metallic coating on the surface. The AA-Teabots exhibited fast autonomous propulsion under the influence of varying sine, pulse, and triangular acoustic waves with productive modes of linear and circular motions. The optimized setup enabled the AA-Teabots to convert the local resonating ultrasound into distinct directional motions.[15–18]

Similarly, the linear motion of the AA-Teabots was monitored at a fixed voltage of 20 V under the influence of sine, pulse, and triangular waveforms of varying frequencies (0 - 20 kHz) and a fixed voltage of 20 V. The random collective motion of the motors in the absence of fluid confirmed their actual acoustic propulsion with the negligible effect of fuel on motors, shown in **Figure 5.8a**.

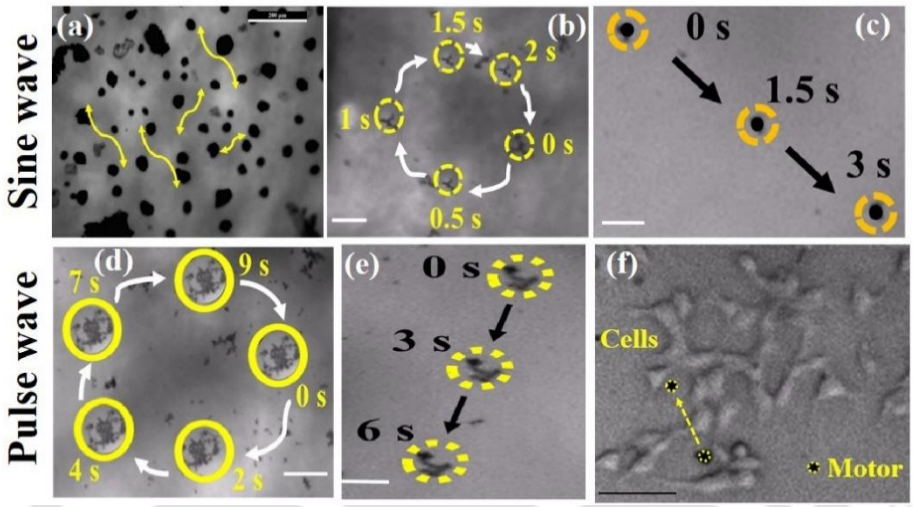

Figure 5.8. (a) Random collective motion of AA-Teabots in the absence of PBS buffer. **(b)** US propelled circular motion of AA-Teabots under the influence of sine waveform (8.5 MHz) in PBS buffer of pH 7.4. The numbers 0-2 represents the position of the AA-Teabots at, *t* = 0 s, 0.5 s, 1 s, 1.5 s, and 2 s, respectively. Scale bar is 20 µm. **(c)** US propelled linear motion of AA-Teabots under the influence of sine waveform (8.5 MHz) in PBS buffer of pH 7.4. The numbers 0-3 represent the position of the motors at, *t* = 0 s, 1.5 s, and 3 s, respectively. The scale bar is 100 µm. **(d)** US propelled circular motion of AA-Teabots under the influence of pulse waveform (8.5 MHz) in PBS buffer of pH 7.4. The numbers 0-9 represents the position of the motors at, *t* = 0 s, 2 s, 4 s, 7 s, and 9 s, respectively. The scale bar is 100 µm. **(e)** US propelled linear motion of AA-Teabots under the influence of pulse waveform (8.5 MHz) in PBS buffer of pH 7.4. The numbers 0-6 represent the position of the nanomotors at, *t* = 0 s, 3 s, and 6 s, respectively. The scale bar is 100 µm. **(f)** Linear motion of AA-Teabots towards oxidative stressed HEK-293 cell lines under the influence of sine waveform (8.5 MHz). The AA-Teabots and cells have been marked with yellow and red circles and the direction of motion has been represented by arrows. The scale bar is 100 µm.

The nanomotors in **Figure 5.8b** exhibited faster circular motion within a time of ~ 2 s, achieving an average velocity of ~ 9.5×10^{-2} m s^{-1} under the influence of sine waveform at

a constant frequency of 8.5 MHz. The numbers 0-2 represents their position at, t = 0 s, 0.5 s, 1 s, 1.5 s, and 2 s, respectively**. Figure 5.8c** shows the linear motion of the AA-Teabots at a fixed voltage of 20 V and sine wave frequency of 8.5 MHz from 0 to 3 s, where the average velocity was found to be maximum, i.e., 5.9×10^{-2} m s^{-1}. The numbers 0-3 represents their position at t = 0 s, 3 s, and 6 s, respectively. On the contrary, the influence of pulse wave decreased the average speed of the rotating motors to 2.7×10^{-2} m s^{-1} rendering a circular motion at around 9 to 10 s, as shown in **Figures 5.8d.**

The linear motion of the AA-Teabots at a fixed voltage of 20 V and pulse wave frequency of 8.5 MHz has been represented in **Figure 5.8e** where the average velocity was found to be 2.2×10^{-2} m s^{-1}. The numbers 0-6 represent the position of the nanomotors at t = 0 s, 1.5 s, and 3 s, respectively. Additionally, the linear motion of AA loaded motors towards stressed HEK-293 cell lines and their attachment to the cell surface has been represented in **Figure 5.8f.**

The intracellular motion of the AA-Teabots was recorded under the influence of acoustic sine waveform with PBS buffer of pH 7.4 in oxidative damaged HEK-293 cell lines. The AA-Teabots could be targeted towards the cells under the influence of ultrasonic waves and undergo release of bound ascorbic acid inside the cells, protecting them from stress-induced damage by scavenging ROS.

However, the influence triangular wave decreased the average speed of the nanomotors to 1.51 x 10^{-2} m s-^{1} rendering a circular motion at around 10 s. The influence of the triangular wave decreased the average speed of the nanomotors to 1.51×10^{-2} m $s^{-1,}$ respectively rendering a circular motion at around 10 s, as shown in **Figure 5.9a.**

At 8.5 MHz, the nanomotors exhibited a maximum average velocity (V_{av}) of 1.51 × 10^{-2} m s^{-1} for a triangular wave. Additionally, the direction of acoustic waves could be altered by placing a small area of the hollow lid on the transducer such that an uneven distribution of ultrasonic sine waves could be introduced on the surface of nanomotors. The highly stable AA-Teabots could convert the applied acoustic energy into mechanical energy achieving spontaneous linear motion. The average velocity of the AA-Teabots undergoing linear motion was calculated under the influence of triangle waveform at 8.5 MHz considering their displacements at *t* = 0 s and 8 s, represented in **Figure 5.9b.**

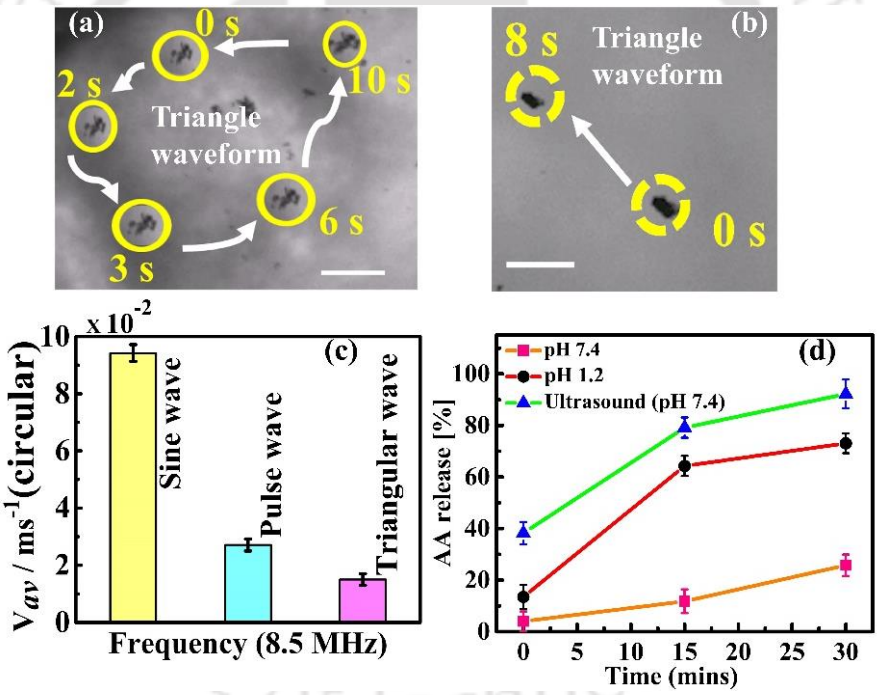

Figure 5.9. (a) US propelled circular motion of AA-Teabots under the influence of a triangular waveform (8.5 MHz) in PBS buffer of pH 7.4. The numbers 0-10 represent the position of the nanomotors at *t* = 0 s, 2 s, 3 s, 6 s, and 10 s, respectively. Scale bar is 50 µm. **(b)** US propelled linear motion of AA-Teabots under the influence of triangle waveform (8.5 MHz) in PBS buffer of pH 7.4. The numbers 0-8 represents the position of the nanomotors at *t* = 0 s and 8 s, respectively. Scale bar is 50 µm. **(c)** Bar graph depicting the maximum average velocities (V_{av}) of AA-Teabots exhibiting circular motion in the presence of sine, pulse, and triangular ultrasonic waveform at 8.5 MHz at 20 V. **(d)** % release of AA from AA-Teabots under the influence of ultrasonic sine wave of 8.5 MHz.

The V_{av} was found to be lowest in the triangular wave (1.29×10^{-2} m s^{-1}), which matches the observed V_{av} of AA-Teabots following a circular path. Comparatively, there was a significant reduction in the maximum V_{av} of linearly moving AA-Teabots w.r.t their circular locomotion. Thus, the optimum frequency of ultrasonic waves was considered to be 8.5 MHz, beyond which the velocity decreases in the presence of a sine wave, shown in **Figure 5.9c**. The % release of AA was also studied under the influence of a sine ultrasonic waveform of 8 MHz for a fixed time interval. The retrieved pellets were dispersed in PBS and exposed to ultrasound waves for 10 min. The solution was then centrifuged, and the supernatant was analyzed spectrophotometrically for a comparative release study of bound AA.

Interestingly, the % release of bound AA was much found to be ~ 80% at the end of 10 min, which was much higher as compared to pH-dependent release at pH 7.4 and 1.2, as depicted in **Figure 5.9d.** Thus, the therapeutic range of ultrasound could lead to a dramatic enhancement in the percentage release of bound AA. Thus, using a therapeutic range of ultrasound triggers, highly accelerated propulsion of AA-Teabots could be realized, leading to a dramatic enhancement in percentage release of bound AA. The possible factors for regulating release rates include ultrasound exposure parameters, the molecular weight of the loaded drug, material density, geometry, and type of polymeric matrix.[15] The mechanism behind deploying incorporated drugs from the carriers using a therapeutic range of ultrasound has been reported to be acoustic activation. However, the detailed manner by which such effects are created due to an interaction between generated bubbles and drug carriers is still unexplained.[16–19]

5.3.4. Anti - Amyloidogenic Studies

The formation of amyloid fiber was confirmed by collecting the samples after 72 h of amyloid growth followed by measuring The ThT selectively binds with amyloid fibrils giving strong fluorescence upon binding.[50-52] The effect of different concentrations of Teabots and AA-Teabots on the growth of amyloid formation has been investigated.

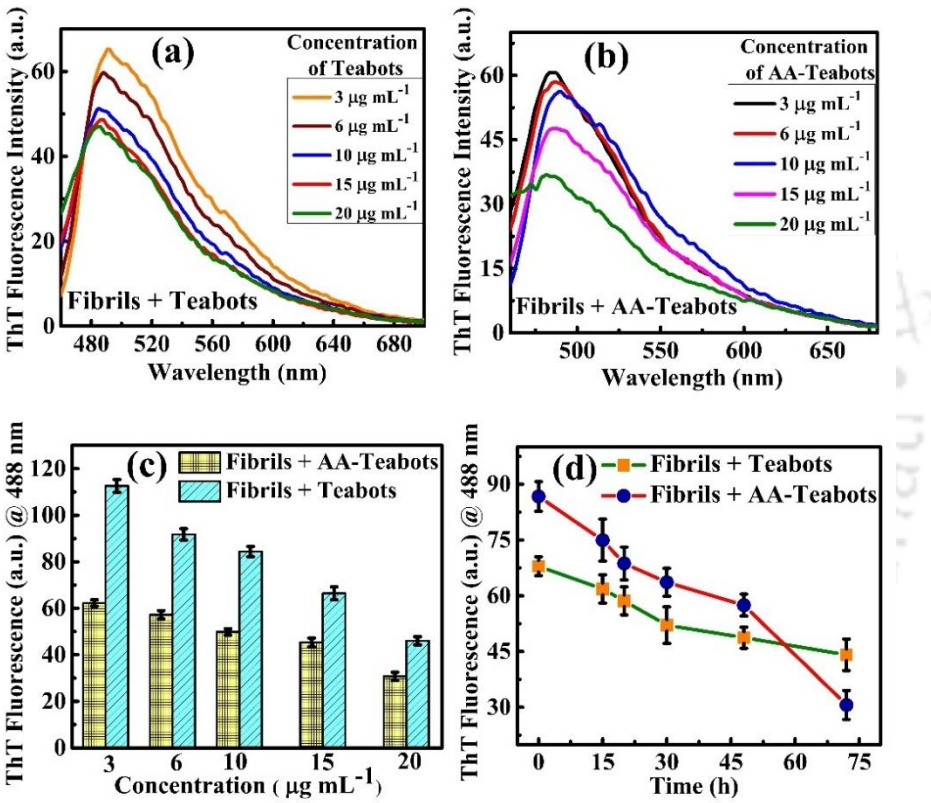

Figure 5.10. (a) Thioflavin-T assay of amyloid samples in presence of different concentrations (3-20 μg mL^{-1}) of **(a)** Teabots and **(b)** AA-Teabots. **(c)** Bar graph depicting the disintegration of amyloid fibrils in presence of different concentrations (3-20 μg mL^{-1}) of Teabots and AA-Teabots. **(d)** Changes in Thioflavin-T intensity of Teabots and AA-Teabots at a concentration of 20 μg mL^{-1}.

The disintegration of the matured fibrils was studied by administering 3 μg mL^{-1} to 20 μg mL^{-1} of the nanomotors in 20 μL protein solution followed by incubation for 72 h at 60°C. Upon analyzing the samples, it was observed that the intensity of ThT decreased gradually

with an increase in concentrations of Teabots and AA-Teabots, where AA-Teabots caused the maximum intensity drop. **Figures 5.10a** and **5.10b** confirmed the disappearance of amyloid fibrils as the ThT signal became negligible with an increase in the concentration of Teabots and AA-Teabots, respectively. However, from **Figure 5.10c**, the results convincingly proved that AA-Teabots (20 µg mL^{-1}) could offer the best performance in the dissolution of the model fibrils as compared Teabots, confirmed by the highest reduction of ThT fluorescence. This finding revealed that encapsulation of anionic AA on the surface of Teabots contributed to attain better performance than Teabots in disintegrating matured amyloid fibrils, indicating low contents of cross β-sheets.[53,54] The ThT assay revealed the disappearance of fibrils as time progressed with a gradual decrease in ThT fluorescence. At the same time, AA-Teabots proved to be more efficient in fibrillar disintegration at the end of 72 h owing to higher intensity drop, as represented in **Figure 5.10d.**

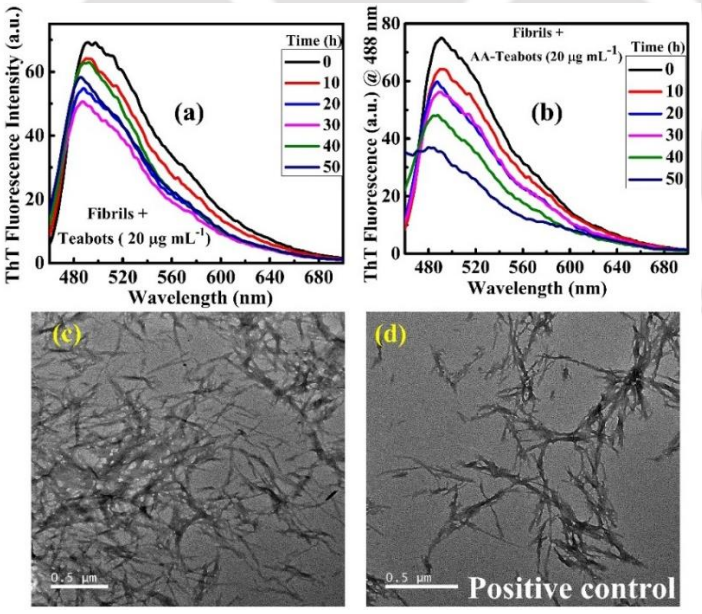

Figure 5.11. (a) Thioflavin –T assay of amyloid samples in presence of 20 µg mL^{-1} of **(a)** Teabots and **(b)** AA-Teabots at different time intervals (0-72 h). FE-TEM images of **(c)** control mature amyloid fibrils and **(d)** 70% Ethanol (positive control) + amyloid fibrils.

Further, the effect of a fixed concentration of Teabots and AA-Teabots (20 µg mL^{-1}) on mature HEWL was investigated by incubating them at varied time intervals (0 – 72 h) under standard conditions and monitoring the ThT fluorescence intensity of the samples at different time intervals (0 - 72 h), as shown in the **Figures 5.11a** and **b,** for Teabots and AA-Teabots, respectively. The ThT assay revealed the disappearance of fibrils as time progressed with a gradual decrease in ThT fluorescence, while AA-Teabots proved to be more efficient in fibrillar disintegration at the end of 72 h owing to higher intensity drop. The FETEM micrographs of control amyloid fibrils and fibrils treated with 70% ethanol (positive control) have been depicted in **Figures 5.11c** and **Figure 5.11d**, respectively.[15] Complete dissolution of long matures fibrils could be observed after ethanol treatment that was almost identical to those obtained from treatment with AA-Teabots.

Accordingly, it could be confirmed that at a concentration of (20 µg mL^{-1}), AA-Teabots can perform better than Teabots in disintegrating matured amyloid fibers due to twin-benefits of both AA and Teabots. Further, the formation of fibrils and their disintegration using Teabots and AA-Teabots (20 µg mL^{-1}) were imaged by FETEM after 72 h incubation. The micrographs of long matured fibrils formed in the absence of any nanomotors were considered as control, shown in **Figures 5.12 (i, iii** and **v)**. The disintegration of long amyloid fibers using free AA (17.6 µg mL^{-1}), Teabots, and AA-Teabots (20 µg mL^{-1}) has been represented in **Figures 5.12 (ii, iv,** and **vi)**, respectively. The results indicated that the length of the amyloid fibrils in the presence of AA-Teabots was significantly reduced than those of Teabots treated fibrils. The fibrils treated with free AA and Teabots exhibited aggregation and minor disintegration in some regions. Conversely, the matured fibrils treated with AA-Teabots got fragmented into shorter pieces that could be considered more effective in reducing amyloid cytotoxicity.

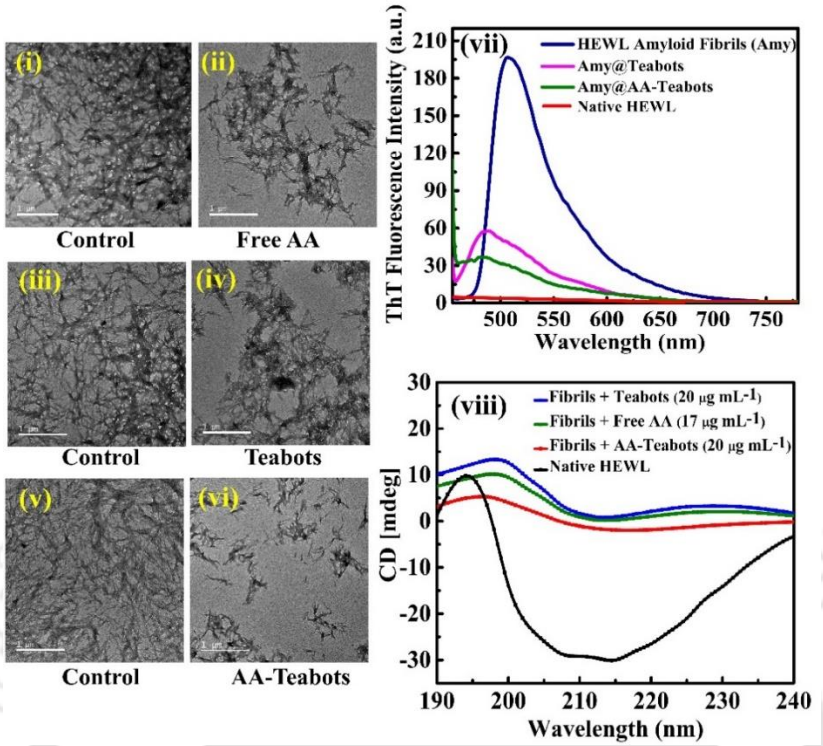

Figure 5.12. FETEM micrographs showing the control long amyloid fibres **(i, iii** and **v)** and the degradation effect of free AA, Teabots and AA-Teabots on mature amyloids **(ii, iv** and **vi)** at a concentration of 20 μg mL^{-1}. **(vii)** ThT fluorescence of HEWL fibrils (blue), native HEWL (red), fibrils treated with Teabots (pink) and AA-Teabots (green). **(viii)** CD spectral analysis of native HEWL (black) and influence of free AA, Teabots and AA-Teabots on mature HEWL fibrils at a concentration of 20 μg mL^{-1}.

As shown in **Figure 5.12 (vii)**, the ThT fluorescence intensity of the formed amyloid fibrils (blue line) was dramatically increased as compared to the free native HEWL (red line) that confirmed the presence of high cross β-sheets contents in formed amyloid fibres. Negligible ThT fluorescence could be observed from the native HEWL due to the absence of amyloid fibrillation. The structural analysis of the native HEWL and treated HEWL fibrils was performed using CD spectroscopy to monitor any alterations in secondary structures associated with fibrillation of the protein. For instance, as represented in **Figure 5.12 (viii),** the presence of a negative peak at 218 nm and 193 nm indicated the formation of β-sheet structures and random coil.

Sample	% β-sheet
HEWL (Native)	19.7
Fibrils	69.4
HEWL Fibrils + Free AA	42.8
HEWL Fibrils + Teabots	53.6
HEWL Fibrils + AA-Teabots	25.2

Table 5.2: % β-sheets of native HEWL, mature fibrils, and treated loose amyloid fragments with different samples.

The representative CD spectra of HEWL fibrils in the presence of AA-Teabots (20 µg mL^{-1}) showed a significant fall in mdeg value at 208 nm and 218 nm, indicating that the amyloid protein did not form a β-sheet structure and disappearance of long fibrillar species along with the increase in helicity. **Table 5.2** display the percentage of β-sheet content of native HEWL and amyloid fibrils after treatment with free AA (17.6 µg mL^{-1}), Teabots, and AA-Teabots. As expected from the other results, AA-Teabots could lower the % β-sheet to 25.2% that is almost close to native HEWL (19.7%) and much lesser than untreated amyloid fibrils (69.4%).

The results also revealed the presence of a monomeric form of HEWL fibrils with a concomitant decrease in β- sheet structures found to possess the highest reduction in the case of AA-Teabots as expected. In contrast, the presence of respective signals from the secondary structures revealed incomplete dissolution of fibrils using Teabots (20 µg mL^{-1}). The % relative lowering in the β-sheet content is ~ 20% in the presence of AA-Teabots (20 µg mL^{-1}) in comparison with Teabots, which proved the inhibition of predominant β-sheet structures. Perturbation of cross-linked β- sheets might be because of the hydrophobic interactions of polyphenols present in Teabots, interactions via specific amino acid residues, and flat aromatic structures of AA with aggregated amyloid structures.[53]

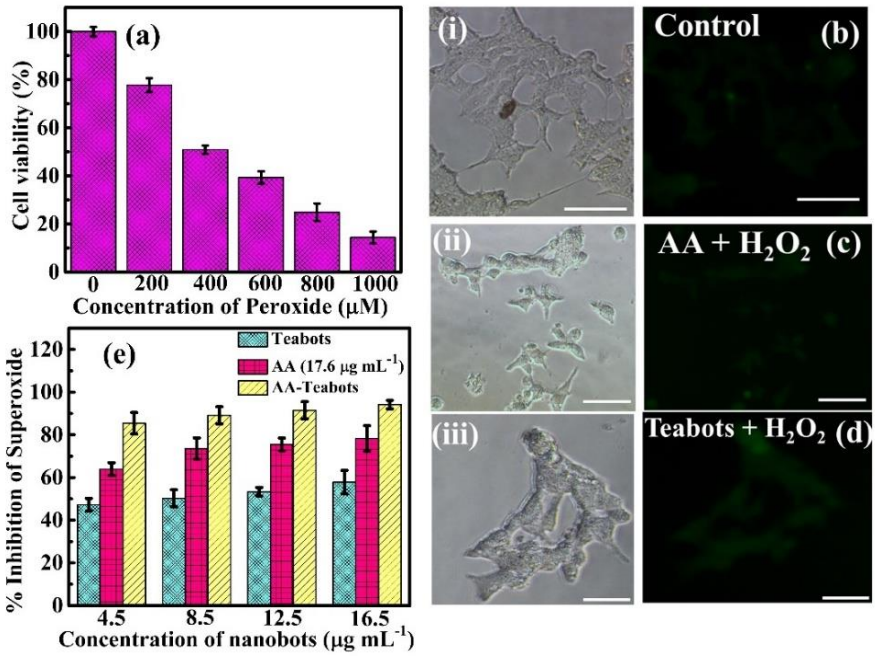

Figure 5.13. (a) Effect of different concentrations (0 to 1000 µM) of H_2O_2 on HEK-293 cells using Alamar blue (AB) assay. Images recorded by an epi-fluorescence microscope under UV excitation of 340 – 380 nm. **(i, ii** and **iii)** Bright field images; **(b, c** and **d)** Fluorescence images of control, H_2O_2 (400 µM) + AA (17.6 µg mL^{-1}) and H_2O_2 (400 µM) +Teabots (12.5µg mL^{-1}) treated cells, respectively. The scale bar is 100 µm. **(e)** *In vitro* superoxide scavenging activities of free AA, Teabots and AA-Teabots.

It is also possible that all these types of interactions could be responsible for reducing the extent of fibrillation and changes in the secondary structure of fibrils.[53-55] The optimum concentration of H_2O_2 to induce oxidative stress in HEK-293 cell lines was achieved by incubating different concentrations (0 to 1000 µM) of H_2O_2 for 5 h at 37°C, and the cell viability assay using AB was performed, as described earlier.

Figure 5.13a shows that there was a significant reduction in the percentage viability of the cells with peroxide loading. The data showed that cell viability was reduced to 50 ± 5% in 400 µM H_2O_2 – a treated group of cells and nearly abolished the cell survival at 900 µM H_2O_2. H_2O_2 induced oxidative damage of cells were proven at a concentration where the cell viability was reduced to 50 – 70%. Hence, the treatment of 400 µM H_2O_2 (13.6 µg mL^{-1}) for 5 h was chosen for further experiments.

Figure 5.13b displays the control cells treated with 1 mM DCF-DA that revealed negligible intensity exhibiting negligible intracellular ROS. Peroxide induced stressed cells treated with free AA (17.6 µg mL^{-1}) display less fluorescence than that of cells treated with Teabots (12.5 µg mL^{-1}), as shown in the **Figures 5.13c** and **d.** The above images validated the fact that free AA could scavenge more ROS than unbound Teabots but exhibited lesser scavenging activity than AA-Teabots. The corresponding bright-field images have been represented in **Figures 5.13 (i), (ii)** and **(iii).**

Additionally, the superoxide scavenging activity of the nanomotors was also investigated at varying concentration range (4.5 – 16.5 µg mL^{-1}) and compared with free AA (17.6 µg mL^{-1}) using PBS-NBT reduction assay.[66] As expected, with an increase in concentration, AA-Teabots exhibited ~ 90 ± 4.5 % inhibition of superoxide anions confirming potent superoxide quenching activity of AA-Teabots. Additionally, Teabots and free AA displayed good scavenging activity (60 ± 10%) in a dose-dependent manner, shown in **Figure 5.13e.** Henceforth, AA-Teabots exhibited excellent antioxidant activities under *in vitro* conditions as well, when compared with standard free AA.

The above results validated the degradation of toxic amyloid fibrils by AA-Teabots thus possibly reducing the amyloidogenic cytotoxicity. In order to analyze the cytotoxicity of free AA (17.6 µg mL^{-1}), Teabots and AA-Teabots, Alamar blue (AB) based *in vitro* cell viability assay were performed on HEK-293 cells. From the binding efficiency calculations, it was determined that AA-Teabots contained 4.4 µg mL^{-1} of loaded AA on their surface.

It was observed that the number of viable cells decreased with an increment in concentrations of nanomotors. Additionally, AA-Teabots proved to be highly non-toxic 4.5 µg mL^{-1}, achieving ~95% cell viability that gradually reduced to ~90% at a concentration of 12.5 µg mL^{-1}, shown in **Figure 5.14a**.

Comparatively, the cell viability of Teabots was found to be ~80% within the defined concentration range. For free AA, ~73% of viable cells were observed, thereby indicating minimal contribution in cellular toxicity. Thus, it was seen that the percentage of cell viability was high for AA-Teabots compared to Teabots in studied concentration range, and therefore AA-Teabots could be a better option for sustained intracellular delivery of AA.

In this study, the H_2O_2 induced oxidative injured HEK-293 cell model was used to investigate the protective effects of AA-Teabots at the cellular level. In order to achieve the ideal H_2O_2 treated level; different concentrations (0 to 1000 µM) of H_2O_2 to HEK-293 cells was exposed for cell viability studies. After that, the oxidative stress inhibitory effect of AA-Teabots, Teabots, and free AA was investigated against oxidative stress-induced damage in HEK-293 cell model. The cells were pre-treated with AA (17.6 µg mL^{-1}) and nanomotors (0 – 12.5 µg mL^{-1}) for 24 h. Then 400 µM H_2O_2 was exposed to the cells for 5 h and cell cytotoxicity was investigated using AB assay.

Figure 5.14b showed that the cell viability was reduced to ~50% after their exposure to 400 µM H_2O_2 for 5 h. However, the cell viability was restored to ~60 ± 5% and 80 ± 2.55 % after the cells were exposed to the varied range of Teabots and AA, respectively. Comparatively, the best protective effect could be observed using 12.5 µg mL^{-1} of AA-Teabots where the cell viability was restored to 93%. These results signified that AA-Teabots (12.5 µg ml^{-1}) could protect cells from H_2O_2 -induced oxidative stress by inhibiting intracellular ROS generation. Consequently, from the above data, it can be presumed that AA-Teabots could down-regulate ROS accumulation and protect cells from oxidative damage. In order to prove this hypothesis, the intracellular levels of ROS in H_2O_2 – treated HEK-293 cells were evaluated using 1 mM DCFH-DA fluorescent stain.

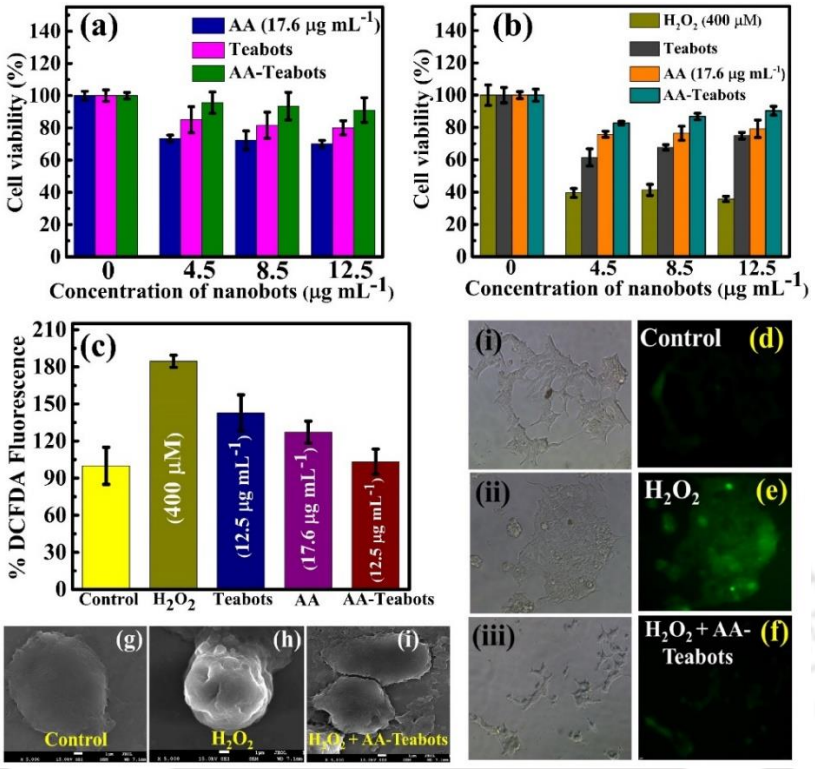

Figure 5.14. Effect of Teabots and AA-Teabots on HEK-293 intracellular ROS. **(a)** The Alamar blue (AB) assay representing cell viability of HEK-293 cells treated with free AA (17.6 µg mL^{-1}), Teabots and AA-Teabots with a concentration range of with respect to control cells (4.5 – 12.5 µg mL^{-1}) for 24 h. **(b)** Protective effect of free AA, Teabots and AA-Teabots on H_2O_2 – induced oxidative damage in HEK-293 cells. The cell viability was assessed by AB assay after treating with 400 µM of H_2O_2. **(c)** % DCF-DA fluorescence of the cells measured with microplate reader where the fluorescence in the control group was designated as 100%, which was used to measure the relative fluorescence intensity of cells in the other groups. Data has been expressed as the mean ± SD of triplicate experiments. Images recorded by an epi-fluorescence microscope under excitation of 340 – 380 nm. **(i, ii** and **iii)** Bright field images; **(d, e** and **f)** Fluorescence images of control, H_2O_2 treated (400 µM) and H_2O_2 (400 µM) + AA-Teabots (12.5 µg mL^{-1}) treated cells, respectively. Scale bar is 100 µm. Field Emission Scanning Electron Microscope (FESEM) micrographs of **(g)** Control cells; **(h)** H_2O_2 – induced oxidative damage (400 µM) in HEK-293 cells and **(i)** H_2O_2 (400 µM) with AA-Teabots (12.5 µg mL^{-1}) treated cells.

The results indicated that the intensity of DCF fluorescence in H_2O_2-treated group was significantly increased to 180 ± 7.39% compared to the control cell group while the fluorescence intensity was drastically reduced 130 ± 5% and 120 ± 10%, respectively, in HEK-293 cells pre-treated with Teabots and free AA **(Figure 5.14c)**. As expected, the cells

treated with AA-Teabots (12.5 µg ml^{-1}) showed the highest ROS scavenging activity with a significant reduction of fluorescence intensity up to 80 ± 10%. The results helped in inferring that indeed the AA-Teabots could suppress intracellular ROS generation and restore H_2O_2 triggered loss inside HEK-293 cells.

Following this, the treated cells were imaged under an epifluorescence microscope under green excitation of 340 – 380 nm. The corresponding bright-field images of control and treated cells have been represented in **Figures 5.14 (i), (ii)** and **(iii)**. The control HEK -293 cells, in **Figure 5.14d,** on treatment with DCFH displayed negligible green fluorescence due to the absence of intracellular ROS species. **Figure 5.14e** shows that the exposure of HEK-293 cells to 400 µM H_2O_2 increased the intensity of DCF green fluorescence displaying an abnormal cell morphology. This confirmed the generation of a large amount of ROS upon H_2O_2 treatment.

However, the cells treated with AA-Teabots displayed slightest green fluorescence, which was nearly identical to the control cells indicating a reduction of ROS to normal levels, as shown in **Figure 5.14f**. Peroxide induced stressed cells treated with free AA (17.6 µg mL^{-1}) and Teabots (12.5 µg mL^{-1}) were analyzed (refer to Figure 5.13b-d) with bright-field images [refer to Figure 5.13 (i) - (iii)]. These pictorial representation results were also in agreement with the graphical representation of DCF fluorescence intensity, as described in Figure 5.14c. Taken together, these results implied that AA-Teabots could significantly reduce the levels of peroxide-induced ROS generation to sustain a balanced cellular redox status associated with the antioxidant activity of bound AA on the Teabots. Additionally, the superoxide scavenging activity of the nanomotors was also investigated at varying concentration range (4.5 – 16.5 µg mL^{-1}) using PBS-NBT reduction assay.[65,66]

AA-Teabots exhibited ~ 90 ± 4.5% inhibition of superoxide anions confirming potent superoxide quenching activity of AA-Teabots (refer to **Figure 5.13 e**). Besides, FESEM micrographs of HEK-293 cells undergoing H_2O_2 exposure revealed the apoptotic phenotype, while AA-Teabots protected the cells from H_2O_2 induced phenotype alterations, as shown in **Figures 5.14 (g)** to **(i)**.

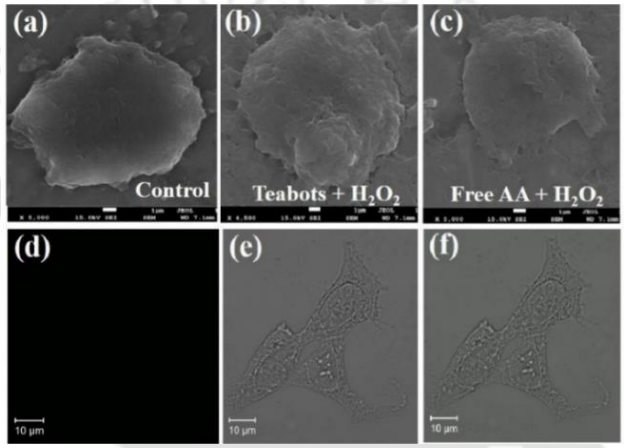

Figure 5.15. Field Emission Scanning Electron Microscope (FESEM) micrographs of **(a)** Control cells; **(b)** H_2O_2 (400 µM) +Teabots (12.5 µg mL^{-1}) and **(c)** H_2O_2 (400 µM) +AA (17.6 µg mL^{-1}) treated cells. Confocal microscopy images of control cells showing, **(d)** Fluorescence image, **(e)** Bright field image and **(f)** Merged image.

The FESEM micrographs revealed the effect of free AA and Teabots on the peroxide-induced stressed cells, depicted in the respective **Figures 5.15 a, b** and **c.** It could be observed that free AA and Teabots could protect the cells from H_2O_2 induced oxidative damage to some extent, however, relatively lesser than AA-Teabots. The confocal images of control cells with no fluorescence have been shown in **Figure 5.15 d, e,** and **f**. The cells were not treated with any FITC labeled fluorescent samples because of which no green fluorescence was observed. To determine the uptake of AA-Teabots by HEK-293 cells, they were conjugated with fluorescent dye FITC by electrostatic interaction.

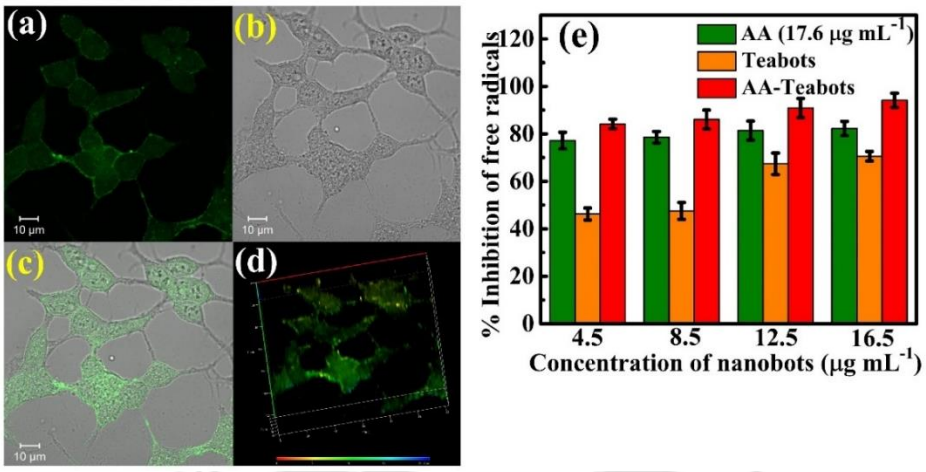

Figure 5.16. Confocal microscopic images. **(a)** Bright-field image, **(b)** fluorescence image, **(c)** merged image and **(d)***z*-stack image of HEK-293 cells treated with FITC labeled AA-Teabots (fAA-Teabots), which depicts the intracellular localization of AA-Teabots. **(e)** DPPH radical scavenging activity.

The ζ-potential of AA-Teabots was found to be around 1.92 ± 0.8 mV that could easily bind to negatively charged FITC (- 5.2 ± 3 mV). The fAA-Teabots exhibited a ζ- potential of about 0.23 ± 0.3 mV. Subcellular localization fAA-Teabots was observed from CLSM micrographs, as depicted in **Figure 5.16.** The bright-field image of HEK-293 cells treated with FITC labeled AA-Teabots was captured, as shown in **Figure 5.16a.** The fluorescence CLSM micrographs in **Figure 5.16b** revealed the uptake of fAA-Teabots into HEK-293 cells as indicated by the green fluorescence arising due to fAA-Teabots.

The merged images in **Figure 5.16c** revealed that the fAA-Teabots were efficiently inoculated by the cells, which was essential for ROS scavenging activity. The depth projection of the confocal micrograph of fAA-Teabots revealed the intracellular intake of AA-Teabots, as presented in **Figure 5.16d.**

The *in vitro* antioxidant assays were carried out using DPPH and PMS-NBT reduction systems to evaluate the free radical quenching activity of free AA, Teabots and AA-Teabots. An odd electron in the nitrogen atom of DPPH reduced to form a yellow colored hydrazine

molecule.[66] The concentration-dependent scavenging activity of free AA (17.6 µg mL^{-1}), Teabots and AA-Teabots (4.5 – 16.5 µg mL^{-1}) have been shown in **Figure 5.16e.** The plot suggests that the AA-Teabots were more effective than free AA and Teabots, leading to 90 ± 2.5% inhibition of free radicals. The results helped in inferring that the AA-Teabots exhibited excellent antioxidant activities under in vitro conditions as well when compared with standard free AA.

5.4. Conclusions

In conclusion, ultrasound-propelled ascorbic acid loaded nanomotors have been deisgned, namely AA-Teabots, from *Camellia sinensis*, which could offer efficient loading, localized transport, and release capabilities of therapeutic payloads for anti-oxidative and anti-amyloidogenic responses. Multiple acoustic waveforms were examined to study the conversion of acoustic energy into different propulsion behaviors of the drug-loaded Teabots. Our findings suggested that the material density of the motors along with the direction of ultrasound plays an important role in their motility. Such observations propose further research to understand the physics behind nanomotor propulsion in the presence of acoustic waveforms involving linear and viscous forces. Additionally, AA-Teabots could protect the HEK-293 cells from peroxide-induced oxidative damage by reducing intracellular ROS. Moreover, the AA-Teabots could efficiently disintegrate the matured amyloid structures into nontoxic loose aggregates.

While these initial proof-of-concept revealed the benefits of using Teabots to carry active ascorbic acid for inhibition of oxidative stress and amyloid cytotoxicity, major efforts are required to further evaluate the therapeutic advantages of such acoustically driven biocompatible drug delivery system (AA-Teabots). Future research efforts will aim at the

clinical interpretation of our preliminary results addressing major challenges such as *in vivo* activity of AA-Teabots steering through the bloodstream, overcoming the blood-brain barrier, and retaining active transport properties on forthcoming theranostic systems with precious targeting. Concisely, the remarkable performances and capabilities of such ultrasound driven AA-Teabots proposing advanced fuel-free propulsion and sustained drug release could open the door to a wide range of biomedical tasks and applications.

References

(1) Gao, W.; Wang, J. Synthetic micro/nanomotors in drug delivery. *Nanoscale* **2014**, 6, 10486–10494.

(2) Medina-Sánchez, M.; Xu, H.; Schmidt, O.G. Micro- and nano-motors: the new generation of drug carriers. *Ther. Deliv.* **2018**, 9, 303-316.

(3) Garcia-Gradilla,V.; Orozco, J.; Sattayasamitsathit, S.; Soto, F.; Kuralay, F.; Pourazary,A.; Katzenberg, A.; Gao, W.; Shen, Y.; Wang, J. Magnetically Guided Nanomotors: Toward Practical Biomedical Applications.*ACS Nano* **2013**, 7, 9232-9240.

(4) Chi, Q.; Wang, Z.; Tian, F.; You, J.; Xu, S. A Review of Fast Bubble-Driven Micromotors Powered by Biocompatible Fuel: Low-Concentration Fuel, Bioactive Fluid and Enzyme. *Micromachines* **2018**, 9**,** 537-552.

(5) Jurado-Sánchez, B. Nanoscale Biosensors Based on Self-Propelled Objects. *Biosensors* **2018**, 8, 59-74.

(6) Campuzano, S.; Fernández de Ávila, B. E.; Yánez-Sedeño, P.; Pingarrón, J. M.; Wang, J. Nano/microvehicles for efficient delivery and (bio)sensing at the cellular level.*Chem. Sci.* **2017**,8, 6750-6763.

(7) Kim, K.; Guo, J.; Liang, Z.; Zhu, F. Q.; and Fan, D. E. Man-Made Rotary Nanomotors: A Review of Recent Development. *Nanoscale* **2016**, 8, 10471-10490.

(8) Xu, L.; Mou, F.; Gong, H.; Luo, M.; Guan, J. Light-driven micro/nanomotors: From fundamentals to applications. *Chem. Soc. Rev.* **2017**, 46, 6905-6926.

(9) Bhuyan, T.; Bhattacharjee, M.; Singh, A.; Ghosh, S.; Bandyopadhyay, D. Boolean-Chemotaxis of Logibots Deciphering the Motions of Self-Propelling Microorganisms. *Soft Matter* **2018**, 14, 3182-3191.

(10) Bhuyan, T.; Singh, A.; Dutta, D.; Unal, A.; Ghosh, S.; Bandyopadhyay, D. Magnetic Field Guided Chemotaxis of iMushbots for Targeted Anticancer Therapeutics.*ACS Biomater. Sci. Eng.* **2017**, 3, 1627-1640.

(11) Singh, A.; Mandal, T.; Bandyopadhyay, D. Magnetically Guided Chemical Locomotion of Self-Propelling Paperbots. *RSC Adv.* **2015**, 5, 64444-64449.

(12) Rao, K. J.; Li, F.; Meng, L.; Zheng, H.; Cai, F.; Wang, W. A Force to Be Reckoned With: A Review of Synthetic Microswimmers Powered by Ultrasound. *Small* **2015**, 11, 2836–2846.

(13) Calvo, P.; Manian, M.; Kagan, D.; Balasubramanian, S.; Cardona, M.; Flechsig, G.U.; Posner, J.; Wang, J. Electrochemically-triggered motion of catalytic nanomotors.*ChemCommun.* **2009**, 45, 4509-4511.

(14) Loget, G.; Kuhn, A. Electric field-induced chemical locomotion of conducting objects. *Nat. Commun.* **2011**, 2, 535-541.

(15) Carovac, A.; Smajlovic, F.; Junuzovic, D. Application of Ultrasound in Medicine. *Acta. Inform. Med.* **2011**, 19, 168-171.

(16) Gradilla, V.G.; Sattayasamitsathit, S.; Soto,F.; Kuralay, F.; Yardımcı, C.; Wiitala, D.; Galarnyk, M.; Wang, J. Ultrasound-Propelled Nanoporous Gold Wire for Efficient

Drug Loading and Release. *Small* **2014**, 10, 4154-4159.

(17) Frenkel, V. Ultrasound mediated delivery of drugs and genes to solid tumors. *Adv. Drug Deliv. Rev.* **2008**, 60, 1193-1208.

(18) Uygun, M.; Jurado-Sánchez, B.; Uygun, D. A.; Singh, V. V.; Zhang, L.; Wang, J. Ultrasound-propelled nanowire motors enhance asparaginase enzymatic activity against cancer cells. *Nanoscale* **2017**, 9, 18423-18429.

(19) Soto, F.; Wagner, G.L.; Gradilla, V.G.; Gillespie, K.T.; Lakshmipathy, D.R.; Karshalev, E.; Angell, C.; Chen, Y.; Wang, J. Acoustically propelled nanoshells. *Nanoscale* **2016**, 8, 17788-17793.

(20) Fernández de Ávila, B. E.; Angell, C.; Soto, F.; Ramirez, M. L.; Báez, D.; Xie, S.; Wang, J.; Chen, Y. Acoustically Propelled Nanomotors for Intracellular siRNA Delivery. *ACS Nano* **2016**, 10, 4997-5005.

(21) Hormigos, R. M.; Sánchez, B. J.; Escarpa, A. Labs-on-a-chip meet self-propelled micromotors. *Lab Chip* **2016**, 16, 2397-2407.

(22) Chen, X.; Wu, G.; Lan, T.; Chen, W. Autonomous micromotor based on catalytically pneumatic behavior of balloon-like MnOx–graphene crumples. *Chem. Commun*. **2014**, 50, 7157-7159.

(23) Garcia, M.; Orozco, J.; Guix, M.; Gao, W.; Sattayasamitsathit, S.; Escarpa, A.; Merkoci, A.; Wang, J. Micromotor-based lab-on-chip immunoassays. *Nanoscale* **2013**, 5, 1325-1331.

(24) Ma, X.; Katuri, J.; Zeng, Y.; Zhao, Y.; Sánchez, S. Surface Conductive Graphene-Wrapped Micromotors Exhibiting Enhanced Motion. *Small* **2015**, 11, 5023-5027.

(25) Orozco, J.; Mercante, L. A.; Pol, R.; .Mercoci, A. Graphene-based Janus micromotors for the dynamic removal of pollutants. *J. Mater.Chem.* A. **2016**, 4, 3371-78.

(26) Ezhilan, B.; Gao, W.; Pei, A.; Rozen, I.; Dong, R.; Jurado-Sanchez, B.; Wang, J.; Saintillan, D. Micro- and nano-motors for biomedical applications. *Nanoscale* **2015**, 7, 7833.

(27) Abdelmohsen, L. K. E. A.; Peng, F.; Tu, Y.; Wilson, D. A. Micro- and nano-motors for biomedical applications. *J. Mater. Chem. B.* **2014**, 2, 2395-2408.

(28) Mano, N.; Heller, A. Bioelectrochemical Propulsion. *J. Am. Chem. Soc*. **2005**, 127, 11574–11575.

(29) Zhang, F.; M-Uribe, R.; Gong, H.; Fernández de Ávila, B. E.; Gastelum, M. B.; Karshalev, E.; Nourhani, A.; Tong, Y.; Nguyen, B.; Gallot, M.; Zhang, Y.; Zhang, L.; Wang, J. A Macrophage–Magnesium Hybrid Biomotor: Fabrication and Characterization. *Adv. Mater*. **2019**, 31, 1901828.

(30) Wei, X.; Beltrán-Gastélum, M.; Karshalev, E.; Fernández de Ávila, B. E.; Zhou, J.; Ran, D.; Angsantikul, P.; Fang, R.H.; Wang, J.; Zhang, L. Biomimetic Micromotor Enables Active Delivery of Antigens for Oral Vaccination. *Nano Lett*. **2019**, 19, 1914-1921.

(31) Gu, Y.; Sattayasamitsathit, S.; Kaufmann, K.; Vazquez-Duhalt, R.; Gao, W.; Wang, C.; Wang, J. Self-propelled chemically-powered plant-tissue biomotors. *Chem. Commun.* **2013**, 49, 7307–7309.

(32) Ren, L.; Zhou, D.; Mou, Z.; Xu, P.; Huang, T. J.; Mallouk, T. E. Rheotaxis of Bimetallic Micromotors Driven by Chemical-Acoustic Hybrid Power. *ACS Nano* **2017**, 11, 10591-10598.

(33) Xu, T.; Gao,W.; Xu, L. P.; Zhang, X.; Wang, S. Fuel-Free Synthetic Micro-Nanomachines. *Adv. Mater*. **2017**, 29, 1603250.

(34) Polat, B.E.; Hart, D.; Langer, R.; Blankschtein, D. Ultrasound-Mediated Transdermal Drug Delivery: Mechanisms, Scope, and Emerging Trends. *J Control*. *Release*. **2011**, 152, 330-348.

(35) Gao, W.; Feng, X.; Pei, A.; Kane, C. R.; Tam, R.; Hennessy, C.; Wang, J. Bioinspired Helical Microswimmers Based on Vascular Plants. *Nano Lett.* **2013**, 14, 305-310.

(36) Wu, Z.; Fernández de Ávila, B. E.; Martin, A..; Christianson, C.; Gao, W.; Thamphiwatana, S. K.; Escarpa, A.; He, Q.; Zhang, L.; Wang, J. RBC micromotors carrying multiple cargos towards potential theranostic applications. *Nanoscale* **2015**, 7, 13680-13686.

(37) Hajiaghaalipour, F.; Kanthimathi, M. S.; Sanusi, J.; Jayakumar, R. White tea (Camellia sinensis) inhibits proliferation of the colon cancer cell line, HT-29, activates caspases and protects DNA of normal cells against oxidative damage. *Food Chem.* **2014**, 169, 401- 410.

(38) Nune, S.K.; Chanda, N.; Shukla, R.; Katti, K.; Kulkarni, R. R.; Thilakavathi, S.; Mekapothula, S.; Kannan, R.; Katti, K.V. Green nanotechnology from tea: phytochemicals in tea as building blocks for production of biocompatible gold nanoparticles.*J. Mater. Chem.* **2009**, 19, 2912–2920.

(39) Mukherjee, S.; Ghosh, S.; Das, D. K; Chakraborty, P.; Choudhury, S.; Gupta, P.; Adhikary, A.; Dey, S.; Chattopadhyay, S. Gold-conjugated green tea nanoparticles for enhanced anti-tumor activities and hepatoprotection — synthesis, characterization and in vitro evaluation . *J. Nutr. Biochem.* **2015**, 26, 1283–1297.

(40) Nimse, S.B.; Pal, D. Free radicals, natural antioxidants, and their reaction mechanisms. *RSC Adv.* **2015**, 5, 27986-28006.

(41) Circu, M. L.; Aw, T. Y. Reactive oxygen species, cellular redox systems and apoptosis. *Free Radic. Biol. Med.* **2010**, 48, 749–762.

(42) Wijeratne, S. S. K.; Cuppett, S. L.; Schlegel, V. Hydrogen Peroxide Induced Oxidative Stress Damage and Antioxidant Enzyme Response in Caco-2 Human Colon Cells. *J. Agric. Food Chem.* **2005**, 53, 8768–8774.

(43) Xia, T.; Yao, J.; Zhang, J.; Zheng, Y.; Song, J.; Wang, M. Protective effects of Shanxi aged vinegar against hydrogen peroxide-induced oxidative damage in LO2 cells through Nrf2-mediated antioxidant responses. *RSC Adv*. **2017**, 7, 17377-17386.

(44) Dong, F.; Wang, Y. Encapsulation of Vitamin C by A Double- Layer Zein/Chitosan Structure with Improved Stability and Controlled Release. *Int. Nanomed. Nanosurg.* **2016**, 2, 1-7.

(45) Chakraborty, A.; Jana, N. Vitamin C-Conjugated Nanoparticle Protects Cells from Oxidative Stress at Low Doses but Induces Oxidative Stress and Cell Death at High Doses.*ACS Appl. Mater. Interfaces.* **2017**, 9, 41807-41817.

(46) Alishahi, A.; Mirvaghefi, A.; Rafiee-Tehrani, M.; Farahmand, H.; Shojaosadati, S.; Dorkoosh, F.; Elsabee, M. Shelf life and delivery enhancement of vitamin C using chitosan nanoparticles. *Food Chem.* **2011**, 126, 935-940.

(47) Heo, H. J.; Lee, C. Y. Protective Effects of Quercetin and Vitamin C against Oxidative Stress-Induced Neurodegeneration. *J. Agric. Food Chem.* **2004**, 52, 7514–7517.

(48) Hardaway, C. M.; Badisa, R. B.; Soliman, K. Effect of ascorbic acid and hydrogen peroxide on mouse neuroblastoma cells. *Mol. Med. Report.* **2012**, 5, 1449-52.

(49) Siddique, Y. H.; Beg, T.; Afzal, M. Protective effect of ascorbic acid against oxidative damage induced by hydrogen peroxide in cultured human peripheral blood lymphocytes. *Indian J. Clin. Biochem.* **2009**, 24, 294–300.

(50) Hasanbasic, S.; Jahić, A.; Berbić, S.; Tušek-Žnidarič, M.; Zerovnik, E. Inhibition of Protein Aggregation by Several Antioxidants.*Oxid. Med. Cell Longev.* **2018**, *vol. 2018*, 1-12.

(51) He, X.; Giurleo, J. T.; Talaga, D. S.Role of small oligomers on the amyloidogenic aggregation free energy landscape.*J. Mol. Biol.* **2010**, 395, 134–154.

(52) Mahdavimehr, M.; Meratan, A. A.; Ghobeh, M.; Ghasemi, A.; Saboury, A. A.; Nemat-Gorgani, M. Inhibition of HEWL fibril formation by taxifolin: Mechanism of action. *PLoS One.* **2017**, 12, e0187841.

(53) Pradhan, N.; Shekhar, S.; Jana, N. R.; Jana, N. R. Sugar-Terminated Nanoparticle Chaperones Are 10^2–10^5 Times Better Than Molecular Sugars in Inhibiting Protein Aggregation and Reducing Amyloidogenic Cytotoxicity. *ACS Appl. Mater. Interfaces.* **2017**, 9, 10554–10566.

(54) Debnath, K.; Pradhan, N.; Singh, B.; Jana, N.R.; Jana, N.R. Poly(trehalose) Nanoparticles Prevent Amyloid Aggregation and Suppress Polyglutamine Aggregation in a Huntington's Disease Model Mouse. *ACS Appl. Mater. Interfaces*. **2017**, 9, 24126-24139.

(55) Palmal, S.; Maity, A. R.; Singh, B. K.; Basu, S.; Jana, N.R.; Jana, N.R. Inhibition of Amyloid Fibril Growth and Dissolution of Amyloid Fibrils by Curcumin–Gold Nanoparticles. *Chem. Eur. J.* **2014**, 20, 6184–6191.

(56) Ban, D. K.; Paul, S. Nano Zinc Oxide Inhibits Fibrillar Growth and Suppresses Cellular toxicity of Lysozyme Amyloid. *ACS Appl. Mater. Interfaces.* **2016**, 8, 31587-31601.

(57) Palmal, S.; Jana, N. R.; Jana, N. R. Inhibition of Amyloid Fibril Growth by Nanoparticle Coated with Histidine-Based Polymer. *J. Phys. Chem. C.* **2014**, 118, 21630–21638.

(58) Ghosh, S.; Pandey, N.; Dasgupta,S.(−)-Epicatechingallate prevents alkali-salt mediated fibrillogenesis of hen egg white lysozyme. *Int. J. Bio. Macromol.* **2012**, 54, 90-98.

(59) Liu, J.; Chen, Z.; He, J.; Zhang, Y.; Zhang, T.; Jiang, Y. Anti-oxidative and anti-apoptosis effects of egg white peptide, Trp-Asn-Trp-Ala-Asp, against H_2O_2-induced oxidative stress in human embryonic kidney 293 cells. *Food Func.* **2014,** 5, 3179-3188.

(60) Baschieri, A.; Amorati, R.; Benelli, T.; Mazzocchetti, L.; D'Angelo, E.; Valgimigli, L. Enhanced Antioxidant Activity under Biomimetic Settings of Ascorbic Acid included in Halloysite Nanotubes. *Antioxidants* **2019**, 8, 30-47.

(61) Alishahi, A.; Mirvaghefi, A.; Rafiee-Tehrani, M.; Farahmand, H.; Shojaosadati, S.; Dorkoosh, F.; Elsabee, M. Shelf life and delivery enhancement of vitamin C using chitosan nanoparticles. *Food Chem.* **2011**, 126, 935-940.

(62) Rampersad, S. N. Multiple Applications of Alamar Blue as an Indicator of Metabolic Function and Cellular Health in Cell Viability Bioassays. *Sensors (Basel)* **2012**, 12, 12347–12360.

(63) Zachari, M.; Chondrou, P. S.; Pouliliou, S. E.; Mitrakas, A.; Abatzoglou, I.; Zois, C. E.; Koukourakis, M. I. Evaluation of the Alamar blue assay for adherent cell irradiation experiments. *Dose-Response* **2014**, 12, 246-258.

(64) Larina, I.; Evers, B. M.; Esenaliev, R. Optimal drug and gene delivery in cancer cells by ultrasound-induced cavitation. *Anticancer Res.* **2005**, 25, 149-156.

(65) Wacker, K.T.; Weems, A.C.; Lim, S. M.; Khan, S.; Felder, S. E.; Dove, A.P.; Wooley, K.L. Harnessing the Chemical Diversity of the Natural Product Magnolol for the Synthesis of Renewable, Degradable Neolignan Thermosets with Tunable Thermomechanical Characteristics and Antioxidant Activity. *Biomacromolecules* **2019**, 20, 109-117.

(66) Venkatachalam, U.; Muthukrishnan, S. Free radical scavenging activity of ethanolic extract of *Desmodiumgangeticum*. *J. Acute Med.* **2012**, 2, 36–42.

(67) Gröning, R.; Breitkreutz, J.; Baroth, V.; Müller, R. S. Nanoparticles in plant extracts: influence of drugs on the formation of nanoparticles and precipitates in black tea infusions. *Eur. J. Pharm. Sci.* **2002,** 15, 149-55.

(68) Said, R.B.; Hamed, A. I.; Mahalel, U. A.; Al-Ayed, A. S.; Kowalczyk, M.; Moldoch, J.; Oleszek, W.; Stochmal, A. Tentative Characterization of Polyphenolic Compounds in the Male Flowers of *Phoenix dactylifera* by Liquid Chromatography Coupled with Mass Spectrometry and DFT. *Int. J. Mol. Sci.* **2017**, 18, 512-530.

(69) Lin, L.-Z.; Chen, P.; Harnly, J. M. New Phenolic Components and Chromatographic Profiles of Green and Fermented Teas.*J. Agric. Food Chem.* **2008**, 56, 8130–8140.

(70) Bastos, D. H. M.; Saldanha, L. A.; Catharino, R. R.; Sawaya, A. C. H.F.; Cunha, I.B.S.; Carvalho, P.O.; Eberlin, M. N. Phenolic Antioxidants Identified by ESI-MS from Yerba Matén (*Ilex paraguariensis*) and Green Tea *(Camelia sinensis*) Extracts. *Molecules* **2007**, 12, 423-32.

(71) Comunian, T.; Thomazini, M.; Alves, A. J. G.; Junior, F. M.; Balieiro, J.; Favaro-Trindade, C. S. Microencapsulation of ascorbic acid by complex coacervation: Protection and controlled release. *Food Res. Int.* **2013**, 52, 373-379.

(72) Panicker, C. Y.; Varghese, H.T.; Philip, D. FT-IR, FT-Raman and SERS spectra of Vitamin C. *Spectrochim. Acta. A. Mol. Biomol. Spectrosc.* **2006,** 65, 802-804.

(73) Desai, K. G.; Liu, C.; Park, H. J. Characteristics of vitamin C immobilized particles and sodium alginate beads containing immobilized particles. *J Microencapsul.* **2005**, 22, 363-376.

भारतीय प्रौद्योगिकी संस्थान गुवाहाटी
Indian Institute of Technology Guwahati

CHAPTER 6

Magnetically Controlled Tea Microbots to Target Biofilms in a Kill-Clean Way

Contents

Abstract

Treatment of persistent biofilm infection is formidable, even with broad-spectrum antibiotic therapies. Thus, low-cost and intelligent micromachines may serve as an active mechanical means to dislodge such deleterious bacterial communities. Herein, biocompatible micromotors from Tea buds (T-Budbots) were designed that can be magnetically driven on the biofilm matrix to kill and remove the fragmented biofilm segments with precision, proposing a "Kill-Clean" strategy. With these principles, the design of a bactericidal robotic platform decorated with magnetite nanoparticles could be achieved aimed at clearing biofilm on the surfaces. The smart T-Budbots were capable of integrating antibiotic Ciprofloxacin (CIP) on their surface to increase their antibacterial efficacy against pathogenic bacterial communities of *Pseudomonas aeruginosa* and *Staphylococcus aureus*. It is noteworthy that the release of bound drug from the porous T-Budbots was triggered by the acidic environment of the biofilm. This work represents a first step in the involvement of a plant-based microbot exhibiting magneto-robotic therapeutic properties, providing a non-invasive and safe approach to dismantle harmful biofilm infections.

This chapter is under submission. I gratefully acknowledge the assistance of A. T. Simon, S. Maity, and Dr. A. K. Singh.

6.1. Introduction

Inside the endless evolution of medical science, the setup of aseptic conditions allowed the practicability of high-level surgeries, with the hope of low infection risk and safe healing.[1,2] In return, major hospital-borne infections have appeared due to the association of heterogeneous bacterial communities on the abiotic (implants and catheters) and biotic (teeth and mucosal) surface .[3-5] Moreover, bacterial outbreaks are pervasive in pipes, water lines, and industrial settings resulting in metallic corrosion.[6,7] Such syntrophic consortium, named biofilm, remains to be a survival strategy of microbes that are notoriously difficult for treatment and eradication.[8-11] An added concern is their high-level resistance towards current antibiotics because of a compact extracellular matrix that prevents aminoglycoside drugs from entering, leading to serious medical complications.[12-15]

Presently, antibacterial research has thus risen to prominence since traditional antibiotic therapies remain to be immensely ineffective towards biofilm destructions.[16-20] Current approaches for the treatment of infections in patients include repeated exposures of antibiotics[21], strong oxidants[22], antifouling nanoparticles[23], unbound liposomes[24,] and replacing the biofilm infected devices at times.[25] However, such anchored materials can only target biofilm at their interfaces, dependent on host circulation and become inactive with time due to adhesions with surface proteins.[26] Additionally, these targeted measures can be time-consuming, life-threatening at a higher dosage and costly in dealing with infected implanted devices, thus limiting their potency.[27,28] Clearly, new technologies need to be introduced for effective killing of the bacterial cells using low-dose therapy and simultaneous removal of disrupted biofilm using a dynamic system.[29,30]

One safe alternative relies on miniaturized robots powered by different chemical fuels and external stimuli that convert accessible energy into movement.[7,18,19,31] Until now, different types of nano/micromotors have been explored in a wide range of applications such as environmental remediation[32,33], sensing[34,35] and drug delivery to precision therapeutics.[36-39] Although several examples of self-propelled synthetic motors using heavy metals have been reported so far[40-44], only a few biodegradable motors exhibiting fuel-free actuation have been reported until now.[19,45-48]

To address the limitations of synthetic motors in biomedical tasks due to toxicity and expensive fabrication techniques[36,47], biocompatible motors using plant-tissues were developed for safe and cost-efficient antimicrobial therapeutics, exhibiting tether-free controlled motion by magnetic actuation. Under suitable conditions, magnetic actuation is an attractive approach because the magnetic field penetrates harmlessly inside the materials or fluids, allows controlled particle motion in confined areas exhibiting varied robotic motility.[36,37,43] To our knowledge, the implementation of magnetically actuated plant-based micromotors in biofilm disruption and removal has been reported for the first time.

The present work introduces magnetotactic microbots, namely T-Budbots, derived from Tea buds of *Camellia sinensis* that offers a sustained release of encapsulated drug and efficient destruction of free-floating bacteria and their biofilms. The enhanced antibacterial activity is attributed to the synergistic effect of Ciprofloxacin (CIP)-modified microbots (CIP@T-Budbots) and their continuum motion on the biofilm surface, which enhances microbot-bacteria interaction. It has been noted that strains of Gram-Negative *Pseudomonas aeruginosa* and Gram-positive *Staphylococcus aureus* are mostly opportunistic for pathogenic biofilm formations that promote chronic infectious diseases, renders ineffective

drug treatments and needs replacement of medical devices.[49-52] Moreover, the combined use of T-Budbots and drug CIP could fight emerging drug-resistance problems by improving the efficacy of free CIP. Such synergistic modification could address the challenges of the free drug that includes growing bacterial resistance, poor solubility, high dose side effects, and inadequate delivery systems for sustained release.[8,53-56]

Thus, fight against such pathogenic bacterial biofilm was conceivable by (i) killing the embedded bacteria using antibiotic (CIP) loaded T-Budbots; (ii) disturbing biofilm architecture to improve penetration of antibiotic; and (iii) removing the degraded matrix using magnetic field actuation by "**Kill-Clean**" approach. Such killing and cleaning modality of biodegradable T-Budbots coupled with magnetic actuation gains unprecedented potential for biofilm eradication, particularly in therapeutic and environmental applications.

6.2. Experimental Section

6.2.1. Materials

Tea buds (*Camellia sinensis*) were collected from Tea garden in IIT Guwahati. The experiments described below involves the use of the following chemicals as-purchased: chitosan (Sigma-Aldrich), phosphate buffer saline (PBS) (Himedia), ciprofloxacin HCl (CIP) (Sigma-Aldrich), magnetite nanoparticles (FeONPs) (Sigma-Aldrich), nutrient broth (NB) (Sigma-Aldrich), brain heart infusion (BHI) broth (Sigma-Aldrich), acridine orange (AO) (Himedia), propidium iodide (PI) (Himedia), Crystal Violet Stain (CV) (Himedia) and agar powder (bacteriological grade, Himedia). All the chemicals were of analytical grade and used without further purification. Milli-Q grade water (> 18 MΩ cm^{-1}, Millipore) was used to perform all the experimental procedures.

6.2.2. Methods

(a) Fabrication of magnetic ciprofloxacin-loaded T-Budbots (CIP@T-Budbots): Tea bud extract was prepared by grinding 30 g of buds and boiling in 150 mL of sterile water for 4 min. The obtained solution possessing suspended particles was separated in terms of size by differential centrifugation at 5000 rpm and 15000 rpm for 30 min and 1 h, respectively. Following this, the supernatant obtained after centrifugation at 5000 rpm for 30 min was re-centrifuged at 15000 rpm for 1 h. The basic reason behind such simplest form of centrifugation was to obtain the particles concerning their sizes at macro and microscale levels. The final pellet obtained after centrifugation at 15000 rpm was carefully retrieved, dried in a vacuum oven, and dispersed in sterile water. The size of the particles was investigated, and the micro-sized particles in the range of 50 µm – 160 µm were considered for further experiments. The microparticles (~5-6 mg) were incubated with 400 µL of 800 µg mL^{-1} of magnetite nanoparticles (FeONPs) and stirred properly in sterile water for 2 h. The solution was mixed with 0.7% chitosan and homogenized for 30 min at room temperature for attaining physiochemical stability. The mixture was filtered, and the obtained FeONPs- loaded microbots (T-Budbots) was washed thrice with 70% ethanol, followed by vacuum drying at 50°C for 2 h.

(b) Loading and release efficiency (%) of drug CIP: The as-obtained FeONPs- loaded microbots (T-Budbots) with varying concentrations of 1-6 mg were incubated in 300 µL of 30 mg mL^{-1} of Ciprofloxacin HCl (CIP) solution and stirred for 2 h at 37°C. Finally, the magnetic CIP- loaded microbots (CIP@ T-Budbots) were centrifuged for 5 min at 5000 rpm, to remove the unbound drug. Following this, the recovered pellets containing CIP – modified magnetic microbots were dispersed in distilled water. The supernatants containing

the unbound CIP were withdrawn, and the intensity of CIP molecules was analyzed by UV-visible spectrophotometric analysis at 278 nm. The Binding Efficiency was calculated using the formula:[8,36]

$$\boldsymbol{B.E.}(\%) = \frac{(CIP)_i - (CIP)_s}{(CIP)_i} \times 100. \quad (1)$$

Here, $(CIP)_i$ denotes the initial concentration of CIP in the solution, and $(CIP)_s$ indicates the concentration of unloaded CIP in the supernatant.

The amount of drug CIP released from 6 mg of CIP@T-Budbots was studied at different time intervals (0 min – 12 h) in acetate buffer of pH 4 and PBS buffer of pH 7.4. The pellets obtained after centrifugation of CIP-loaded motors were washed carefully with water and then dispersed in 100 µL of acetate buffer of pH 4 and PBS buffer of pH 7.4. The solution was incubated in the buffers at 37ºC up to 12 h followed by centrifugation, and the supernatants were collected. Finally, the intensity of CIP at 278 nm peak was recorded for the supernatants using UV-spectrophotometer. The % release was calculated using the formula[8,36]:

$$Cumulative\ Release\,(\%) = \frac{Drug\ release\ in\ supernant}{Drug\ loaded\ in\ microbot} \times 100. \quad (2)$$

(c) Antibacterial studies: The antibacterial activity of the microbots was screened against Gram-negative bacteria (*Pseudomonas aeruginosa* MTCC 2488) and Gram-positive bacteria (*Staphylococcus aureus* MTCC 96). *Pseudomonas aeruginosa* were grown in NB and *Staphylococcus aureus* were propagated in BHI followed by 12 h incubation at 37°C under shaking condition (180 rpm). The bacterial strains were treated with different concentrations of CIP@T-Budbots (where CIP concentration ranges from 50 to 120 µg mL^{-1}), free CIP (50 to 120 µg mL^{-1}), T-Budbots (50 to 120 µg mL^{-1}) and FeONPs (200 to 400

μg mL^{-1}). The optical density (OD) was recorded at 595 nm using a UV-visible spectrophotometer in triplicates to monitor bacterial growth.

Further, minimum inhibitory concentration (MIC) and minimum bactericidal concentration (MBC) were again confirmed by plating the bacterial strains of concentrations ~1×10^8 CFU mL^{-1} on agar media. The bacterial colonies treated with MIC and MBC of CIP@T-Budbots were spread-plated on the solidified media using L-rod. Similarly, the bacteria treated with MIC and MBC of free CIP, T-Budbots, and FeONPs were also plated and incubated at 37°C for 12 h.

In addition, the growth curve was analyzed for the bacterial strains after treating them with MIC and MBC of CIP@T-Budbots, T-Budbots, and free CIP, followed by monitoring the growth for 12 h at 37°C. The morphology of the untreated (control) and treated bacterial strains was observed by FETEM analysis.

(d) Crystal violet (CV) biofilm assay: The bacterial strains were diluted to 1×10^6 CFU mL^{-1} using the respective media from which 100 μL of *Pseudomonas aeruginosa* and 200 μL of *Staphylococcus aureus* cultures were added to a 96-well plate and incubated at 37°C in a static environment for 24 h. The wells were washed with PBS after followed by the addition of fresh media. After this, different concentrations of CIP@T-Budbots, free CIP, T-Budbots, and FeONPs (100 – 300 μg mL^{-1} for *Pseudomonas aeruginosa* biofilm and 80-140 μg mL^{-1} for *Staphylococcus aureus* biofilm) was added followed by 12 h incubation. Following this, the biofilm was stained with 0.01% crystal violet in fresh media and incubated for 15 min at 37°C in static condition. Wells with untreated biofilm and blank wells were used as controls. The crystal violet stain was dissolved in 95% ethanol, and the absorbance was recorded in triplicates at 595 nm using microplate reader. The statistical significance of the data was evaluated by one-way analysis of variance (ANOVA).

(e) Acridine orange (AO)/ propidium iodide (PI) dual staining assay: The bacterial strains were diluted to 1×10^6 CFU mL^{-1} using the respective media from which 100 µL of *Pseudomonas aeruginosa* and 200 µL of *Staphylococcus aureus* cultures were added to a 96-well plate and incubated at 37°C for 24 h in a static environment. After this, grown biofilm was treated with CIP@T-Budbots and free CIP at their minimum biofilm inhibitory concentration ($MBIC_{50}$) and incubated for 12 h. The biofilm was treated with 0.01 mg mL^{-1} of AO/PI stain and incubated in dark conditions. The imaging was carried out using confocal microscopy at an excitation wavelength of 495 nm for AO and 540 nm for PI.

(f) Magnetic actuation of CIP@T-Budbots for biofilm eradication: The motion-based experiments were carried out in a 6-well plate on which *Pseudomonas aeruginosa and Staphylococcus aureus* biofilm was grown at a concentration of 1×10^8 CFU mL^{-1}. The magnetic T-Budbots (50 µm – 100 µm) were introduced on the biofilms, and their magnetotactic motion was remotely controlled using a neodymium bar magnet generating a magnetic field of strength 0.01 T. Actuation was performed by introducing an aligned magnetic field to achieve a chosen motion pattern. The microbots were magnetized perpendicularly to their long axis or direction of travel for achieving linear motion on the surface of biofilm. Uniform rotating magnetic fields were generated by moving the magnet around an axis or center to drive the drug-loaded T-Budbots in a spinning arrangement. The T-Budbots could drill through the biofilm matrix, remove the degraded products, and the videos of the cleared area displaying the removal process were captured using a Leica upright microscope.

The displacement of the microbots in the presence of magnetic field was investigated by placing the 6-well plate on a paper grid of dimensions 1 mm × 1 mm. The velocity was measured after every ~ 1mm displacement of T-Budbots per unit time in one direction.[36] To

determine the position of magnetic T-Budbots, the videos were processed by extracting the image frames per second using Image J software. The rotational speed (ω) of the T-Budbots was measured by measuring the number of turns of the T-Budbots divided by time, specified as revolutions per minute (rpm).[57] In addition, the magnetotactic motion of T-Budbots in a petriplate filled with 6 mL of water was considered as control.

After cleaning of surface biofilm, the percentage viability of biofilm attached on the surface of microbots was calculated using CV assay, where untreated biofilm was considered as control. Additionally, the biomass of the T-Budbots before and after biofilm removal was measured and compared to confirm the adhesion of destroyed biofilm debris on their surface. This was done by measuring the weight of T-Budbots (~ 10 mg) before introducing them on the surface of the biofilm matrix. Simultaneously, the magnetically actuated T-Budbots were collected from the matrix after biofilm removal, and their biomass was measured for comparative analysis.

(g) FESEM analysis: The morphologies of both treated and control biofilm was studied using FESEM. During the analysis, the biofilms of *Pseudomonas aeruginosa and Staphylococcus aureus* was treated with CIP@T-Budbots at their $MBIC_{50}$ in 96-well plate and incubated at 37°C for 24 h in static condition. The biofilm was washed gently with PBS and fixed with 2.5% glutaraldehyde. The sample was allowed to dry in a glass slide covered with aluminum foil, air dried, sputter-coated with a gold film, and analyzed.

Also, the disruption of biofilm debris collected by magnetotactic CIP@T-Budbots was confirmed by using FESEM analysis to validate the killing and attachment of the biofilm matrix on the surface of microbots. The T-Budbots were recovered gently from the substrate, placed on an aluminum covered glass slide and allowed to dry in vacuum at room temperature for analysis.

(h) Equipment: The surface morphologies and size of the T-Budbots were examined by Field emission transmission electron microscope (FETEM, JEOL 2100F) and transmission electron microscope (TEM, JEOL JEM 2100). The microbots were sonicated in water and the drop-casted onto a carbon-coated copper TEM grid for drying. The elemental composition of the samples was analyzed by TEM- energy-dispersive X-ray spectroscopy (EDX, JEOL JEM 2100). A dynamic light scattering (DLS) based particle size analyzer was used to determine the ζ-potential of the samples.

The mass analysis of the samples was measured using Liquid Chromatography-Mass Spectrometer (LCMS, Waters; Model: Q-Tof Premier) in positive and negative detection mode with a desolavtion temperature of 400°C at 3.5 V. The UV visible spectrophotometer (JASCO V-630) was used to calculate the loading-release percentage of drug CIP and to monitor the bacterial growth. The chemical analysis of the T-Budbots was done using Raman spectroscopy (CPX 100) in the range of 400-3000 cm^{-1}. The magnetization curve of the magnetic samples was obtained by using vibrating sample magnetometer (VSM, Lakeshore magnetic systems 7410 series). The treated biofilms were imaged using confocal laser scanning microscope (ZEISS LSM 880). The surface of the free-floating bacteria and biofilm was examined by FESEM (Zeiss Sigma FESEM, Germany). A 15 μL of the sample was dropped on a glass side wrapped with aluminum foil, dried and sputtered with a gold film (SC7620"Mini", Polaron Sputter Coater, Quorum Technologies). The pH of the solutions was measured by pH meter (CyberScan pH 510, Eutech Instruments). The magnetically controlled motion of T-Budbots was recorded under a Leica DM 2500 upright microscope.

6.3. Results and Discussion

6.3.1. Fabrication and Characterization

Till date, significant research suggested the antimicrobial properties of Tea extract owing to the presence of several polyphenols, however the presence of active microparticles in the extract and their contributions need to be explored.[58-60] This has drawn our attention to isolate and investigate the contribution of microparticles from Tea buds of *Camellia sinensis*, particularly in robotic therapeutics. Surprisingly, the particles exhibited efficient drug loading capability, accelerated antibacterial killing, and could remove biofilm via magnetic actuation. The tea solution with suspended particles was separated in terms of size by differential centrifugation at 5000 rpm and 15000 rpm for 30 min and 1 h, respectively. Following this, the supernatant obtained after centrifugation at 5000 rpm for 30 min was re-centrifuged at 15000 rpm for 1 h to obtain the particles concerning their sizes at macro and microscale levels. The final pellet obtained after centrifugation at 15000 rpm was carefully retrieved, dried in vacuum oven, and dispersed in sterile water. The size of the particles was investigated, and the micro-sized particles in the range of 50 µm – 160 µm were considered for further experiments. Such inexpensive plant-based methods involving the use of non-toxic chemicals ensures the development of biocompatible and biodegradable microbots, thus lowers the chances of rejection by the immune system.[36,47]

The T-Budbots were navigated under the influence of magnetic field to kill the biofilm and drill out the debris from the surface, as represented schematically in **Figure 6.1(i-ii)**. The detailed experimental procedure for the fabrication of microparticles derived from Tea buds illustrated schematically in **Figure 6.1(a-e)**.

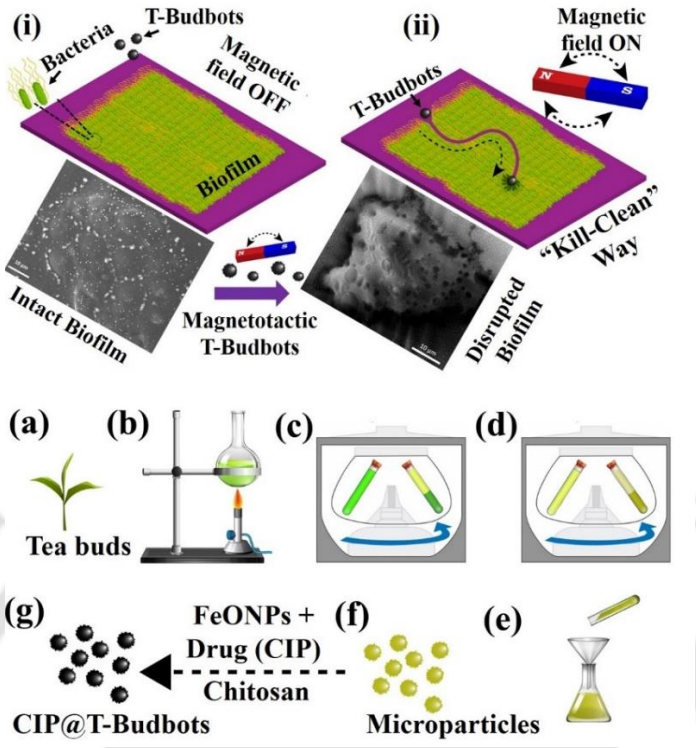

Figure 6.1. Schematic representation of **(i)** intact bacterial biofilm grown on a substrate before treating them with T-Budbots and **(ii)** magnetically driven T-Budbots across biofilm surface under the influence of a magnetic field for biofilm disruption and removal by "Kill-Clean" approach. Schematics describing fabrication of CIP loaded T-Budbots showing **(a)** collected Tea buds **(b)** preparation of Tea extract and their differential centrifugation at **(c)** 5000 rpm **(d)** 15,000 rpm followed by **(e)** filtration to form **(f)** microparticles of size (50-160 µm). **(g)** The microparticles were decorated with chitosan-modified FeONPs followed by loading of drug (CIP) to fabricate CIP@T-Budbots.

The microparticles obtained from Teabuds (~5-6 mg) of size 50 µm – 100 µm were incubated with 400 µL of 800 µg mL^{-1} of magnetite nanoparticles (FeONPs) and mixed with 0.7% chitosan for 30 min at room temperature that offered physicochemical stability of FeONPs.[61] Also, the cationic chitosan (ζ-potential of 16.5 ± 3.0 mV) was used to modify the surface charge of negatively charged T-Budbots towards a positive value of 5.03 ± 1.0 mV. The obtained FeONPs- loaded microbots (T-Budbots) was washed thrice with 70% ethanol, followed by vacuum drying at 50°C for 2 h.

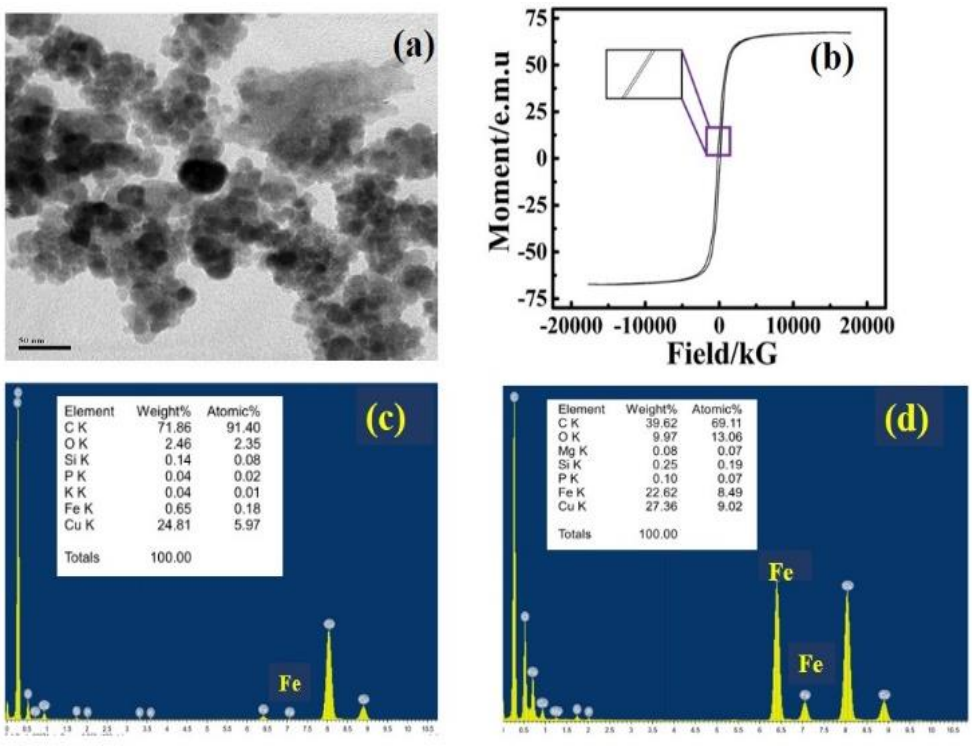

Figure 6.2. **(a)** TEM images of FeONPs with scale bar 50 nm. **(b)** VSM analysis of FeONPs. EDX spectra of **(c)** Tea microparticles and **(d)** FeONPs decorated T-Budbots.

Pseudo-spherical particles of size ~50 µm – 100 µm were considered for physical disruption of bacterial biofilm due to their inherent polyphenols, optimized loading of FeONPs on their porous surface for collective motion and their suitable dimensions to scrub away dead biofilms from substrates. The FeONPs (~800 µg mL^{-1}) were decorated on the surface microparticles (~6 mg) to form magnetically responsive T-Budbots. The TEM micrographs of FeONPs has been shown in **Figure 6.2a**, illustrating spherical morphology of size range between 20 nm – 60 nm. The magnetization saturation of FeONPs was measured using VSM analysis that was found to be ~ 66 emu g^{-1}, shown in **Figure 6.2b**. The elemental analysis of Tea bud microparticles and FeONPs coated T-Budbots measured by EDX analysis has been displayed in **Figure 6.2c and 6.2d,** respectively. The presence of high content of Fe (% weight of 22.62) in FeONPs decorated T-Budbots as compared to microparticles (%

weight of 0.65) confirmed the electrostatic encapsulation of negatively charged FeONPs on cationic microparticles.

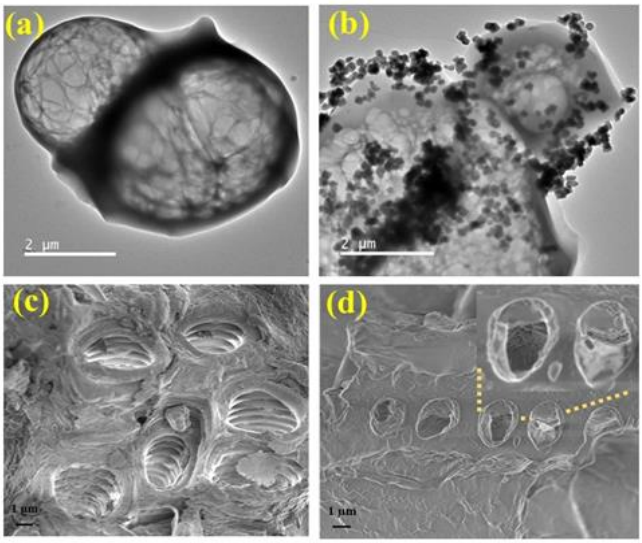

Figure 6.3. FETEM micrographs of **(a)** microparticles from Tea buds and **(b)** FeONPs decorated microparticles to form T-Budbots. FESEM images of **(c)** open porous surface of T-Budbots and **(d)** T-Budbots after encapsulation with drug, CIP hydrochloride to form CIP@T-Budbots. The loading of CIP on the surface led to the closing of the pores, shown in the magnified inset indicated by yellow dotted lines.

FE-TEM micrograph of Tea bud microparticles revealing mesh-like porous structures has been shown in **Figure 6.3a**. Also, the FeONPs decorated on the surface of microparticles have been displayed in **Figure 6.3b**, which confirmed the design of magnetic T-Budbots. Further, the anionic drug CIP was entrapped on the chitosan-stabilized surface of magnetic T-Budbots (to form CIP@T-Budbots) by electrostatic interaction, revealing their loading capability, combating resistance with improved antibacterial efficacy.

The surface morphologies of T-Budbots and CIP@T-Budbots analyzed using FESEM have been shown in **Figure 6.3c** and **6.3d,** respectively, confirming the closing of pores on the surface of T-Budbots after CIP loading, therefore forming CIP@T-Budbots. The

encapsulation of drugs resulted in the closing of the pores present on the surface of T-Budbots, as displayed in the magnified inset of Figure 6.3d.

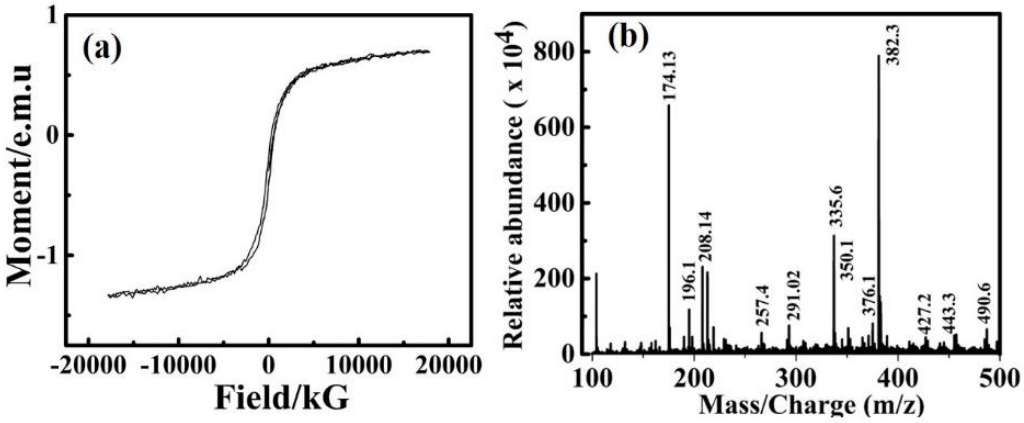

Figure 6.4. **(a)** VSM analysis of tea microparticles showing negligible magnetization saturation. **(b)** LCMS spectra of T-Budbots.

On the contrary, the magnetic moment of the tea microparticles was found to be insignificant, as measured by VSM analysis, displayed in **Figure 6.4a,** which falls in agreement with its EDX spectra in Figure 6.2c. The peak of protonated ion $[M+H]^+$ for T-Budbots has been analyzed using LCMS spectra, shown in **Figure 6.4b,** that are consistent with standard data.[62,63] The catechin content in the microbots showed the m/z for gallocatechin (307), a characteristic product ion of epicatechin gallate (459) and epicatechins gallate (443). The m/z signal at 291 corresponds to a distinctive fragment ion identified in the mass spectrum of epicatechin. Further, the peak of protonated ion $[M+H]^+$ for free T-Budbots has been compared that confirmed the loading of CIP on the surface of T-Budbots.

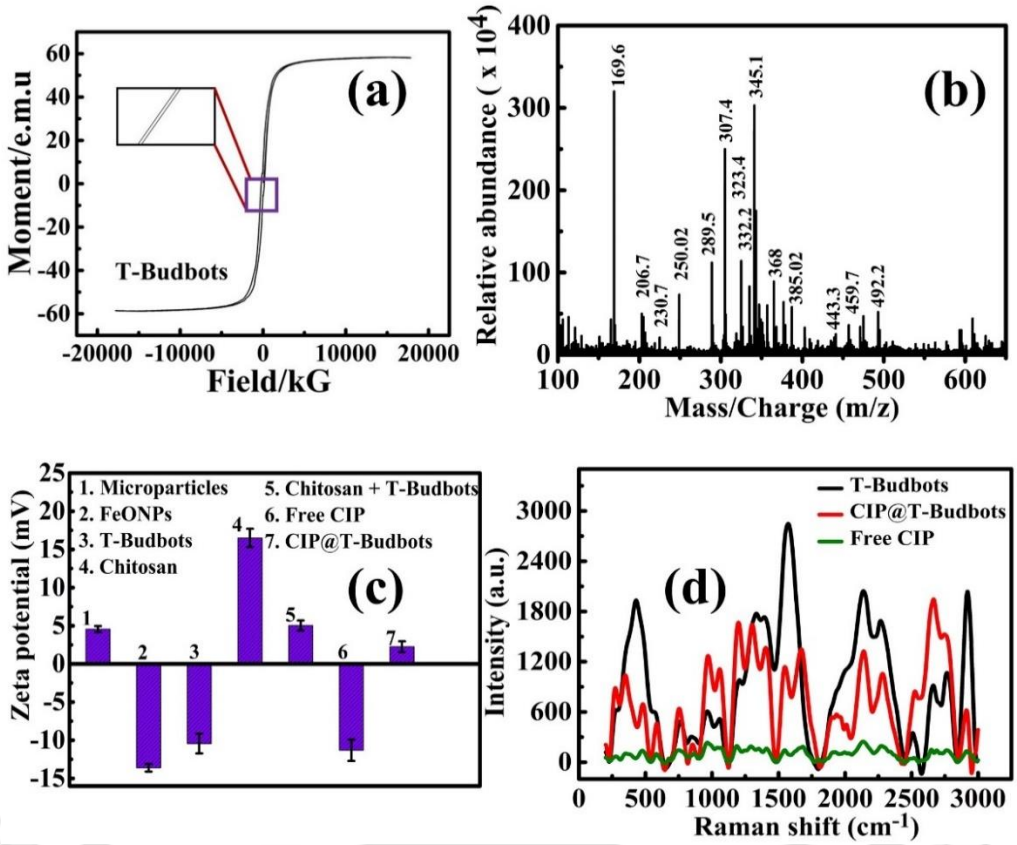

Figure 6.5. (a) VSM analysis of FeONPs decorated T-Budbots. **(b)** Liquid Chromatography (LCMS) of CIP@T-Budbots indicating the presence of catechin and their derivatives w.r.t. m/z ratio. **(c)** ζ- potential measurements **(d)** Raman spectroscopy of free drug, CIP and T-Budbots, and CIP modified T-Budbots.

Comparatively, the magnetic moment of FeONPs decorated T-Budbots was found to be ~ 58.5 emu g^{-1}, because of which they can be magnetically steered and navigated in the presence of a magnetic field as shown in **Figure 6.5a**. The mass spectra of CIF@T-Budbots has been analyzed using LCMS to determine the compounds present, as shown in **Figure 6.5b**. The ion transitions from peaks 332.2 to 230.7 were monitored for the presence of encapsulated CIP on T-Budbots. The m/z peaks at 385, 368, and 345 also confirmed the simultaneous determination of bound CIP that matches well with the existing literature. The appearance of peaks at m/z 307, 443 and 459 revealed the presence of epicatechins gallate

and epigallocatechins gallate from the T-Budbots in CIP@T-Budbots.[62-66] Further, the peak of protonated ion $[M+H]^+$ for free T-Budbots has been compared that confirmed the loading of CIP on the surface of T-Budbots, as shown in Figure 6.4b.

Figure 6.5c shows the ζ-potential of Tea microparticles, FeONPs, FeONPs- decorated microbots (T-Budbots), chitosan, chitosan modified T-Budbots, free CIP, and CIP@T-Budbots. The ζ-potential of Tea microparticles and FeONPs was measured to be 4.57 ± 1.5 mV and – 13.6 ± 0.5 mV respectively that allowed the electrostatic binding of FeONPs on Tea particles, forming T-Budbots with ζ-potential of -10.43 ± 2.0 mV. The cationic chitosan (ζ-potential of 16.5 ± 3.0 mV) was used to modify the surface charge of negatively charged T-Budbots towards a positive value of 5.03 ± 1.0 mV. The electrostatic interactions between anionic CIP drug (-11.31 ± 0.5 mV) and positively-charged T-Budbots decreased the net positive charge on the microbot to 2.26 ± 0.5 mV, which lead to the absorption of CIP molecules on a mesoporous cavity of T-Budbots. The porous surface of microbots provided minimal exposure of loaded CIP to external surroundings and thus shielded CIP from rapid degradation. The bio-distribution of bound CIP can be investigated by alterations of pH value in the surrounding microenvironment. Correspondingly, the overall positive surface charge of CIP@T-Budbots could bind specifically to the negatively charged bacterial cell wall facilitating surface design for the killing of bound bacterial cells.

The Raman spectra of T-Budbots, free CIP, and CIP@T-Budbots has been represented in **Figure 6.5d** that agreed quite well with existing literature. In case of free CIP, low-intensity peaks were observed, which might be due to poor aqueous solubility of CIP. The peaks at 1379 cm^{-1} and 1622 cm^{-1} was observed due to ring vibrations. For T-Budbots, the prominent peaks at 440 cm^{-1}, 2915 cm^{-1}, 1728 cm^{-1}, 1467 $cm^{-1,}$ and 2788 cm^{-1} indicated bending

vibrations of 4-aminobutyric acid with CH_2 (C_3) assignments, C-H stretching vibrations (epicatechin), C6 ring breathe vibrations (theophylline) CH_2 N_7 asymmetric stretching vibrations (caffeine) and presence of theophylline respectively.[67-69] The Raman shifts for CIP@T-Budbots was associated at 1655 cm^{-1}, 1411 cm^{-1}, 771 cm^{-1} and 484 cm^{-1} that indicated stretching vibration of aromatic C-C rings, symmetric stretching vibration of O-C-O group in carboxylic acid, stretching vibration of C-F group and bending vibration of C-C group in aliphatic chain of cyclopropyl group respectively.[67-70] Besides, the increase in peak intensity of CIF bound on the surface of T-Budbots confirmed the enhanced activity of CIP w.r.t free CIP.

6.3.2. Drug loading and release studies for bacterial killing

The amount of CIP loaded on various concentrations of T-Budbots, ranging from 1 mg to 6 mg has been represented in **Figure 6.6a**. It was observed that with a steady increase in microbot concentration, the binding efficiency of CIP was increased, which was confirmed by a gradual decrease in absorbance intensity of unbound CIP in the supernatant. The binding efficiency of CIP got saturated to ~ 88.56% at a concentration of 6 mg of T-Budbots, corresponding to ~ 22.4 µg mL^{-1} of CIP. Thus, 6 mg of CIP@T-Budbots were used for release studies of CIP and other experiments unless mentioned otherwise. To quantify the *in vitro* release of CIP from T-Budbots, the time-dependent release profile was studied that was found to be more significant at pH 4 with a maximum release of 85% at 8^{th} h and gradually reducing to 64% at 12^{th} h. At pH 7.4, a maximum release of 25% was found at 8^{th} h, which was gradually reduced to 18% at 12^{th} h.

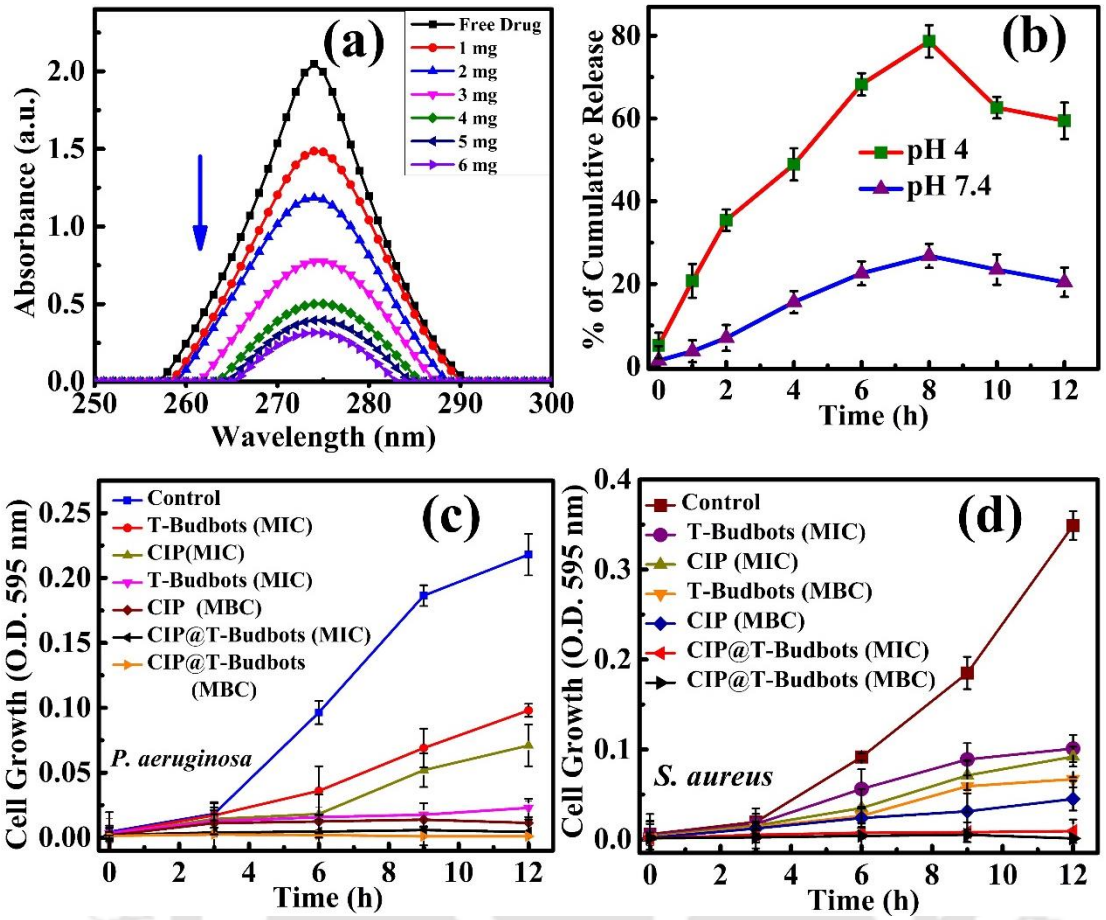

Figure 6.6. (a) UV-visible absorption spectra of the supernatant obtained after treatment of ciprofloxacin hydrochloride (CIP) solution (300 µL of 30 mg mL^{-1}) with various concentrations of T-Budbots (1-6 mg) for 2 h. **(b)** Release profile of CIP from CIP@T-Budbots at different intervals of time in PBS buffer of pH 7.4 and acetate buffer of pH 4. Growth curve study showing the inhibitory and killing effect of T-Budbots, free CIP, CIP@T-Budbots by measuring the OD at 595 nm on **(c)** *Pseudomonas aeruginosa* and **(d)** *Staphylococcus aureus*.

As shown in **Figure 6.6b**, the release pattern was biphasic at pH 4, exhibiting an initial burst release, followed by sustained release of CIP from T-Budbots. Such a phenomenon is vital to prevent bacterial proliferation at initial stages of infection, thereby eradicating them from their affluent acidic environment.[8] Also, the sustained release pattern of CIP from biocompatible T-Budbots would inhibit infection, offering effective therapeutic index at low

drug concentrations and reduced toxicity, thus proving to be advantageous over continuous antibiotic intake.

After successful loading of CIP on T-Budbots, the antibacterial activity of CIP@T-Budbots was investigated against Gram-negative bacteria (*Pseudomonas aeruginosa*) and Gram-positive bacteria (*Staphylococcus aureus*). Among different concentrations tested, the minimum concentration of CIP@T-Budbots, T-Budbots, FeONPs, and free CIP that measurably inhibited the bacterial growth and killed the bacteria was considered as MIC and MBC, respectively. The antibacterial activity was investigated against Gram-negative bacteria (*Pseudomonas aeruginosa*) and Gram-positive bacteria (*Staphylococcus aureus*). The bacterial strains were treated with different concentrations of CIP-loaded T-Budbots (CIP concentration ranging from 50 to 120 µg mL^{-1}), free CIP (50 to 120 µg mL^{-1}), T-Budbots (50 to 120 µg mL^{-1}) and FeONPs (200 to 400 µg mL^{-1}).

The growth curve studies on *Pseudomonas aeruginosa* revealed that at MIC (78 µg mL^{-1}) of CIP@T-Budbots, there was an arrest in bacterial growth and at its MBC (85 µg mL^{-1}), the bacterial growth was killed entirely. Comparatively, the free CIP exhibited higher values of MIC and MBC of 95 and 110 µg $mL^{-1,}$ respectively. The declined growth curve intensity suggested bactericidal activity for free CIP and T-Budbots, which was less than CIP@T-Budbots, as represented in **Figure 6.6c.** Similarly, the growth curve studies on *Staphylococcus aureus* revealed that at MIC (56 µg mL^{-1}) of CIP@T-Budbots, arrest in bacterial growth was observed and bactericidal activity was observed at its MBC (44 µg mL^{-1}). Comparatively, the free CIP exhibited higher MIC and MBC of 77 and 92 µg $mL^{-1,}$ respectively, that could be inferred from the growth curve, as shown in **Figure 6.6d.** Interestingly, the MIC and MBC for *Pseudomonas aeruginosa* was higher as compared to

Staphylococcus aureus due to the presence of a thick cell wall in Gram-negative bacteria that remains unaffected at low toxin concentration and hinders their penetrability.[71,72]

Among different concentrations tested, the minimum concentration of CIP@T-Budbots, T-Budbots, FeONPs, and free CIP that measurably inhibited the bacterial growth and killed the bacteria was considered as MIC and MBC, respectively. The MIC and MBC of the samples have been represented in **Table 6.1**. As interpreted from the table above, the MIC and MBC value of CIP@T-Budbots was less for both the bacterial strains indicating the synergistic antibacterial therapy involving bound drug CIP and T-Budbots.

	(μg mL^{-1})	T-Budbots	FeONPs	Free CIP	CIP@T-Budbots
Pseudomonas aeruginosa	**MIC**	**85**	**250**	**95**	**78**
	MBC	**100**	**315**	**110**	**85**
	(μg mL^{-1})	T-Budbots	FeONPs	Free CIP	CIP@T-Budbots
Staphylococcus aureus	**MIC**	**70**	**180**	**77**	**56**
	MBC	**81**	**220**	**92**	**74**

Table 6.1. MIC and MBC of samples against *Pseudomonas aeruginosa and Staphylococcus aureus* bacteria.

The growth curve studies on *Pseudomonas aeruginosa* revealed that at MIC (78 μg mL^{-1}) of CIP@T-Budbots, there was an arrest in bacterial growth and at its MBC (85 μg mL^{-1}), the bacterial growth was completely killed. Comparatively, the free CIP exhibited higher values of MIC and MBC of 95 and 110 μg $mL^{-1,}$ respectively. Similarly, the growth curve studies on *Staphylococcus aureus* revealed that at MIC (56 μg mL^{-1}) of CIP@T-Budbots,

arrest in bacterial growth was observed and bactericidal activity was observed at its MBC (74 µg mL^{-1}). Comparatively, the free CIP exhibited higher MIC and MBC of 77 and 92 µg $mL^{-1,}$ respectively. Interestingly, the T-Budbots alone could exhibit MIC and MBC values close to free drug CIP. Also, Gram-negative bacteria were susceptible at higher MIC and MBC concentrations than Gram-positive bacteria due to their thick cell wall.[72]

It is important to note that T-Budbots alone could exhibit bactericidal activity against both the strains with MIC and MBC values more or less as free CIP due to their inherent compounds with antibacterial properties.[58,59] The drug CIP bound to microbots have several merits over free form in terms of their effectiveness, stability, and reduced side effects due to their less content than in pure form. The pattern of activity exhibiting higher detrimental effect of drug-loaded microbot than the free drug in the physiological environment was probably due to synergistic combination with active T-Budbots that shielded the bound drug from early degradation, thus preventing bacterial resistance.[73-75]

Moreover, to confirm the respective MIC and MBC, the bacteria were plated on nutrient agar media where only a few bacterial colonies were observed at MIC and no colony at MBC of CIP@T-Budbots, T-Budbots, FeONPs and free CIP **(Figure 6.7**). The respective MIC and MBC were confirmed by plating both the bacterial colonies (~1×10^8 CFU mL^{-1}) on nutrient agar media and treating them with respective MIC/MBC concentrations of CIP@T-Budbots, T-Budbots, FeONPs, and free CIP. For *Pseudomonas aeruginosa*, the control bacterial cells were incubated on agar media resulting in a confluent growth of bacterial colonies, presented in **Figure 6.7I (a)**.

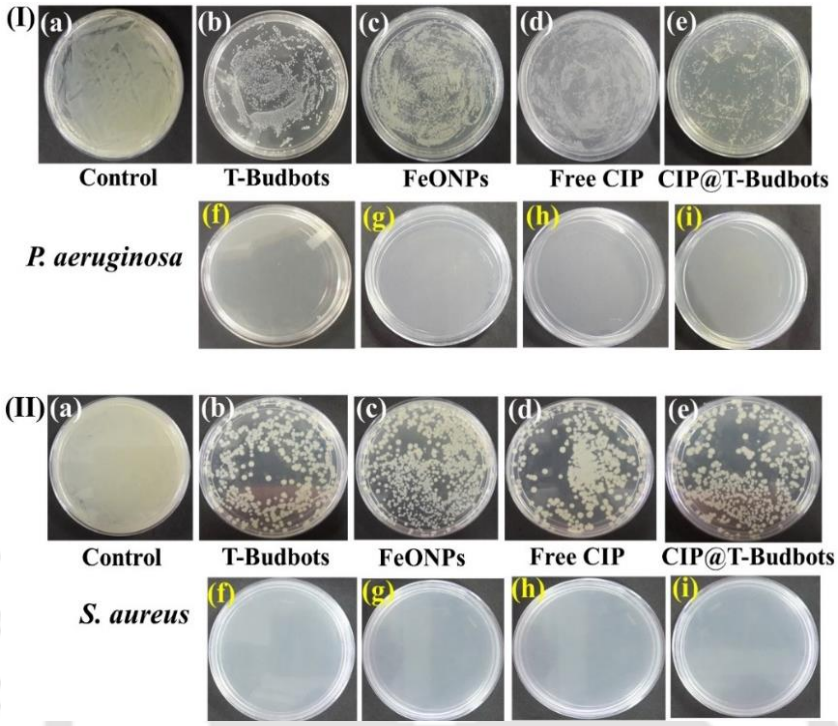

Figure 6.7. **(I)** Plating of *Pseudomonas aeruginosa* colonies **(a)** control; with MIC concentrations of **(b)** T-Budbots at 85 µg mL^{-1}, **(c)** FeONPs at 250 µg mL^{-1}, **(d)** Free CIP at 95 µg mL^{-1} and **(e)** CIP@T-Budbots at 78 µg mL^{-1}; with MBC concentrations of **(f)** T-Budbots at 100 µg mL^{-1}, **(g)** FeONPs at 315 µg mL^{-1}, **(h)** Free CIP at 110 µg mL^{-1} and **(i)** CIP@T-Budbots at 85 µg mL^{-1}. **(II)** Plating of *Staphylococcus aureus* colonies **(a)** control; with MIC concentrations of **(b)** T-Budbots at 70 µg mL^{-1}, **(c)** FeONPs at 180 µg mL^{-1}, **(d)** Free CIP at 77 µg mL^{-1} and **(e)** CIP@T-Budbots at 56 µg mL^{-1}; with MBC concentrations of **(f)** T-Budbots at 81 µg mL^{-1}, **(g)** FeONPs at 220 µg mL^{-1}, **(h)** Free CIP at 92 µg mL^{-1} and **(i)** CIP@T-Budbots at 74 µg mL^{-1}.

The bacterial colonies treated with MIC of T-Budbots (85 µg mL^{-1}), FeONPs (250 µg mL^{-1}), free CIP (95 µg mL^{-1}) and CIP@T-Budbots (78 µg mL^{-1}) resulted in few colonies on the plate, as shown in **Figure 6.7I (b-e)** respectively. However, no bacterial colonies were observed on the plate after treating with MBC of T-Budbots (100 µg mL^{-1}), FeONPs (315 µg mL^{-1}), free CIP (110 µg mL^{-1}) and CIP@T-Budbots (85 µg mL^{-1}), shown in **Figure 6.7 I (f-i)** respectively. Similarly, control *Staphylococcus aureus* bacterial colonies were grown on an agar plate that resulted in confluent growth, as shown in **Figure 6.7II (a)**. The bacteria

treated with MIC of T-Budbots (70 µg mL^{-1}), FeONPs (180 µg mL^{-1}), free CIP (77 µg mL^{-1}) and CIP@T-Budbots (56 µg mL^{-1}) resulted in few colonies on the plate, as shown in **Figure 6.7II (b-e)** respectively. However, no bacterial colonies were observed on the plate after treating with MBC of T-Budbots (81 µg mL^{-1}), FeONPs (220 µg mL^{-1}), free CIP (92 µg mL^{-1}) and CIP@T-Budbots (74 µg mL^{-1}), shown in **Figure 6.7II (f-i)** respectively.

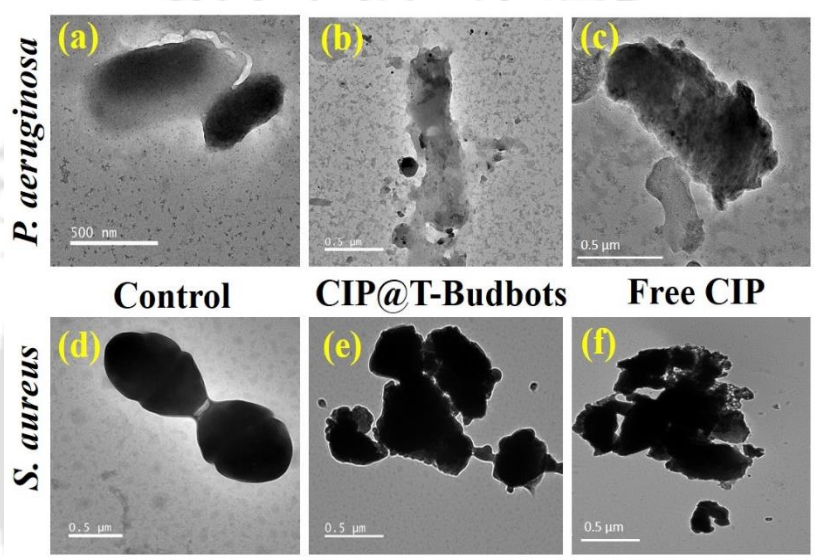

Figure 6.8. FETEM images of **(a)** control bacteria **(***Pseudomonas aeruginosa*), bacteria (*Pseudomonas aeruginosa*) treated **(b)** CIP@T-Budbots at their MIC (85 µg mL^{-1}) and **(c)** free drug CIP at their MIC (95 µg mL^{-1}). **(d)** Control bacteria (*Staphylococcus aureus*) and bacteria treated with **(e)** CIP@T-Budbots at their MIC (56 µg mL^{-1}), **(f)** bacteria treated with free drug CIP at their MIC (77 µg mL^{-1}). The images were taken at a scale bar of 500 nm.

Images of untreated (control) *Pseudomonas aeruginosa* and *Staphylococcus aureus* having smooth cell surfaces were captured using FETEM analysis, as shown in **Figure 6.8a and 6.8d,** respectively. In addition, the FETEM micrographs showing the disrupted cell morphologies of *Pseudomonas aeruginosa* and *Staphylococcus aureus* treated with CIP@T-Budbots confirmed the combination antibacterial therapy of CIF@T-Budbots, as shown in **Figure 6.8b and 6.8e,** respectively**.** Also, the bound CIP could probably use the iron present in FeONPs coated CIP@T-Budbots, thus forming hydroxyl radicals via tricarboxylic acid

cycle leading to NADH depletion and damage.[76] Moreover, treatment of *Pseudomonas aeruginosa* and *Staphylococcus aureus* with free CIP at their respective MIC values resulted in a loss of cellular integrity, causing cell death, as shown in **Figure 6.8c** and **6.8f,** respectively.

6.3.3. Biofilm killing

The effective bactericidal activity of CIP@T-Budbots led us to investigate their activity towards *the* destruction of pathogenic biofilms formed by *Pseudomonas aeruginosa* and *Staphylococcus aureus*, which causes life-threatening infections.

	(μg mL^{-1}) MBIC$_{50}$	**T-Budbots**	**FeONPs**	**Free CIP**	**CIP@T-Budbots**
Pseudomonas aeruginosa		300	300	250	200
Staphylococcus aureus	**(μg mL^{-1}) MBIC$_{50}$**	140	140	120	100

Table 6.2. MBIC$_{50}$ of samples against *Pseudomonas aeruginosa and Staphylococcus aureus* biofilms.

The antibiofilm studies performed on *Pseudomonas aeruginosa and Staphylococcus aureus* at different concentrations of T-Budbots, FeONPs, free CIP, and CIP@T-Budbots revealed their 50% (MBIC$_{50}$) inhibition values represented in **Table 6.2**. Different concentrations of CIP@T-Budbots, free CIP, T-Budbots, and FeONPs (100 – 300 μg mL^{-1} for *Pseudomonas aeruginosa* and 80-140 μg mL^{-1} for *Staphylococcus aureus* biofilm) was added. In case of

Pseudomonas aeruginosa, treatment with free CIP (100-300 µg mL^{-1}) exhibited 50% ($MBIC_{50}$) inhibition at a concentration of 300 µg mL^{-1}.

However, treatment with CIP@T-Budbots (100-300 µg mL^{-1}) showed 50% ($MBIC_{50}$) inhibition at a concentration of 200 µg mL^{-1}, which was far more less than free drug CIP. Similarly, *Staphylococcus aureus* biofilm treated with CIP@T-Budbots (80-140 µg mL^{-1}) exhibited 50% ($MBIC_{50}$) inhibition at a concentration of 100 µg mL^{-1}, which was far more less than $MBIC_{50}$ of free CIP observed at a concentration of 140 µg mL^{-1}. The crystal violet stain was used to record the absorbance 595 nm using microplate reader. As noted, the $MBIC_{50}$ value of CIP@T-Budbots was less indicating the synergistic antibiofilm efficacy involving bound drug CIP and T-Budbots. Also, Gram-negative bacterial biofilm was disrupted at higher $MBIC_{50}$ concentrations due to the thick cell wall of bacterial cells.

In case of *Pseudomonas aeruginosa*, treatment with free CIP (100-300 µg mL^{-1}) exhibited 50% ($MBIC_{50}$) inhibition at a concentration of 300 µg mL^{-1}, presented in **Figure 6.9a**. However, treatment with CIP@T-Budbots (100-300 µg mL^{-1}) exhibited 50% ($MBIC_{50}$) inhibition at a concentration of 200 µg mL^{-1}, which was far more less than free drug CIP. Similarly, *Staphylococcus aureus* biofilm treated with CIP@T-Budbots (80-140 µg mL^{-1}) exhibited 50% ($MBIC_{50}$) inhibition at a concentration of 100 µg mL^{-1}, which was far more less than $MBIC_{50}$ of free CIP observed at a concentration of 140 µg mL^{-1}, as shown in **Figure 6.9b.** Notably, the T-Budbots alone could also show direct antibacterial and antibiofilm effect against both the bacterial strains with MIC/MBC and $MBIC_{50}$ values not far from free CIP, which is due to the presence of bactericidal catechin derivatives.[58,59]

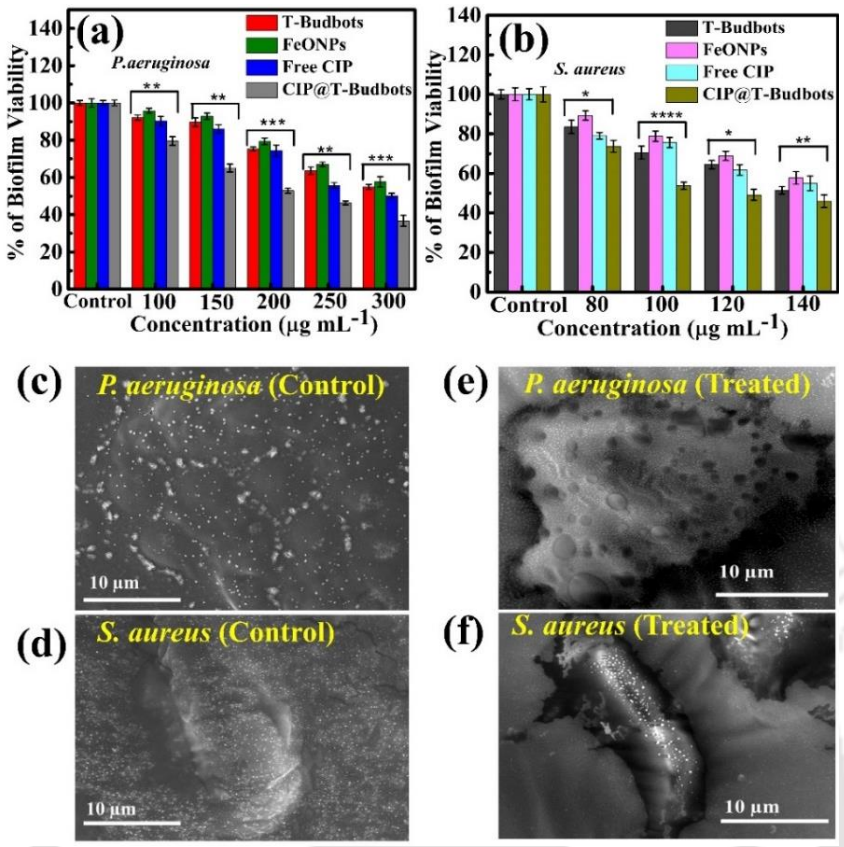

Figure 6.9. Antibiofilm activity of T-Budbots, FeONPs, free CIP, and CIP@T-Budbots on **(a)** *Pseudomonas aeruginosa* and **(b)** *Staphylococcus aureus*. The ANOVA test revealed the statistical significance of T-Budbots, FeONPs, free CIP, and CIP@T-Budbots samples with respect to control sample. Statistical significance is signified by * ($p < 0.05$), ** ($p < 0.005$), *** ($p < 0.001$), and **** ($p < 0.0001$). The data are represented as mean ± SD of three individual experiments. FESEM images showing control biofilms formed by **(c)** *P. aeruginosa* and **(d)** *Staphylococcus aureus*. The biofilms were treated with respective $MBIC_{50}$ of CIP@T-Budbots (200 μg mL^{-1} for *Pseudomonas aeruginosa* and 100 μg mL^{-1} for *Staphylococcus aureus*). FESEM images of destroyed biofilms formed by **(e)** *Pseudomonas aeruginosa* and **(f)** *Staphylococcus aureus*. Scale bar is 10 μm.

The results obtained for antibiofilm activity supported the results of antibacterial studies proving *Staphylococcus aureus* biofilm to be susceptible to lower toxin concentrations[71-75] than *Pseudomonas aeruginosa* biofilm and enhanced biofilm killing activity of CIP@T-Budbots. FESEM micrographs of untreated (control) *Pseudomonas aeruginosa* and *Staphylococcus aureus* biofilm with even surfaces have been shown in **Figure 6.9c-d,**

respectively. Besides, the micrographs showing the degraded biofilm of *Pseudomonas aeruginosa* and *Staphylococcus aureus* treated with respective $MBIC_{50}$ of CIP@T-Budbots confirmed the combination antibacterial therapy of CIF@T-Budbots, as shown in **Figure 6.9e-f,** respectively**.**

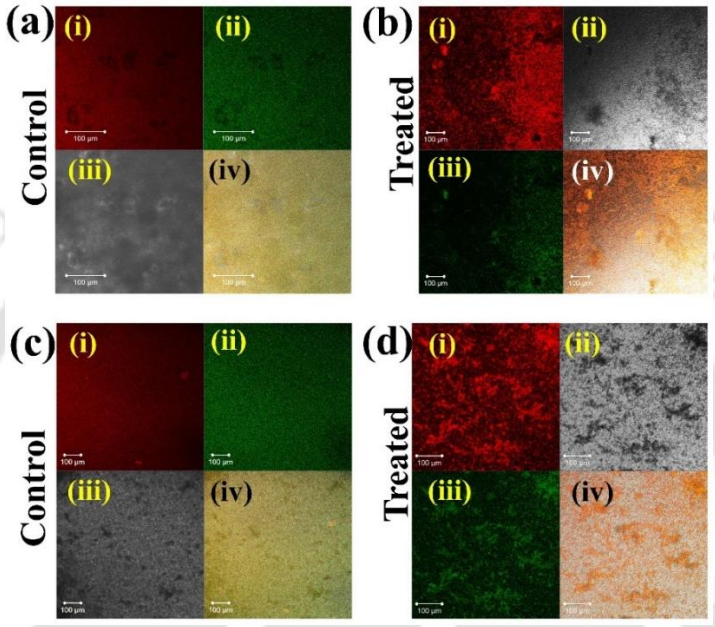

Figure 6.10. CLSM images of **(a)** control *Pseudomonas aeruginosa* biofilm stained with **(i)** PI **(ii)** AO **(iii)** bright field and **(iv)** merged image. **(b)** *Pseudomonas aeruginosa* biofilm treated with $MBIC_{50}$ (200 µg mL^{-1}) of CIP@T-Budbots **(i)** stained with PI **(ii)** bright-field image **(iii)** stained with AO and **(iv)** merged image. **(c)** Control *Staphylococcus aureus* biofilm stained with **(i)** PI **(ii)** AO **(iii)** bright field and **(iv)** merged image. **(d)** *Staphylococcus aureus* biofilm treated with $MBIC_{50}$ (100 µg mL^{-1}) of CIP@T-Budbots **(i)** stained with PI **(ii)** bright-field image **(iii)** stained with AO and **(iv)** merged image. The control biofilm exhibited high intensity of green fluorescence, as observed from the merged images, due to greater number of viable cells and their uptake of AO stain. The red fluorescence emitted from the biofilms treated with CIP@T-Budbots is due to dead cells stained by PI. The imaging was carried out using confocal microscopy at an excitation wavelength of 495 nm for AO and 540 nm for PI. The scale bar for all the images is 100 µm.

The dual staining performed using the AO/PI dyes indicated that the CIP@T-Budbots could reduce the biofilm masses by preventing bacterial proliferation. **Figure 6.10a (i-iv)** shows the fluorescence micrographs of PI stain, AO stain, bright field, and merged image of control *Pseudomonas aeruginosa* biofilm, respectively, that was visualized under confocal

microscopy. As can be seen from the merged image, the cells emitted out maximum intensity of green fluorescence because of the uptake of AO by live bacterial cells. This indicated the presence of a very less number of dead cells with a negligible intensity of red fluorescence from PI stain.

Figure 6.10b (i-iv) shows the fluorescence micrographs of PI stain, bright field image, AO stain, and merged image of *Pseudomonas aeruginosa* biofilm, respectively, treated with the $MBIC_{50}$ of CIP@T-Budbots (200 µg mL^{-1}). A prominent red fluorescence could be visualized from the merged image due to the permeability of PI stain through the dead bacterial cells. The green fluorescence was emitted out from a limited area indicating a lesser number of viable cells. Similarly, **Figure 6.10c (i-iv)** shows the confocal micrographs of PI stain, AO stain, bright field and merged image of control *Staphylococcus aureus* biofilm, respectively. The cells emitted out maximum intensity of green fluorescence, indicating more viable cells, as observed from the merged image.

The fluorescence micrographs of PI stain, bright field image, AO stain, and merged image of *Staphylococcus aureus* biofilm was treated with the $MBIC_{50}$ of CIP@T-Budbots (100 µg mL^{-1}), presented in **Figure 6.10d (i-iv)** respectively. Consistently, the merged image achieved maximum red fluorescence due to penetration of PI stain through the damaged cells. Only a limited area emitted green fluorescence confirming few live cells. Likewise, the confocal micrographs of control biofilms and biofilms treated with $MBIC_{50}$ of free drug, CIP has been captured, which confirmed that CIP@T-Budbots were more effective in killing and reducing biofilm masses than free CIP. The dual staining using the AO/PI dyes was carried out to study the effect of free drug against biofilms formed by *Pseudomonas aeruginosa* and *Staphylococcus aureus* and comparing with detrimental effects CIP@T-Budbots.

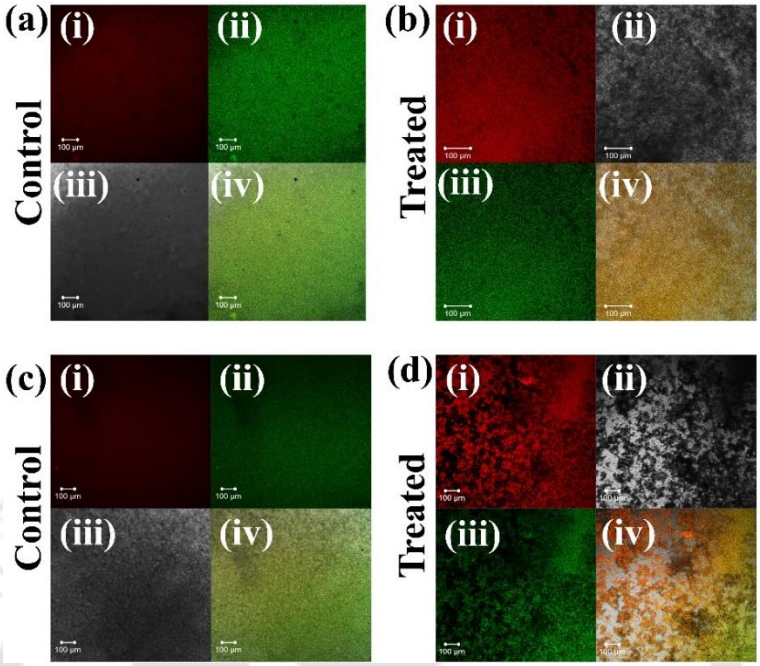

Figure 6.11. CLSM images of **(a)** control *Pseudomonas aeruginosa* biofilm stained with **(i)** PI **(ii)** AO **(iii)** bright field and **(iv)** merged image. **(b)** *Pseudomonas aeruginosa* biofilm treated with $MBIC_{50}$ (250 µg mL^{-1}) of free drug CIP **(i)** stained with PI **(ii)** bright-field image **(iii)** stained with AO and **(iv)** merged image. **(c)** Control *Staphylococcus aureus* biofilm stained with **(i)** PI **(ii)** AO **(iii)** bright field and **(iv)** merged image. **(d)** *Staphylococcus aureus* biofilm treated with $MBIC_{50}$ (120 µg mL^{-1}) of free drug CIP **(i)** stained with PI **(ii)** bright-field image **(iii)** stained with AO and **(iv)** merged image. The control biofilm exhibited high intensity of green fluorescence, as observed from the merged images, due to greater number of viable cells and their uptake of AO stain. The red fluorescence emitted from the biofilms treated with CIP@T-Budbots is due to dead cells stained by PI. The imaging was carried out using confocal microscopy at an excitation wavelength of 495 nm for AO and 540 nm for PI. The scale bar for all the images is 100 µm.

Figure 6.11a (i-iv) shows the fluorescence micrographs of PI stain, AO stain, bright field, and merged image of control *Pseudomonas aeruginosa* biofilm, respectively that was visualized under confocal microscopy. As can be seen from the merged image, the cells emitted out maximum intensity of green fluorescence because of the uptake of AO by live bacterial cells. This indicated the presence of a very less number of dead cells with negligible intensity of red fluorescence from PI stain. **Figure 6.11b (i-iv)** shows micrographs of PI stain, bright field image, AO stain, and merged image of *Pseudomonas*

aeruginosa biofilm, respectively, that was treated with the $MBIC_{50}$ of free CIP (250 µg mL^{-1}). A red fluorescence could be visualized from the merged image due to the permeability of PI stain through the dead bacterial cells. The green fluorescence was emitted out from a limited area indicating a lesser number of viable cells.

Similarly, **Figure 6.11c (i-iv)** shows the confocal micrographs of PI stain, AO stain, bright field, and merged image of control *Staphylococcus aureus* biofilm, respectively. The cells emitted out maximum intensity of green fluorescence, indicating more viable cells, as observed from merged image. The fluorescence micrographs of PI stain, bright field image, AO stain, and merged image of *Pseudomonas aeruginosa* biofilm was treated with the $MBIC_{50}$ of free CIP (120 µg mL^{-1}) has been presented in **Figure 6.11d (i-iv)** respectively. Consistently, the merged image achieved maximum red fluorescence due to penetration of PI stain through the damaged cells. Only a limited area emitted green fluorescence confirming few live cells.

Remarkably, the intensity of red fluorescence emitted out from the merged images [Figure 6.11b (iv) and 6.11d (iv)] was comparatively less than the fluorescence of biofilms treated with $MBIC_{50}$ of CIP@T-Budbots [Figure 6.10b (iv) and 6.10d (iv)]. Hence, this study confirmed that $MBIC_{50}$ of CIP@T-Budbots was more effective in killing and reducing biofilm masses than $MBIC_{50}$ of free CIP. Therefore, the reduction in the biomass of biofilms realized from CV assay and AO/PI-based staining suggested that T-Budbots releasing CIP could combat recurrent biofilm infections more efficiently than the free drug.

6.3.4. Cleaning of Biofilm by Robotic T-Budbots

Robotic biofilm killing and cleaning platforms that exploit FeONPs decorated T-Budbots was formulated to achieve magnetic field induced removal of biofilm debris using a

permanent magnet (0.01 T) on *Pseudomonas aeruginosa* and *Staphylococcus aureus biofilm*. It is important to note that T-Budbots could be propelled in a magnetic field to dismantle biofilms and simultaneously kill them as soon as they come in contact with dislodged bacterial cells. The enhanced killing of bacterial cells was attributed due to the pH-dependent release of bound CIP from T-Budbots and combinatorial antibacterial efficacy. Interestingly, the introduction of a linear magnetic field could drive the T-Budbots in a distinctive unidirectional pattern following a straight path across the biofilm surface while leaving the neighboring domains intact.

By defining a trajectory that was initiated upon magnetic actuation, which gradually removed the degraded biofilm biomass following a linear path. The clearing of biofilms in a linear motion might be desired to clear biofilms at specific pathological areas without harming the adjacent healthy tissues and identification of microbial compositions. In this process, a droplet of microbots with magnetization placed near the targeted site and simultaneous introduction of a magnetic field could lead to localized biomass eradication.

The magnetic steering of T-Budbots to sweep *Staphylococcus aureus* and *Pseudomonas aeruginosa* biofilm in a directed linear motion was recorded. The linear trajectory and position of the microbots at different time points *(t)* that confirmed the clearance of the cleaned area across *Staphylococcus aureus* and *Pseudomonas aeruginosa* biofilm, has been represented in **Figure 6.12 (a-c)** and **6.12 (d-f)** respectively. The positions of the microbots exhibiting linear motion on surface of *Staphylococcus aureus* biofilm and *Pseudomonas aeruginosa* biofilm has been represented at time, *t* = **(a)** 5 s, **(b)** 50 s and **(c)** 100 s and *t* = **(d)** 10 s, **(e)** 130 s and **(f)** 200 s respectively.

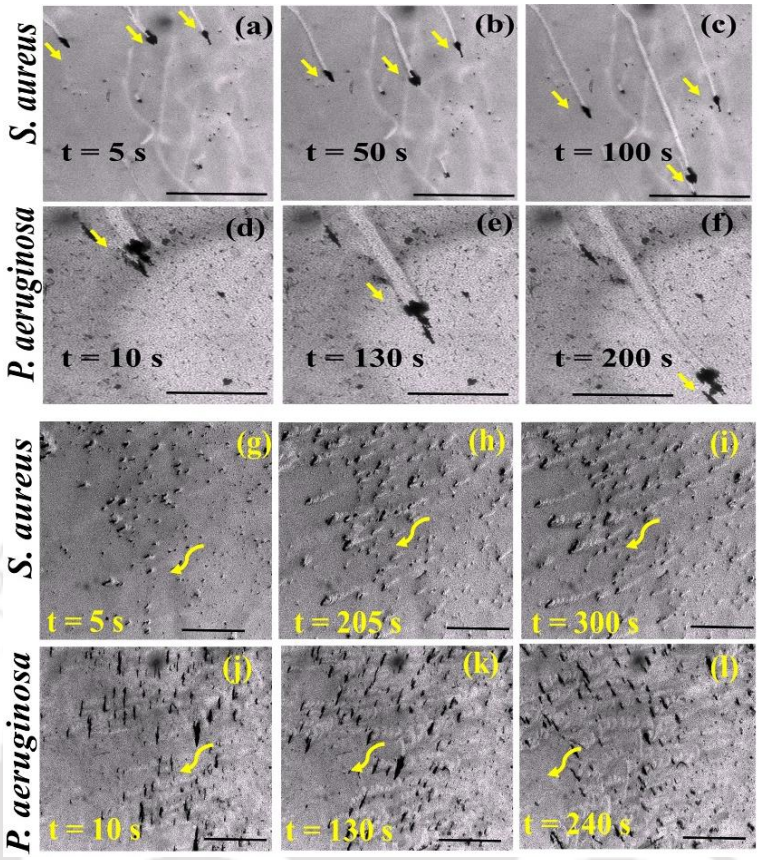

Figure 6.12. Motion of T-Budbots in biofilm under magnetic control. Initially, the microbots with linear footprints were formed on the surface of *Staphylococcus aureus* biofilm. The positions of the microbots have been denoted at time, *t* = **(a)** 5 s, **(b)** 50 s, and **(c)** 100 s. The positions of the microbots with linear footprints on the surface of *Pseudomonas aeruginosa* biofilm has been denoted at time, *t* = **(d)** 10 s, **(e)** 130 s, and **(f)** 200 s. Similarly, spinning microbots with circular footprints were formed on the surface of *Staphylococcus aureus* biofilm. The positions of the micromotors have been denoted at time, *t* = **(g)** 5 s, **(h)** 205 s and **(i)** 300 s. The positions of the micromotors with circular footprints on the surface of *Pseudomonas aeruginosa* biofilm has been denoted at time, *t* = **(j)** 10 s, **(k)** 130 s and **(l)** 240 s. The scale bar for the images is 1 mm. The direction of T-Budbots has been indicated by yellow arrows.

Interestingly, the formation of lined footprints could be observed as the microbots were driven linearly towards a direction, drilling out the biofilms from the surface.

Thereafter, a circular magnetic field was introduced by rotating the magnet to spin the magnetotactic CIP@T-Budbots in a circular pattern across the biofilm surface. During this process, a trajectory was defined from the center point that progressively swept outward in

a coordinated manner, indicating the capability of large scale cleaning of biofilm matrix. The microbots realigned themselves with the direction of rotating magnetic field along their short axis. The magnetic steering of T-Budbots to sweep *Staphylococcus aureus* and *Pseudomonas aeruginosa* biofilm in a spinning motion was recorded. The circular trajectory and position of the microbots at different time points *(t)* across *Staphylococcus aureus* and *Pseudomonas aeruginosa* biofilm, has been represented in **Figure 6.12 (g-i)** and **6.12 (j-l),** respectively. The positions of the microbots exhibiting spinning motion on surface of *Staphylococcus aureus* biofilm and *Pseudomonas aeruginosa* biofilm has been represented at time, *t* = **(a)** 5 s, **(b)** 205 s and **(c)** 300 s and *t* = **(d)** 10 s, **(e)** 130 s and **(f)** 240 s respectively.

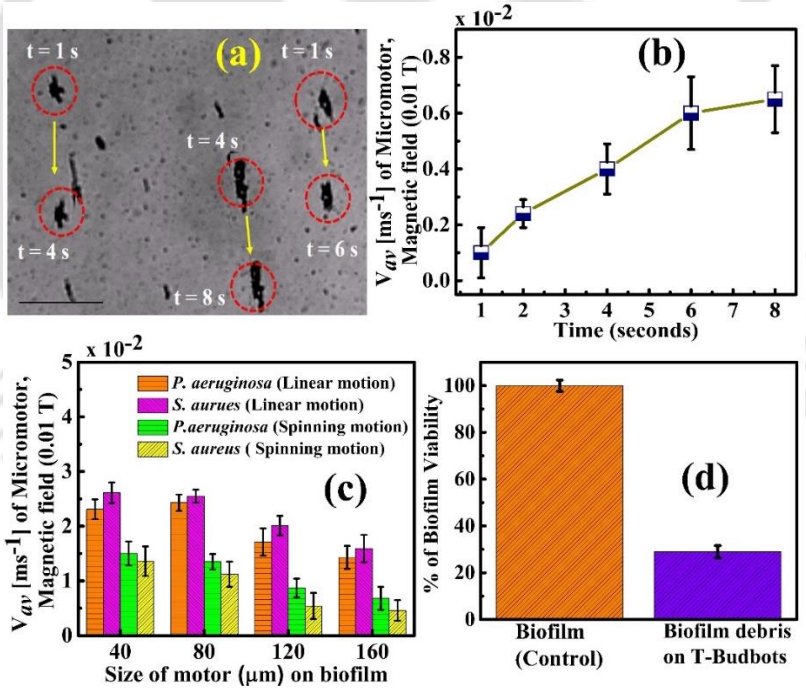

Figure 6.13. **(a)** Linear motion of T-Budbots in biofilm under magnetic control in water. The positions of the micromotors have been denoted at time, *t* = 1 s to 8 s. Scale bar is 1 mm. **(b)** Average velocity, V_{av} of the T-Budbots in water. **(c)** Variations in average velocity, V_{av} of T-Budbots with respect to their varied size range of 40 µm to 160 µm. **(d)** Measurement of biofilm viability (in %) to confirm the death of biofilm debris attached on the surface of micromotors after their removal from the surface.

Similarly, the formation of spiral footprints could be observed as the microbots were drilling out the biofilms from the surface. The magnetotactic motion of T-Budbots moving linearly in water was considered to be control **Figure 6.13a**, describing the positions of the microbots at varied time points *(t)* from 1 s to 8 s. The average velocity of magnetically driven T-Budbots in water was found to be ~ 0.63 × 10^{-2} ms^{-1}, as shown in **Figure 6.13b**. The V_{av} of microbots on the surface of *Pseudomonas aeruginosa* and *Staphylococcus aureus* biofilm with varied size range (size ~ 40 to 160 µm) has been depicted in **Figure 6.13c**. In case of *Pseudomonas aeruginosa* biofilm, the microbots (size range ~ 40 µm to 80 µm) moving linearly attained a maximum average velocity of ~ 2.5 × 10^{-2} ms^{-1} whereas the V_{av} of spinning T-Budbots was found to be ~1.3 × 10^{-2} ms^{-1}. For *Staphylococcus aureus* biofilm, the microbots (size range ~ 40 µm to 80 µm) moving linearly attained a maximum average velocity of ~ 2.7 × 10^{-2} ms^{-1} whereas the V_{av} of spinning T-Budbots was found to be 1.1 × 10^{-2} ms^{-1}. The average velocity was gradually reduced with increasing size of the microbots that can be regulated by introducing a strong magnetic field. The minor variations in average speed of microbots across the biofilm could possibly due to more surface roughness of *Staphylococcus aureus* biofilm than *Pseudomonas aeruginosa*.[77]

In addition, the T-Budbots exhibited rapid linear motion than spinning motion because of more complications of rotational motion to go around the circle than linearly moving microbots from one point to another in a straight line. Further, the rotational speed depends on the time-dependent angular acceleration of the spinning microbots and how rapidly the microbots are rotating about an axis w.r.t their size.[78,79] Contrarily, the linearly moving T-Budbots were independent of complicated angular rotations showing fast magnetic response and scrubbing out the degraded biofilms in a straight path.[79]

The electrostatic binding of negatively charged biofilms on the surface of cationic microbots destroyed the cellular integrity in *Staphylococcus aureus* and *Pseudomonas aeruginosa* biofilms. After clearing of biofilm debris from the surface, the % viability of the attached biofilm was studied by CV assay. Predictably, the % viability of the removed biofilm attached on the surface was measured to be less than 30 % as compared to untreated biofilms that further confirmed their complete disruption, as shown in **Figure 6.13d**. From the graph, it can be concluded that the biofilm debris removed from the surface by magnetically propelled T-Budbots revealed negligible amount of viable bacterial cells.

The average velocity of T-Budbots (size ~ 90 to 120 µm) exhibiting linear and spinning motion across *Staphylococcus aureus* and *Pseudomonas aeruginosa* biofilm was calculated at varied time points of t= 0 to 20 s, presented in **Figure 6.14a**. The V_{av} of microbots exhibiting a linear motion was found to be ~2.9×10^{-2} ms^{-1}, which was far more than the spinning motion of microbots with V_{av} of ~1.3×10^{-2} ms^{-1} because of more complications of rotational motion to go around the circle than linearly moving microbots from one point to another in a straight line.[78]

Further, the rotational speed depends on the time-dependent angular acceleration of the spinning microbots and how rapidly the microbots are turning about an axis w.r.t their size.[78,79] On the contrary, the linear motion of the T-Budbots on the biofilms were independent of complicated angular rotations exhibiting fast motion in less time.[79] The V_{av} of microbots on the surface of *Staphylococcus aureus* and *Pseudomonas aeruginosa* biofilm with varied size range (size ~ 40 to 160 µm) has already been described in Figure 6.13c.

Additionally, the rotational speed, ω for the spinning microbots on both the bacterial biofilms grown at a concentration of 1×10^{8} CFU mL^{-1} was calculated.

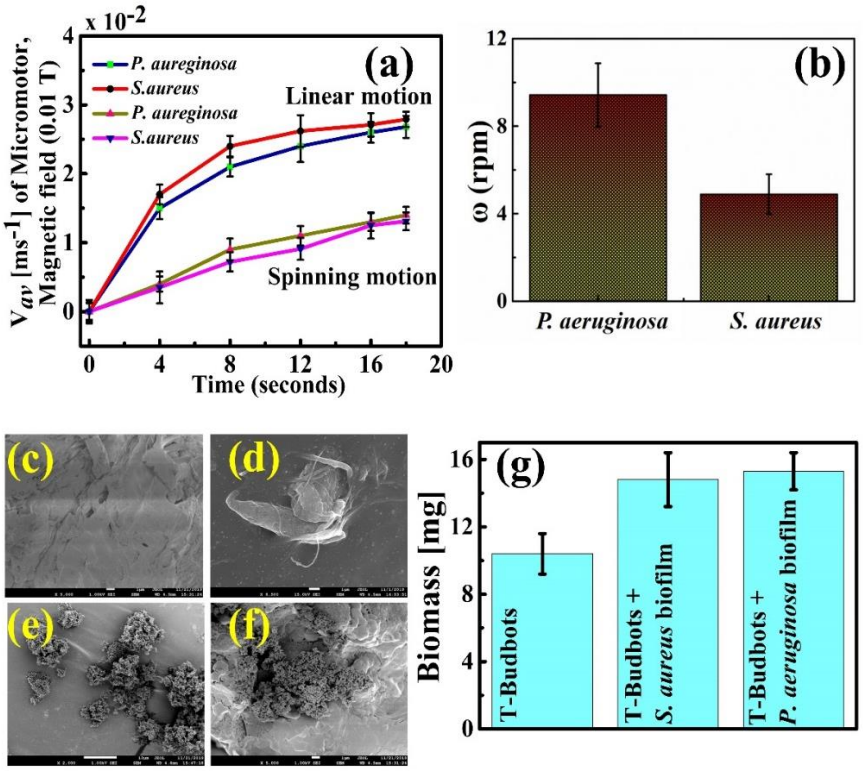

Figure 6.14. **(a)** Average velocity of T-Budbots in the presence of magnetic field (0.01 T) exhibiting linear and spinning motion-based biofilm removal. **(b)** Rotational speed, ω for the spinning microbots on both the bacterial biofilms grown at a concentration of 1×10^8 CFU mL^{-1}. FESEM micrographs of **(c)** control CIP@T-Budbots, **(d)** untreated bacterial biofilm, **(e)** degraded *Staphylococcus aureus* biofilm debris on the surface of T-Budbots and **(f)** degraded *Pseudomonas aeruginosa* biofilm debris on the surface of T-Budbots, Scale bar 1 µm. **(g)** Quantitative measurement of biomass for T-Budbots (control) and T-Budbots after being magnetically driven on the biofilm surface leading to killing and attachment of debris on their surface.

As observed from **Figure 6.14b**, the ω of T-Budbots on *Pseudomonas aeruginosa* biofilms was found to be ~ 9 rpm that was higher than T-Budbots spinning on *Staphylococcus aureus* biofilm (~ 4 rpm). The difference in rotational speeds could possibly due to more surface roughness of *Staphylococcus aureus* biofilm than *Pseudomonas aeruginosa*[77-79], thus taking a long time to complete their spins about an axis.

The FESEM image CIP@T-Budbots and a control biofilm matrix have been represented in **Figure 6.14c** and **6.14d,** respectively. The FESEM micrographs of degraded

Staphylococcus aureus and *Pseudomonas aeruginosa* biofilms attached on the surface of magnetically actuated T-Budbots has been shown in **Figure 6.14e and 6.14f** respectively**.** This confirmed the electrostatic binding of negatively charged biofilms on the surface of cationic microbots, thus proving the disappearance of cellular integrity and biofilm degradation. Moreover, the amount of degraded biomass attached on the surface of microbots was confirmed by calculating the average weight of collective CIP@T-Budbots before and after placing them on biofilm matrix.

As expected, the microbots were showing an incremental increase in weight (from ~10 mg to 14.8 mg) after clearing the debris from the surface confirming removal of debris with precision, represented in **Figure 6.14g**. The control microbot exhibited an average biomass of ~10 mg that was introduced on the surface of biofilms. Later, as the microbots moved on the surface to plow through and remove biofilms, quantitative analysis showed a significant increase of microbot biomass to ~14.8 ± 1 mg. Even the % viability of the drilled-out biofilm attached on the surface of T-Budbots was demonstrated and found to be significantly less than control cells, as described in Figure 6.13d.

Remarkably, the free-floating bacteria were killed, the biofilms were degraded, and debris was removed from the surface to avoid regrowth. Above all, the efficacy of robotic T-Budbots have been demonstrated for bacterial destruction and uprooting of degraded biofilm in a “Kill-Clean” manner. Even though this proof-of-concept is at the initial stage, further optimization for bulk production is being envisioned to increase the potency of the combinatorial therapeutic systems with other resistant antibiotics and target infected biostructures *in vivo* from confined spaces.

6.4. Conclusions

In summary, biocompatible microbots derived from Tea buds was fabricated as a modality for magneto-robotic eradication of biofilms that can effectively address both Gram-positive and Gram-negative bacterial strains. In the first platform, the CIP-modified T-Budbots could show improved antibacterial and antibiofilm susceptibility of drug CIP hydrochloride that was electrostatically integrated on porous T-Budbots, as compared to free CIP and T-Budbots alone. This platform ensures an efficient drug delivery system with sustained release of drug at acidic microenvironment of biofilms. In the second platform, the magnetically driven linear and spinning motion of CIP@T-Budbots could efficiently uproot the degraded biofilms, thus restoring the paths clogged by biofilm in a kill-clean way. Thus, the synergistic kill-clean approach of microfighters have been proposed that provides a conceptual robotic platform offering therapeutic defense against pathogenic bacterial infections and eradicate harmful biofilms from medical and industrial settings.

References

(1) Høiby, N.; Ciofu, O.; Johansen, H. K.; Song, Z.; Moser, C.; Jensen, P. Ø.; Molin, S.; Givskov, M.; Tolker-Nielsen, T.; Bjarnsholt. T. The clinical impact of bacterial biofilms. *Int. J. Oral Sci.* **2011**, 3, 55-65.

(2) Li, X.; Wu, B.; Chen, H.; Nan, K.; Jin, Y.; Sun, L.; Wang, B. Recent developments in smart antibacterial surfaces to inhibit biofilm formation and bacterial infections. *J. Mater. Chem. B.* **2018**, 6, 4274-4292.

(3) Ramasamy, M.; Lee, J. Recent Nanotechnology Approaches for Prevention and Treatment of Biofilm-Associated Infections on Medical Devices. *BioMed. Res. Int.* **2016**, 1851242, 1-17.

(4) Koo, H.; Allan, R. N.; Howlin, R. P.; Stoodley, P.; Hall-Stoodley, L. Targeting microbial biofilms: current and prospective therapeutic strategies. *Nat. Rev*. **2017**, 741-755.

(5) Peterson, B. W.; He, Y.; Ren, Y.; Zerdoum, A.; Libera, M. R.; Sharma, P. K.; Winkelhoff, A. J. V.; Neut, D.; Stoodley, P.; van der Mei, H. C.; Busscher, H. J. *FEMS Microbiol. Rev.* **2015**, 39, 234–245.

(6) Flemming, H. C.; Wingender. J.; Szewzyk, U.; Steinberg, P.; Rice, S. A.; Kjelleberg, S. Biofilms: an emergent form of bacterial life. *Nat. Rev*. **2016**, 563-575.

(7) Stanton, M. M.; Park, B. W.; Vilela, D.; Bente, K.; Faivre, D.; Sitti, M.; Sánchez, S. Magnetotactic Bacteria Powered Biohybrids Target *E. coli* Biofilms. *ACS Nano* **2017**, 11, 9968−9978.

(8) Simon, A. T.; Dutta, D.; Chattopadhyay, A.; Ghosh, S. S. Copper Nanocluster-Doped Luminescent Hydroxyapatite Nanoparticles for Antibacterial and Antibiofilm Applications. *ACS Omega* **2019**, 4, 4697−4706.

(9) Algburi, A.; Comito, N.; Kashtanov, D.; Dicks, L. M. T.; Chikindas, M. Control of Biofilm Formation: Antibiotics and Beyond. *Appl. Environ. Microbiol*. **2017**, 83, e02508-16.

(10) Singh, S.; Singh, S. K.; Chowdhury, I.; Singh, R. Understanding the Mechanism of Bacterial Biofilms Resistance to Antimicrobial Agents. *Open Microbiol. J*. **2017**, 11, 53-62.

(11) Khatoon, Z.; McTiernan, C. D.; Suuronen, E. J.; Mah, T. F.; Alarcon, E. I. Bacterial biofilm formation on implantable devices and approaches to its treatment and prevention. *Heliyon* **2018**, 4, e01067-36.

(12) Jones, E.; Boenink, N. M.; Verhoef, J.; Köhrer, K.; Schmitz, F. Z. Multiple mutations conferring ciprofloxacin resistance in *Staphylococcus aureus* demonstrate

long-term stability in an antibiotic-free environment. *J. Antimicrob. Chemother*. **2000**, 45, 353-356.

(13) Ciofu, O.; Tolker-Nielsen, T. Tolerance and Resistance of *Pseudomonas aeruginosa* Biofilms to Antimicrobial Agents—How *P. aeruginosa* Can Escape Antibiotics. *Front. Microbiol*. **2019**, 10, 1- 15.

(14) Sharma, D.; Misba, L.; Khan, A. U. Antibiotics versus biofilm: an emerging battleground in microbial communities. *Antimicrob. Resist. Infect. Control*. **2019**, 8, 76-86.

(15) Sobisch, L. Y.; Rogowski, K. M.; Fuchs, J.; Schmieder, W.; Vaishampayan, A.; Oles, P.; Novikova, N.; Grohmann, E. Biofilm Forming Antibiotic Resistant Gram-Positive Pathogens Isolated From Surfaces on the International Space Station. *Front. Microbiol*. **2019**, 10, 1- 16.

(16) Kadam, S.; Shai, S.; Shahane, A.; Kaushik, K. S. Recent Advances in Non-Conventional Antimicrobial Approaches for Chronic Wound Biofilms: Have We Found the 'Chink in the Armor'? *Biomedicines* **2019**, 7, 35-61.

(17) Petchiappan, A.; Chatterji, D. Antibiotic Resistance: Current Perspectives. *ACS Omega* **2017**, 2, 7400-7409.

(18) Rediske, A. M.; Roeder, B. L.; Brown, M. K.; Nelson, J. L.; Robison, R. L.; Draper, D. O.; Schaalje, G. B.; Robison, R.A.; Pitt, W. G. Ultrasonic Enhancement of Antibiotic Action on *Escherichia coli* Biofilms: an *In Vivo* Model. *Antimicrob. Agents. Chemother.* **1999**, 43, 1211-1214.

(19) Kiristi, M.; Singh, V. V.; Esteban-Ferna´ndez de Avila, B.; Uygun, M.; Soto, F.; Uygun, D. A.; Wang, J. Lysozyme-Based Antibacterial Nanomotors. *ACS Nano* **2015**, 9, 9252-9259.

(20) Eckert, R.; Brady, K. M.; Greenberg, E. P.; Qi, G.; Yarbrough, D. K.; He, J.; McHardy, I.; Anderson, M. H.; Shi, W. Enhancement of Antimicrobial Activity against *Pseudomonas aeruginosa* by Coadministration of G10KHc and Tobramycin. *Antimicrob. Agents. Chemother*. **2006**, 50, 3833-3838.

(21) Kim, J.; Pitts, B.; Stewart, P. S.; Camper, A.; Yoon, J. Comparison of the Antimicrobial Effects of Chlorine, Silver Ion, and Tobramycin on Biofilm. *Antimicrob. Agents. Chemother*. **2008**, 52, 1446-1453.

(22) Dodd, M. C.; Kohler, H. P. E.; Gunten, U. V. Oxidation of Antibacterial Compounds by Ozone and Hydroxyl Radical: Elimination of Biological Activity during Aqueous Ozonation Processes. *Environ. Sci. Technol*. **2009**, 43, 2498–2504.

(23) Francolini, I.; Vuotto, C.; Piozzi, A.; Donelli, G. Antifouling and antimicrobial biomaterials: an overview. *Acta Pathologica microbiologica, et immunologica Scandinavica*. **2017**, 125, 392-417.

(24) Forier, K.; Raemdonck, K.; De Smedt, S. C.; Demeester, J.; Coenye, T.; Braeckmans, K. Lipid and polymer nanoparticles for drug delivery to bacterial biofilms. *J. Control. Release*. **2014**, 190, 607–623.

(25) VanEpps, J. C.; Younger, J. G. Implantable Device Related Infection. *Shock* **2016**, 46, 597-608.

(26) Tuson, H. H.; Weibel, D. B. Bacteria-surface interactions. *Soft Matter* **2013**, **9**, 4368-4380.

(27) Del Pozo, J. L.; Patel, R. The Challenge of Treating Biofilm-associated Bacterial Infections. *Sci. Transl. Med*. **2007**, 82, 204-209.

(28) Tse, B. N.; Adalja, A. A.; Houchens, C.; Larsen, J.; Inglesby, T. V.; Hatchett, R. Challenges and Opportunities of Nontraditional Approaches to Treating Bacterial Infections. *Clin Infect Dis*. **2017**, 65, 495-500.

(29) Lebeaux, D.; Ghigo, J. M.; Beloin, C. Biofilm-Related Infections: Bridging the Gap between Clinical Management and Fundamental Aspects of Recalcitrance toward Antibiotics. *Microbiol. Mol. Biol. R*. **2014**, 78, 510-543.

(30) Hughes, G.; Webber, M. A. Novel approaches to the treatment of bacterial biofilm infections. *Br. J. Pharmacol*. **2017**, 174, 2237-2246.

(31) He, N.; Hu, J.; Liu, H.; Zhu, T.; Huang, B.; Wang, X.; Wu, Y.; Wang, W.; Qu, D. Enhancement of Vancomycin Activity against Biofilms by Using Ultrasound-Targeted Microbubble Destruction. *Antimicrob. Agents. Chemother*. **2011**, 55, 5331-5337.

(32) Soler, L.; S´anchez, S. Catalytic Nanomotors for Environmental Monitoring and Water Remediation. *Nanoscale* **2014**, 6, 7175-7182.

(33) Parmar, J.; Vilela, D.; Villa, K.; Wang, J.; S´anchez, S. Micro- and Nanomotors as Active Environmental Microcleaners and Sensors. *J. Am. Chem. Soc.* **2018**, 140, 9317-9331.

(34) Zhang, Y.; Yuan, K.; Zhang, L. Micro/Nanomachines: from Functionalization to Sensing and Removal. *Adv. Mater. Technol*. **2019**, 4, 1800636-58.

(35) Patiño, T.; Porchetta, A.; Jannasch, A.; LLado, A.; Stumpp, T.; Schäffer, E.; Ricci, F.; S´anchez, S. Self-sensing enzyme-powered micromotors equipped with pH responsive DNA nanoswitches. *Nano Lett*. **2019**, 19, 3440-3447.

(36) Bhuyan, T.; Singh, A. K.; Dutta, D.; Unal, A.; Ghosh, S. S.; Bandyopadhyay, D. Magnetic Field Guided Chemotaxis of iMushbots for Targeted Anticancer Therapeutics. *ACS Biomater. Sci. Eng*. **2017**, 3, 1627−1640.

(37) Srivastava, S. K.; Clergeaud, G.; Andresen, T. L.; Boisen, A. Micromotors for drug delivery in vivo: The road ahead. *Adv. Drug Deliv. Rev*. **2019**, 138, 41–55.

(38) Medina-S´ anchez, M.; Xu, H.; Schmidt, O. G. Micro- and nano-motors: the new generation of drug carriers. *Ther. Deliv*. **2018**, 9, 303–316.

(39) Tu, Y.; Peng, F.; Andre, A. A. M.; Men, Y.; Srinivas, M.; Wilson, D. A. Biodegradable Hybrid Stomatocyte Nanomotors for Drug Delivery. *ACS Nano* **2017**, 11, 1957-1963.

(40) Delezuk, J. A. M.; Ramírez-Herrera, D. E.; Esteban-Fernández de Ávila, B.; Wang, J. Chitosan-based water-propelled micromotors with strong antibacterial activity. *Nanoscale* **2017**, 9, 2195–2200.

(41) Pena-Francesch, A.; Giltinan, J.; Sitti, M. Multifunctional and biodegradable self-propelled protein motors. *Nat. Commun*. **2019**, 10, 11141-9.

(42) Eskandarloo, H.; Kierulf, A.; Abbaspourrad, A. Light-harvesting synthetic nano- and micromotors: a review. *Nanoscale* **2017**, 9, 12218-12230.

(43) Jin, D.; Yu, J.; Chan, K. H.; Zhang, L. Self-propelled magnesium based micromotors: synthesis and magnetic steering. *MATEC Web. Conf*. **2015**, 32, 04004-5.

(44) Gao, W.; Wang, J. Synthetic micro/nanomotors in drug delivery. *Nanoscale* **2014**, 6, 10486-10494.

(45) Dong, R.; Li, J.; Rozen, I.; Ezhilan, B.; Xu, T.; Christianson, C.; Gao, W.; Saintillan, D.; Ren, B.; Wang, J. Vapor-Driven Propulsion of Catalytic Micromotors. *Sci. Rep.* **2015**, 5, 13226-33.

(46) Abdelmohsen, L. K. E. A.; Peng, F.; Tu, Y.; Wilson, D. A. Micro- and nano-motors for biomedical applications. *J. Mater. Chem. B*, **2014**, 2, 2395-2408.

(47) Gao, W.; Feng, X.; Pei, A.; Kane, C. R.; Tam, R.; Hennessey, C.; Wang, J. Bioinspired Helical Microswimmers Based on Vascular Plants. *Nano Lett*. **2014**, 14, 305−310.

(48) Garcia-Gradilla, V.; Orozco, J.; Sattayasamitsathit, S.; Soto, F.; Kuralay, F.; Pourazary, A.; Katzenberg, A.; Gao, W.; Shen, Y.; Wang, J. Functionalized Ultrasound-Propelled Magnetically Guided Nanomotors: Toward Practical Biomedical Applications. *ACS Nano* **2013,** 7, 9232-924.

(49) Rasamiravaka, T.; Labtani, Q.; Duez, P.; El Jaziri, M. The Formation of Biofilms by *Pseudomonas aeruginosa*: A Review of the Natural and Synthetic Compounds Interfering with Control Mechanisms. *BioMed. Res. Int*. **2015**, 2015, 59348-59365.

(50) Furiga, A.; Lajoie, B.; Hage, S. E.; Baziard, G.; Roques, C. Impairment of *Pseudomonas aeruginosa* Biofilm Resistance to Antibiotics by Combining the Drugs with a New Quorum-Sensing Inhibitor. *Antimicrob. Agents. Chemother*. **2016**, 60, 1676-1686.

(51) Archer, N. K.; Mazaitis, M. J.; Costerton, J. W.; Leid, J. G.; Powers, M. E.; Shirtliff, M. E. *Staphylococcus aureus* biofilms Properties, regulation and roles in human disease. Virulence **2011**, 2, 445-459.

(52) Moormeier, D. E.; Bayles, K. W. *Staphylococcus aureus* Biofilm: A Complex Developmental Organism. *Mol Microbiol*. **2017**, 104, 365-376.

(53) Kumar, P.; Kandi, S. K.; Manohar, S.; Mukhopadhyay, K.; Rawat, D. S. Monocarbonyl Curcuminoids with Improved Stability as Antibacterial Agents against *Staphylococcus aureus* and Their Mechanistic Studies. *ACS Omega* **2019**, 4, 675-687.

(54) Dong, P.; Zhou, Y.; He, W.; Hua, D. A strategy for enhanced antibacterial activity against *Staphylococcus aureus* by the assembly of alamethicin with a thermo-sensitive polymeric carrier. *Chem. Commun*. **2016**, 52, 896-899.

(55) Osonwa, U. E.; Ugochukwu, J. I.; Ajaegbu, E. E.; Chukwu, K. I.; Azevedo, R. B.; Esimone, C.O. Enhancement of antibacterial activity of ciprofloxacin hydrochloride by complexation with sodium cholate. *Bull. Fac. Pharm. Cairo. Univ*. **2017**, 55, 233–237.

(56) Vazquez-Muñoz, R.; Meza-Villezcas, A.; Fournier, P. G. J.; Soria-Castro, E.; Juarez-Moreno, K,; Gallego-Herna´ndez, A. L.; Bogdanchikova, N.; Vazquez-Duhalt, R.; Huerta-Saquero, A. Enhancement of antibiotics antimicrobial activity due to the silver nanoparticles impact on the cell membrane. *PLoS One* **2019**, 14, e0224904-18.

(57) Faulkner, A.; van Leeuwen, T.; Feringa, B. L.; Wezenberg, S. J. Allosteric Regulation of the Rotational Speed in a Light-Driven Molecular Motor. *J. Am. Chem. Soc*. **2016**, 138, 13597−13603.

(58) Hamilton-Miller, J. M. T. Antimicrobial Properties of Tea (*Camellia sinensis* L.). *Antimicrob. Agents. Chemother*. **1995**, 39, 2375-2377.

(59) Reygaert. W. C. The antimicrobial possibilities of green tea. *Front. Microbiol*. **2014**, 5, 1-8.

(60) Gopal, J.; Muthu, M.; Paul, D.; Kim, D. H.; Chun, S. Bactericidal activity of green tea extracts: the importance of catechin containing nano particles. *Sci. Rep.* **2016**, 6, 19710-19724.

(61) Frank, L. A.; Onzi, G. R.; Morawski, A. S.; Pohlmann, A. R.; Guterres, S. S.; Contri, R. V. Chitosan as a coating material for nanoparticles intended for biomedical. *React. Funct. Polym.* **2020**, 147, 104459-104473.

(62) Tariq, M.; Patole, S.; Aruna, K. Antibacterial activity of green tea (Camellia sinensis) leaf extract against Metallo-β-lactamase producing uropathogens. *Int. J. Adv. Res. Biol. Sci.* **2015**, 2, 9–15.

(63) Susanti, E.; Ciptati.; Ratnawati, R.; Aulanni'am.; Rudijanto, A. Qualitative analysis of catechins from green tea GMB-4 clone using HPLC and LC-MS/MS. *Asian. Pac. J. Trop. Biomed*. **2015**, 5, 1046–1050.

(64) Matta, M.K.; Chockalingam, A.; Gandhi, A.; Stewart, S.; Xu, Lin.; Shea, K.; Patel, V.; Rouse, R. LC-MS/MS based quantitation of ciprofloxacin and its application to antimicrobial resistance study in Balb/c mouse plasma, urine, bladder and kidneys. *Anal. Methods*. **2018**, 10, 1237-1246.

(65) Veach, B.; Hawk, H.; Fong, A.; Langley, D. LC/MS/MS Determination of Fluoroquinolones in Honey, *Laboratory Information Bulletin* **2007**, 4389, 1–11.

(66) El-bagary, R.; El-Zaher, A. A.; Elkady, E.; Abdelkerim Mandour, A. Simultaneous determination of ciprofloxacin hydrochloride and metronidazole in spiked human plasma by ultra performance liquid chromatography-tandem mass spectroscopy. *J. Appl. Pharm. Sci*. **2016**, 6, 041-047.

(67) Buyukgoz, G. G.; Soforoglu, M.; Akgul, N. B.; Boyaci, I. H. Spectroscopic fingerprint of tea varieties by surface enhanced Raman spectroscopy. *J. Food. Sci. Technol*. **2016**, 53, 1709–1716.

(68) Xia, J.; Wang, D.; Liang, P.; Zhang, D.; Du, X.; Ni, D.; Yu, Z. Vibrational (FT-IR, Raman) analysis of tea catechins based on both theoretical calculations and experiments. *Biophys. Chem*. **2020**, 256, 106282-291.

(69) Venkatasubbu, G. D.; Ramasamy, S.; Ramakrishnan, V.; Kumar, J. Nanocrystalline hydroxyapatite and zinc-doped hydroxyapatite as carrier material for controlled delivery of ciprofloxacin. *3 Biotech* **2011**, 1, 173-186.

(70) Sahoo, S.; Chakraborti, C. K.; Mishra, S. C. Qualitative analysis of controlled release ciprofloxacin/carbopol 934 mucoadhesive suspension. *J. Adv. Pharm. Tech. Res*. **2011**, 2, 195-204.

(71) Delcour, A. H. Outer Membrane Permeability and Antibiotic Resistance. *Biochim. Biophys. Acta.* **2009**, 1794, 808-816.

(72) Miller, S. I. Antibiotic Resistance and Regulation of the Gram-Negative Bacterial Outer Membrane Barrier by Host Innate Immune Molecules. *mBio* **2016**, 7, e01541-16.

(73) Pignatello, R.; Leonardi, A.; Fuochi, V.; Petronio, G. P.; Greco, A. S.; Furneri, P. M. A Method for Efficient Loading of Ciprofloxacin Hydrochloride in Cationic Solid Lipid Nanoparticles: Formulation and Microbiological Evaluation. *Nanomaterials* **2018**, 8, 304-315.

(74) Tiwari, R. P.; Bharti, S. K.; Dikshit, R. P.; Hoondal, G. S. Synergistic antimicrobial activity of tea & antibiotics. *Indian. J. Med. Res.* **2005**, 122, 80-84.

(75) Conley, Z. C.; Bodine, T. J.; Chou, A.; Zechiedrich, L. Wicked: The untold story of ciprofloxacin. *PLoS Pathog.* **2018**, 14, e1006805-13.

(76) Kohanski, M. A.; Dwyer, D. J.; Hayete, B.; Lawrence, C. A.; Collins, J. J. A common mechanism of cellular death induced by bactericidal antibiotics. *Cell* **2007**, 130, 797−810.

(77) Cucarella, C.; Solano, C.; Valle, J.; Amorena, B.; Lasa, I.; Penadés, J. R. Bap, a *Staphylococcus aureus* Surface Protein Involved in Biofilm Formation. *J. Bacteriol. Res.* **2001**, 183, 2888-2896.

(78) Grosjean, G.; Hubert. M.; Collard, Y.; Sukhov, A.; Harting, J.; Smith, A.; Vandewalle, N. Capillary assemblies in a rotating magnetic field. *Soft Matter* **2019**, 15, 9093-9103.

(79) Porter, K. B.; Caplovitz. G. B.; Kohler, P. J.; Ackerman, C. M.; Tse, P. U. Rotational and translational motion interact independently with form. *Vision Res*. **2011**, 51, 2478-2487.

CHAPTER 7

Summary and Future Scopes

Contents

7.1. Summary

In summary, the thesis reports the fabrication of a host of micro and nanomotors derived from plants. The miniaturized motors could be efficiently guided to achieve a controlled motion under the influence of either *in situ* chemical fuel gradient or fuel-free acoustic or magnetic field. These fabricated micromotors were employed in pH sensing, drug loading, on-demand sustained drug release at targeted site to perform vital therapeutic tasks. The attractive propulsion and near fuel-free requirements of plant-derived motors are expected to revolutionize disease treatments owing to their future practical endeavors – specifically biomedical ones.

In **Chapter 2,** controlled migration of an intelligent and biocompatible "iMushbot" composed of *Agaricus bisporus*, mushroom microcapsules coated with magnetite nanoparticles has been studied. The otherwise randomly moving microbot could meticulously direct itself toward and away from the acid- and alkali-rich regions with the help of acid, acidic catalase, and alkali stimuli, emulating the chemotaxis of microorganisms. The presence of magnetite nanoparticles not only helped in improving the "activity" of the motor through the heterogeneous catalytic decomposition of the peroxide fuel but also provided a remote magnetic control on the chemotaxis. The mesoporous iMushbots having negative ζ-potential could easily be loaded with the cationic anticancer drugs, which were magnetically guided toward the cancerous cells to cause apoptosis.

In **Chapter 3,** the feasibility of a self-propelling mushroom motor, namely a 'logibot' has been explored as a functional unit for the construction of a host of optimized binary logic gates. Emulating the chemokinesis of unicellular prokaryotes or eukaryotes, the logibots

made stimuli-responsive conditional movements at varying speeds towards a pair of acid-alkali triggers. A series of integrative logic operations and cascaded logic circuits, namely, AND, NAND, NOT, OR, NOR, and NIMPLY, have been constructed employing the decisive chemotactic migrations of the logibot in the presence of the pH gradient established by the sole or coupled effects of acid (HCl-catalase) and alkali (NaOH) drips inside a peroxide bath. The external stimuli-responsive self-propulsion of the logibots following different logic gates and circuits can not only be an eco-friendly alternative to the silicon-based computing operations yet also be a promising strategy for the development of intelligent pH-responsive drug delivery devices.

Chapter 4 describes a proficient method for disinfecting water-borne coliform bacterial strains of *Escherichia coli DH5α* from contaminated water samples using magnetic microbots decorated with curcumin conjugates. These magnetic microbots, namely iButtonbots, were composed of soft *Agaricus bisporus* (button mushroom) microcapsules with inherit antimicrobial properties. The locomotives were coated with magnetite nanoparticles for their remote guidance towards cells and collection along with curcumin for an enhanced bactericidal response. The presented biocompatible microbots offer an innovative method for the rapid decontamination of bacteria-laden drinking water samples.

In **Chapter 5,** the fabrication of ascorbic acid (AA) template nanomotors has been reported using buds of *Camelia sinensis*, undergoing fuel-free propulsion. The motors, namely, Teabots, display propulsion by converting the sound energy from the acoustic field into a mechanical one. The mesh-like structures of the anionic Teabots facilitate superior adsorption of ascorbic acid (AA-Teabots) undergoing a controlled release. The motors show antioxidant properties at the physiological pH range by scavenging intracellular reactive

oxygen species. . The acoustic delivery of AA-Teabots could protect HEK-293 cells from oxidative injuries alongside preventing protein-aggregation derived diseases.

In **Chapter 6**, biocompatible micromotors from Tea buds (T-Budbots) were designed that can be magnetically driven on the biofilm matrix to kill and remove the fragmented biofilm segments with precision, a "Kill-Clean" strategy. With these principles, bactericidal robotic platform decorated with magnetite nanoparticles has been presented aimed at clearing biofilm on the surfaces. The smart T-Budbots can integrate antibiotic Ciprofloxacin on their surface and increase their antibacterial efficacy against pathogenic bacterial communities of *Pseudomonas aeruginosa* and *Staphylococcus aureus*. It is noteworthy that the release of bound drug from the porous T-Budbots was triggered by the acidic environment of the biofilm. This work represents a first step in the involvement of a plant-based microbot exhibiting magneto-robotic therapeutic properties, providing a non-invasive and safe approach to dismantle harmful biofilm infections.

Briefly, this thesis has covered the new principles based on exploiting plant tissues for designing micro- and nanomotors, which seems to improve drug transport, tissue penetration, and, most importantly, physical and/or chemical actuation of motors. The scientific findings can be listed in the following ways:

- The thesis shows that mushrooms can be thought of smart alternative against the synthetic materials for fuel-driven and fuel-free controlled drug delivery applications with minimal side effects, which opens new avenues for mushroom-based futuristic biomaterials for anticancer therapeutics. However, selection of mushroom species based on attributes such as toxicological profiles, porosity, enzyme content and medicinal values are extremely important to ensure reproducibility. On the contrary, same species

of mushrooms cultivated in different localities would certainly portray a lesser extent of non-reproducibility, upon standardization.

- The thesis reports the design of versatile operational logic gates and cascaded circuits based on the pH sensing ability of tissue-based mushroom logibots. It is expected that this study may provide an important starting point for the future design of plant tissue-based logic gates, which may also be of significance in various next-generation biomedical, mechanical, pharmaceutical, and electronic applications at the micro or nanoscale.
- A highly effective bacterial killing approach has been demonstrated based on the coupling of the antibacterial activity of biocompatible curcumin loaded micromotor (CU@iButtonbots) with their magnetically guided motion. The biocompatibility of such mushroom-based bacterial microfighters makes them promising candidates not only to *in vitro* applications yet also for diverse *in vivo* therapeutics.
- The thesis also reports an ultrasound-propelled ascorbic acid loaded nanomotors, namely AA-Teabots, from *Camellia sinensis*, which could offer efficient loading, localized transport, and release capabilities of therapeutic payloads for anti-oxidative and anti-amyloidogenic responses.
- Besides this, struggle against pathogenic bacterial biofilm was possible by (i) killing the embedded bacteria using antibiotic (CIP) loaded T-Budbots; (ii) disturbing biofilm architecture to improve penetration of antibiotic; and (iii) removing the degraded matrix using magnetic field actuation by "**Kill-Clean**" approach.

To summarize, the fabricated microbots have been classified in a tabulated form (**Table 7.1**) based on their size, shape, fabrication materials, actuation, applications, advantages and challenges.

Microbots	**Size /Shape**	**Materials**	**Actuation**	**Applications**	**Advantages**	**Challenges**
iMushbots	50-160 µm/ Pseudo-spherical	FeONPs-coated Button Mushroom	Self-propulsion and Magnetic	Drug delivery and Anticancer therapeutics	Powered, controlled, autonomous actuation, biocompatible, porosity, sophisticated pH sensing, low cost	Miniaturization, shape control, unstable under acoustic waves, fuel requirement, *in vivo* application
Logibots	50-160 µm/ Pseudo-spherical	FeONPs-coated Button Mushroom	Self-propulsion and Magnetic	Designing logic gates	Dual pH sensing, easy to fabricate, biocompatible, autonomous propulsion, magnetic steering, low cost	Multiple inputs responsiveness, poor robustness under ultrasonic waves, sophisticated control
iButtonbots	40-200 µm/ Pseudo-spherical	FeONPs-coated Button Mushroom	Magnetic	Drug delivery, Bactericidal agents for water remediation	Biocompatible, low cost, easy to fabricate, fuel-free motion, inherent antibacterial components, magnetic control, porosity	Large-scale water treatment, collective magnetic motion, costly set up, advanced control strategies
Teabots	200-500 nm/ Spherical	Tea leaves	Acoustic	Drug delivery and ROS scavenging	Stable, high speed, linear and circular motion, effective drug release, low cost, fuel-free motion, biocompatible, bio-imaging, porosity	Intracellular tracking, trained person, bulky power sources, *in vivo* activity, optimizing ultrasound- mediated drug release
T-Budbots	50-100 µm/ Irregular	FeONPs-coated Tea Buds	Magnetic	Drug delivery, Antibacterial and Anti-biofilm	Stable, biocompatible, antibacterial components, robust, porosity, fuel-free linear and spinning motion	Large-scale setup, advanced control strategies, bulk production, activity in confined spaces

Table 7.1. Major categories, advantages and challenges of plant-based microbots.

7.2. Future Scopes

The fabrication of plant-derived functional micro/nanomotors will require a culmination of all research avenues that have been discussed here as well as for new applications. Notably, despite these current advancements in plant-based MNMs, many challenges remain to be addressed for rendering these initial proof-of-concept studies into real-world *in vivo* applications. Some of the tremendous yet exciting challenges include immune rejection, partial tissue penetration, precise navigation, spontaneous release of the drug payloads and propulsion against the dynamic blood flow. In this regard, standardized methodologies, duration of treatment, the selection of species, sensitivity of assay, warranty of subjective evaluation and calculating sample size of animals are critically important. Key factors such as toxicity of the material and environmental fate needs to be considered. Additionally, checking formulations, monitoring of controls, tested animals, measured effects and level of doses is of great importance. By considering comparable nature of disease between the human and animal models, the data obtained can be more reliable. For instance, xenograft mouse model used for cancer studies may exhibit different levels of immunodeficiency and their difference in tumor microenvironment might affect the experiment, resulting in poor data correlation with in vitro studies. Further, treatment of micro/nanomotors as pharmaceutical formulations in studies with detailed pharmacokinetic and pharmacodynamic parameters could bridge the gap between medical doctors and researchers.Even in well-designed in vivo experiments, the translatability of data may weaken due to some dissimilarities between human and animal components. Developments into microelectromechanical systems (MEMS)/nanoelectromechanical systems (NEMS) technology could create a vision for materializing allied research into clinical setup. Thus,

considering the above-mentioned points will increase the reproducibility and reliability of preclinical results-with a brighter future ahead- towards clinical trials. Eventually, with careful attention to key challenges and requirements, such externally driven plant-based MNMs will create new avenues for delivering therapeutic payloads directly to targeted destinations.

Where do we go from here? The ability of plant-based MNMs to address biomedical and environmental problems is just beginning to be investigated. In the not-so-distant future, presented work can be extended in various ways:

- The work in Chapter 2 confirmed the killing of two-dimensional (2D) cancer cells by self-propelling iMushbots. However, the efficiency of iMushbots to destroy three-dimensional (3D) cancer models can be envisioned to study the physiologic drug responses. Hence, the investigation of signaling in spheroids and the reactions in the mice models upon drug treatment will be advantageous for anticancer therapeutics.
- The work in Chapter 3 can be further extended by designing logic gates based on the multi-stimuli-responsive motion behavior of logibots. Their on-off motion can be studied by the application of varying concentration of H_2O_2, and ultrasound induced-collective motion of logibots. Also, it is likely that micromotors moving collectively in a pH gradient will undergo a change in zeta potential, resulting in aggregation of motors. Propulsion of aggregated motors in a pH gradient based on surface charges can be further investigated using ultrasonic waves and magnetic fields along a predetermined route for *in vitro* and *in vivo* experiments.
- The Chapter 4 details in explaining the antibacterial activity of biocompatible curcumin loaded micromotors (CU@iButtonbots) against Gram-Negative bacteria. In this regard,

their antibacterial efficacy can be tested against Gram-Positive bacteria coupled with their anti-biofilm efficacies. Swarms of micromotors could be used for accelerating the bacterial killing in large contaminated areas, while guidance of the micromotors could be achieved by the assistance of a magnetic segment. Thus, stochastic models for predicting magnetotactic behavior of swarms in large-scale spaces need to be urgently developed, perceiving the environment actions and creating feedback loop.

- In Chapter 5, a swarm of acoustically propelled Teabots could be investigated exhibiting neuroprotective efficacy in neuronal cells, mainly targeting Alzheimer's disease.
- In Chapter 6, our preliminary data revealed the organized schooling of T-Budbots to eradicate and destroy biofilms at laboratory scale. Magnetic manipulation of such biocompatible microbots could be used to eliminate biofilm in model human teeth as well as ocular biofilms.
- It is hoped that more efforts to understand the physical and chemical mechanisms involved in plant-based biomotors will undoubtedly lead to huge technological breakthroughs in the field of therapeutics. The concept of studying the dynamics of motor motion by time-dependent mean square displacement (MSD) and coupling to a non-Newtonian fluid rheology is very much the key components in future attempts to overcome challenges of propulsion. Specifically, the technique of motor tracking microrheology can be performed within living cells using bio-microrheology (BMR) for an exciting understanding of cell physiology and monitoring the effects of targeted drug delivery.

Appendix - I

PUBLICATIONS, PATENTS, CONFERENCES

A1.1. Publications (From Thesis Work)

1. **T. Bhuyan**, A. T. Simon, S. Maity, A. K. Singh, S.S. Ghosh, D. Bandyopadhyay, Magnetically Controlled Tea Microbots to Target Biofilms in a Kill-Clean Way, 2020 - *Submitted, under review.*

2. **T. Bhuyan**, A. K. Singh, S.S. Ghosh, D. Bandyopadhyay, Magnetotactic Curcumin iButtonbots as Efficient Bactericidal Agents, *Bulletin of Material Sciences*, 2020, 43, 111 -121.

3. **T. Bhuyan,** D. Dutta, M. Bhattacharjee, A.K. Singh, S.S. Ghosh, D. Bandyopadhyay, Acoustic Propulsion of Vitamin C Loaded Teabots for Targeted Oxidative Stress and Amyloid Therapeutics, *ACS Applied Bio Material***s,** 2019, 2, 4571-4582.

4. **T. Bhuyan**, A. K. Singh, M. Bhattacharjee, S. S. Ghosh, D. Bandyopadhyay Boolean-Chemotaxis of logibots deciphering the motions of Self-propelling Microorganisms, *Soft Matter*, 2018, 14, 3182-3191.

5. **T. Bhuyan**, A. K. Singh, D. Dutta, A. Unal, S. S. Ghosh, D. Bandyopadhyay, Magnetic Field Guided Chemotaxis of iMushbots for Targeted Anticancer Therapeutics, *Biomaterial Science & Engineering*, 2017, 3, 1627-1640.

A1.2. Publications (In Collaboration)

1. S. Maity, **T. Bhuyan**, D. Das, D. Bandyopadhyay, Microfluidic Immunosensor for Point-of-Care-Testing of Beta-2-Microglobulin in Tear, *ACS Sustainable Chemistry & Engineering*, 2020 – *Just accepted.*

2. A. K. Singh, **T. Bhuyan**, S. Maity, T. K. Mandal, D. Bandyopadhyay, Multimodal Self-Propulsion of CARBOts for Water Detoxification and Oil-spill Recovery, *ACS Applied Nanomaterial*, 2020, 4, 3459-3470.

3. Lankipalli Harsha, **T. Bhuyan**, Pranab K Mondal, Siddhartha Sankar Ghosh, and Dipankar Bandyopadhyay, Robust Liquid Marbles for Microscale Transport of Hydrogen Peroxide, 2020 -*Submitted, under review.*

A1.3. National Patents (In Collaboration)

1. S. Maity, S. Ghosh, **T. Bhuyan**, D. Das, D. Bandyopadhyay, A microfluidic POCT immunosensor for the Plasmonic detection of beta-2-microglobulin in tear or urine, *The Office Journal of the Patent Office,* Journal no. 32/2019, Page no. 35395. Application number: 201931028121 A.

A1.4. Conferences

1. **T. Bhuyan,** D. Ghosh, D. Bandyopadhyay, S. S. Ghosh. Extracellular Matrix-based Micromotors for Anticancer Therapeutics, *Third International Conference on Material Science (ICMS 2020),* Department of Physics, Tripura University, Tripura, India.

2. **T. Bhuyan,** D. Dutta, M. Bhattacharjee, A.K. Singh, S.S. Ghosh, D. Bandyopadhyay. Acoustically propelled Teabots for ROS Scavenging Activity, *6th International Conference on Advanced Nanomaterials and Nanotechnology (ICANN 2019),* Centre for Nanotechnology, IIT Guwahati.

3. S. Maity, **T. Bhuyan,** S.S. Ghosh, D. Bandyopadhyay. Advanced Microfluidic Reactor Based Nanomedicine for Antibacterial Treatment. *6th International Conference on Advanced Nanomaterials and Nanotechnology (ICANN 2019),* Centre for Nanotechnology, IIT Guwahati.

4. **T. Bhuyan**, A. K. Singh, M. Bhattacharjee, S. S. Ghosh, D. Bandyopadhyay, Synthesizing Boolean Logic Gates based on Chemotaxis-guided Micromotor, *International Conference on Biotechnology & Biological Sciences BIOSPECTRUM* 2019, UEM, Kolkata.

5. **T. Bhuyan**, A. K. Singh, S. S. Ghosh, D. Bandyopadhyay, Fabrication of drug loaded biocompatible micromachines for antibacterial efficacy, *Research Conclave 2019*, IIT Guwahati. **(Best Oral in Oral Presentation).**

6. **T. Bhuyan**, A. K. Singh, D. Dutta, A. Unal, S. S. Ghosh, D. Bandyopadhyay, Fabrication of plant-based motors for therapeutic applications, *International Conference on Advanced Materials (ICAM-2019)*, Jamia Millia Islamia, New Delhi.

7. **T. Bhuyan**, A. K. Singh, M. Bhattacharjee, S. S. Ghosh, D. Bandyopadhyay, Boolean Chemotaxis of Logibots, *Annual Chemical Engineering Symposium Reflux 2018, IIT Guwahati*.

8. **T. Bhuyan**, A. K. Singh, D. Dutta, A. Unal, S. S. Ghosh, D. Bandyopadhyay, Chemo-Magnetotactic Mushroom tissue-based Microbots for Antitumor Drug delivery, *International Conference on Nanotechnology: Ideas, Innovations and Initiatives (ICN3I-2017)* IIT Roorkee, India, 2017.

9. **T. Bhuyan**, A. K. Singh, D. Dutta, A. Unal, S. S. Ghosh, D. Bandyopadhyay, *Plant Tissue – based self-propelling biomotors: A Review*, *International Symposium on Micro- and Nanomachines*, 2016 Schloss Herrenhausen, Hannover, Germany.

10. **T. Bhuyan.** Participated in *3rd National workshop on MRMS/NEMS and Theranostic Devices, February*, 2017, organized by Centre for Excellence in Research and Development of Nano electronic Devices under the aegis of Centre for nanotechnology, IIT Guwahati, India.